First Mass Measurements of Highly Charged, Short-lived Nuclides in a Penning Trap and the Mass of ^{74}Rb

by

Stephan Ettenauer

Dipl. Ing., Vienna University of Technology, 2006

A THESIS SUBMITTED IN PARTIAL FULFILLMENT
OF THE REQUIREMENTS FOR THE DEGREE OF

Doctor of Philosophy

in

THE FACULTY OF GRADUATE STUDIES

(Physics)

The University Of British Columbia

(Vancouver)

May 2012

Abstract

To date, V_{ud} of the Cabibbo-Kobayashi-Maskawa quark mixing matrix is most precisely determined from superallowed $0^+ \rightarrow 0^+$ nuclear β-decays. In addition to half-life, Branching Ratio, and transition energy (called Q_{EC}-value) of a superallowed decay, theoretical corrections have to be considered to extract V_{ud}. Among those, the isospin symmetry breaking corrections, δ_C, show discrepancies between different theoretical models, which are critical to be resolved. ^{74}Rb has the largest δ_C of all 13 superallowed β-emitters used to obtain V_{ud} and would carry particular weight to discriminate between models were it not limited by the uncertainty in the Q_{EC}-value. However, ^{74}Rb's half-life of 65 ms has previously posed a real challenge to the experimental precision in its Q_{EC}-value, which is best determined by direct mass measurements in Penning traps.

In this work, Penning trap mass measurements of short-lived nuclides have been performed for the first time with highly-charged ions, using the TITAN facility. Compared to singly-charged ions, this provides an improvement in experimental precision that scales with the charge state q. Neutron-deficient Rb-isotopes have been prepared in an electron beam ion trap to $q = 8 - 12+$ prior to the mass measurements. In combination with a Ramsey scheme, this opens the door to unrivalled precision with gains of 1-2 orders of magnitude. The method is particularly suited for short-lived nuclides such as ^{74}Rb and its mass has been determined.

In the realm of fundamental symmetries studied in low-energy nuclear systems such as in ^{74}Rb, the precision achieved by highly-charged ions is essential. For mass measurements motivated by nuclear structure or nuclear astrophysics, where the present experimental precision is already sufficient, this novel technique significantly reduces the measurement time and thus allows one to map the nuclear mass landscape more broadly. In the exploration towards the limits of nuclear existence where experimental efforts typically face shorter half-lives and lower production yields of radioisotopes, the same precision can be achieved by compensating for both challenges with the higher charge state. Finally, highly-charged ions provide opportunities for an unprecedented resolving power to identify low-lying nuclear isomers. This potential has firstly been demonstrated with ^{78,78m}Rb$^{q=8+}$.

Preface

As with almost every experimental work in contemporary nuclear physics, the studies presented in this thesis are the result of a collaboration between many people. The multi-ion-trap setup at TRIUMF's Ion Trap for Atomic and Nuclear science (TITAN) has been operational since 2007. For the present work, several improvements and modifications of the setup, or in its operation, were necessary of which my most significant contributions are listed below. All people in the TITAN group at TRIUMF helped at all stages of the work.

- From fall 2009 to spring 2011, I was in charge of the mass measurement program at TITAN. This involved the planning and preparation of measurements, leadership during the experiments, and the coordination with TRIUMF's accelerator division before and during experimental beamtimes.

- The preparation of the online beamtime of $^{44}K^{4+}$ was done together with Maxime Brodeur, Paul Finlay, and Alain Lapierre (see Section 3.4). This beamtime represented a proof-of-principle experiment and was crucial to identify challenges in the program of Penning trap mass measurements with Highly Charged Ions (HCI).

- Performance tests of the Pulsed Drift Tube (PLT) after the Radio-Frequency Quadrupole (RFQ) were carried out initially together with Thomas Brunner and later with Ernesto Mané (Section 3.3.1 and Section A.1). As a result, critical issues regarding the reliability of the PLT could be resolved.

- In collaboration with Mel Good, I carried out the work regarding the baking of the Measurement Penning Trap (MPET), the hardware upgrade of its vacuum system as well as MPET setup modifications (Section 3.7.8 and Section A.5). Due to charge exchange with the residual gas in the MPET, an improved vacuum was essential for HCI.

- The major part of the preparation for the neutron deficient Rb runs I conducted together with Martin Simon (among others Section 3.5 and Section A.3). This required the development of a suitable optimization procedure to yield fast and efficient charge breeding to higher charge states in the Electron Beam Ion Trap (EBIT). Based on the previous experience for $^{44}K^{4+}$, the efficiency had been identified as one of the most challenging aspects of the present work.

- The extension of the mass measurements to ^{78,78m}Rb to demonstrate the improved resolving power for low-lying isomeric states was based on my idea.

- For the first time at TITAN, I implemented and tested the Ramsey excitation scheme (Section 3.7.4). The Ramsey excitation technique led to an improvement in measurement precision by a factor of ≈ 2.

- By utilizing Aaron Gallant's work on a code which fits the theoretical line shape to a Time-Of-Flight (TOF)-resonance, I wrote an analysis code to perform the present analysis (Chapter 4). Aaron Gallant and I independently derived the covariant matrix to take into account correlations between extracted frequency ratios (Appendix B). Analysis progress was discussed weekly with Ankur Chaudhuri, Aaron Gallant, and Vanessa Simon.

- I developed the idea for the new test of the Isospin Symmetry Breaking (ISB) corrections for superallowed β-decays (Section 5.1).

A letter describing the main part of the work, i.e. the mass measurement of neutron-deficient Rb-isotopes, is published in
S. Ettenauer et al., Phys. Rev. Lett. 107, 272501 (2011)
First Use of High Charge States for Mass Measurements of Short-Lived Nuclides in a Penning Trap

A second publication is planned to cover more details of the experimental setup, the analysis, as well as the implications of the result.

The mass measurement of $^{44}K^{4+}$ (see Section 3.4) is part of two publications"
A. Lapierre et al., Phys. Rev. C 85,024317 (2012)
Penning-trap mass measurements of the neutron-rich K and Ca isotopes: Resurgence of the N = 28 shell strength
and

A. Lapierre et al., Nucl. Instr. and Meth. A 624, 54 (2010)
The TITAN EBIT charge breeder for mass measurements on highly charged short-lived isotopes- First online operation

The newly demonstrated technique to resolve low-lying isomeric states (Section 5.4) will be published. A manuscript is available at http://arxiv.org/abs/1112.0614v1:
A. T. Gallant et al., arXiv:1112.0614
Highly charged ions in Penning traps, a new tool for resolving low lying isomeric states

Table of Contents

ix

List of Tables

List of Figures

Glossary

AME   Atomic Mass Evaluation

ARIEL   Advanced Rare IsotopE Laboratory

BNG   Bradbury Nielsen ion Gate

BNL   Brookhaven National Laboratory

BR   Branching Ratio

χ**EFT**   chiral Effective Field Theory

CKM   Cabibbo-Kobayashi-Maskawa

CPET   Cooler Penning Trap

CVC   Conserved Vector Current

DFT   Density Functional Theory

EBIT   Electron Beam Ion Trap

EC   Electron Capture

EFT   Effective Field Theory

EXO   Enriched Xenon Observatory

FAIR   Facility for Antiproton and Ion Research

FEBIAD   Forced Electron Beam Induced Arc Discharge

FRIB   Facility for Rare Isotope Beams

FSU   Florida State University

FT-ICR	Fourier-Transform Ion-Cyclotron-Resonance
GUT	Grand Unified Theory
HCI	Highly Charged Ions
IMME	Isobaric Mass Multiplet Equation
ISAC	Isotope Separator and ACcelerator
ISB	Isospin Symmetry Breaking
ISOL	Isotope Separator On-Line
LEBIT	Low-Energy Beam and Ion Trap facility
MCP	Multi Channel Plate
MCS	Multi Channel Scaler
MOSFET	Metal-Oxide Semiconductor Field-Effect Transistors
MPET	Measurement Penning Trap
NCSM	No-Core Shell Model
NSCL	National Superconducting Cyclotron Laboratory
OLIS	Off-Line Ion Source
PDG	Particle Data Group
PLT	Pulsed Drift Tube
PMNS	Pontecorvo-Maki-Nakagawa-Sakata
PPB	Parts-Per-Billion
PPG	Programmable Pulse Generator
QCD	Quantum Chromodynamics
QED	Quantum Electrodynamics
RF	Radio-Frequency
RFQ	Radio-Frequency Quadrupole

RH Relativistic Hartree

RHF Relativistic Hartree-Fock

RIBF RadioIsotope Beam Factory

RMS Root-Mean-Square

RPA Random-Phase Approximation

SCEPTAR Scintillating Electron Positron Tagging Array

SCI Singly Charged Ions

SMILETRAP Stockholm-Mainz-Ion-LEvitation-TRAP

SUSY SUperSYmmetry

SWIFT Stored Waveform Inverse Fourier Transform

TITAN TRIUMF's Ion Trap for Atomic and Nuclear science

TOF Time-Of-Flight

TOF-ICR Time-Of-Flight Ion-Cyclotron-Resonance

UCN Ultra Cold Neutrons

Acknowledgements

To my family

Chapter 1

Introduction

Since their introduction into the research of radioisotopes over twenty years ago
[3, 4], Penning traps have made major contributions to the exploration of the nu-
clear mass surface. This is evidenced by the large number of existing and proposed
facilities [5] as well as the wealth of experimental results [6]. Advances in ex-
perimental techniques now allow measurements for virtually all low energy, rare
isotope beams as Penning traps have been able to access nuclides with half-lives
below 10 ms [7] as well as superheavies (elements with proton number $Z > 92$)
with production cross sections that correspond to yields of less than 1 particle per
second [8, 9]. The widespread success of Penning traps is due to their precision
following the expression

$$\frac{\delta m}{m} \propto \frac{m}{qBT_{\mathrm{rf}}\sqrt{N_{\mathrm{ion}}}} \tag{1.1}$$

[10], where $\delta m/m$ is the achievable relative precision in mass m, q is the ion's
charge state and B is the magnetic field strength. The measurement time T_{rf} and
the number of ions N_{ion} are limited by a nuclide's half-life and possibly by its pro-
duction yield at radioactive beam facilities, but also by the efficiency of the spec-
trometer. Measurements are generally performed with Singly Charged Ions (SCI)
or in special cases, where coupled to a gas stopper cell, with $q = 2+$. Penning
trap mass studies utilizing Highly Charged Ions (HCI) have been successfully pio-
neered with stable nuclides [11]. Here the requirements of high efficiency and short
measurement times are less relevant compared to the requirements when working
with radioactive ions. In the realm of rare isotope science with Penning traps,
HCI represent a thus far unexplored opportunity to improve the experimental preci-
sion further circumventing constraints imposed by short half-lives and lower yields
when probing the limits of nuclear existence.
The superallowed β emitter ^{74}Rb is a prime example where a short half-life of

only 65 ms poses a real challenge to experiment. Despite several Penning trap mass measurements [12–14], the total transition energy, Q_{EC}, still contributes significantly to the uncertainty of its corrected $\mathcal{F}t$-value, only surpassed by theoretical uncertainties of the isospin-symmetry breaking corrections δ_C [15]. The latter have recently been reduced by experimentally providing the ^{74}Rb Root-Mean-Square (RMS) charge radius as an input for the calculation of δ_C [16]. The Q_{EC}-value and δ_c are now close to sharing the same weight to the total uncertainty of the $\mathcal{F}t$-value. Among all superallowed β emitters used to extract V_{ud} of the Cabibbo-Kobayashi-Maskawa (CKM) matrix [15], ^{74}Rb has the highest atomic number, Z. Hence, it is of special importance in attempts to distinguish between conflicting nuclear models of δ_C since δ_C approximately scales as Z^2 [17, 18].

This work presents the first Penning trap mass measurements of short-lived HCI, performed with TRIUMF's Ion Trap for Atomic and Nuclear science (TITAN) [19], including a successful mass determination of ^{74}Rb^{8+}. The high charge states were attained by breeding SCI delivered from the Isotope Separator and ACcelerator (ISAC) facility in an Electron Beam Ion Trap (EBIT).

1.1   Outline of the thesis

Theoretical background to the physics motivation of the present work, i.e. the measurement of the Q_{EC}-value of the superallowed β-emitter ^{74}Rb, is provided in Chapter 2. The theory of nuclear β-decays is derived from first principles of the Standard Model (Section 2.1 to Section 2.4) and is discussed in more detail for superallowed β-decays (Section 2.5). The determination of V_{ud} from this type of decays requires theoretical corrections which are explained in Section 2.6. Among those corrections, the isospin-symmetry breaking corrections, δ_C, show discrepancies between different theoretical models which are reviewed in Section 2.7. Experimental data are critical to discriminate between different models (Section 2.8). Particularly, an improved Q_{EC}-value of ^{74}Rb (Section 2.9) could make tests of δ_C calculated in different models more stringent because ^{74}Rb has the largest δ_C among the 13 precise superallowed β-decays which are considered for the determination of V_{ud}. Here, HCI for Penning trap mass spectrometry can provide the needed gain in experimental precision in the Q_{EC} of ^{74}Rb.

The experimental setup utilized for the Penning trap mass measurements of radioactive HCI is introduced in Chapter 3. The radioactive beam of SCI produced at ISAC (Section 3.2) is cooled and bunched at TITAN's Radio-Frequency Quadrupole (RFQ) cooler and buncher (Section 3.3). Ion bunches are further transferred into an EBIT (Section 3.4) where the charge breeding to higher states takes place. Finally, the mass measurements themselves are carried out in TITAN's Measurement Penning Trap (MPET) which is discussed in Section 3.7.

The mass measurements of $^{74-76,78}$Rb and ^{74}Ga in charge states $q = 8 - 12+$, the analysis of the data, as well as systematic uncertainties are described in Chapter 4. The consequences of the present result are discussed for the Q_{EC}-value of ^{74}Rb and a new test for models of δ_C is introduced in Section 5.1. A general perspective of the opportunities offered by the introduction of HCI for Penning trap mass measurements of short-lived nuclides is given in Section 5.3 and its implications for resolving low-lying nuclear isomers (Section 5.4) is explained. The thesis is concluded by Chapter 6, which summarizes the experimental work and provides an outlook on the use of HCI for Penning trap mass measurements at radioactive beam facilities in general and for the Q_{EC}-value of ^{74}R in particular.

Chapter 2

The Standard Model and Theory of Nuclear β-Decay

The current formulation of the Standard Model of particle physics was developed in the 1960s and 1970s and has since withstood experimental tests both in the low and high energy regimes. Neutrino oscillations which were established during the last decade [20] imply neutrinos are massive particles, in contradiction to the Standard Model. To account for neutrinos with non-vanishing masses, an extension of the theory is necessary for the first time. Some proposed models deviate quite substantially from the principles which the current Standard Model is built upon, and introduce new concepts, for instance, non-renormalizable interaction terms (compare to Section 2.1). An alternative solution is based on the assumption that the Standard Model is incomplete in its particle content. In contrast to quarks or the other leptons, the Standard Model does not include any right handed neutrinos (see Section 2.1). Adding right handed neutrinos while keeping the fundamental principles and symmetries intact generates a mass term for neutrinos. The new neutrinos would be sterile, i.e. they would not couple to any other Standard Model particles, explaining why they have not been observed so far. While such an extension might appear to be natural, it raises questions about the tiny coupling constants it would constitute to match with the experimental and cosmological upper limits on the neutrino masses. Further experimental data are required to constrain and to guide theory in the effort to correctly incorporate massive neutrinos. Particularly, the search for a neutrino-less double β-decay is expected to shed light onto the origin of neutrino masses.

Apart from this manifested shortcoming, many other issues remain open and the emergence of a more general theory of particle physics is expected. However, the strong agreement of all experimental data, except for neutrino-oscillation, with the

Standard Model provides confidence that the current description must at least be a low energy approximation of a more complete theory. When interpreting the Standard Model as an effective theory, its fundamental particles and forces would resemble the degrees of freedom which are relevant for energies below several hundreds of GeV. Any search for new physics, especially on the low- energy, high-precision frontier, has to rely on the Standard Model as a starting point.

This Chapter will introduce the basic concepts of the Standard Model as relevant to the experimental work and its theoretical description of (nuclear) β-decay. An attempt is made to bridge between today's description of the Standard Model in particle physics and that of nuclear β-decays which are typically described within Fermi's theoretical framework. As V_{ud} is part of the former's language but not necessarily of the latter, it is sought to accentuate their connection more explicitly in the following sections. To properly establish the link, some generally accepted basics of the Standard Model will be introduced.

The first sections aim to emphasize the connection of the fundamentals of particle physics to one of its phenomena, the β-decay, and hence natural units ($\hbar = c = 1$) will be used in the beginning. SI units will be introduced starting from Section 2.7.8, when theory and experiment of nuclear β- decays are more closely explained. The (implicitly) used metric follows the West Coast convention (see [21]) with $g_{\mu\nu} = \mathtt{diag}[1, -1, -1, -1]$. Although neutrinos are now known to be massive, their absolute masses and relative mass differences are small. β-decay experiments generally do not detect neutrinos directly. Consequently, neutrino oscillation or their non-vanishing masses will not affect the described β-decay experiments and neutrinos are assumed to be massless following the original formulation of the Standard Model.[1]

2.1   The Standard Model of particle physics

The Standard Model is a quantum field theory which is grounded on

- a set of basic principles such as Lorentz invariance and the conservation of probability (i.e. unitarity of the Hamiltonian),

- the experimentally observed particle content of fermions,

- fundamental symmetries,

- a scalar particle, i.e. the Higgs field, whose negative mass term is responsible for the spontaneous symmetry breaking, and

---

[1]The discussion of the Standard Model and its connection to β-decays is, if not otherwise indicated, based on the following references: [21][22][23][24][25][26][27][28]

- the use of the most general, renormalizable Lagrangian given the previous constraints.

Before introducing the specifics of the Standard Model, the relation between continuous symmetry groups and fundamental forces in our current description of particle physics will be discussed. By imposing invariance of a theory under local symmetry transformation, so-called gauge bosons are generated in the Lagrangian which are seen as the mediators of the force. A fundamental interaction is thus given by the underlying symmetry or gauge group and its representations in which different particle fields transform under the symmetry. Motivated by its success, theoretical work on physics beyond the Standard Model attempts to unify fundamental forces and utilizes a similar framework but employs different symmetry groups.

2.1.1 Local gauge invariance

In a Lie group any infinitesimal group element g can be expressed as an expansion around the identity with the expansion parameters α^a following

$$g(\alpha) = 1 + i \sum_a \alpha^a T^a + \mathcal{O}(\alpha^2). \tag{2.1}$$

T^a are the generators of the group and are Hermitian operators, i.e. $T^a = T^{a+}$. For notational clarity, sums are implicit over all doubled indices and the $\sum$-symbol will be omitted. Any finite group member can be constructed by repeated application of the infinitesimal group element.

$$G(\alpha) = \lim_{N \to \infty} (1 + \frac{i}{N}\alpha^a T^a)^N = e^{i\alpha^a T^a} \tag{2.2}$$

Since G depends on the parameters α^a in a continuous way, a Lie group is a continuous group. Its generators follow the commutator relation

$$[T^a, T^b] = if^{abc}T^b, \tag{2.3}$$

where the fully antisymmetric f^{abc} are the group's structure constants. Different Lie groups may have the same commutation relations. Up to this point, we are dealing with abstract objects. A mapping of all group generators onto $n \times n$ Hermitian matrices t^a which fulfill the same commutator relations as in Equation 2.3 is called a representation of the group. Essential for our purposes is that different particles live in different representations of the same group. They act differently under the symmetry group and, hence, under the respective fundamental force.

Without loss of generality, we introduce an n-plet of Dirac particle fields $\psi(x)^T = \big(\psi(x)_1, ..., \psi(x)_n\big)$. The $n \times n$ representation t^a of the group G transforms $\psi(x)$ according to

$$\psi(x) \rightarrow e^{i\alpha^a(x) \cdot t^a} \psi(x), \tag{2.4}$$

where α is also evaluated at the space-time position x. The α-dependence on x depicts this transformation as local, in contrast to a global transformation which would be independent of x. If we require the Lagrangian to be invariant under the continuous symmetry group G, a Dirac mass term $m\overline{\psi}\psi$ is trivially left unmodified by the transformation. However, the kinetic term $\overline{\psi}i\partial\!\!\!/\psi$ involving a derivate ∂_μ is not. In order to compensate for the additional terms arising through the local gauge transformation, the derivate ∂_μ requires a generalization to the covariant derivative D_μ

$$D_\mu = \partial_\mu - ig A_\mu^a(x) \cdot t^a \tag{2.5}$$

where the new vector fields $A_\mu^a(x)$ are added and g is, at this point, an arbitrary constant extracted from the vector field. The transformation properties of the vector fields under the group G have to follow the expression

$$A_\mu^a(x) \rightarrow A_\mu^a(x) + \frac{1}{g}\big(\partial\alpha(x)^a\big) + f^{abc} A_\mu^b \alpha^c(x) \tag{2.6}$$

to cancel the terms arising in the derivative of $\psi(x) \rightarrow \big(1 + i\alpha^a(x) \cdot t^a\big)\psi(x)$. This can be shown by applying the commutator rules in Equation 2.3.

Although the initial Lagrangian of the n-plet of free Dirac fields is now gauge invariant under the transformation of G, it is incomplete. Through the introduction of the new vector field $A_\mu^a(x)$ and the intention to use the most general renormalizable Lagrangian, additional terms are accommodated. Indeed, $A_\mu^a(x)$ is lacking a kinetic term. However, it can be added with the help of the definition of the field tensor

$$F_{\mu\nu}^a = \partial_\mu A_\nu^a - \partial_\nu A_\mu^a + g f^{abc} A_\mu^b A_\nu^c \tag{2.7}$$

to gain a new, gauge invariant Lagrangian[2]

$$\mathcal{L} = \overline{\psi}\big(i D\!\!\!/ - m\big)\psi - \frac{1}{4}\big(F_{\mu\nu}^a\big)^2 = \overline{\psi}\big(i\partial\!\!\!/ - m\big)\psi - \frac{1}{4}\big(F_{\mu\nu}^a\big)^2 + g\overline{\psi}A\!\!\!/^a \cdot t^a \psi \tag{2.8}$$

The first two terms are the free Dirac equations of the n Dirac fields followed by the kinetic and interaction terms among the vector fields, $\big(F_{\mu\nu}^a\big)^2 = F_{\mu\nu}^a \cdot F^{a,\mu\nu}$. Finally, $g\overline{\psi}A\!\!\!/^a \cdot t^a \psi$ reflects the interaction between the Dirac fields and the vector

---

[2]For simplicity, the subtlety of an additional, renormalizible, and gauge invariant term violating Parity and Time Reversal conservation is not discussed.

fields $A_\mu^a(x)$ with g being the coupling constant. Since $A_\mu^a(x)$ are consequences of the postulation of gauge invariance, they are called gauge bosons of the local gauge transformation G. Note that gauge invariance does not allow for a mass term for the gauge bosons. Since the generators of the group do not commute (see Equation 2.3), it is referred to as a non-Abelian gauge theory.

The classical Lagrangian equations for Equation 2.8 lead to the Dirac equation for the fermion $(i\slashed{\partial} - m)\psi = -g\slashed{A}^a \cdot t^a \psi$ and to the equation of motions for the gauge boson,

$$\partial_\mu F_{\mu\nu}^a + g f^{abc} A^{b,\mu} F_{\mu,\nu}^c = -g\overline{\psi}\gamma_\nu t^a \psi \equiv -g J_\nu^a, \tag{2.9}$$

where in analogy to electromagnetism a current of g- charged fermions was defined as $J_\nu^a = \overline{\psi}\gamma_\nu t^a \psi$.

To summarize, an interaction is characterized by its Lie group; when a Lagrangian is required to be invariant under the action of this local symmetry, massless gauge bosons are created to establish the invariance. These manifest as the exchange particles of the interaction.

2.1.2 Symmetries and particle content of the Standard Model

Our most fundamental description of particle physics requires three symmetry groups, SU(3), SU(2), and U(1). SU(N) are the groups corresponding to all unitary transformations of N dimensional vectors with $\det(U) = 1$. The last requirement is relieved in U(N) symmetry groups. U(1) is associated with a simple phase rotation, $\exp(ia)$, and has only one generator. Trivially, this implies that all generators commute with each other and U(1) creates an Abelian gauge theory. Quantum Chromodynamics (QCD), the part of the Standard Model which deals with the strong interaction, only acts among quarks and is reflected by SU(3). We know of 6 types of quarks, called flavours, which are organized in 3 generations (see Table 2.1). The strong interaction, however, acts upon the colors of a quark, which motivates the often used notation SU(3)$_c$. As there are three colors, the representation of SU(3)$_c$ is of dimension 3. The derivation of the Lagrangian essentially follows Equation 2.3 to Equation 2.8 where the generators of SU(3)$_c$ lead to the 8 gauge bosons called gluons. More details about QCD as it is relevant for nuclear physics will be discussed below.

At the fundamental level, Quantum Electrodynamics (QED) and the weak interaction are unified in the electroweak force represented by SU(2)xU(1). QED also follows U(1), but instead of the electric charge U(1) refers to the so-called weak hypercharge Y. In comparison to the previous discussions, the force carriers of the weak force are experimentally known to be massive, although gauge invariance forbids massive gauge bosons. This problem can be overcome through the Higgs

Table 2.1: Quark generations in the Standard Model. All masses as listed in [29].

	up-type			down-type		
	name		mass	name		mass
1$^{\text{st}}$	up	u	1.7-3.1 MeV	down	d	4.1-5.7 MeV
2$^{\text{nd}}$	charm	c	$1.29^{+0.05}_{-0.11}$ GeV	strange	s	100^{+30}_{-20} MeV
3$^{\text{rd}}$	top	t	$172.9 \pm 0.6 \pm 0.9$ GeV	bottom	b	$4.19^{+0.18}_{-0.06}$ GeV

mechanism which spontaneously breaks the SU(2)xU(1) symmetry. Here, a scalar particle is introduced whose ground state has a vacuum expectation value that does not follow the symmetry. This generates mass terms for 3 gauge bosons (W^+, W^-, and Z) and another massless gauge boson which is the photon γ, the force carrier of QED. With respect to SU(2), the left handed fermions are arranged in doublets. Right handed fermions are not affected by this local symmetry and are thus singlets. Without the Higgs mechanism, such a construction would not allow any Dirac mass term for fermions, because left and right handed fermion spinors are in different representation of the same group. Again, the spontaneous symmetry breaking restores the masses of fermions. There is no direct experimental evidence for right-handed neutrinos and they are omitted from the particle content of the Standard Model. Therefore, it is not possible to form a Dirac mass term $m_\nu \overline{\nu}_L \nu_R$ even after the spontaneous symmetry breaking. A more detailed discussion of the electroweak interaction can be found in Section 2.2.

Table 2.2 summarizes all fermions and the scalar Higgs particle of the Standard Model (SM) as well as their transformation properties under the respective local symmetries. With the exception of the Higgs particle, all particles have been observed in experiments.

2.1.3   QCD and nuclear structure

Given that protons and neutrons, each composites of quarks, can be bound to atomic nuclei by the strong force, QCD does in principle play a decisive role in studies of weak decays in nuclear systems. As explained later in Section 2.6, theoretical, nuclear structure dependent corrections dominate the uncertainty on the extraction of V_{ud} from superallowed $0^+ \rightarrow 0^+$ β-decays. Owing to its much smaller coupling constant, the weak force is not of relevance for the structure of nuclei, which are governed by the strong and the electromagnetic force only. For practical purposes, however, peculiar features of QCD such as its non-perturbative character

Table 2.2: Fermions and scalar particles in the Standard Model. U-type quarks u are up, charm, and top quark, while down-type quarks d stand for down, strange, and bottom quark. ℓ denotes the massive leptons e, μ, and τ. ν are their respective neutrinos (ν_e, ν_μ, and ν_τ). The last two columns show the dimension of the representation in which the particles transform under $SU(3)_C$ and $SU(2)$.

Particle(s)	Notation	$SU(3)_C$	$SU(2)$
right handed up-type quarks	u_R	3	1
right handed down-type quarks	d_R	3	1
left handed quarks	$\begin{pmatrix} u \\ d \end{pmatrix}_L$	3	2
right handed ℓ	ℓ_R	1	1
left handed leptons	$\begin{pmatrix} \nu \\ \ell \end{pmatrix}_L$	1	2
Higgs scalar	$\begin{pmatrix} \phi^+ \\ \phi^0 \end{pmatrix}$	1	2

at lower energies make direct calculations of large quark compounds unpractical. In the past, nuclear structure research has thus treated nucleons as its elementary particles and developed its phenomenological nucleon-nucleon potentials which are to one degree or another inspired by, but not ultimately based on QCD. The nuclear force, i.e. the force between nucleons, is a residual interaction of QCD comparable to the van der Waals force in QED: Just as electrically charged electrons and atomic nuclei bond to form electrically neutral and energetically favourable atoms or molecules, quarks form color-neutral or color-less hadrons. Gluons acting only on color-charged objects will not be directly exchanged between nucleons. Modern phenomenological potentials are constructed based on meson-exchange between nucleons (e.g. [30][31][32][33][34]). For instance, the long range part of the potential is described by a one-pion exchange model proposed by H. Yukawa. While very successful in many applications for nuclear structure, these potentials struggle with a consistent formulation of many-nucleon forces and lack an explicit link between QCD and nuclear forces. These problems are overcome in nuclear potentials derived from effective field theory. Noting that the light quarks, u and d, which neutrons and protons are made of, have small masses compared to their typical

momenta, they can be treated ultra-relativistically as (almost) massless particles. Their QCD-Lagrangian,

$$\mathcal{L} = \overline{q}(i\slashed{D})q - \frac{1}{4}\left(F^a_{\mu\nu}\right)^2, \tag{2.10}$$

decouples the left- and the right-handed quarks. It is thus invariant under any transform among left (or right) handed quark fields, i.e.

$$\begin{pmatrix} u \\ d \end{pmatrix} \rightarrow \frac{i}{2}\alpha^a_{L/R}\sigma^a P_{L/R}\begin{pmatrix} u \\ d \end{pmatrix}. \tag{2.11}$$

σ^a is the 2x2 representation of the three generators of U(2), which act upon $(u, d)^T$, thus in flavour space. $P_L = \frac{1}{2} \cdot (1 - \gamma_5)$ and $P_R = \frac{1}{2} \cdot (1 + \gamma_5)$ are the left- and right-handed projection operators acting in the 4 dimensional spinor space. U(2)$_L$xU(2)$_R$ is not anomaly-free and the correct symmetry is in fact SU(2)$_L$x SU(2)$_R$xU(1)$_B$. The latter rotates all quarks by a phase and is an exact symmetry not only of QCD but of the entire Standard Model. Since each continuous symmetry implies (according to Noether's theorem) a conserved quantity, U(1)$_B$ corresponds to the quark (or baryon-) number conservation, $B = 1/3 \cdot (n_q - n_{\overline{q}}) = const.$ SU(2)$_L$xSU(2)$_R$ is called the chiral symmetry of massless (or light) QCD. This symmetry is explicitly broken by the mass term, however, since the u and d quark masses are small, it is considered to be an approximate symmetry. Additionally, a subgroup of the chiral symmetry is considered to be broken spontaneously, meaning that the ground state of QCD is, despite the symmetry, an asymmetric state. This is a necessary construction to reproduce the experimentally observed spectrum of compound quark particles. According to the Goldstone theorem (see [23]), a spontaneously broken symmetry induces a massless Goldstone boson. In the case of chiral symmetry, pions are identified as these Goldstone bosons. Their non-vanishing mass is due to the approximate character of the symmetry. More details on the general mechanism of spontaneous symmetry breaking can be found in Section 2.2.

Although it remains a challenge to derive nuclear forces based on QCD, it is possible to construct an Effective Field Theory (EFT) which bridges QCD and the inter-nucleon interaction. An EFT is a low energy approximation of a more complete theory taking only those degrees of freedom into account which are relevant at the energy scale to be described by the EFT. In modelling the nuclear forces, chiral Effective Field Theory (χEFT)[35, 36] considers neutrons and protons, as well as pions. Pions have to be included explicitly because their mass corresponds to typical nucleon momenta Q in atomic nuclei. The link to QCD is established by the most general Lagrangian involving nucleons and pions which is consistent with the

11
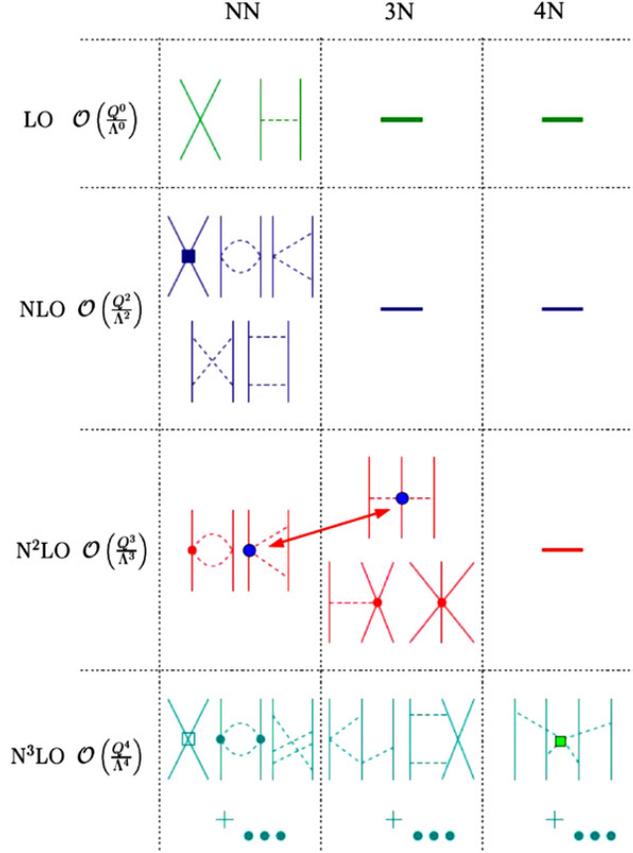
Figure 2.1: Chiral expansion of nuclear forces. Figure from [37].

chiral symmetries discussed above, thus the name chiral Effective Field Theory. The Lagrangian can be systematically expanded order-by-order with higher orders contributing less than lower orders. Figure 2.1 shows the expansion up to next-to-next-to-next-to leading order or N^{3}LO. Individual terms consist of (multiple) pion exchange reflecting the long range part of the force (see Figure 2.2a) or contact terms (Figure 2.2b) which cover short range physics not resolved at this energy scale. As the short range details will become visible at higher energies the theory naturally has a hard cut-off scale Λ_B above which it is expected to fail. For chiral Effective Field Theory, this scale is typically $\Lambda_B \approx 0.5$ GeV and the perturbative expansion of the Lagrangian follows in orders of Q/Λ_B. Short range physics just above Λ_B also manifests itself in the non-renormalizible character of the theory. As a consequence new terms will appear order-by-order in contrast to a renormaliz-
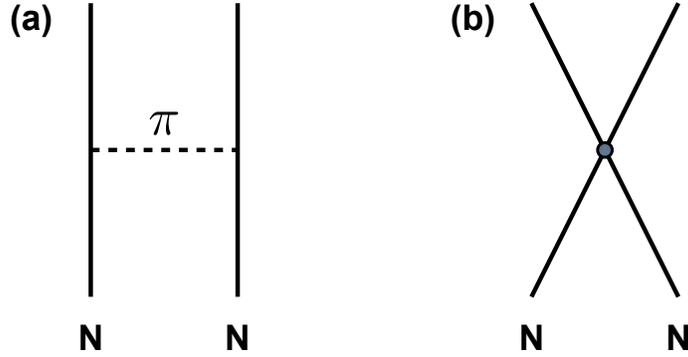
Figure 2.2: Chiral expansion at leading order with one-pion exchange between two nucleons N in (a) and a contact term (b).

ible theory which only produces counter-terms to already existing terms. However, since the cut-off corresponds to a true, physical separation of scales these terms are suppressed by $(Q/\Lambda_B)^n$ with n being the order of the expansion. Many-body forces naturally appear within the frame work of chiral Effective Field Theory. Because they contribute only at higher orders, their impact is smaller than the two-body force. This hierarchy is consistent with phenomenological models, but puts this observation on solid theoretical ground. The absence of (Q/Λ_B) terms in Figure 2.1 is related to parity conservation. As long as the low energy coupling constants cannot be derived from first principles, they have to be matched with experiment. Typically, nucleon(N)-nucleon(N) and pion-nucleon scattering phase shifts are used for the NN-force while 3-body (3N) forces are derived by fitting the couplings to binding energies or other observables of light nuclei (e.g. [36]).

The chiral expansion can be connected to potentials which can be employed in the Schrödinger equation. The solution of nuclear many-body problems is found there with the help of modern few- and many-body techniques. A major problem already present in phenomenological potentials is the strong repulsive part of the nuclear potentials for small distances between nucleons (see Figure 2.3a). It is also referred to as the hard repulsive core of the potential. As illustrated in Figure 2.3b, it couples the low and the high momentum modes. Such off-diagonal couplings in momentum space complicate practical calculations severely because a larger model space is required or they even become non-perturbartive. Modern potentials, both phenomenological and χEFT based, can be further transformed to lower energies by utilizing renormalization group techniques [37]. While observables remain unchanged, potentials and basis are evolved by integrating out the
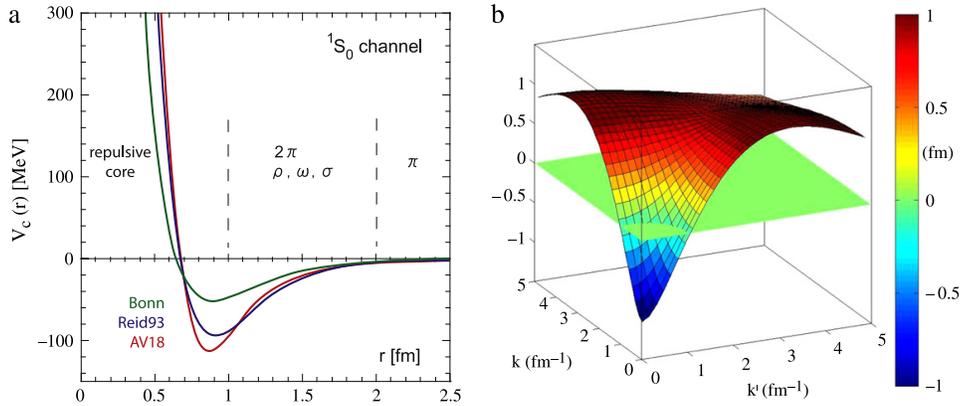
Figure 2.3: (a) Illustration of the repulsive core for three phenomenological NN-potentials (Bonn, Reid93, and AV18) in the $^1S_0$ channel. The repulsive core leads to coupling of high and low momentum modes as shown in (b) for the Argonne v_{18} potential, again in the $^1S_0$ channel. Figure from [37].

short-range correlations above a cut-off Λ. This softens the hard core of the potentials and consequently decouples low and high momenta, which improves the convergence of nuclear structure calculations dramatically. It is important to stress that the hard-cut off Λ_B of χEFT and Λ, the evolution parameter, are not the same. Simply reducing Λ_B to lower energies would have led to a larger truncation error when neglecting more and more physics at higher nucleon momenta. On the other hand, in the evolution of Λ to lower momenta the renormalization keeps the short range parts of the χEFT expansion in Λ_B/Q, but integrates them out by shifting strength between different coupling constants. Different initial potentials converge to similar ones after the renormalization which is referred to as the universality of the evolved low-momentum potentials. Aside from the renormalization group, other methods have been successfully developed to tackle the problem of short range correlations due to the hard core as, for example, the Unitary Correlation Operator Method [38].

χEFT has become the bond between QCD and nuclear structure. In combination with modern techniques to soften nuclear potentials, the research of atomic nuclei can now be approached in a consistent framework over the whole nuclear chart [39]. Different methods to solve the nuclear many-body problem will remain to be more suitable to their specific mass regions. While different in their techniques,

their underlying physics input, i.e. the interaction potentials between nucleons, can now be solidly linked to QCD. Although χEFT based potentials have so far not been used in the context of superallowed β decays, two recent developments shall be noted: nuclear matrix elements for neutrinoless-double β decays and thus related to weak interaction studies with atomic nuclei have been calculated for the first time with χEFT [40]. Secondly, theoretical isospin symmetry corrections important for superallowed nuclear β decays have been derived microscopically within density functional theory [41]. Hence, it would be interesting to calculate these corrections also based on χEFT.

Before concluding the topic of QCD with light quarks, let's rearrange the symmetry transformation due to $P_{L/R} = \frac{1}{2}(1 \pm \gamma_5)$ in Equation 2.11 to a vector

$$\begin{pmatrix} u \\ d \end{pmatrix} \rightarrow \frac{i}{2}\alpha^a\sigma^a \begin{pmatrix} u \\ d \end{pmatrix} \tag{2.12}$$

and an axial-vector transformation

$$\begin{pmatrix} u \\ d \end{pmatrix} \rightarrow \frac{i}{2}\alpha^a\sigma^a\gamma_5 \begin{pmatrix} u \\ d \end{pmatrix}. \tag{2.13}$$

While the latter symmetry is broken by any mass term in the Lagrangian, the vector transformation in SU(2) is a pure rotation in flavour space and remains an exact symmetry as long as the masses of u and d quark are identical, which is assumed here. Its associated quantum numbers are called isospin T. We define its z-projection for the u-quark as $T_z = -1/2$ and for d-quark as $T_z = +1/2$, such that in the baryon doublet with $T = 1/2$ of neutron (udd) and proton (uud), $T_z = +1/2$ corresponds to the neutron. The isospin symmetry is in fact broken, too. This gives rise to the small mass difference between neutron and proton.

2.2 Electroweak interaction in the Standard Model and V_{ud}

The existence of massive gauge bosons in the electroweak interaction necessitates a modification of the protocol for gauge theories outlined in Section 2.1. In the Higgs mechanism, spontaneous symmetry breaking appears through a scalar doublet $\phi^T = (\phi_1, \phi_2)$ which transforms under SU(2)xU(1) according to

$$\phi \rightarrow e^{i\alpha^a\sigma^a}e^{i\frac{\beta}{2}} \begin{pmatrix} \phi_1 \\ \phi_2 \end{pmatrix}. \tag{2.14}$$

σ^a are the Pauli matrices. Following Equation 2.5, its covariant derivate is expressed as

$$D_\mu \phi = \left(\partial_\mu - i g_1 A_\mu^a(x) \cdot \sigma^a - i g_2 B_\mu(x) \right) \phi. \tag{2.15}$$

The condition of the Standard Model to use the most general, renormalizible Lagrangian requires the addition of

$$\Delta \mathcal{L} = +\mu^2 \phi^+ \phi - \lambda (\phi^+ \phi)^2. \tag{2.16}$$

Although $\mu^2 \phi$ has the form of a scalar mass term, we are allowed to choose $\mu > 0$ as long as $\lambda > 0$. Then, $V_{Higgs} = -\mu^2 \phi^+ \phi + \lambda (\phi^+ \phi)^2$ remains bound from below. When expanding around the minimum of the potential, $\phi(x) = (0, \mu/\sqrt{2\lambda} + H(x))$, the kinetic term of the scalar field, $(D_\mu \phi)(D_\mu \phi)$ contains a term independent of $H(x)$. It resembles mass terms for three gauge bosons when the four initial gauge fields A_μ^a and B_μ are redefined to

$$
\begin{aligned}
W^\pm &= \frac{1}{\sqrt{2}} \left(A_\mu^1 \mp i A_\mu^2 \right) \\
Z &= \frac{1}{\sqrt{g_1^2 + g_2^2}} \left(g_1 A_\mu^3 - g_2 B_\mu \right).
\end{aligned} \tag{2.17}
$$

These are identified as the exchange particles for the weak interaction. The remaining field,

$$A_\mu = \frac{1}{\sqrt{g_1^2 + g_2^2}} \left(g_2 A_\mu^3 + g_1 B_\mu \right), \tag{2.18}$$

is the massless photon as the force carrier of QED. With respect to U(1) of QED, the Z- boson is neutral, i.e. it does not couple to the photon alone. W^+ and W^- are charged with $+e$ and $-e$, respectively, when the electromagnetic coupling constant is defined as $e = g_1 \cdot g_2 / \sqrt{g_1^2 + g_2^2}$.

2.2.1 Masses of fermions

The weak interaction only operates on left-handed fermions. Left- and right-handed fermions act in two different representations of SU(2). Latter ones are unchanged under SU(2) and are singlets. Left-handed fermions are arranged in doublets, each generation within one doublet. Hence,

$$\begin{pmatrix} \nu_e \\ e^- \end{pmatrix}_L, \begin{pmatrix} \nu_\mu \\ \mu^- \end{pmatrix}_L, \begin{pmatrix} \nu_\tau \\ \tau^- \end{pmatrix}_L \tag{2.19}$$

for the leptons and

$$\begin{pmatrix} u \\ d \end{pmatrix}_L, \begin{pmatrix} c \\ s \end{pmatrix}_L, \begin{pmatrix} t \\ b \end{pmatrix}_L \qquad (2.20)$$

for quarks. Consequently, no direct mass term can be part of the initial Lagrangian, because it would not be gauge invariant as left- and right-handed fermions transform differently. Fermionic masses are created due to the so-called Yukawa coupling which ties left-handed doublets and right-handed singlets to the scalar field. For instance, in the quark sector it becomes

$$\Delta \mathcal{L} = -\ \Lambda^{ij} \cdot (\overline{u}, \overline{d})_L^i \cdot \begin{pmatrix} 0 \\ \mu/\sqrt{2\lambda} + H(x) \end{pmatrix} d_R^j$$
$$-\ \tilde{\Lambda}^{ij} \cdot (\overline{u}, \overline{d})_L^i \cdot \begin{pmatrix} -\mu/\sqrt{2\lambda} - H(x) \\ 0 \end{pmatrix} u_R^j + h.c., \qquad (2.21)$$

where i and j sum over the 3 generations with $u^{i=1,2,3} = (u, c, t)$ and $d^{i=1,2,3} = (d, s, b)$. In the second part of the sum the scalar doublet is included as $-i\sigma^2 \phi^*$. All other combinations of u_R^i, d_R^i, $(\overline{u}, \overline{d})_L^i$, and ϕ would either violate SU(2) or U(1). The components without $H(x)$ are seen as quark mass terms.

$$\mathcal{L}_{m_q} = -M_d^{ij} \overline{d}_L^i d_R^j - M_u^{ij} \overline{u}_L^i u_R^j + h.c. \qquad (2.22)$$

M_d^{ij} and M_u^{ij} are not constrained by any symmetry and are thus not necessarily diagonal. This implies that the quark eigenbasis of the weak interaction is not identical to its mass eigenbasis. With the unitarity transformations,

$$\begin{aligned} u_L^{\prime i} &= U_L^{ij} u_L^j, & d_L^{\prime i} &= D_L^{ij} d_L^j \\ u_R^{\prime i} &= U_R^{ij} u_L^j, & d_R^{\prime i} &= D_L^{ij} d_R^j \end{aligned} \qquad (2.23)$$

we rotate the weak eigenbasis into the mass eigenbasis, where the mass matrices are diagonal.

2.2.2 The Cabibbo-Kobayashi-Maskawa matrix

Most terms in the Standard Model Lagrangian contain both $\overline{u}_{R/L}$ and $u_{R/L}$ (or $\overline{d}_{R/L}$ and $d_{R/L}$). Hence, in these cases there is no difference in the Lagrangian between bases connected by the unitarity transformations of Equation 2.23. The only exceptions are the contractions of quarks with W-bosons which arise from

the covariant derivatives of (left-handed) quarks.

$$\mathcal{L} = \frac{g}{\sqrt{2}} \left[\overline{u}_L^i \gamma^\mu d_L^i \cdot W_\mu^+ + \overline{d}_L^i \gamma^\mu u_L^i \cdot W_\mu^- \right] \tag{2.24}$$

in the weak eigenbasis turns into

$$\mathcal{L} = \frac{g}{\sqrt{2}} \left[U_L^{ij} D_L^{+,jk} \cdot \overline{u}_L^{\prime i} \gamma^\mu d_L^{\prime k} \cdot W_\mu^+ + D_L^{ij} U_L^{+,jk} \cdot \overline{d}_L^{\prime i} \gamma^\mu u_L^{\prime k} \cdot W_\mu^- \right] \tag{2.25}$$

when transforming into the mass eigenbasis. Since these are the only terms where the transformations of Equation 2.23 can explicitly appear in the Lagrangian of the Standard Model, we set for convenience

$$U_R^{ij} = D_R^{ij} = U_L^{ij} = \delta^{ij}, \tag{2.26}$$

where δ^{ij} is the Kronecker Delta and define $V = U_L \cdot D_L^+$ which transforms the left-handed, down-type quarks from the mass into the weak eigenbasis $d = V \cdot d'$ or

$$\begin{pmatrix} d \\ s \\ b \end{pmatrix}_L = \begin{pmatrix} V_{ud} & V_{us} & V_{ub} \\ V_{cd} & V_{cs} & V_{cb} \\ V_{td} & V_{ts} & V_{tb} \end{pmatrix} \cdot \begin{pmatrix} d' \\ s' \\ b' \end{pmatrix}_L. \tag{2.27}$$

This unitary matrix is called the Cabibbo-Kobayashi-Maskawa (CKM) quark mixing matrix. The physical quarks are the mass eigenstates. However, the weak interaction acts within a different basis which results in mixing of quark flavours as seen by the contraction of one up-type quark with all three flavours of the down-type quarks in Equation 2.25. The unitarity of the CKM matrix requires that its Hermitian conjugate is its inverse, i.e. $V^+ \cdot V = 1$ or $V_{ji}^* \cdot V_{jk} = \delta_{ik}$. From these, 9 linearly independent equations reduce the 18 real parameters of any 3 x 3 complex matrix to 9 real parameters (3 real amplitudes or rotation angles and 6 phases) of a unitary matrix. Additionally, not all of the 9 real parameters of the CKM matrix can actually appear in the Lagrangian of the SM, analogously to the rotational matrices U_R and D_R in Equation 2.23. Hence, they cannot be observed in any physical process. The physically significant parameters of the CKM matrix further reduce to three real numbers and one complex phase. As previously mentioned, these four parameters are not given by the Standard Model itself. But the requirements of unitarity and the consistency with only four parameters in the CKM matrix allows stringent experimental tests of the electro-weak quark sector of the Standard Model. While in mathematical sense $V \cdot V^+ = 1$ is equivalent to $V^+ \cdot V = 1$, we can experimentally examine both $V_{ji}^* \cdot V_{jk} = \delta_{ik}$ and $V_{ij} \cdot V_{kj}^* = \delta_{ik}$. These are each 3, hence totally 6, vanishing equations which one can picture as triangles in
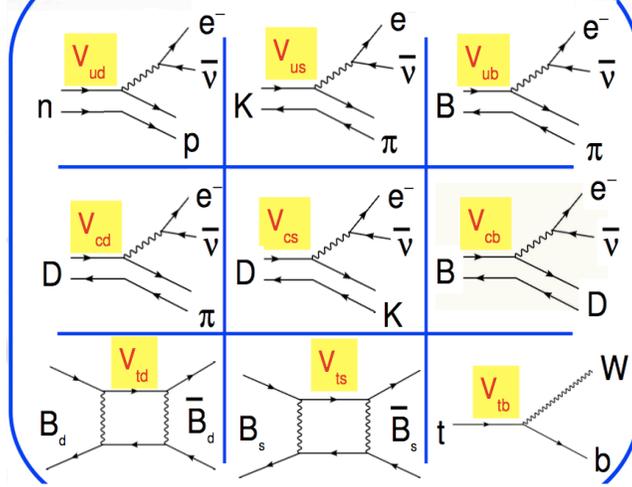
Figure 2.4: Feynman diagrams corresponding to possible experimental determinations of the CKM matrix elements. Figure from [42].

the complex plane. Among these, the so-called unitarity triangle

$$V_{ud}V_{ub}^* + V_{cd}V_{cb}^* + V_{td}V_{tb}^* = 0 \tag{2.28}$$

is commonly tested. The triangle in the complex plane is constructed by dividing the equation by $V_{cd}V_{cb}^*$, identifying the absolute value of each summand as a side length of the triangle. The area of the triangle is related to the violation of CP, i.e. combined charge conjugation and parity symmetry, in the CKM sector.
Additionally, the non-vanishing parts of $V^+ \cdot V = V \cdot V^+ = 1$ constitute 6 real equations among which the first row

$$|V_{ud}|^2 + |V_{us}|^2 + |V_{ub}|^2 = 1 \tag{2.29}$$

sets the most stringent limits on physics beyond the Standard Model [26]. Figure 2.4 provides an overview of how individual entries of the CKM matrix can be accessed experimentally.

2.3 CKM-unitarity test via $|V_{ud}|^2 + |V_{us}|^2 + |V_{ub}|^2 = 1$

In order to probe the unitarity of the CKM quark mixing matrix within the first row, precise and accurate experimental data in addition to theory are required to extract
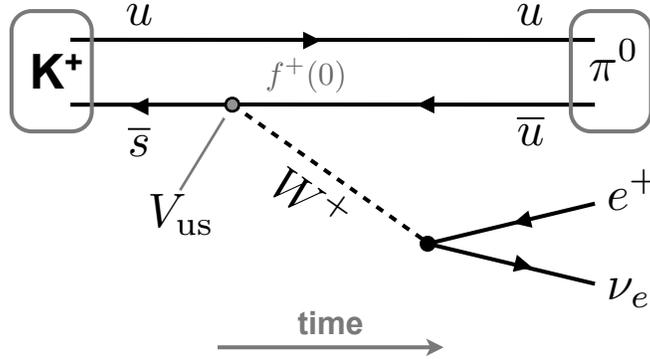
Figure 2.5: Feynman diagram of an example for a $K_{\ell 3}$ decay: $K^+ \rightarrow \pi^0 e^+ \nu_e$ can be used to measure V_{us}.

V_{ud} and V_{us}. At the current level of precision of V_{ud} and V_{us}, the value of V_{ub} is too small, $|V_{ub}| = (3.93 \pm 0.36) \cdot 10^{-3}$ [26], and only marginally affects the unitarity test. This particular test had for a long time fallen short of unity by more than 2 standard deviations. Less than a decade ago, this deviation had been resolved by new measurements of V_{us}, which is most precisely known from kaon decays. In semi-leptonic decays called $K_{\ell 3}$, a kaon disintegrates into a pion and a pair of leptons following $K \rightarrow \pi \ell \nu$. An example for a $K_{\ell 3}$ decay is shown in Figure 2.5. Following the E865 experiment [43] at Brookhaven National Laboratory (BNL) several collaborations [44, 45][46][47][48][49] have confirmed a new value of V_{us} which re-establishes the unitarity condition in the first row of the CKM matrix. Previous, conflicting measurements were rejected by the Particle Data Group (PDG) due to inadequate treatment of radiative decay [29]. Results of the recent measurements provide $|V_{us}| \cdot f^+(0)$, where $f^+(0)$ is the form factor of the respective $K_{\ell 3}$ decay at momentum transfer $q^2 = 0$. Form factors take into account that we are not dealing with free quarks, but quarks bound to form hadrons. A kaon's quark content also involves an s- quark, the third light quark. Although heavier than the u- and d- quark, it is sufficiently light that the SU(2) of light QCD in Section 2.1.3 can be extended to SU(3) when adding the s-quark. In this limit and assuming the later discussed Conserved Vector Current hypothesis, $f^+(0) = 1$ holds. As this SU(3) is broken, QCD calculations are needed as small symmetry breaking corrections. Recent lattice QCD calculations yield $f^+(0) = 0.960^{+5}_{-6}$ [50, 51] and $0.9560(84)$[52], respectively, when correcting for isopin-symmetry breaking, SU(2), separately. Information about V_{us} can also be gained through pure leptonic kaon decays, $K_{\ell 2}$, from $K \rightarrow \ell \nu$. Their form factors (in this case also often called decay constants)
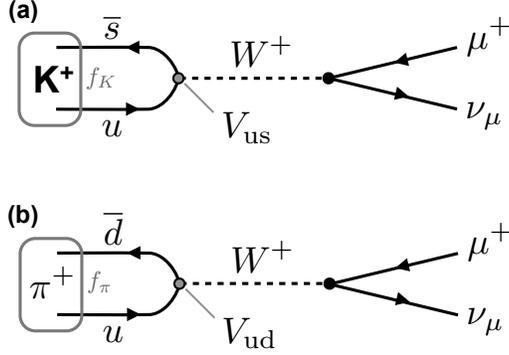
Figure 2.6: Feynman diagrams of K^+ (a) and π^+ (b) decay branches to extract $|V_{us}| \cdot f_K / (|V_{ud}| \cdot f_\pi)$.

Table 2.3: V_{ud} and V_{us} extracted from various decays.

Quantity	Type of Decay(s)	Value	Reference
$\|V_{ud}\|$	superallowed $0^+ \to 0^+$ β-decays	0.97425(22)	[15]
$\|V_{us}\|$	$K_{\ell 3}$	0.2254(13)	FlaviaNet [54][a]
$\|V_{us}\|/\|V_{ud}\|$	$K_{\ell 2}$	0.2312(13)	FlaviaNet [54][b]
$\|V_{us}\|/\|V_{ud}\|$	τ-decay	0.2314(24)	[55][c]

[a] Values are taken from [54] because other recent evaluations in [56] and the PDG [29] do not include a new value for $f^+(0)$ in [51].
[b] Values are taken from [54] because it takes all calculations of f_K/f_π into account.
[c] [55] uses 1.189(7) from [53] for f_K/f_π instead of the averaged 1.193(6) in [54].

are calculable, but at lower precision. Thus, $K_{\ell 2}$ cannot directly compete with $K_{\ell 3}$. However, the ratio of the kaon's form factor f_K to the pion's form factor f_π is known from lattice QCD with similar relative precision [53]. Hence, decay rate measurements of $K^+ \to \mu\nu_\mu$ and $\pi^+ \to \mu\nu_\mu$ provide $|V_{us}| \cdot f_K/(|V_{ud}| \cdot f_\pi)$ (see Figure 2.6), from which $|V_{us}|/|V_{ud}|$ is inferred.

An interesting cross check of the previous determination of $|V_{us}|/|V_{ud}|$ is found in the hadronic decay of the τ- lepton which is heavy enough to decay into both kaon ($\tau^- \to K^-\nu_\tau$) and pion ($\tau^- \to \pi^-\nu_\tau$) (see Figure 2.7). Analogously to $K_{\ell 2}$-decays, $|V_{us}| \cdot f_K/(|V_{ud}| \cdot f_\pi)$ can be accessed in experiment with the same f_K/f_π as above.

The measurement of V_{ud} is the main topic of this work and will be discussed in
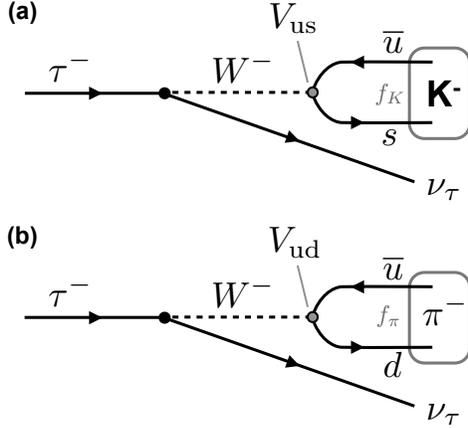
Figure 2.7: Feynman diagrams of τ^- decay branches to K^- (a) and π^- (b) which allow the determination of $|V_{us}| \cdot f_K / (|V_{ud}| \cdot f_\pi)$.

more detail in the next chapter. Nuclear β- decays, the neutron decay and the pion's β-decay branch are studied to yield V_{ud}. Table 2.3 summarizes measurements of V_{us} and the most precise value for V_{ud} from superallowed $0^+ \rightarrow 0^+$ nuclear β-decays. Fitting V_{ud} and V_{us} from this data neglecting the less precise τ-decay leaves $|V_{ud}| = 0.97425(22)$ unchanged, but yields $|V_{us}| = 0.2253(9)$ [54]. The correlation between the two is negligible. Hence, the unitarity test of the first row of the CKM matrix results in

$$|V_{ud}|^2 + |V_{us}|^2 + |V_{ub}|^2 = 0.9999(4)(4), \tag{2.30}$$

in agreement with unity. Respective uncertainties are due to V_{ud} and V_{us}. Even though V_{ud} is known much more precisely than V_{us}, its larger value causes an equal share of V_{ud} and V_{us} to the uncertainty of the unitarity test.

2.3.1 Implications for physics beyond the Standard Model

While Equation 2.30 does not highlight any deviations, it puts stringent limits on models beyond the Standard Model.

- *4th quark generation*: Missing decay strength could indicate a fourth generations of quarks usually denoted t' and b'. Equation 2.30 sets constraints on $V_{ub'}$ according to the given uncertainty. However, at the present level of precision, sensitivity to a fourth generation is only possible if it does not follow the hierarchy $|V_{ud}| > |V_{us}| > |V_{ub}| > |V_{ub'}|$ as observed for the first three

generations. As mentioned before, to date not even $|V_{ub}|$ has a significant impact on this unitarity test. *A priori*, the SM does not demand this hierarchy and on the (massive) neutrino sector the CKM equivalent, the Pontecorvo-Maki-Nakagawa-Sakata (PMNS) matrix, is not as hierarchically structured. This constraint is complementary to direct searches at colliders which put limits on the masses of new quarks [29]. As the number of quark and lepton generations have to be equal in order to cancel the gauge anomaly in the weak interaction, limits on a fourth generation also arise from respective heavy lepton searches [29].

- *Coupling universality:* In the Standard Model the left-handed lepton doublets couple to the $W^{\pm}$-bosons analogously to the quark doublets (see Equation 2.24). The quark coupling only differs by the additional factor due to the CKM-element V_{ij}. In the low-energy effective Lagrangian the coupling constant is called the Fermi constant G_F (see section Section 2.4). In the Standard Model

$$G_F^{\mu} = G_F^{\text{CKM}}\big(|V_{ud}|^2 + |V_{us}|^2 + |V_{ub}|^2\big) = G_F^{\tau} = G_F^{b} \qquad (2.31)$$

holds, where the respective Fermi constants are extracted from muon decay, CKM-studies, leptonic tau-decay, and from the fine structure constant α in combination with weak boson properties. Although in agreement with the other estimates, G_F^{τ}'s precision is too low for stringent Standard Model tests. Assuming CKM unitarity, deviations from $G_F^{\mu} = G_F^{\text{CKM}}$ could be caused by exotic muon-decays.[3] In fact, some possibilities for non-standard muon decays are orders of magnitude more constrained by direct searches. But others such as $\mu^+ \to e^+ \bar{\nu}_e \nu_{\mu}$, where both neutrinos are the respective antineutrinos of the regular μ- decay ($\mu^+ \to e^+ \nu_e \bar{\nu}_{\mu}$), receive the most stringent limit by $G_F^{\mu} = G_F^{\text{CKM}}$ [56, 57].
  G_F^{b} is known about 4 times less precise than G_F^{CKM} (again assuming unitarity in the CKM matrix). The experimental agreement between G_F^{μ}, G_F^{CKM}, and G_F^{b} poses limits on new heavy SU(2)$_L$ doublets or excited $W^{*\pm}$ bosons in extra dimensions with $m_{W^*} > 2 - 3$ TeV [56, 57].

- *New boson Z_{χ} in SO(10):* A candidate for a Grand Unified Theory (GUT), the unification of all forces in the Standard Model, could be SO(10) which is the group of all orthogonal transformations in 10 dimensions with $\det = 1$, i.e. all rotations. SO(10) can be broken down to SU(3) x SU(2) x U(1) x

---

[3]Note that $G_F^{\mu} = G_F^{\text{CKM}}\big(|V_{ud}|^2 + |V_{us}|^2 + |V_{ub}|^2\big)$ and $|V_{ud}|^2 + |V_{us}|^2 + |V_{ub}| = 1$ are not two independent tests of the Standard Model. The CKM- matrix elements are calculated assuming $G_F^{\mu} = G_F^{\text{CKM}}$ (see Section 2.6.3).
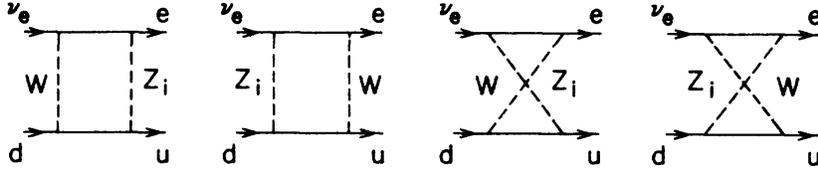
Figure 2.8: Feynman diagrams in the electroweak interaction between quarks and leptons involving an extra Z boson. Figure from [58].

U(1) where the first three groups mirror the Standard Model and the last U(1) corresponds to a new, neutral gauge boson Z_χ. Z_χ enters in Feynman diagrams used to measure CKM-matrix elements (Figure 2.8), but also to the muon decay [58]. Currently, the lower mass limit on Z_χ based on the unitarity test is $m_{Z_\chi} > 460$ GeV which is less stringent than the tightest bound from collider searches ($m_{Z_\chi} > 822$ GeV) [26].

Moreover, the unitarity test constrains right-handed currents, in addition to the Standard Model's left-handed current in the weak interaction [26] or aspects of SUperSYmmetry (SUSY) [59].

Many of these probes of the Standard Model are at or close to the TeV scale and impose tight constraints on models for new physics. Due to the equal contributions of V_{ud} and V_{us} to the uncertainty in the unitarity test, progress on both sides is essential for a further error reduction. Additionally, all doubts about the accuracy of theory and experiment in respect to V_{ud} and V_{us} have to be carefully investigated. Otherwise the precision is not worth as much as is claimed. The importance of later considerations has been demonstrated in the already discussed shift of V_{us} which had incorrectly created a tension of the unitarity in the CKM matrix. We will next turn to the determination of V_{ud}. Here, concern was raised about theoretical isospin-symmetry corrections (see Section 2.7) and discrepancies in the measurement of β-decay transition energies were found and resolved through Penning traps (Section 2.9). Searches for physics beyond the Standard Model on the level of the effective Lagrangian of nuclear β-decays such as scalar or tensor interactions are also discussed in [15, 60].

2.4 Nuclear β-decays from first principles of the Standard Model

Before we develop the formalism for nuclear β-decay, we describe the decay at the quark-level only. Hence, we neglect the hadronic structure in which the quark is

24

embedded in and treat the quark as a free particle. In the rest frame of the decaying particle, a decay rate Γ in quantum field theory is given as

$$d\Gamma = \frac{1}{2m_i}\Big(\prod_f \frac{d^3 p_f}{(2\pi)^3}\frac{1}{2E_f}\Big) \cdot |M(i \to f)|^2 \cdot (2\pi)^4 \delta^{(4)}(p_i - \sum_f p_f), \quad (2.32)$$

where m_i is the mass of the particle, the product and sum are over all particles in the final state, and E_f is the energy of a particle after the decay. The four Dirac deltas, notated as $\delta^{(4)}$, enforce energy and momentum conservation and $M(i \to f)$ is the transition matrix element. The interaction Lagrangian responsible for the weak decay of a u- to a d-quark and *vice versa* follows according to Equation 2.25

$$\mathcal{L}_I = \frac{g}{\sqrt{2}} \quad \Big[\quad V_{ud} \cdot \overline{u}_L \gamma^\mu d_L \cdot W_\mu^+ + V_{ud}^* \cdot \overline{d}_L \gamma^\mu u_L \cdot W_\mu^-$$

$$+ \quad \overline{e}_L \gamma^\mu \nu_{e,L} \cdot W_\mu^- + \overline{\nu}_{e,L} \gamma^\mu e_L \cdot W_\mu^+ \Big]. \quad (2.33)$$

Here we have dropped the u' because we will from now on always operate in the physical mass basis. The (charged) weak interaction Lagrangian for electrons e and electron neutrinos ν_e is identical to the quarks with the exception of the additional factor V_{ud}. Second and third generation leptons are not considered, because the transition energy in nuclear β-decays is less than the muon or tau mass. It is common to drop the L-subscript in favour of the left-handed projection operator $P_L = 1/2 \cdot (1 - \gamma^5)$, e.g. $\overline{e}_L \gamma^\mu \nu_{e,L} = 1/2 \cdot \overline{e}\gamma^\mu (1 - \gamma^5)\nu_e$. The right handed part of the fermion fields will thus vanish.

The transition matrix element of the decay $u \to de^+\nu_e$ is constructed by utilizing respective Feynman rules. Although these are typically derived in standard textbooks, we will recapitulate some critical steps which will later be essential to expand the formalism to hadrons and to derive the effective low-energy Lagrangian. The transition matrix element M is related to the S-matrix of the process via

$$\langle (\vec{p}_{e^+}, s_{e^+}), (\vec{p}_{\nu_e}, s_{\nu_e}), (\vec{p}_d, s_d) \mid S \mid (\vec{p}_u, s_u)\rangle. \quad (2.34)$$

Here, each fermion is annotated with its 3-momentum $\vec{p}$ and its z-projection in spin, i.e. $s = \pm 1/2$. With $S = 1 + iT$, it can be evaluated to[4]

$$\langle (\vec{p}_{e^+}, s_{e^+}), (\vec{p}_{\nu_e}, s_{\nu_e}), (\vec{p}_d, s_d) \mid iT \mid (\vec{p}_u, s_u)\rangle = \quad (2.35)$$

$$\langle (\vec{p}_{e^+}, s_{e^+}), (\vec{p}_{\nu_e}, s_{\nu_e}), (\vec{p}_d, s_d) \mid \mathtt{T}\exp\Big(i\int d^4 x \mathcal{L}_I(x)\Big) \mid (\vec{p}_u, s_u)\rangle_{\mathtt{f.c.d.}}$$

---

[4]f.c.d. stands for fully connected diagrams and $\mathtt{T}$ in front of the exponential means time-ordered.

Non-trivial terms will first appear at the second order of the exponential's expansion. Since $\langle (\vec{p}_{e+}, s_{e+}) \mid \overline{e}$ and $\langle (\vec{p}_{e+}, s_{e+}), (\vec{p}_{\nu_e}, s_{\nu_e}), (\vec{p}_d, s_d) \mid \overline{u}$ cannot contract, the only remaining terms of Equation 2.33 at second order expansion are

$$
\frac{2i^2 g^2}{2! \cdot 2} \quad \langle \quad (\vec{p}_{e+}, s_{e+}), (\vec{p}_{\nu_e}, s_{\nu_e}), (\vec{p}_d, s_d) \mid
$$
$$
\mathrm{T} \quad \left(\int d^4 x V_{ud}^* \cdot \overline{d}(x) \gamma^\mu \frac{1-\gamma^5}{2} u(x) \cdot W_\mu^-(x) \right) \times
$$
$$
\left(\int d^4 y \overline{\nu}_e(y) \gamma^\nu \frac{1-\gamma^5}{2} e(y) \cdot W_\nu^+(y) \right) \mid (\vec{p}_u, s_u) \rangle. \quad (2.36)
$$

Putting the numerical factor and the integrals aside, the bracket can be separated by Wick's theorem (e.g. in [23]) to

$$
\langle (\vec{p}_{e+}, s_{e+}), (\vec{p}_{\nu_e}, s_{nu_e}) \mid \overline{\nu}_e(y) \gamma^\nu \frac{1-\gamma^5}{2} e(y) \mid 0 \rangle \times
$$
$$
\langle 0 \mid \mathrm{T} W_\nu^+(y) W_\mu^-(x) \mid 0 \rangle \times
$$
$$
\langle (\vec{p}_d, s_d) \mid V_{ud}^* \cdot \overline{d}(x) \gamma^\mu \frac{1-\gamma^5}{2} u(x) \mid (\vec{p}_u, s_u) \rangle. \quad (2.37)
$$

$\langle 0 \mid \mathrm{T} W_\nu^+(y) W_\mu^-(x) \mid 0 \rangle$ is the W-boson's propagator which can be expressed as

$$
\langle 0 \mid \mathrm{T} W_\nu^+(y) W_\mu^-(x) \mid 0 \rangle = \int \frac{d^4 q}{(2\pi)^4} \frac{-i g_{\mu\nu}}{q^2 - m_W^2} e^{iq \cdot (x-y)}. \quad (2.38)
$$

The contraction of the brackets with the fields and the integrations over the four-vectors x and y create $\delta^{(4)}$-functions which establish 4-momentum conservation at each vertex, hence, $q^\mu = p_u^\mu - p_d^\mu$. Considering the available transition energies of a few MeV in nuclear β-decays the momentum transfer q is negligible compared to the mass of the W-bosons ($m_W \sim 80$ GeV). The propagator (in momentum space) can be approximated by $i g_{\mu\nu}/m_W^2$. The resulting transition matrix element

$$
i \cdot M(u \to d e^+ \nu_e) = \frac{V_{ud}^* g^2}{8 m_W^2} \overline{d}^{s_d}(p_d) \gamma^\mu (1-\gamma^5) u^{s_u}(p_u) \cdot \overline{\nu}_e^{s_\nu}(p_\nu) \gamma_\mu (1-\gamma^5) e^{s_{e+}}(p_{e+})
$$
$$
(2.39)
$$

could have also be obtained at first order expansion of Equation 2.36 with an effective Lagrangian

$$
\mathcal{L}_I(x) = \frac{g^2}{8 m_W^2} V_{ud}^* \overline{d}(x) \gamma^\mu (1-\gamma^5) u(x) \cdot \overline{\nu}_e(x)(1-\gamma^5) e(x). \quad (2.40)
$$

26
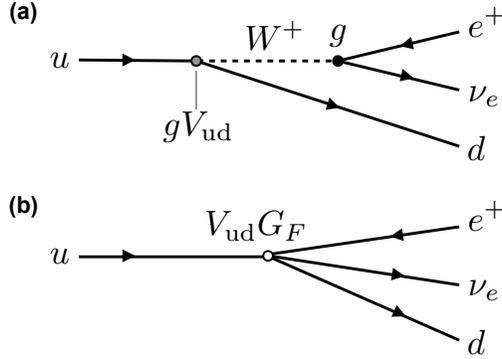
Figure 2.9: Lowest order Feynman diagram for the 'decay' of a u-quark within the Standard Model (a) and its low energy approximation in means of a contact term (b).

All fermions are now evaluated in the expansion at the same space-time point x. As expected, in the effective Lagrangian the short-range physics (i.e. the exchange of the W-boson) is not resolved at the lower energy. Instead, it is moved into a contact term (see Figure 2.9). The coupling constant relates to the definition of the Fermi constant as $G_F/\sqrt{2} = g^2/(8m_W^2)$. In correspondence to Equation 2.9, $\bar{\nu}_e(1-\gamma^5)e$ and $\bar{d}\gamma^\mu(1 - \gamma^5)u$ are called the leptonic and quark current, respectively.

Equation 2.32 can now be evaluated utilizing the derived matrix element. However, since quarks only exist in colourless hadrons, we will first discuss the hadronic complications to the matrix elements.

2.4.1 Neutron β-decay

The computation of the transition matrix element of the neutron decay follows analogously the derivation on the previous pages. Within the neutron (udd) a d-quark decays into a u-quark resulting in a proton (uud) (Figure 2.10). Pending an exact description of the neutron by means of QCD, we can not evaluate the hadronic part (compare to Equation 2.37 for the u-quark decay) from first principles. Instead, one arrives at

$$\frac{V_{ud}G_F}{\sqrt{2}} \langle p \mid \bar{u}\gamma^\mu(1 - \gamma^5)d \mid n \rangle \cdot \langle e, \bar{\nu}_e \mid \bar{e}\gamma_\mu(1 - \gamma^5)\nu_e \mid 0 \rangle. \tag{2.41}$$

The leptonic current can be dealt with as before. The hardronic part is usually split into the vector (or Fermi) $\langle p \mid \bar{u}\gamma^\mu d \mid n \rangle$ and an axial-vector (or Gamow-Teller) part $\langle p \mid \bar{u}\gamma^\mu\gamma^5 d \mid n \rangle$. Lacking knowledge about the QCD details, we parameterize
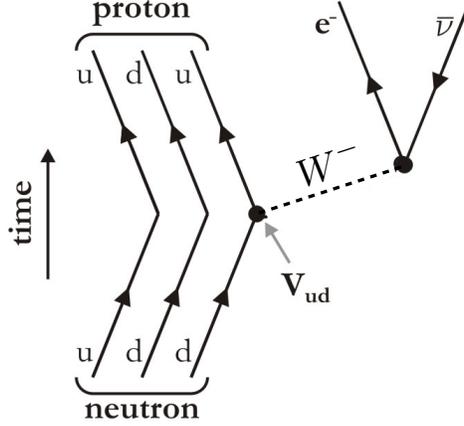
Figure 2.10: Feynman diagram of the neutron decay

each part and introduce form factors to cover the hadronic structure. In momentum space, the most general vector based on all available momenta and spins allows the Fermi component to be written as

$$\langle p \mid \overline{u}\gamma^\mu d \mid n \rangle = \overline{\psi}_p^{s_p}(p_p)\Big[f_1 p^\mu + f_2 q^\mu + f_3 \gamma^\mu + f_4 i\sigma^{\mu\nu}p_\nu + f_5 i\sigma^{\mu\nu}q_\nu\Big]\psi_n^{s_n}(p_n)$$
(2.42)

with $p^\mu = p_n^\mu + p_p^\mu$ and $q^\mu = p_n^\mu - p_p^\mu$. ψ_p and ψ_n are the Dirac spinors of the neutron and proton respectively which are themselves spin-1/2 fermions. Applying the Gordon identity (see e.g. in [23]) for free Dirac particles, the previous expression can be simplified to

$$\langle p \mid \overline{u}\gamma^\mu d \mid n \rangle = \overline{\psi}_p^{s_p}(p_p)\Big[g_V(q^2)\gamma^\mu + \frac{f_M(q^2)}{2M}i\sigma^{\mu\nu}q_\nu + \frac{f_S(q^2)}{2M}q^\mu\Big]\psi_n^{s_n}(p_n).$$
(2.43)

M is an arbitrarily chosen mass to keep the form factors dimensionless. g_V and f_S are called the vector and the induced scalar form factors. In analogy to QED, where the corresponding form factor gives rise to the anomalous magnetic moment, f_M is known as the weak magnetism form factor.

A second analogy to QED will lead to another reduction in the number of required form factors: For an electromagnetic current J^μ, charge conservation is manifested in $\partial_\mu J^\mu = 0$. With a Fourier transform, $J(q = p_1 - p_2) = \int d^4x \cdot \exp(iqx)J(x)$, the continuity equation is $q_\mu J^\mu = 0$ in momentum space. Since the structure of the weak vector current in Equation 2.43 is identical to the electromagnetic current, it is expected that $q_\mu \langle p \mid \overline{u}\gamma^\mu d \mid n \rangle = 0$ holds. This is one aspect of the Conserved
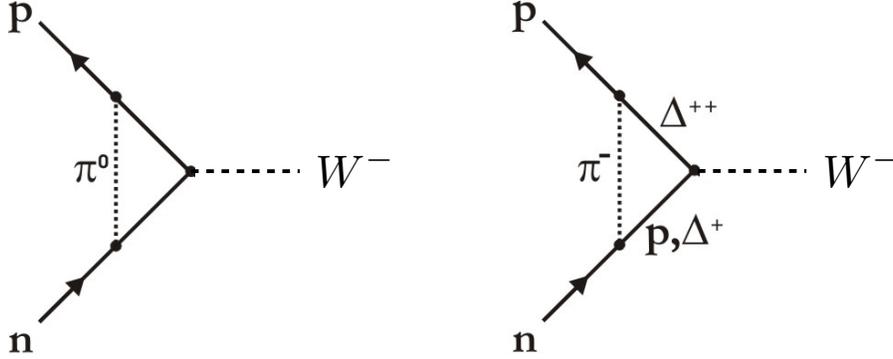
Figure 2.11: Two examples of Feynman diagrams which modify the weak
axial-vector coupling constant g_A due to the strong interaction.

Vector Current (CVC) hypothesis [61]. Then, the weak magnetic component vanishes naturally due to the antisymmetry of the Dirac matrices, $\sigma^{\mu\nu}q_\mu q_\nu = 0$. In the limit of exact isospin-symmetry the masses of protons and neutrons are equal. Hence,

$$\overline{\psi}_p(p_p)q_\mu\gamma^\mu\psi_n(p_n) = \overline{\psi}_p(p_p)(\not{p}_n - \not{p}_p)\psi_n(p_n) = (m_n - m_p)\overline{\psi}_p(p_p)\psi_n(p_n) = 0 \tag{2.44}$$

when the free Dirac equation is employed. In contrast, the induced scalar contribution does not vanish; therefore, CVC, $q_\mu J^\mu = 0$, requires f_S to vanish.

Similar steps can be undertaken for the axial part of the hadronic weak current. Due to the negligible momentum transfer in neutron and nuclear β-decays, we continue by working in the limit $q^2 \to 0$ and neglect all terms in q.

$$\langle p \mid \overline{u}\gamma^\mu(1 - \gamma^5)d \mid n \rangle = \overline{\psi}_p^{s_p}(p_p)\Big[g_V(0)\gamma^\mu - g_A(0)\gamma^\mu\gamma^5\Big]\psi_n^{s_n}(p_n) \tag{2.45}$$

g_A is renormalized in the presence of the strong force as illustrated by meson exchange diagrams in Figure 2.11. However, g_V is protected by the CVC hypothesis. The strong interaction does not renormalize the electric charge as evident by the equality of the absolute charge value of electrons and protons. In the same manner, the CVC hypothesis assumes g_V is not affected by the strong force and should for $q^2 \to 0$ be equal to the free quark limit, $g_V(0) = 1$. The validity of CVC itself is subject to intense experimental scrutiny, particularly through studies of superallowed nuclear β-decays.

In the standard or Dirac representation of the γ matrices (see e.g. in [22]) the (4

dimensional) spinor of a free fermion (which we will associate with a nucleon)

$$\psi^s(p) = \begin{pmatrix} \chi^s \\ \frac{\sigma_i \cdot p_i}{E+m} \chi^s \end{pmatrix} \xrightarrow{p \ll m} \begin{pmatrix} \chi^s \\ 0 \end{pmatrix} \tag{2.46}$$

is in the non-relativistic limit $p \ll m$ represented by the 2-dimensional χ^s only. For the neutron at rest this is exact. For the proton it is a good approximation due to the small momentum transfer, $q^2 \ll m_p^2$, i.e. the recoil of the proton is neglected. When applying Equation 2.46 to Equation 2.45 and using again the standard representation, one obtains

$$\langle p \mid \overline{u}\gamma^\mu(1 - \gamma^5)d \mid n\rangle = g_V(0)\chi_p^+\chi_n\delta^{\mu 0} - g_A(0)\chi_p^+\sigma_i\chi_n\delta^{\mu i}. \tag{2.47}$$

The vector or Fermi component consequently cannot flip the nucleon's spin ($\Delta S = 0$), while the axial or Gamow-Teller part may, due to the presence of σ_i, change the spin ($\Delta S = 1$). This implies that in the Fermi decay contribution the anti-neutrino and electron couple to $S = 0$, and for Gamow-Teller to $S = 1$. Since the neutron decay is spin 1/2 to spin 1/2, it involves both components.
Combining the results (Equation 2.47, Equation 2.41) we end up with

$$iM = \frac{V_{ud}G_F}{\sqrt{2}}(g_V\chi_p^{s,+}\chi_n^{s'}\delta^{\mu 0} - g_A\chi_p^{s,+}\sigma_i\chi_n^{s'}\delta^{\mu i}) \cdot \overline{e}^{s_e}(p_e)\gamma_\mu(1 - \gamma^5))\nu^{s_{\overline{\nu}}}(p_{\overline{\nu}}) \tag{2.48}$$

for the transition matrix element. We have dropped the explicit notation of $q^2 \to 0$ for g_V and g_A. The leptonic current was obtained analogously to the u-quark decay. Equation 2.32 yields the neutron's lifetime $\tau = \Gamma^{-1}$, but also momentum correlations between the outgoing fermions. Correlation measurements in neutron and nuclear β-decay are themselves a wide field of study to probe the Standard Model because they could be sensitive to new physics in the form of scalar or tensor interactions or deviations from the maximal parity violation in the $V - A$ theory [60]. The measurements discussed in this thesis are neither with spin-polarized neutrons or nuclei nor are they sensitive to the spin of the outgoing particles. When averaging over all initial spin states and summing over all final spins the total decay rate of the neutron becomes

$$\Gamma = \frac{G_F^2 \mid V_{ud} \mid^2}{2\pi^3}(g_V^2 + 3g_A^2)\int_{m_e}^{Q+m_e} dE_e(E_e - Q - m_e)^2 E_e\sqrt{E_e^2 - m_e^2} \tag{2.49}$$

where the phase space integral is over the electrons' total energy and Q is the mass difference between initial and final (massive) particles, $Q = m_n - m_p - m_e$. The literature commonly defines $\lambda = g_V/g_A$ and normalizes the integral to the

electron's rest energy, m_e. V_{ud} is then related to the neutron's mean lifetime τ and λ according to

$$\mid V_{ud}\mid^2 = \frac{2\pi^2}{G_F^2 g_V^2 m_e^5} \cdot \frac{1}{\tau(1+3\lambda^2)f} \qquad (2.50)$$

with the statistical rate function f

$$f = \int_1^{W_0} dW (W - W_0)^2 W \sqrt{W^2 - 1}. \qquad (2.51)$$

Hence a measurement of the neutron's half-life as well as λ allows for an experimental determination of V_{ud}, when taking G_F from measurements of the muon decay. The mass difference between neutron and proton is well known. Although a more exact treatment has to take radiative corrections as well as a modification of f into account, the neutron decay is a theoretically clean way to determine V_{ud} because there are no nuclear corrections to consider. This feature is also shared by the β-decay of the pion, but this pion decay branch has a tiny Branching Ratio (BR) in the order of only 10^{-8}. Thus, the neutron β-decay is often considered to be the most attractive option to determine V_{ud}. However, the uncertainty is dominated by experiment, particularly, since the neutron lifetime remains intensely debated with considerable shifts in its mean-value over the decades (Figure 2.12). More recently, a measurement by Serebrov et al. in 2005 [62] deviated from the previous world average by 6.5 σ and from the previously most precise single measurement [63] by 5.6 σ. The debate about these seriously conflicting data was intensified in 2010 by Pichlmaier et al. [64] who reported a neutron lifetime closer to [62] (see Figure 2.12b). Furthermore, Serebrov and Fomin [65] have challenged the analysis of systematic errors in previous experiments of trapped Ultra Cold Neutrons (UCN), including the one in [63].

Following a recent review [66], these discrepancies can only be resolved by detailed re-analysis of existing measurements or through improved next generation experiments. In the latter context, consistency between results from trapped UCN and currently less precise neutron beam experiments (see Figure 2.12b) would be of particular importance as both are dealing with very different sources of systematic errors.

In addition to the unsatisfactory situation regarding the neutron lifetime, the determination of V_{ud} by studying the neutron β-decay requires knowledge about $\lambda = g_V/g_A$ (see Equation 2.50). Experimental results for λ show a larger spread than statistically expected, too, and the PDG had to inflate the uncertainty on the weighted average accordingly [29]. Hence, all these difficulties make V_{ud} from neutron decay less competitive in comparison to superallowed nuclear β-decays.
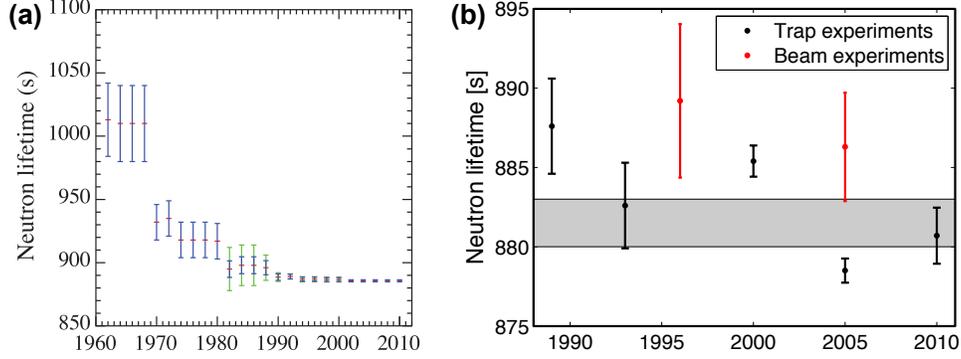
Figure 2.12: Neutron lifetime τ: (a) historical evolution of τ measurements over the last half-century. Figure from [29]. (b) Experimental results currently considered by the Particle Data Group (PDG)[29]. The horizontal band represents the PDG average which includes a scale factor to take into account the inconsistencies between the data. See text for details.

2.4.2 Nuclear β-decays

In the previous section the formalism of the neutron's β-decay has been introduced. The proton β-decay is energetically forbidden ($m_n > m_p$), but its decay formalism could be developed along the same lines. Within an atomic nucleus this energy might be available and in the nuclear environment the decay of a neutron into a proton and *vice versa* are observed. According to the electric charge of the lepton, they are known as β^- and β^+. Related to each other by the crossing symmetry, the β^+ is in competition with the nuclear Electron Capture (EC). In this process, an electron from an atomic shell is captured into the nucleus.

With the introduction of form factors, the formalism of the previous section is operating on nucleons instead of the fundamental quarks. Nucleons are also the entities nuclear theory is working with. In this sense, the framework is already well suited for the correct resolution scale. However, it needs to be further adapted to properly integrate the nuclear surrounding in the β-decay. Following Equation 2.41 we will need to evaluate

$$i \cdot M_{\beta^-} = \frac{V_{ud} G_F}{\sqrt{2}} \langle \psi_D \mid \gamma^\mu (1 - \gamma^5) \mid \psi_P \rangle \cdot \overline{e}^{s_e}(p_e) \gamma_\mu (1 - \gamma^5)) \nu^{s_{\overline{\nu}}}(p_{\overline{\nu}}) \quad (2.52)$$

for β^- and

$$i \cdot M_{\beta^+} = \frac{V_{ud}^* G_F}{\sqrt{2}} \langle \psi_D \mid \gamma^\mu (1 - \gamma^5) \mid \psi_P \rangle \cdot \overline{\nu}_e^{s_\nu}(p_\nu) \gamma_\mu (1 - \gamma^5) e^{s_{e^+}}(p_{e^+}) \quad (2.53)$$

for β^+ decays. ψ_P and ψ_D denote the parent and daughter nucleus of the decay. But in contrast to Equation 2.42 and later equations, we cannot describe a nucleus as a Dirac spinor. Nuclei are generally not spin 1/2 objects and are compound objects with a spectrum of excited states built upon the ground-state. It is our aim to translate $\langle \psi_D \mid \gamma^\mu (1 - \gamma^5) \mid \psi_P \rangle$ into a language of nuclear theory such that nuclear wavefunctions can be employed. To do so, let's reconsider the neutron decay. According to Equation 2.47 and Equation 2.48, the non-vanishing components in the approximation of $\vec{p}_p \ll m_p$ for the proton are

$$\langle p, e, \overline{\nu} \mid iT \mid n \rangle = \frac{V_{ud} G_F}{\sqrt{2}} \int d^4 x e^{ix(p_p + p_{\overline{\nu}} + p_e - p_n)} \times$$
$$\chi_p^{s,+}(p_p) \big[g_V \delta^{0\mu} - g_A \sigma_i \delta^{\mu i} \big] \chi_n^{s'}(p_n) \cdot \ell_\mu, \quad (2.54)$$

where ℓ_μ is the leptonic current in momentum space. Neglecting the recoil of the proton ($\vec{p}_p \ll m_p$) yields a decay rate $d\Gamma$ which is independent of $\vec{p}_p$ except for the Dirac delta in three momentum $\delta^{(3)}(\vec{p}_p + \vec{p}_{\overline{\nu}} + \vec{p}_e)$. Hence, the integration over the proton's three-momentum in Equation 2.32 will not have any impact on the decay rate and we drop $d^3 p_p$ in Equation 2.32. In other words, neglecting $\vec{p}_p$ does not mean $\vec{p}_{\overline{\nu}} = -\vec{p}_e$ from the Dirac delta, but the proton absorbs any momentum which the electron and anti-neutrino might have. Consequently, the integration of x in Equation 2.54 which generates the $\delta^{(4)}$ is only needed to enforce energy conservation. The transition matrix element is then redefined as

$$\langle p, e, \overline{\nu} \mid iT \mid n \rangle = 2\pi \delta(E_n - E_p - E_{\overline{\nu}} - E_e) \cdot iM \quad (2.55)$$

with

$$iM = \frac{V_{ud} G_F}{\sqrt{2}} \int d^3 x e^{i\vec{x}\vec{p}_p} \chi_p^{s,+}(p_p) \times$$
$$\big[g_V \delta^{0\mu} - g_A \sigma_i \delta^{\mu i} \big] e^{-i\vec{x}\vec{p}_n} \chi_n^{s'}(p_n) \cdot \ell_\mu e^{i\vec{x}(\vec{p}_e + \vec{p}_{\overline{\nu}})}. \quad (2.56)$$

In a plane wave ansatz $\chi_p^s(\vec{x}) = e^{-i\vec{x}\vec{p}_p} \chi_p^s(p_p)$ and $\chi_n^{s'}(\vec{x}) = e^{-i\vec{x}\vec{p}_n} \chi_n^{s'}(p_n)$ this is further simplified to

$$iM = \frac{V_{ud} G_F}{\sqrt{2}} \int d^3 x \chi_p^{s,+}(\vec{x}) \big[g_V \delta^{0\mu} - g_A \sigma_i \delta^{\mu i} \big] \chi_n^{s'}(\vec{x}) \cdot \ell_\mu e^{i\vec{x}(\vec{p}_e + \vec{p}_{\overline{\nu}})}. \quad (2.57)$$

Next, we re-call the isospin symmetry of Section 2.1.3 and associate neutron and proton as isospin $T_z = 1/2$ and $T_z = -1/2$ projections of the same doublet respectively. Isospin is in many ways analogous to regular spin or angular momentum and we can describe the neutron-decay matrix element with the isospin lowering operator $\hat{t}^-$ as

$$
iM = \quad \frac{V_{ud}G_F}{\sqrt{2}} \int d^3x \chi^+(\vec{x}, s, -1/2) \times
$$
$$
\left[g_V \delta^{0\mu} - g_A \sigma_i \delta^{\mu i} \right] \hat{t}^- \chi(\vec{x}, s', +1/2) \cdot \ell_\mu e^{i\vec{x}(\vec{p}_e + \vec{p}_{\bar{\nu}})}. \quad (2.58)
$$

Because the isospin-symmetry is broken, we will at a later point need to introduce theoretical corrections to this approximation. In this formulation we are dealing with nucleon wave-functions in position space including their isospin projections. In this picture, the β-decay on nucleon level is a change in the z-projection of the isospin and is taken care of by the isospin-lowering operator.

This result can now be generalized to nuclear wave-functions where the nuclear isospin lowering and raising operators are defined as the sum over all A nucleons in a nucleus

$$
\hat{T}^- = \sum_{i=1}^{A} t^-_{(i)}, \qquad \hat{T}^+ = \sum_{i=1}^{A} t^+_{(i)}, \qquad (2.59)
$$

where $t^\pm_{(i)}$ acts upon nucleon i. Suppose a parent nucleus P with A nucleons of which Z are protons; it is described by a nuclear wave-function $\psi_P(\alpha, T_z)$ where α denotes all quantum numbers including its total angular momentum J, but not its isospin projection $T_z = (N - Z)/2$. The wave-function is the Slater determinant over the individual nucleons,

$$
\psi_P(\alpha, T_z) = \mathcal{A}[\chi_{p_1}(x_1) \cdot \chi_{p_2}(x_2) \cdot ... \cdot \chi(x_Z)_{p_Z} \cdot \chi(x_{Z+1})_{n_1} \cdot ... \cdot \chi(x_A)_{n_{A-Z}}],
$$
$$
(2.60)
$$

with $\mathcal{A}$ yielding the full anti-symmetrization. If we assume non-relativistic nucleons ($\vec{p}_i \ll m$) in the atomic nucleus, the same approximations as in the neutron-decay can be followed. In the β^- decay of a nucleus $\psi_P(\alpha, T_z)$ to the daughter nucleus $\psi_D(\alpha', T_z - 1)$, Equation 2.58 is then generalized by summing over all nucleons. This combines to the nuclear isospin lowering operator as defined above (Equation 2.59). Instead of integrating over just one nucleon's spatial coordinates, the integration over all nucleons' positions is necessary. Thus, the transition matrix

34

element follows

$$iM = \frac{V_{ud}G_F}{\sqrt{2}} \int d^3x_1...d^3x_A \psi_D(x, \alpha', T_z - 1) \times$$
$$\left[g_V \delta^{0\mu} - g_A \sigma_i \delta^{\mu i} \right] \hat{T}^- \psi_P(x, \alpha, T_z) \cdot \ell_\mu. \tag{2.61}$$

In the previous step, the exponential with the lepton momenta was expanded, $\exp \left[i\vec{x}(\vec{p}_e + \vec{p}_{\bar\nu}) \right] \approx 1 + i\vec{x} \cdot (\vec{p}_e + \vec{p}_{\bar\nu})$ and only the first constant term was kept. This is possible due to the small momentum transfer in nuclear β-decays in comparison to the size of the nucleus. The expansion corresponds in the phenomenology of β-decays to allowed (first term) and forbidden transitions (all remaining terms). As the expansion term of the 1st forbidden transition, $i\vec{x} \cdot (\vec{p}_e + \vec{p}_{\bar\nu})$, is linear in $\vec{x}$, the parity of parent and daughter wave-function must be opposite parity states, i.e. $\pi_P = \pi_D \cdot (-1)$, otherwise the spatial integration would vanish. Conversely, for allowed transition the parity of the two wave-functions must be the same. In allowed transitions, the total angular momentum of the leptons couples to $L = 0$ and, hence, $L_P = L_D$. The derivation will continue in the allowed approximation only.

In the last equation, the only part which remains dependent on the lepton momenta is the leptonic current, which is formally independent of any spatial coordinate. This was correct for the neutron decay, however, in the nuclear decay one cannot assume a free outgoing (anti-) electron as the other nucleons will distort the β-particle. This is usually accounted for by adding a term $F(Z, E_e)$, which is calculated by solving the Dirac equation for continuum states in the presence of a point-like nucleus with charge Ze and compare the solution to the free Dirac equation. $F(Z, E_e)$ is known as the Fermi function. In this formulation, the leptonic current ℓ_μ remains identical to the neutron decay and independent of the spatial integrations. The hadronic and leptonic part are thus separated. When summing over all initial and averaging over all final spin projections, we obtain analogously to the neutron a decay rate of

$$\Gamma = \frac{G_F^2 \mid V_{ud} \mid^2 m_e^5}{2\pi^3} f \cdot \left[g_V^2 \mid M_F \mid^2 + g_A^2 \mid M_{GT} \mid^2 \right] \tag{2.62}$$

with a statistical rate function of

$$f = \int_1^{W_0} dW(W - W_0)^2 W \sqrt{W^2 - 1} \cdot F(Z, W). \tag{2.63}$$

Following its definition in Equation 2.51, the maximal (normalized) energy of the outgoing electron is $W_0 = (Q + 1)/m_e$. M_F and M_{GT} are known as the nu-
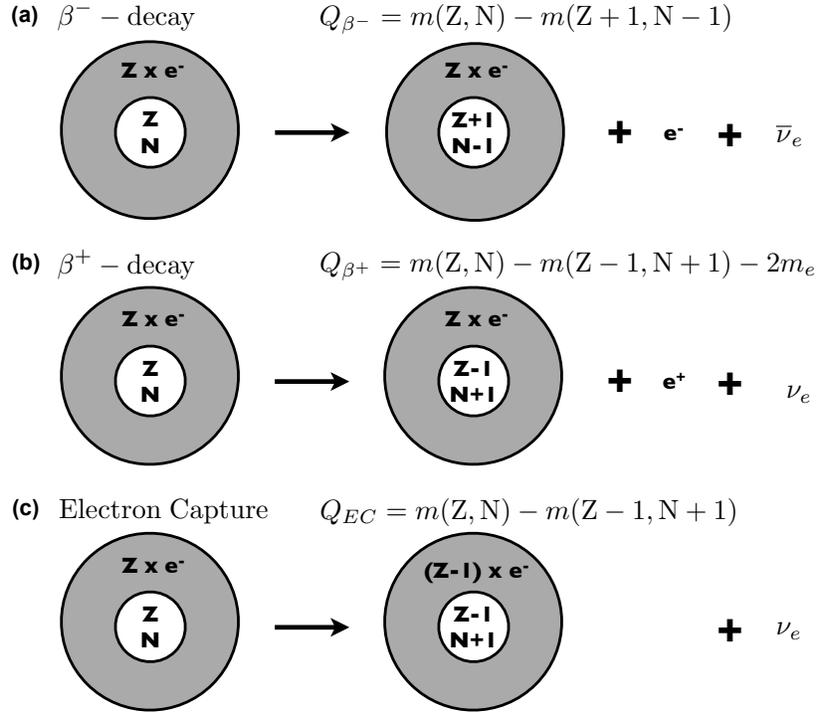
Figure 2.13: Schematics to illustrate the definition of Q-values with atomic masses m(Z,N) for β^-, β^+-decay, and nuclear electron capture.

clear matrix elements for the Fermi (vector) or Gamow-Teller (axial-vector) parts. According to Equation 2.61, they are expressed as

$$
\begin{aligned}
M_F &\equiv \langle f \mid \hat{T}^- \mid i \rangle \equiv \int d^3x_1...d^3x_A \psi_D(x, \alpha', T_z - 1)\hat{T}^- \psi_P(x, \alpha, T_z) \quad (2.64) \\
M_{GF,i} &\equiv \langle f \mid \sigma_i \cdot \hat{T}^- \mid i \rangle \equiv \int d^3x_1...d^3x_A \psi_D(x, \alpha', T_z - 1)\sigma_i \cdot \hat{T}^- \psi_P(x, \alpha, T_z)
\end{aligned}
$$

For β^+-decays, the same equations hold except that $\hat{T}^-$ is replaced by $\hat{T}^+$ and the transition undergoes from T_z to $T_z + 1$. Additionally, the Q-values for β^- and β^+-decays are defined differently, see Figure 2.13.

When energetically possible, i.e. $Q > 0$, the decay can proceed to the ground state or to excited states in the daughter nucleus. As discussed above, according to the selection rules for the relation between the initial and final states, the leptons couple to $S = 0$ for Fermi-transitions and to $S = 1$ for Gamow-Teller. Allowed

transitions further require $\Delta L = 0$ and according to $\pi_f = \pi_i \cdot (-1)^{\Delta L}$ also $\Delta \pi = 0$. Generally, transitions involve both Fermi and Gamow-Teller parts. However, when the total angular momentum $J = S + L$ changes by $\Delta J = 1$ the transition is a pure Gamow-Teller decay. Pure Fermi decays are transitions between nuclear states with total angular momentum $J_i = J_f = 0$.

The half-life $T_{1/2}$ of a nuclide is related to the individual transitions by

$$T_{1/2} = \frac{\ln(2)}{\sum_f \Gamma_f}, \tag{2.65}$$

where the sum is over the transition rates to all populated states in the daughter nucleus. For β^+-decays this includes the electron-capture branches as well. The Branching Ratio (BR), R, of a specific transition is defined as $R = \Gamma_k/(\sum_f \Gamma_f)$. Individual transitions are usually characterized by their ft-values. f is the statistical rate function with the transition energy or Q-value to this specific state and t is the partial half-life $t = T_{1/2}/R = \ln(2)/\Gamma$. In β^+-decays with competing electron-capture it is further corrected for the probability of an electron capture to this state,

$$t = \frac{T_{1/2}}{R}(1 + P_{\mathrm{EC}}), \tag{2.66}$$

when we define the BR as the transition strength to a particular nuclear level, independent of whether it was populated by EC or β^+-decay. P_{EC} is the electron capture fraction, which is discussed in [67]. Its calculation depends, among others, also on the Q-value.

In other words, the ft-value describes how 'fast' a particular transition is, correcting for the available phase space. To determine an ft-value experimentally, the half-life and the BR are required for the partial half-life t and the transition energy has to be measured which enters into the statistical rate function f. For allowed transitions it is equal to

$$(ft)^{-1} = \frac{\ln(2)G_F^2 \mid V_{ud} \mid^2 m_e^5}{2\pi^3} \cdot \left[g_V^2 \mid M_F \mid^2 + g_A^2 \mid M_{GT} \mid^2 \right]. \tag{2.67}$$

In order to extract V_{ud} from nuclear β-decays, the ft-value, the nuclear matrix elements M_F and M_{GT}, as well as its g_A have to be known. The nuclear matrix elements are generally not calculable precisely enough to obtain a competitive estimate of V_{ud}. Isospin $T = 1/2$ mirror and superallowed $0^+ \to 0^+$ β-decays are more favourable because they proceed between isobaric analog states whose wavefunctions only differ by the isospin projection. Consequently, the nuclear matrix elements are simpler to calculate. The value of V_{ud} from $T = 1/2$ mirror decays has been evaluated recently for the first time [68]. Since these decays are Fermi-
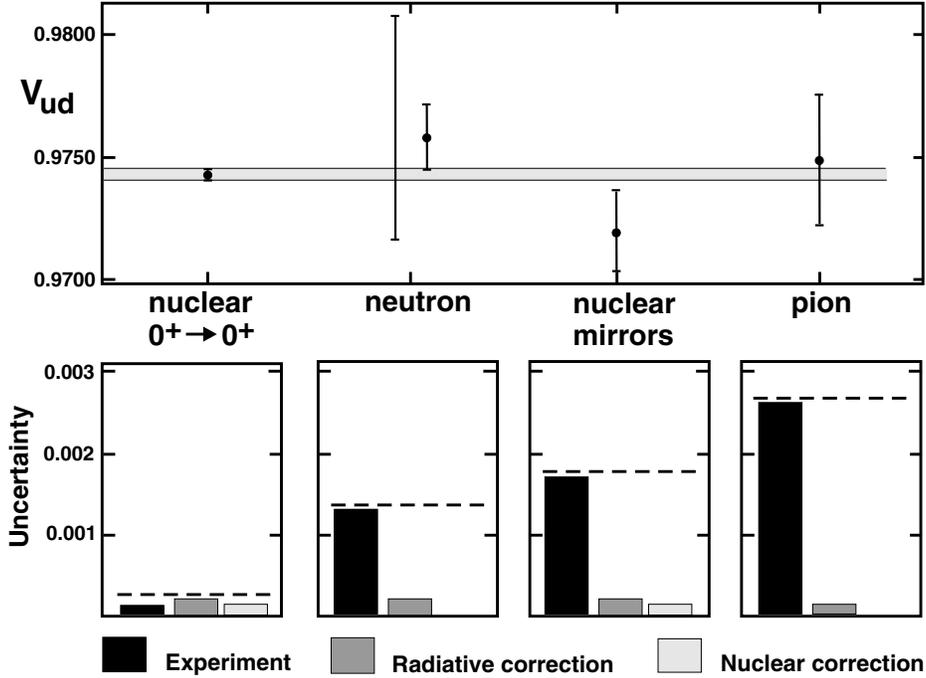
Figure 2.14: Top: V_{ud} extracted from different types of decays. For the neutron decay, the larger error bar reflects the large, non-statistical spread of neutron lifetime measurements, while the smaller one only takes the neutron-lifetime of [62] and the asymmetry measurement in [69] into account. The lower panels display the partial contribution of experiment and theoretical corrections. Figure from [26].

Gamow-Teller admixtures and involve g_A, which is renormalized in the presence of the strong force, additional experimental input in the form of a correlation measurement is necessary. Superallowed $0^+ \rightarrow 0^+$ β-decays are less cumbersome; because of $J_f = J_i = 0$ they are pure Fermi decays. They are currently the most precise way to gain V_{ud} (see Figure 2.14).

2.5 Superallowed $0^+ \rightarrow 0^+$ β decays

Quantum mechanical addition of angular momentum allows for transitions between nuclear states with total angular momentum $J_i = J_f \neq 0$ to have both Fermi and Gamow-Teller contributions. However, for $J_i = J_f = 0$ and $\Delta L = 0$ in

the allowed approximation, any change in spin S is forbidden, thus $\Delta S = 0$, too, and we deal with a pure Fermi decay and $M_{GT} = 0$.

As a consequence of the (approximate) isospin-symmetry in the nuclear force, there are states in isobars, i.e. nuclides with the same mass number A, which are (almost) identical except for their T_z quantum number. These states are called isobaric analog states or members of an isobaric multiplet. In accordance with angular momentum rules, a multiplet with total isospin T will have $2T + 1$ isobaric analog states with T_z ranging from $-T$ to $+T$. Since the isospin-symmetry is broken, isobaric analog states are not degenerate. Their relative position in energy is described by the Isobaric Mass Multiplet Equation (IMME) [70]. Assuming that all $t_z^{(i)}$ dependent contributions (including Coulomb) to the nuclear force can be expressed like the Coulomb force as a sum of isoscalar, isovector, and isotensor parts (i.e. spherical tensors with rank ≤ 2 in isospin space), the masses of isobaric analog states follow a parabola in T_z.

$$M(A, T, T_z) = a(A, T) + b(A, T) \cdot T_z + c(A, T) \cdot T_z^2. \qquad (2.68)$$

The IMME can be derived in first order perturbation theory by utilizing the Wigner-Eckart theorem.

It is essential for the description of the β-decay branch between isobaric analog states that the nuclear wave-functions of parent and daughter are identical requiring $\Delta L = \Delta J = \Delta S = \Delta T = 0$. To first order, they only differ by their isospin projection T_z. All nuclear structure details of the wave-functions are consequently irrelevant when the nuclear matrix element M_F is evaluated in Equation 2.64. Referring once more to the analogy of isospin to angular momentum, the action of the isospin raising or lowering operator $\hat{T}^{\pm}$ is well understood and we obtain

$$M_F = \langle \alpha, T, T_z \pm 1 \mid \hat{T}^{\pm} \mid \alpha, T, T_z \rangle = \sqrt{(T \mp T_z) \cdot (T \pm T_z + 1)}. \qquad (2.69)$$

Due to the maximal overlap of the nuclear wave-function, β-decays between isobaric analog states are called superallowed decays.

A superallowed $0^+ \rightarrow 0^+$ nuclear β-decay occurs between isobaric analog states which have both a total angular momentum of $J = 0$. It combines the advantages of a pure Fermi decay and simple nuclear matrix elements. Due to the Coulomb repulsion, isobaric analog states with larger Z are generally less bound and all superallowed decays discussed here are β^+-decays. $T = 1$ cases are studied most extensively although ft-values of $T = 2$ superallowed β emitters have been measured (e.g. [71]).

The $T = 1$ cases are divided into two groups of decays, $T_z = -1 \rightarrow 0$ and $T_z = 0 \rightarrow 1$. In both cases, the nuclear matrix element yields $M_F = \sqrt{2}$ (see

Equation 2.69). The ft-value for superallowed $0^+ \rightarrow 0^+$, $T = 1$ nuclear β-decays is simply

$$ft = \frac{\pi^3}{\ln(2)g_V^2 G_F^2 \mid V_{ud} \mid^2 m_e^5} = \frac{K}{2g_V^2 G_F^2 \mid V_{ud} \mid^2}, \tag{2.70}$$

where the constant $K = 2\pi^3 \ln 2 / m_e^5$ has been introduced. Note that this result for the ft-value is independent of any specifics of the transition and should be the same for all superallowed $0^+ \rightarrow 0^+$, $T = 1$ nuclear β-decays. This will allow one to test the validity of the CVC-hypothesis experimentally, which requires that $g_V = 1$ for all β-decays. Before doing so, the ft-values need to be adjusted by several theoretical corrections to account for critical approximations in the previous derivations.

2.6   Theoretical corrections to the ft-values

Theoretical corrections to the ft-values are small and only a few percent. But at the present experimental precision they dominate the uncertainty in the so-called corrected $\mathcal{F}t$-values. The origin of these corrections are

- isospin symmetry breaking,

- radiative correction, and

- shape correction and atomic overlap correction in the statistical rate function.

In the evaluation of the nuclear matrix element, isospin-symmetry has been assumed. Although an approximate symmetry of chiral QCD, it is broken even in QCD itself but most notably by the Coulomb interaction as neutrons are electrically neutral while protons are not. Respective inaccuracies are repaired by the isospin-symmetry breaking corrections δ_C. They are dependent of the nuclear structure and are thus specific to each decay. More details are elaborated in Section 2.7. In this section, we will only consider the to-date most reliable calculations of δ_C based on the nuclear shell model with Saxon-Woods radial wave functions [72, 73].

2.6.1   Corrections to the statistical rate function f

In Equation 2.63, the statistical rate function was defined as the normalized phase space integral over the β-particle's energy. It was already corrected with the Fermi function $F(Z, E_e)$, which took into account that the outgoing β particle is not a free Dirac spinor but is influenced by the charge of the daughter nucleus. The framework of $F(Z, E_e)$ assumed the nucleus as a point-like particle. However, at the level of experimental precision this approximation is insufficient. The finite

size of the nucleus cannot be ignored and a more accurate model for the nuclear charge distribution is appropriate. Additionally, the atomic electrons are shielding the charge of the nucleus. Both effects are accommodated by adding the shape-correction function $S(Z, W)$ to the statistical rate function [74]. $S(Z, W)$ incorporates a mild dependence on the nuclear structure of the involved nucleus. The theoretical uncertainty in f (0.01% for light nuclei up to 0.1% for $A = 74$) due to the different shell model calculations is currently small compared to the uncertainty due to the Q-value and is not added to the error budget of f [75].

Since the β-decay changes the charge Z of the nucleus, the atomic electron wave-function of the parent and daughter nucleus are not identical. The mismatch in the atomic wave-functions hinders the β-decay slightly. This is taken into account by the atomic overlap correction $r(Z, W)$ [15]. That such a small effect is considered necessary to be dealt with at all, accentuates the level of experimental precision in regards to the Q-value.

With these two new modifications, the statistical rate function is corrected to

$$f = \int_1^{W_0} dW (W - W_0)^2 W \sqrt{W^2 - 1} \cdot F(Z, W) \cdot S(Z, W) \cdot r(Z, W). \quad (2.71)$$

In this treatment, care has to be taken that parts of the electromagnetic interaction between the β-particle and the daughter nucleus incorporated in $F(Z, W)$ are not accounted for in the radiative corrections which are discussed in the next subsection.

Neglecting the shape correction function $S(Z, W)$ would change the statistical rate function by 0.2% at $A = 10$ up to 5.7% at $A = 74$ [74]. When considering $r(Z, W)$, f is modified by maximally 0.02% [15].

2.6.2 Radiative corrections

Radiative corrections consider the emission of bremsstrahlung photons, which are usually not detected in experiment, as well as loop effects of exchange of photons and Z-bosons [76][77, 78][79][80]. For superallowed β-decays, the β-decay rate Γ^0 is correct to $\Gamma = \Gamma^0 \cdot (1 + RC)$ with

$$RC = \frac{\alpha}{2\pi} \left[\overline{g}(E_m) + \delta_2 + \delta_3 + 3\ln \frac{m_Z}{m_p} + \ln \frac{m_Z}{m_p} + A_g + 2C \right]. \quad (2.72)$$

For details, the reader is referred to the literature. Here, only the origin of the corrections is discussed. The first four terms are due to loop corrections and bremsstrahlung which involve the electromagnetic and weak vector interactions. A comprehensive description of $\overline{g}(E_m)$ is found in [76]. It is a universal func-

41
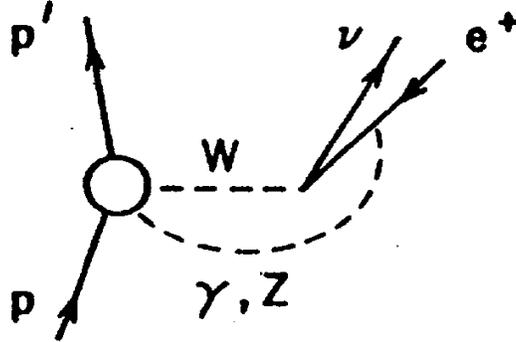
Figure 2.15: γW-box and ZW-box diagram. Figure from [77].

tion which depends on the energy of the (anti-)electron with a maximal energy E_m and is averaged over the available β-decay spectrum. δ_2 and δ_3 are higher order expansion terms in $Z\alpha^2$ and $Z^2\alpha^3$. The remaining terms are related to the weak axial-current, which, as derived in the previous sections, does not enter to first order (or tree-level) for pure Fermi-decays. Loop corrections at higher orders are nevertheless sensitive to the axial-vector interaction, where g_A is not protected by CVC. A dominant contribution to these terms is the loop in the γW- box diagram [80] (see Figure 2.15). For instance, the weak axial-vector might change the spin, but the electromagnetic interaction between the nucleus and the outgoing β-particle could reverse it, which is allowed even for $J_i = J_f = 0$. This particular contribution is part of the correction term C. In [72], C is divided into the two components. In one part, the same nucleon is spin-flipped twice, while in the second component two different nucleons are involved. Consequently, the latter one depends on nuclear structure. Furthermore, the coupling of spin-flip processes is quenched in the nuclear medium. Hence, they are nuclear structure dependent, too, but different from free nucleons [72]. As a consequence, the nuclear structure dependent contributions in C are separated from the universal part according to $C = C(\text{free}) + C_{\text{NS}}$.

It is conventional to separate these terms into transition independent (Δ_R^V) and transition dependent parts. Latter ones are further divided into those which depend on the specifics of the transition, i.e. the charge Z of the daughter nucleus and the Q-value, but are independent of nuclear structure (δ_R') and those which depend on

42

the structure of the nucleus δ_{NS}.

$$\Delta_R^V = \frac{\alpha}{2\pi}\left[3\ln\frac{m_Z}{m_p} + \ln\frac{m_Z}{m_p} + A_g + 2C(\text{free})\right] \tag{2.73}$$

$$\delta_R' = \frac{\alpha}{2\pi}\left[\bar{g}(E_m) + \delta_2 + \delta_3\right] \tag{2.74}$$

$$\delta_{NS} = \frac{\alpha}{2\pi}C_{\text{NS}}. \tag{2.75}$$

Recent improvements in the radiative corrections [80] have led to an alteration of these expressions, but the same conventions for Δ_R^V, δ_R', and δ_{NS} remain [73]. For the transition independent radiative correction one obtains $\Delta_R^V = (2.361\pm0.038)\%$ [73]. δ_R' are $\approx 1.5\%$ and the nuclear structure dependent corrections δ_{NS} range from $0.005(20)\%$ in ^{26m}Al to $-0.345(35)\%$ in ^{10}C [73].

2.6.3 Corrected $\mathcal{F}t$-values

Collecting all contributions together, we end up with the corrected $\mathcal{F}t$-value, which is related to V_{ud} as follows:

$$\mathcal{F}t = ft(1+\delta_R')(1+\delta_{NS}-\delta_C) = \frac{K}{2g_V^2 G_F^2\mid V_{ud}\mid^2 (1+\Delta_R^V)} = const, \tag{2.76}$$

where $g_V = 1$ according to CVC. This equation summarizes the program of super-allowed $0^+ \to 0^+$ nuclear $T = 1$ β-decays. In principle, a single superallowed β-decay would allow one to derive $\mathcal{F}t$. However, in order to minimize errors it is important to measure as many superallowed decays as possible with high precision to establish their ft-values experimentally. Figure 2.16(a) illustrates the experimental status of the 13 most precisely measured cases whose $\mathcal{F}t$ have uncertainties of less than $0.4\,\%$. Appyling the transition dependent theoretical corrections, δ_R', δ_{NS}, and δ_C yields the corrected $\mathcal{F}t$-value, which should, according to the CVC-hypothesis, be identical for all $T = 1$ superallowed decays. Hence, the agreement of all $\mathcal{F}t$-values represents a stringent test of CVC. When considering the isospin-symmetry breaking corrections from shell model with Saxon-Woods radial wave functions (see Figure 2.16(b)), the CVC hypothesis is indeed confirmed at the $1.3\cdot 10^{-4}$ level [15]. This consistency between $\mathcal{F}t$-values also highlights another advantage of the V_{ud} extraction from superallowed β-decays over neutron and pion decay: experimental or theoretical errors are minimized because the same quantity is extracted from and cross checked between a group (currently 13) of individual decays. Any deviations should show up in Figure 2.16(b) before the calculation of V_{ud}.
In combination with Δ_R^V and the Fermi constant G_F from muon decay, the weighted average of currently $\overline{\mathcal{F}t} = 3072.08(79)$ s [15] finally yields V_{ud}. Figure 2.17 dis-
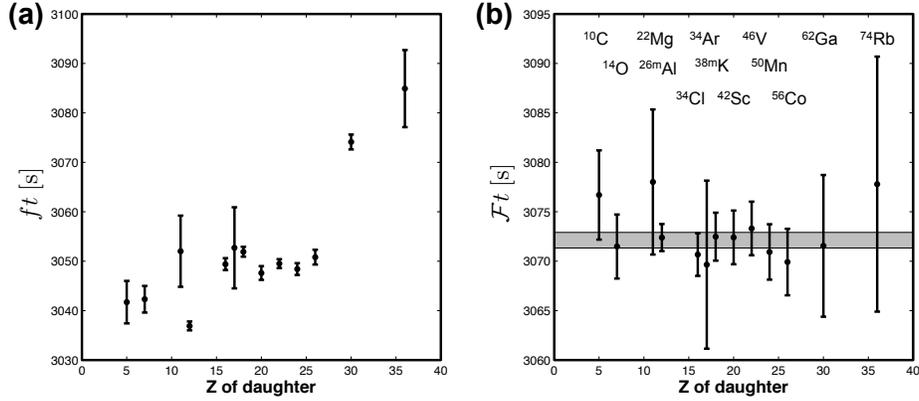
Figure 2.16: ft-values (a) and corrected $\mathcal{F}t$-values (b) for the 13 most precisely measured superallowed $0^+ \to 0^+$ β decays. The grey band in (b) represents the weighted average. The plots are based on data from [15].
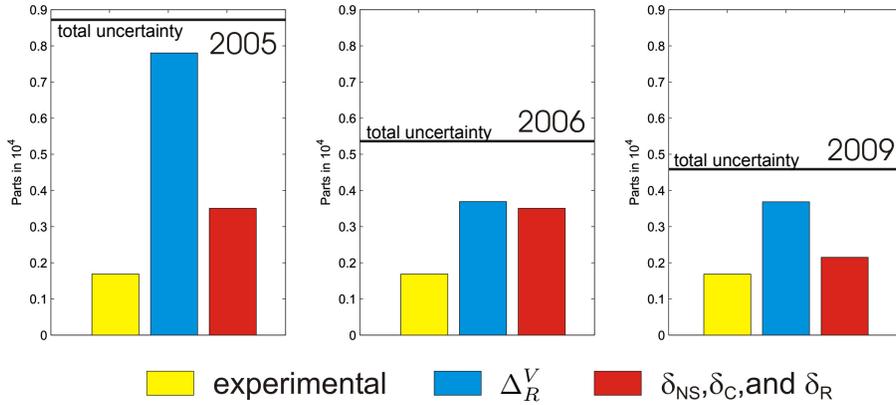
Figure 2.17: Development of partial uncertainties of $\mid V_{ud} \mid^2$ since 2005. The estimated error due to transition dependent corrections is dominated by the Isospin Symmetry Breaking (ISB) corrections δ_C. The reduction from 2005 [74] to 2006 is due to the improved calculation for Δ_R^V [80]. The development of a new Hartree-Fock protocol while rejecting the old one led to smaller systematic discrepancies between models of δ_C and a subsequently reduced partial uncertainty in 2009 [15].

44

plays the partial uncertainties to V_{ud} from experiment, nuclear structure dependent corrections (δ_C and δ_{NS}), and the radiative corrections δ_R' and Δ_R^V. The dominating contribution has its source in Δ_R^V. A future error reduction over today's value in [80] might be feasible [81]. The second largest source of uncertainty is found in the isospin-symmetry breaking corrections. Previous to [15], their contribution to the total uncertainty in V_{ud} was almost identical to Δ_R^V. In earlier surveys of superallowed β-decays, the uncertainty of δ_C had to be inflated because their determination in the shell model with radial wave-function from Hartree-Fock calculations with Skyrme-type interactions [82, 83] showed systematic discrepancies to the already mentioned shell model with Saxon-Woods radial wave-functions. In their latest survey [15], Towner and Hardy have performed their own Hartree-Fock calculations. This was motivated by the fact that the older Hartree-Fock corrections used a model space which was shown to be too small [73]. Towner and Hardy's Hartree-Fock calculations of δ_C are in much better agreement with their own Saxon-Woods approach and the inflation of the theoretical uncertainty in δ_C was reduced accordingly. However, in [15], the protocol of the Hartree-Fock method has been altered in comparison to the original calculations [82, 83]. As expressed by Towner and Hardy themselves [15], it remains desirable to compare the current values for δ_C to independent calculations. As pointed out in [84], the isospin-symmetry breaking corrections δ_C were subject to significant revisions over the last 10 years. From 2002 [72] to 2008 [73], the uncertainties of δ_C for individual superallowed β emitters actually increased (see for instance Table II in [73]). The reduction on its associated error for V_{ud} is due to the smaller systematic difference between the Saxon-Woods and Hartree-Fock calculation only. This situation has triggered a lot of effort both on the experimental and theoretical side. New models of δ_C have produced their first results. These will be discussed in the next subsection.

Although the experimental uncertainty is smaller than the error contributions from theory, measurements of superallowed β-decays have by no means lost their importance. Efforts continue to add new precision cases to the current 13 most studied decays. Experimental data provide input for the isospin symmetry breaking corrections such as spectroscopic factors or branching ratios to non-analog 0^+ states. Very recently, laser spectroscopy determined a more precise charge radius of ^{74}Rb [16] which is used in the Saxon-Woods calculation of δ_C. New, more precise measurements of the ft-values of the 13 most-studied cases allow more stringent comparisons of conflicting theoretical models. This could challenge perceived consistencies between a set of δ_C-calculations, experimental results, and the conserved vector current hypothesis. These experimental 'tests' of the ISB corrections are described in Section 2.8.

2.7 Different models for isospin symmetry breaking corrections

The result of the Fermi matrix element for the superallowed decay branch, Equation 2.69, assumed isospin to reflect an exact symmetry. Already in Section 2.1.3 it was stated, that even within QCD the symmetry is broken by the quark mass difference. In the full Lagrangian of the Standard Model (SM) the difference in the electric charge of u- and d- quarks (or neutron and proton) in QED is also inconsistent with an exact isospin symmetry. For the present purpose, the latter is in fact the dominating effect [85]. As a consequence, the simplicity of Equation 2.69 only holds as an approximation and the ISB corrections add to the Fermi matrix element.

$$| M_F |^2 = | M_0 |^2 (1 - \delta_C) \qquad (2.77)$$

where for $T = 1$ decays $| M_0 |^2 = 2$ as before. These corrections are of the order of $\sim 1\%$, but have to be known to about 10% of their value to fully take advantage of the experimental precision. During the last years, these corrections have received a new focus in theoretical and experimental research on weak interaction studies with nuclear systems. Several new approaches have been explored recently, mostly in disagreement with the most developed δ_C by Towner and Hardy. This section provides an overview over models and ideas in this ongoing discussion.

2.7.1 Nuclear shell model with Saxon-Woods radial wave-functions

Due to its many improvements over the last decades, the nuclear shell model approach with Saxon-Woods radial wave-functions is, to date, the most advanced calculation of δ_C which all new models are compared against. The surveys of superallowed β-decays [15, 74] are presented around this set of ISB corrections though the comparison to the shell model with Hartree-Fock radial wave-functions has always served to highlight potential shortcomings.
In order to calcualte δ_C, the nuclear matrix element of the Fermi decay

$$M_F = \langle f \mid \hat{T}^+ \mid i \rangle = \int d^3 x_1 ... d^3 x_A \psi_D(x, \alpha', T_z - 1) \hat{T}^+ \psi_P(x, \alpha, T_z) \quad (2.78)$$

with $\hat{T}^+ = \sum_{i=1}^A t_{(i)}^+$ is expressed in second quantization by utilizing creation and annihilation operators for neutron and proton quantum states. This means that the initial and final nuclear wave-functions are embodied by (combinations of) creation operators a^+ acting upon the vacuum state $\mid 0 \rangle$ in Fock space. More importantly for our purposes, operators are also expressed as annihilation and creation operators. Hence, for the total isospin raising operator $\hat{T}^+$, the sum is taken over all states of

a single-particle basis and not over the nucleons. Towner and Hardy [73] write the Fermi matrix element as

$$M_F = \langle f \mid \hat{T}^+ \mid i \rangle = \sum_{\alpha,\beta} \langle f \mid a_\alpha^+ a_\beta \mid i \rangle \langle \alpha \mid \hat{\tau}^+ \mid \beta \rangle, \qquad (2.79)$$

where a_β annihilates a proton in state β and a_α^+ creates a neutron in state α instead. $\langle \alpha \mid \hat{\tau}^+ \mid \beta \rangle$ is the single-particle matrix element between the neutron state α and the proton state β. It is intended to take the difference in the radial wave-function $R^n(r)$ and $R^p(r)$ of neutron and proton in the single-particle basis into account.

$$\langle \alpha \mid \hat{\tau}^+ \mid \beta \rangle = \delta_{\beta\alpha} \int_0^\infty dr r^2 R^n(r) R^p(r) \equiv \delta_{\beta\alpha} r_\alpha. \qquad (2.80)$$

Finally, as both $\langle f \mid a_\alpha^+$ and $a_\beta \mid i \rangle$ are wave-functions of $(A-1)$ nucleons, Towner and Hardy [73] insert a full basis of $(A-1)$ nucleon states $\mid \pi \rangle$,

$$M_F = \sum_{\pi,\alpha} \langle f \mid a_\alpha^+ \mid \pi \rangle \langle \pi \mid a_\alpha \mid i \rangle r_\alpha. \qquad (2.81)$$

Noting that without ISB, r_α would be unity and $\langle f \mid a_\alpha^+ \mid \pi \rangle = \langle \pi \mid a_\alpha \mid i \rangle^*$, this result allows an important separation in δ_C which is used by some other models as well. Assuming that both contributions are small, the leading order correction for ISB would be a sum $\delta_C = \delta_{C1} + \delta_{C2}$. The corrections due to the deviations from $r_\alpha = 1$ are reflected in δ_{C2}, where it is assumed that $\langle f \mid a_\alpha^+ \mid \pi \rangle$ and $\langle \pi \mid a_\alpha \mid i \rangle$ are Hermitian conjugates. Conversely, for δ_{C1}, $r_\alpha = 1$ holds and the corrections are due to $\langle f \mid a_\alpha^+ \mid \pi \rangle \neq \langle \pi \mid a_\alpha \mid i \rangle^*$.

Details of these calculations are found in [72, 73]. As pointed out in [73] the consideration of shell model orbitals from closed-shells can be essential for δ_{C2}. However, to open up all shells is computationally intractable. Spectroscopic factors from pick-up reactions are used as an experimental criterion which shells are expected to contribute. The difference in the radial wave functions between $R^n(r)$ and $R^p(r)$ is calculated with a Saxon-Woods potential. Here the potential's well radius was matched to reproduce the empirical RMS charge radius $\langle r^2 \rangle_{\text{ch}}^{1/2}$. Furthermore, the asymptotic form of $R^n(r)$ and $R^p(r)$ was fixed to the respective neutron and proton separation energies S_n and S_p. Towner and Hardy use sets of different parameterizations of the Saxon-Woods potential as well as different shell model interactions. The spread of the result is taken as the uncertainty on δ_{C2} in addition to the error which is due to the uncertainty in $\langle r^2 \rangle_{\text{ch}}^{1/2}$. Their numerical values increase from $\delta_{C2} = 0.165(15)\%$ for ^{10}C to $\delta_{C2} = 1.50(30)\%$ for ^{74}Rb [73]. The determination of δ_{C1} is also constrained by experimental input. Differences
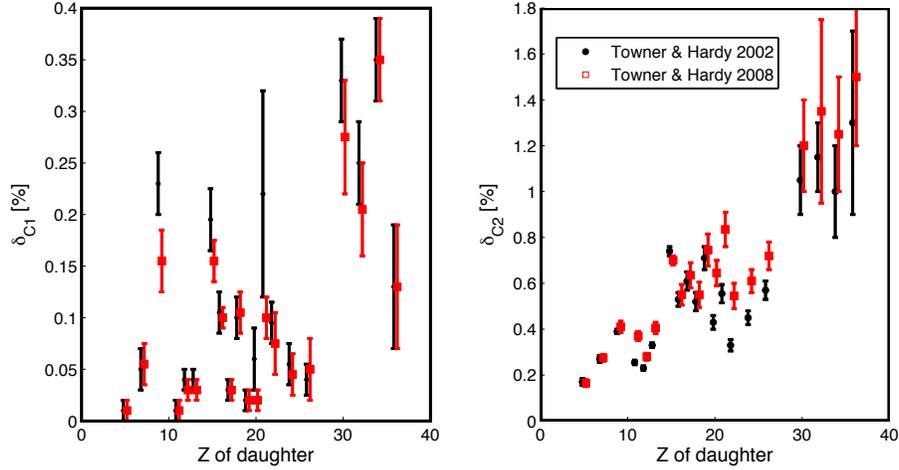
Figure 2.18: Comparison of shell-model ISB corrections without [72](2002) and with [73](2008) the inclusion of core orbitals. The radial wavefunctions for δ_{C2} were calculated based on Saxon-Woods potentials.

in single-particle states for neutrons and protons were modified to match the experimental single-particle shifts in energies. Charge dependent interactions were adjusted to reproduce the linear and quadratic coefficients b and c of the IMME (see Equation 2.68), which are in most cases known from experiment [86]. δ_{C1} can be linked to the Fermi matrix elements to other 0^+ states which are not isobaric analog states to the parent nucleus. If isospin was an exact symmetry, these matrix elements would vanish. In a sense, isospin mixing due to the ISB moves decay strength from the superallowed decay branch into branches to other 0^+ states. In perturbation theory the matrix elements are then related to each other by the difference in energy between analog and the non-analog 0^+ state through $1/\Delta E^2$. The comparison between the experimental ΔE and the one calculated in the shell model are used to scale δ_{C1} accordingly. The latest determination lists $\delta_{C1} = 0.010(10)\%$ for ^{10}C which increased to maximally $\delta_{C1} = 0.350(40)\%$ for ^{70}Br. Hence δ_{C1} is, in comparison to δ_{C2}, a factor of 5-10 smaller.

All numerical values for the ISB corrections are shown in Figure 2.18. It also compares the most recent results from 2008 with those of 2002. The latter did not consider closed shells in the shell model calculations.
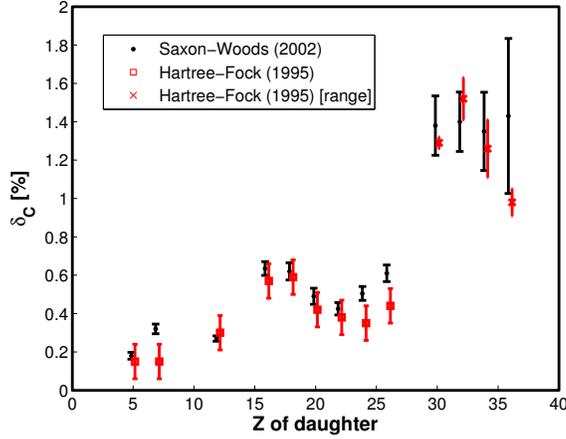
Figure 2.19: Comparison of shell-model ISB corrections with radial wave-functions from Saxon-Woods [72] and Hartree-Fock potentials [83]. Only those cases are displayed where results are available in both procedures. For the Saxon-Woods radial wave-functions, the calculations from 2002 are shown, because both use the same shell model space. For the heavier superallowed emitters ^{62}Ga, ^{66}As, ^{70}Br, and ^{74}Rb, reference [83] does not provide uncertainties, but two different calculations. Here, the respective data points refer to the mean and spread of these two calculations.

2.7.2 Nuclear shell model with Hartree-Fock radial wave-functions

ISB corrections in which the radial wave-functions were based on Skyrme-Hartree-Fock calculations were initially proposed and evaluated by Ormand and Brown [82, 83, 87, 88]. This approach was motivated by the fact that in a Hartree-Fock calculation the mean field is inherently proportional to the proton and neutron densities. The effect of the Coulomb repulsion, which pushes the protons further out and leads to the extended proton radial wave-functions, is, in the Hartree-Fock procedure, reduced by an isovector potential. Induced by extended proton densities, this isovector potential counteracts the Coulomb repulsion and as a consequence results in smaller δ_{C2} compared to the Saxon-Woods potential. This expectation is generally confirmed as shown in Figure 2.19. In the past, both sets of δ_C led to corrected $\mathcal{F}t$-values which were each consistent with the CVC hypotheses, but resulted in different averaged $\mathcal{F}t$-values. The difference between the two models was added as a systematic uncertainty to the extraction of V_{ud}. The total partial un-

certainty on V_{ud} from δ_C was similar to the error contribution due to the transition independent radiative corrections Δ_R^V [80] which, to date, dominate the uncertainty in V_{ud}.

The latest assessment of the Hartree-Fock procedure by Ormand and Brown in 1995 does not cover all of today's 13 superallowed precision cases. Furthermore, a direct comparison between [83] and [73] is no longer appropriate because of different shell model spaces. In [15], Towner and Hardy introduced their own Hartree-Fock calculations for δ_{C2} utilizing the same model space of [73], however, with a substantial deviation from the method of Ormand and Brown. In their approach, they note that the direct term of the Hartree-Fock equation for the parent nucleus leads to an asymptotic Coulomb potential $\lim_{r \to \infty} V_C^{\mathrm{direct}} = (Z+1)e^2/r$, with Z being the number of protons in the daughter nucleus. This appears as an unphysical charge. It is too large by one unit in e, because we are interested in the mean field for the last proton in the field of Z protons and $A - Z - 1$ neutrons. In the complete Hartree-Fock formalism, the exchange term would account for this but only at the price of a non-local integral in the potential which is notoriously hard to solve and is often approximated. In Towner and Hardy's view, such an approximation would not yield satisfactory results for asymptotic quantities such as the required asymptotic differences in neutron and proton radial wave-functions. So, instead of two Hartree-Fock calculations for the parent nucleus $(Z+1, N)$ and the daughter $(Z, N+1)$, they perform only one with the nucleus (Z, N). The resulting mean field is used to derive the single particle wave-functions for the last proton and neutron in the parent or daughter nucleus respectively. Although some discrepancies between the Saxon-Woods and the Hartree-Fock approaches remain, their overall agreements are improved (see Figure 2.20). Consequently, the uncertainties in V_{ud} associated with δ_C are reduced in the latest survey of superallowed β-decays [15]. Figure 2.17 shows how the partial uncertainties to V_{ud} have evolved over the last years. Despite the success of the recent calculations, a better understanding of the discrepancies to the Hartree-Fock method designed by Ormand and Brown remains desirable. Assuming CVC, an experimental test of isospin breaking corrections for the $T = 2$ superallowed β-decay ^{32}Ar [71] obtained $\delta_C = 2.1 \pm 0.8\%$ which is in agreement with Brown's calculations of $\delta_C = 2.0 \pm 0.4\%$ in the same publication. Generally, $T = 2$ cases are considered to provide a good testing ground to discriminate between different models of δ_C as they are expected to be larger for $T = 2$ superallowed decays [89].

2.7.3   Isovector monopole resonance

In the debate on the ISB corrections, Auerbach [85] has developed a qualitative model in which charge-dependent components of the complete nuclear Hamilto-
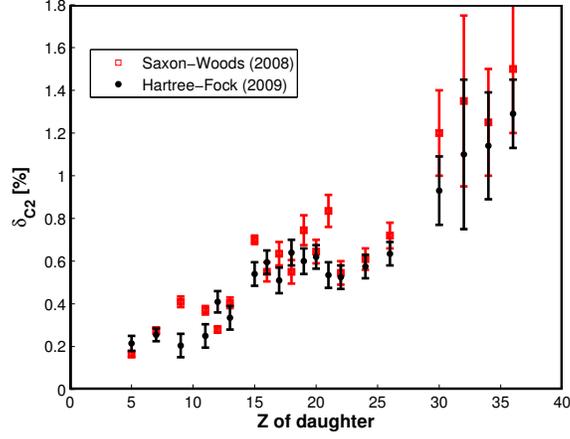
Figure 2.20: Comparison of the most recent shell-model ISB corrections with radial wave-functions from Saxon-Woods [73] and Hartree-Fock potentials [15], both performed by Towner and Hardy.

nian $H = H_0 + V_C$ are treated perturbatively on top of a charge independent Hamiltonian H_0 [85]. For β^+-decays between eigenstates of H_0 the nuclear transition matrix element would follow the derived relations due to the isospin raising operator T^+, hence, $M_F = \sqrt{2}$ for a decay within a $T = 1$ multiplet. Auerbauch considers the Coulomb part as the dominant part of the charge dependent part V_C, which is approximated by a uniformly charged sphere inside a radius R.

$$V_C(r) = -\frac{Ze^2}{R^3} \sum_{i=1}^{A} \left(\frac{r_i^2}{2} - \frac{3R^2}{2} \right) \left(\frac{1}{2} - t_z(i) \right) \qquad r \leq R \qquad (2.82)$$

of which the isovector part is linked to the giant isovector monopole state. This relationship is used to calculate the matrix element and a simple equation for the ISB correction is obtained.

$$\delta_C = 8 \frac{V_1}{41\xi A^{2/3}} \epsilon_1^2 \qquad (2.83)$$

The symmetry potential strength V_1 and the model dependent ξ are chosen by Auerbach to be $V_1 = 100$ MeV and $\xi = 3$. For the isospin admixture ϵ_1^2 several models
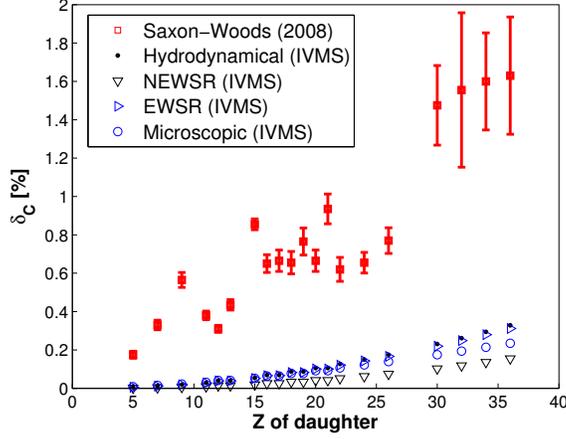
Figure 2.21: ISB corrections by Auerbach [85] based on the model employing the isovector monopole resonance state in comparison to shell-model ISB corrections with radial wave-functions from Saxon-Woods potentials [73].

are being discussed which result in the following expressions for δ_C.

$$
\begin{aligned}
\delta_C &= 6.0 \cdot 10^{-7} A^2 & \text{(hydrodynamical)} \\
&= 0.67 \cdot 10^{-7} A^{7/3} & \text{(NEWSR)} \\
&= 5.7 \cdot 10^{-7} A^2 & \text{(EWSR)} \\
&= 18.0 \cdot 10^{-7} A^{5/3} & \text{('microscopic')}
\end{aligned}
$$

(2.84)

Although this approach lacks the structural details of the considered nuclei and omits charge dependent interactions other than the Coulomb force, it has some critical features. While previous calculations do not include collectivity, it is considered here since the giant isovector monopole state itself is a collective excitation. Furthermore, it does not require the division of δ_C into δ_{C1} and δ_{C2}, which is model dependent [85, 90]. The difference to all previous calculations is apparent (see Figure 2.21). Even if Auerbach assumes a 50 % uncertainty his results are still significantly smaller than the ISB corrections by Towner and Hardy.
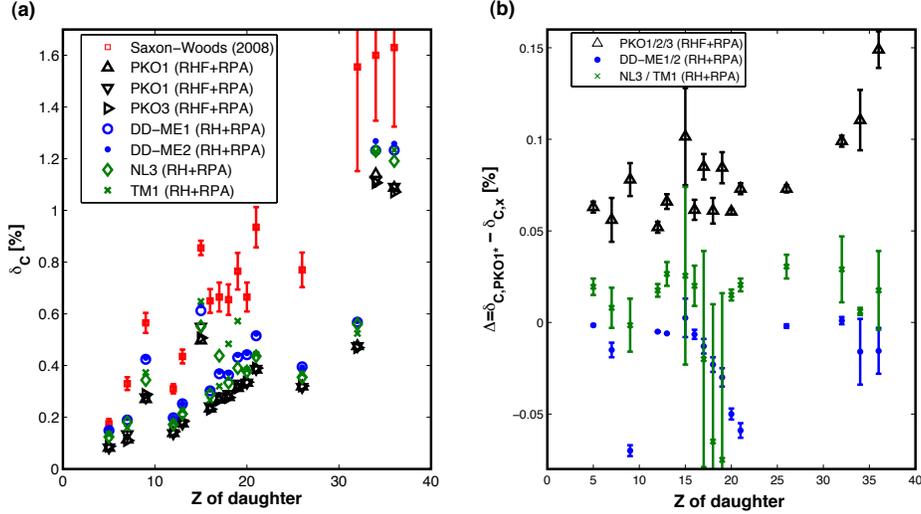
Figure 2.22: (a) Results for δ_C of Relativistic Hartree-Fock (RHF) + Random-Phase Approximation (RPA) and Relativistic Hartree (RH)+RPA[91] compared to Saxon-Woods shell model calculations [73]. Only those cases are displayed where both models have published results. (b) In PKO1* the exchange term of the Coulomb force is turned off. The results are contrasted to the full RHF + RPA calculation as well as to RH+RPA with the density dependent meson-nucleon Lagrangian in DD-ME1 and DD-ME2 and the Lagrangian with nonlinear meson coupling (NL3 and, TM1). Error bars reflect the spread of the respective results as shown in (a).

2.7.4 Self-consistent relativistic random-phase approximation

In [91], the ISB corrections are approached in a self-consistent, relativistic Random-Phase Approximation (RPA). The starting point is a relativistic Hartree-Fock theory in which a Lagrangian density is built upon Dirac spinors describing the nucleons which interact through exchange-mesons and photons. In order to investigate the importance of an exact treatment of the Coulomb interaction, RPA calculations were performed on the basis of both RHF and RH mean field. As an approximation, latter ones neglect the exchange or Fock term in the potential. Additionally, for RHF+RPA and RH+RPA different effective interactions have been used to probe for the model dependence of the interaction. The results are shown in Figure 2.22(a), of which all are consistently lower than the values from the shell model. The full calculations (RHF+RPA) show very little dependence on the interaction and yield

distinctively smaller ISB corrections δ_C than the approach of RH+RPA. Within the latter the effective interaction DD-ME1 and DD-ME2 are, with regard to δ_C, almost identical. Both are based on a Lagrangian density with density dependent nucleon-meson couplings. However, they are still different to the RH+RPA approach using a Lagrangian density with nonlinear couplings (TM1 and NL3). Utilizing the effective interactions TM1 and NL3, very similar results are generally obtained, although for δ_C of the decays in ^{30}S, ^{34}Ar, ^{38}Ca, as well as ^{38m}K the deviations between the two interactions are rather large. Unfortunately, neither the differences between DD-ME1/2 on the one hand and TM1 / NL3 on the other nor the large differences for some cases among TM1 and NL3 are highlighted or discussed in [91]. However, the distinction between results of RH+RPA and RHF+RPA is well explained: Utilizing the interaction PKO1 another RHF+RPA is being performed but this time the exchange term regarding the Coulomb interaction is turned off (PKO1*). This calculation recovers most of the differences to RH+RPA (compare Figure 2.22(b)) in which all exchange terms are neglected. Hence, the observed deviations between RH+RPA and RHF+RPA are not due to the respectively used interactions, but caused by the incomplete treatment of the Coulomb interaction in RH. This reflects Towner and Hardy's concern regarding the correct implementation of the Fock term in Hartree-Fock calculations [15]. RHF+RPA in [91] represents a full treatment of the exchange term, but it appears that by including the exchange term, δ_C is reduced further in respect to the shell model calculations. Liang and collaborators speculate in [91] why their result could be different and envision more work on the implementation of the correct neutron-proton mass difference, isoscalar and isovector pairing, and deformation. The proper mass difference between neutron and protons has been investigated [92], but although this tends to shift δ_C up, the effect is rather small.

2.7.5 Nuclear density functional theory

The most recent model of δ_C by Satula *et al.* employs the self-consistent nuclear density theory [41]. As the Density Functional Theory (DFT) breaks rotational and isospin symmetry spontaneously, both have to be restored through projection onto a good angular momentum and isospin basis while retaining the true physical isospin breaking of the Coulomb interaction. Other charge-dependent interactions in the nuclear interaction were not considered. A technical difficulty regarding the application of DFT for odd-odd $N = Z$ nuclei limits the approach to use the specific Skyrme V energy density functional. Skyrme V is of low spectroscopic quality which according to Satula *et al.* [41] particularly impacts δ_C for lighter nuclei in a negative manner. Additionally, ISB corrections of $\delta_C = 10$ % were obtained for the superallowed β emitter ^{38m}K, which appears much too large in
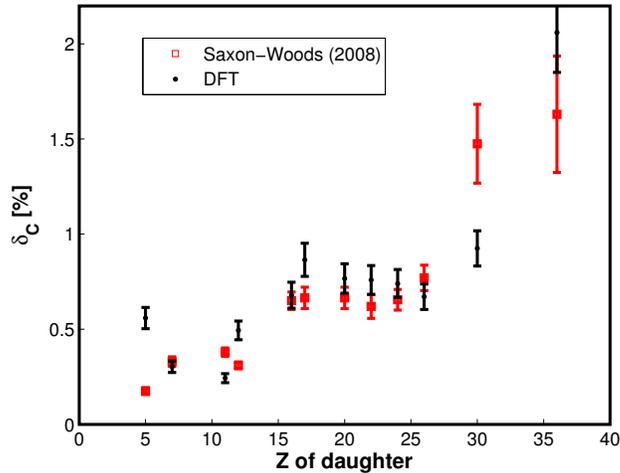
Figure 2.23: δ_C obtained from nuclear Density Functional Theory (DFT) [41] in contrast to the shell-model with Saxon-Woods radial wave-functions [73]. Only those cases are displayed where both models have published results.

comparison with any other model or the CVC hypothesis. This deviation is considered to be a consequence of an incorrectly predicted shell structure in Skyrme V. ^{38m}K was consequently disregarded in [41]. Despite these difficulties, one should note that the nuclear DFT approach has no adjustable parameters and represents a fully microscopic model. Indeed, for heavier, open shell nuclides it is presently the only microscopic description available. We note that the DFT is the only existing model which tends to predict larger δ_C than the shell model with Saxon-Woods radial wave-functions.

Figure 2.23 shows the DFT results for δ_C together with the shell model calculations. Compared with other previous models, the agreement is reasonable, apart from the exception in ^{62}Ga. As mentioned before, caution is advised for lighter nuclei.

2.7.6 *Ab-initio* calculation by the no-core shell model in ^{10}C

Ab-initio methods play a particularly important role in contemporary nuclear physics. They attempt to describe atomic nuclei from first principles. This means that they work with a full A-body Hamiltonian in contrast to cluster models, the shell model
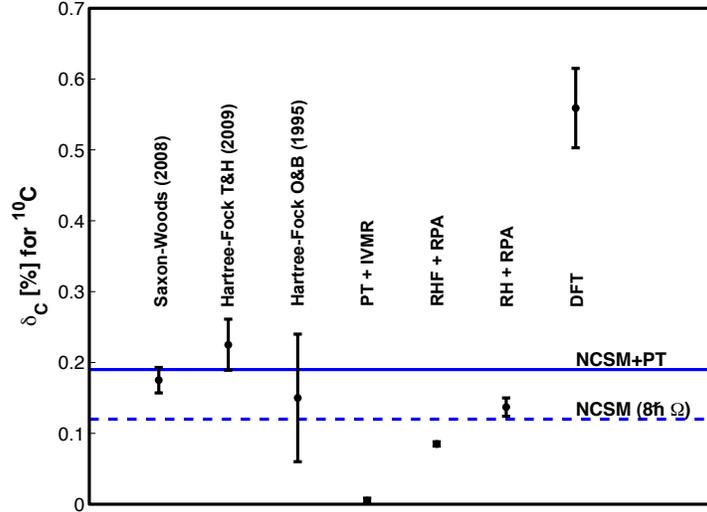
Figure 2.24: Direct comparison of δ_C for ^{10}C from the No-Core Shell Model (NCSM) with the largest model space, but not converged (NCSM $8\hbar\Omega$) and the perturbation theory based on the NCSM results (NCSM+PT) to all other presented models.

(assuming closed shells and effective interactions between valence nucleons), DFT, etc. *Ab-initio* methods are in this sense exact, provided that the employed nuclear potentials are accurate. Due to numerical reasons (note A!), these methods are limited to light nuclei with typically $A \leq 16$. In light of modern high precision, nuclear potentials such as those from χEFT (compare Section 2.1.3), this mass range naturally bridges the underlying physics of quarks with the rest of the nuclear chart. As such, nuclear potentials and *ab-initio* methods can be benchmarked in the light mass sector providing confidence in the nuclear potential especially in their many-body forces, which can then be used in many-body methods for all heavier nucleon systems.

With respect to superallowed β-decays, ^{10}C and ^{14}O are within the currently accepted range accessible by *ab-initio* methods. A determination of the ISB corrections have been attempted for ^{10}C within the No-Core Shell Model (NCSM) [93]. Although the calculation did not converge, perturbation theory was employed to gain δ_C from the non-converged result. The NCSM and the regular shell model both use a harmonic oscillator basis and have a similar second quantization framework, but the NCSM is distinct in treating all nucleons as 'active' and not in an inert core, hence the name. The calculation reported in [93] only included two-body forces in

the nuclear potential, more specifically for the superallowed decay matrix element it used the CD-Bonn 2000 NN potential [94] which includes the isospin symmetry breaking. As a cross check, the NCSM calculation of ^{10}C also determined the coefficients of the IMME (Equation 2.68) in the $A = 10$, $T = 1$ multiplet. The agreement with experiment is within $\approx 2\%$ of the experimental value for b , but is less accurate for c (0.535 MeV in the NCSM compared to experimental 0.362 MeV) although the trend with increasing model space reduced the differences. In the largest tractable model space $\delta_C = 0.12\%$ is obtained, however, the calculation is not converged and a larger model space would be required. Utilizing this result, an estimate based on perturbation theory yields $\delta_C \approx 0.19\%$. It is stated in [93] that the perturbative result might be overestimated. As δ_C increases with increasing model space, we compare in Figure 2.24 both results to the other models of ISB corrections assuming that the converged δ_C in the NCSM would lie in-between, likely closer to $\delta_C = 0.19\%$. The shell model calculations are all in agreement with the NCSM, though for the Hartree-Fock approach by Ormand and Brown the large uncertainty covers a wide range of possibilities. Towner and Hardy's Hartree-Fock method barely touches the NCSM results from above. The calculations utilizing the giant isovector monopole state and DFT are both in strong disagreement with the NCSM, one far below, one far above. However, the lighter nuclides are due to Skyrme V more problematic for the DFT and their descriptions are thus expected to be less reliable in DFT. Finally, assuming that the perturbative result based on the NCSM is indeed overestimated, the NCSM agrees well with RPA+RH. However, on a conceptual basis, RPA+RHF should obtain the more accurate value as it also incorporates the Coulomb exchange term. This result is, however, below the non-converged δ_C in the NCSM.

So, if one considered the NCSM due to its *ab-initio* character as the most reliable result, a few conclusions about the reliability of other calculations could be drawn. Auerbach's perturbative method would be rejected and so would the DFT. RPA results would be somewhat problematic because the RHF would perform less accurately than the approximate RH. No discrimination regarding the shell model variants could be made. Making a broader statement based on such a (dis-)agreement with NCSM on the general performance of a method would arguably be inappropriate as the full set of superallowed β-decays spans a large mass range with different shell effects involved. This is particularly true for the implementation of the DFT, where better validity for heavier systems is expected (compare discussion in previous subsection).

Generally, all of the conclusions in the previous paragraph for which the NCSM is considered as the benchmark result, have to be dealt with cautiously especially as the NCSM calculation is not converged. A better comparison could be made with converged results for ^{10}C and ^{14}O, possibly also including 3N-forces.

57

2.7.7 Exact formalism for δ_C

Miller and Schwenk have reviewed the formalism of Towner and Hardy in terms of the ISB corrections [90, 95] though without numerical results of their own. They observe that the implementation of the isospin-raising operator for the calculation of the Fermi matrix element in Equation 2.79 and Equation 2.80 is in fact not following the exact definition of isospin in the Standard Model. Instead Towner and Hardy's operator is the analog spin or W-spin raising operator. In simplified words, instead of a pure transformation of a proton into a neutron, it transforms a proton from a certain proton state into a neutron in the neutron state with identical quantum numbers as the initial proton state. This is apparent in Equation 2.80 by the Kronecker delta between the states of the neutron and proton single particle-basis,

$$\langle \alpha \mid \hat{\tau}^+ \mid \beta \rangle = \delta_{\beta\alpha} \int_0^{\infty} dr r^2 R^n(r) R^p(r) \equiv \delta_{\beta\alpha} r_{\alpha}. \qquad (2.85)$$

This implies that on the level of single-particle states, the only difference is due to the differences in radial wave-function between neutron and proton. On the contrary, in [90, 95] it is argued that the correct $\hat{T}^+$ operator can result in changes in the radial quantum numbers, hence leading to radial excitations, too.

Moreover, the use of the W-spin raising operator does not follow the usual commutation rules which one expects to hold for the isospin raising operator. It can be shown that Towner and Hardy's isospin raising operator $\hat{T}^+_{\mathrm{TH}}$, though part of the Standard Model operator $\hat{T}^+$, is incomplete.

It is argued that the component in the isospin raising operator which is missing in the description of Towner and Hardy might even cancel δ_{C2} and could lead to reduced ISB corrections.

2.7.8 Implications of different models for ISB corrections

After the introduction of different models of ISB corrections in superallowed $0^+ \to 0^+$, $T = 1$ nuclear β-decays in the previous subsections, we will discuss aspects of what the discrepancies between different models imply for the CVC hypothesis, for V_{ud}, and the CKM unitarity test.

Table 2.4 lists the weighted averages for the corrected $\mathcal{F}t$-values when considering different theoretical models of the ISB corrections. Some authors have not published δ_C for all 13 well-measured superallowed β-decays for their respective model. $\overline{\mathcal{F}t}$ of Table 2.4 includes all superallowed emitters for each model for which a δ_C has been calculated. From the Hartree-Fock approach by Ormand and Brown, which generally provides theoretical uncertainties for δ_C, the heavier cases ^{62}Ga, ^{66}As, ^{70}Br, ^{74}Rb were omitted because no uncertainties are given. This follows
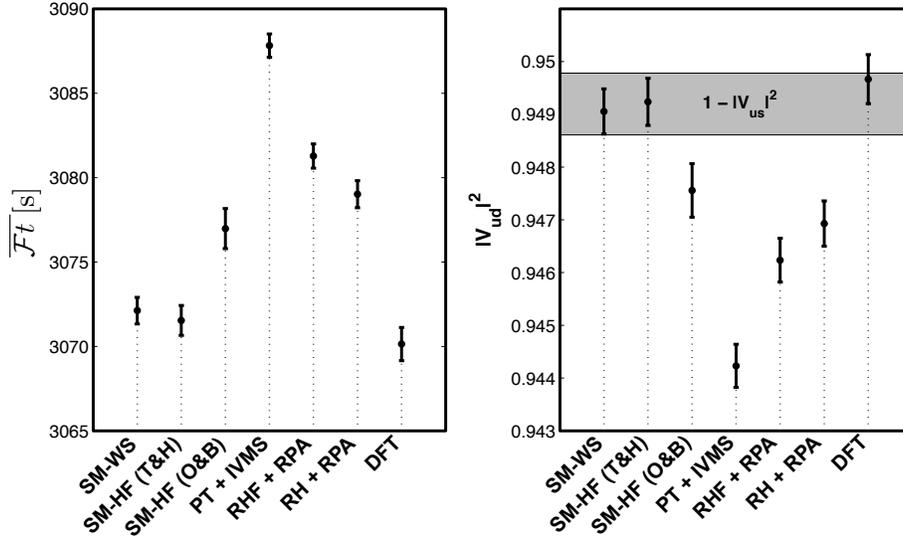
Figure 2.25: Comparison of averaged $\overline{\mathcal{F}t}$ and $\mid V_{ud} \mid^2$ with the ISB corrections δ_C taken from different models. Experimental data from [15]. For PT+IVMS, RHF+RPA, and RH+RPA the error in δ_C is due to the spread of different models or effective interactions only. In the plot on the right, $\mid V_{ud} \mid^2$ is compared to $1- \mid V_{us} \mid^2$, with $\mid V_{us} \mid$ from $K_{\ell 3}$-decays only.

the approach of the superallowed survey from 2005 [74]. As the RHF and RH plus RPA calculations do not estimate an uncertainty of δ_C, we take in each the spread of results caused by different effective interaction as an estimate of the error. Similarly, in the case of Auerbach's δ_C with perturbation theory and isovector monopole state, the uncertainty was chosen to be the spread in δ_C due to different models. The $\overline{\mathcal{F}t}$-values of Table 2.4 are plotted in Figure 2.25 highlighting the already discussed discrepancies between different models. Since the averaged $\overline{\mathcal{F}t}$ only has a physical meaning if the CVC hypothesis holds, the reduced χ^2 for a constant fit through the individual $\mathcal{F}t$ is also found in Table 2.4. Its interpretation in terms of a goodness of fit in comparison to the χ^2 distribution has to be regarded with caution because of the non-statistical character of the theoretical uncertainties of δ_C, δ_{NS}, and δ'_R. Furthermore, the compilation of the experimental data in [15] proceeds very conservatively and often inflates experimental uncertainties if a possibility of inconsistent measurements occurs. Hence, the total uncertainty on a superallowed β emitter's $\mathcal{F}t$-value is largely of non-statistical origin. Assuming CVC as valid, a

Table 2.4: Averaged $\overline{\mathcal{F}t}$ with different models for δ_C. Experimental data, δ_{NS}, and δ'_R were taken from [15]. For each model all available δ_C were taken out of the 13 well-measured superallowed β emitters.

Model	ref.	# cases	$\overline{\mathcal{F}t}$ [s]	$\chi^2/\text{d.o.f}$
SM-WS	[73]	13	3072.1(0.8)	0.3
SM-HF T&H	[15]	13	3071.5(0.9)	0.9
SM-HF O&B	[83]	9	3077.0(1.2)	0.9
PT + IVMS	[85]	13	3087.8(0.7)	7.9
RHF+RPA	[91]	9	3081.3(0.7)	2.3
RH+RPA	[91]	9	3079.0(0.8)	1.4
DFT	[41]	12	3070.1(1.0)	2.6

Table 2.5: Averaged $\overline{\mathcal{F}t}$ over the same 6 cases with different models for δ_C. Experimental data, δ_{NS}, and δ'_R were taken from [15]. The superallowed β-emitters ^{10}C, ^{14}O, ^{26m}Al, ^{34}Cl, ^{42}Sc, and ^{54}Co were considered for which all listed models have published ISB corrections.

Model	$\overline{\mathcal{F}t}$ [s]	$\chi^2/\text{d.o.f}$
SM-WS	3072.0(0.9)	0.4
SM-HF T&H	3070.7(1.1)	0.8
SM-HF O&B	3076.2(1.5)	0.9
PT + IVMS	3085.2(0.9)	4.9
RHF+RPA	3080.5(0.8)	2.4
RH+RPA	3078.7(0.9)	1.8
DFT	3069.0(1.2)	0.9

smaller χ^2 than usually expected is likely.

By far the worst value for the reduced $\chi^2/\nu = 7.9$ is found in the perturbative approach with isovector monopole state. This is not too surprising considering that details of nuclear structure are not included in this calculation. The model rather attempts to estimate the typical size of δ_C for different mass ranges. Assuming that the right physics is taken into account when linking the isovector monopole state to δ_C, it is concluded that the $\overline{\mathcal{F}t}$ should be larger than generally assumed in the established calculations.

The relatively large value $\chi^2/\nu = 2.6$ for the DFT is dominated by ^{62}Ga. With δ_C from RHF and RH plus RPA a χ^2/ν of 2.3 and 1.4 are obtained, respectively,

which appears too large given the non-statistical contributions to the uncertainty.[5] However, the present evaluation might underestimate these models' uncertainties. All shell-model calculations result in reasonable χ^2/ν although the difference in $\overline{\mathcal{F}t}$ between Hardy and Towner on one hand and Ormand and Brown on the other is significant [15]. One might reject the older Hartree-Fock model by Ormand and Brown based on doubts regarding the correct implementation of the Fock term or because of its smaller model space (as it is done in the latest survey on superallowed decays [15]), but certainly not because of unexpected violation of the CVC hypothesis.

To treat all methods on an equal footing, we have performed a second evaluation; we only take those 6 superallowed β-decays into account for which values of δ_C are published in all models. The results in Table 2.5 generally confirm the previous observations. Since the problematic case of ^{62}Ga is not part of this group, the DFT model is also characterized by a $\chi^2/\nu \approx 1$.

As none of the models can claim a breakdown of CVC, we proceed with a calculation of $\mid V_{ud} \mid^2$ according to Equation 2.76 with $\overline{\mathcal{F}t}$ from Table 2.4, $K/(\hbar c)^6 = (8120.2787 \pm 0.0011) \times 10^{-10}$ GeV^{-4} s, $g_V = 1$ (CVC), and $G_F/(\hbar c)^3 = 1.16637(1) \times 10^{-5}$ GeV^{-2} from muon decay [29]. The results are shown in Figure 2.25 in comparison to $1- \mid V_{us} \mid^2$. A deviation from unitarity in the CKM matrix would be a consequence of some of the recent models. Notably, even Ormand and Brown's shell model calculation would lead to a deviation by falling short of unitarity.

To summarize this section, there are many indications that the most advanced calculations of Towner and Hardy yield correct δ_C:

- agreement with the macroscopic calculations of NCSM for ^{10}C and generally with DFT,

- consistency in δ_{C2} between their own Saxon-Woods and Hartree-Fock radial wave-functions,

- considerations of core orbitals, and

- agreement of constant $\mathcal{F}t$-values with the expectation from CVC.

Other models show systematic differences to Towner and Hardy's results and all of these sets obtain smaller δ_C. This is also to be expected from the exact formalism by Miller and Schwenk. However, all of these calculations are either in an exploratory state and require more refinement or, for the case of Ormand and

---

[5]Liang et al. have used a non-standard format of a χ^2- test [96] which yields their small χ^2/ν in [91].

Brown's δ_C, should extend their model space. A discussion about the correct implementation of the Hartree-Fock procedure would also be crucial. In light of the importance of V_{ud} for the Standard Model the issue of discrepancies in δ_C needs to be resolved. Otherwise an inflation of the uncertainties in δ_C might be required with a subsequent increase in the partial uncertainty for transition dependent corrections (see Figure 2.17). The next section will explain how experiments can impact this debate.

2.8 Experimental input to the debate around the isospin symmetry breaking corrections

Generally, there are two areas where experimental results can influence the debate on ISB corrections and help to discriminate between different models of δ_C. First, some models (usually the shell model based approaches) rely on experimental quantities such as the nucleon separation energies, IMME coefficients, etc. as input to the calculation. Improved input quantities or measurements for those cases, where only extrapolated values exists, will help the respective model. Conversely, an observable which is not needed to fine-tune a model, could serve as an independent benchmark of the model.

Secondly, more precise ft-values, either of the 13 most studied cases, or of new ones, can be used for experimental tests of the ISB corrections. Usually, in these tests the validity of the CVC hypothesis is assumed to some level. Since CVC is an hypothesis and needs to be confirmed experimentally itself in superallowed β-decays, it is more accurate to formulate that these measurements can highlight discrepancies between a set of δ_C, the CVC hypothesis, and experimental results.

2.8.1 Input parameters and independent benchmark quantities

The shell-model methods typically use neutron and proton separation energies, charge radii, spectroscopic factors, coefficients of the IMME, and excitation energy of other 0^+ states as input for their calculations. Particularly for the heavier superallowed decays this information is only sparsely available. As a consequence the uncertainties in δ_C are larger than for the lighter masses leaving lots of room for improvements. For instance, the Coulomb part of the Saxon-Woods potential is adjusted to reflect the experimental RMS charge radii [72, 73]. These have not been measured for all superallowed emitters and are then extrapolated from stable isotopes. Their uncertainties are consequently large and if sudden unexpected structural changes occur towards more exotic nuclides, they might be incorrect altogether. For this purpose, a campaign has been started at TRIUMF to measure iso-

tope shifts [97] which are sensitive to differences in RMS charge radii. A successful measurement was performed recently involving TITAN's cooler and buncher which confirmed the extrapolated RMS charge radius of ^{74}Rb with a tenfold error reduction compared to the extrapolation. As a result the theoretical uncertainty on δ_{C2} for ^{74}Rb in the shell model with Saxon-Woods radial wave-functions could be reduced by about 20 % [16]. An analogous measurement is planned for ^{62}Ga.

In the discussion of the calculation of ^{10}C with the NCSM it was mentioned that the IMME parameters have also been calculated and compared to experiment. This is an example when independent benchmark parameters have been used to test the reliability of a calculation. The shell-model calculations have also been tested by a comparison of measured and theoretical transition strength to non-analog 0^+ states [98].

2.8.2 Improvement of ft-values

Different strategies are employed to test for inconsistencies between a set of δ_C, experimental results, and the conserved vector current hypothesis. For instance, in [15] Towner and Hardy assume the validity of CVC and compare the individual ft-values with the ft-values extracted from

$$\widetilde{ft} = \frac{\overline{\mathcal{F}t}}{(1 + \delta'_R)(1 - \delta_C + \delta_{NS})} \qquad (2.86)$$

where $\overline{\mathcal{F}t}$ is the weighted average of all cases (see Figure 2.26). This test is circular and hence insensitive to the correct absolute value of $\mathcal{F}t$, but it can help to identify inconsistencies. Similarly (and with analog deficiencies), 'experimental' nuclear structure dependent corrections $(\delta_C - \delta_{NS})^{\text{exp}}$ are calculated

$$(\delta_C - \delta_{NS})^{\text{exp}} = 1 - \frac{\overline{\mathcal{F}t}}{(1 + \delta'_R) \cdot ft} \qquad (2.87)$$

and compared to the individual theoretical $(\delta_C - \delta_{NS})$ [99].

Avoiding the circularity of using the same δ_C to extract $\overline{\mathcal{F}t}$ and for the test, the 13 precise superallowed β-decays can be grouped and the $\overline{\mathcal{F}t}$-value of each group is compared against each other. After a high precision measurement of the halflife of ^{26m}Al [84] its $\mathcal{F}t = 3073.0(12)$ s rivals the precision of the other 12 cases combined, $\overline{\mathcal{F}t} = 3072.0(10)$, both with the Saxon-Woods ISB corrections. This is a particularly strong test because δ_C for ^{26m}Al is among the smallest absolute values of δ_C and its theoretical uncertainty is the smallest. Considering the other 12 cases, the $\overline{\mathcal{F}t}$ of 3072.3(10) s with Hardy and Towner's Hartree-Fock
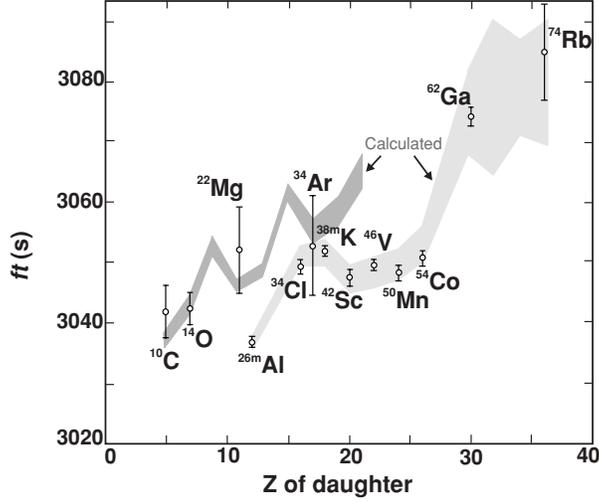
Figure 2.26: Comparison of experimental ft-values to one which is extracted from the weighted average $\overline{\mathcal{F}t}$ and the transition dependent corrections. See text for details. Figure from [15].

approach is in agreement with the value calculated with the Saxon-Woods radial wave-functions. But for ^{26m}Al former corrections lead to 3069.0(19) s which is neither in agreement with the 12 other cases with Hartree-Fock corrections nor with its own $\mathcal{F}t$-value derived from Saxon-Woods based δ_C. This difference is due to a much larger $\delta_{C2} = 0.410(50)\%$ for the new Hartee-Fock calculation compared to $\delta_{C2} = 0.280(15)\%$ in Saxon-Woods [73] and Ormand and Brown's older Hartree-Fock with $\delta_{C2} = 0.29(9)\%$. It is important to resolve this discrepancy considering that, to date, only the Towner and Hardy's Hartree Fock calculations are employed as benchmarks of their Saxon-Woods approach. In fact the new half-life measurement leads to an increase in the δ_C model associated uncertainty.

Recently, Towner and Hardy have introduced a comparative test between models of ISB corrections. Following

$$\delta_C = 1 + \delta_{NS} - \frac{\overline{\mathcal{F}t}}{(1 + \delta'_R) \cdot ft} \tag{2.88}$$

$\overline{\mathcal{F}t}$ is treated as a single free parameter to minimize the difference in all available cases between δ_C and $1 + \delta_{NS} - \overline{\mathcal{F}t}/[(1 + \delta'_R) \cdot ft]$, whose uncertainty is dominated from experiment. As a figure of merit the reduced χ^2 was employed. Figure 2.27

64
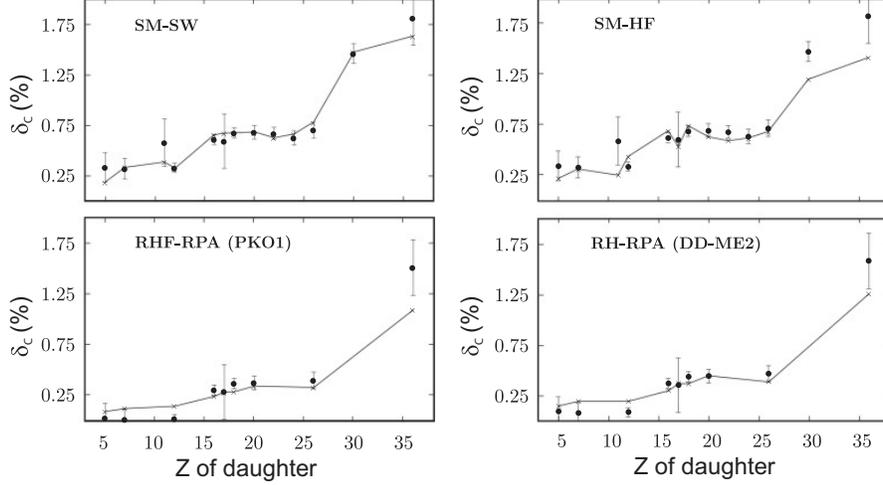
Figure 2.27: Results for δ_C of a χ^2 minimization with a free parameter $\overline{\mathcal{F}t}$. The solid lines are the theoretical ISB corrections while the points with errors are the minimization results. See text for details. Figures from [18].

shows details of the test results. Overall the shell model with Saxon-Woods radial wave-functions yields the best internal agreement.

An alternative, semi-empirical viewpoint [17] tries to emphasize similarities, and not differences, between different models. Especially, the shell model calculations of δ_C show similar relative patterns in the development of δ_C over Z, though their absolute values might differ. In view of Auerbach's publication [85] and other works (see references in [17]) for $N \sim Z$ the transition dependent corrections are expected to scale approximately as Z^2. Hence, the individual models are only considered for their representation of nuclear structure effects but not for their general (approximate) Z^2 behaviour. Instead of correcting all individual superallowed cases to the transition independent $\mathcal{F}t$-values, one only corrects by the shell-structure effects in δ_C and extrapolates the resultant $\widetilde{f}t$-values to the charge-independent limit where isospin-symmetry breaking and Coulomb effects are negligible. This is not the case for an extrapolation towards $Z = 0$, but at $Z = 0.5$ where the total mass splitting within an isospin multiplet vanishes [17]. Finally, these extrapolated $\mathcal{F}t$ values can be compared between different models of δ_C and a V_{ud} can be obtained.

In summary, all of these tests benefit from new precision cases or improved ft-
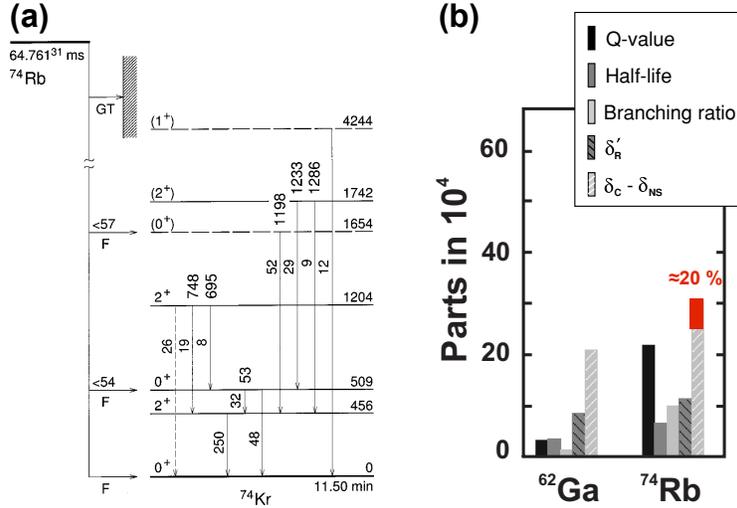
Figure 2.28: (a) Decay scheme of ^{74}Rb. The superallowed decay branch is a ground-state to ground-state transition. Figure from [100]. (b) Partial uncertainties for the $\mathcal{F}t$-value of ^{62}Ga and ^{74}Rb. The uncertainty in δ_C for ^{74}Rb is to about 20 % due to the extrapolation of its RMS charge radius. This was measured recently at TRIUMF [16] and led to a reduction in the associated uncertainty. Adaptation of a figure from [15].

values for the 13 well-studied superallowed decays. The heavier superallowed emitters are of particular importance as they have larger δ_C corrections. Figure 2.26 and Figure 2.27 highlight that an improvement in the ft-value for ^{74}Rb would lead to much more stringent tests and discrimination between different models of ISB corrections. In the next section the present experimental situation regarding ^{74}Rb will be reviewed.

2.9 The case of ^{74}Rb and the need for highly charged ions in Penning trap mass measurements

The superallowed $0^+ \rightarrow 0^+$, $T = 1$ β-decay of ^{74}Rb proceeds to the isobaric analog ground state of ^{74}Kr. Its decay scheme is displayed in Figure 2.28(a). As the superallowed decay in ^{74}Rb connects two ground states its only detectable signature is the outgoing positron or the neutrino of which the latter is usually not detected. The kinematics of a decay into three particles (daughter, positron, and

neutrino) results in a spectrum of positron energies which overlays with the spectra of transitions to non-analog states. A direct measurement of the superallowed branching ratio is thus not easily possible. Instead the sum of all non-analog decays is determined to obtain the superallowed BR. In those decay branches, the β-decay populates excited states in ^{74}Kr which decay via emission of γ-rays towards the ground-state. Except for longer lived isomers, the life-times of these states are very short and the γ-decay occurs instantaneously. $\gamma - \gamma$ coincidences further allow the reconstruction of the level-scheme and, normalized to the counted β- particles, a BR can be obtained. Because of the relatively large Q-value in ^{74}Rb many high lying 1^+ excited states in ^{74}Kr are populated by Gamow-Teller β-decay transitions. Their individual population is small and below the experimental sensitivity level. However, when their BR are added, the value is not negligible for the extraction of the superallowed branching ratio. The remedy to this problem is found in lower lying levels in ^{74}Kr, which act as collector states of the weak Gamow-Teller transition. This means that the many high lying states will not decay directly into the ground state, but feed to a few low lying states. The γ- decays from these levels can be detected. However, to achieve complete accounting for the total non-analog decays, assistance from theory is required as some direct feeding of the ground state from high lying levels will remain unobserved. With the benchmark that the theoretical description properly describes the relative feeding of the observed transitions, the remaining component of Gamow-Teller strength can be calculated by theory. Such a measurement and analysis has been performed in [100] with shell-model calculations by Towner and Hardy. The total non-analog BR was determined to be 0.5(1)% resulting in a superallowed BR of 99.5(1)%.

The most recent survey of superallowed β-decays lists two precision measurements of the half-life of ^{74}Rb. Their uncertainties are almost overlapping (see Figure 2.29(a)), but following the conservative procedures of the survey a scaling factor is introduced to account for a potential non-statistical difference in the two measurements. The combined half-life is 64.776(43) ms, which makes ^{74}Rb the shortest-lived nuclide among all 13 well measured superallowed decays.

An approximation of Equation 2.63 shows that the statistical rate function roughly scales with the fifth power in the Q-value. Hence, the Q-value has to be measured 5 times more precisely than half-life and BR for the determination of the ft-value. In the past, masses and Q-values for β-decays have been measured by nuclear reactions or β-decay end-point measurements. In order to obtain the required precision for superallowed β-decay studies, these have been restricted to the following: (^{3}He,t) reactions, (p,n) threshold measurements, or (p,γ) and (n,γ) on the same target to reach parent and daughter of the superallowed decay. The emergence of Penning traps in the realm of rare isotope research led to unprecedented precision in atomic masses and, thus, also for Q-values. The impact of Penning trap
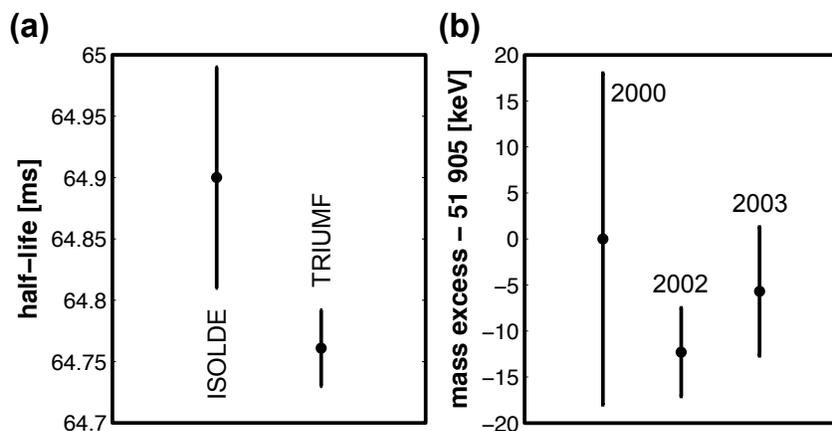
Figure 2.29: (a) Precision half-life measurements of ^{74}Rb at ISOLDE [101] and TRIUMF [102]. (b) Direct mass measurement of ^{74}Rb with ISOLTRAP [103] from [12, 13], and summarized in [14].

mass measurements was indeed critical not only from a precision point of view, but it also brought deficiencies in accuracy of older measurements to light, e.g. for ^{46}V [104]. In the meantime, all Q-values of superallowed β-decays have been measured in Penning traps, except for ^{14}O [15, 105]. Penning traps are able to perform mass measurements even of short-lived nuclides with relative precisions of $\delta m/m \approx 10^{-9}$. By taking the mass differences the Q-value of the β-decay is obtained (see Figure 2.13). Traditionally, Towner and Hardy list the Q_{EC}-value of the electron capture, which is simply the difference in atomic mass between the parent and the daughter. In those cases where the superallowed decay populates an excited state in the daughter nucleus, precise knowledge of the excitation energy of the state is also required. This can be achieved via γ-ray spectroscopy.

The atomic mass of ^{74}Rb's daughter, ^{74}Kr, has been measured with a precision of 2.1 keV at the Penning trap facility ISOLTRAP at CERN [106]. The mass measurement of ^{74}Rb in a Penning trap is, due to its short half-life of 65 ms, more challenging. Before TITAN's measurement of ^{11}Li ($T_{1/2} = 8.8$ ms)[7], ^{74}Rb was the shortest-lived nuclide whose mass has been measured in a Penning trap. In order to achieve this, ISOLTRAP carried out three campaigns on ^{74}Rb [12–14] (see Figure 2.29). Other measurements of the mass of ^{74}Rb published in [107, 108] are in agreement with the ISOLTRAP result, but because of their poorer precision, they do not carry any weight. Since the nuclear binding energies with typically ≈ 8 MeV per nucleon are small compared to the mass of a nucleon (≈ 1 GeV) it

is common to express the atomic mass of a nuclide with mass number A in terms of the mass excess $m.e. = [M - A \cdot M(^{12}\text{C})/12] \cdot c^2$. For ^{74}Rb, the three mass measurements at ISOLTRAP lead to a mass excess of 51914.7(3.9) keV and combined with the mass of ^{74}Kr to $Q_{\text{EC}} = 10417.3(44)$ keV.

The partial uncertainties to the corrected $\mathcal{F}t$ of ^{74}Rb are shown in Figure 2.28b, when considering δ_C from the shell model with Saxon-Woods radial wave-functions. As mentioned before, its associated uncertainty contains the RMS charge radius of ^{74}Rb, which was previously not known experimentally. With the recent laser spectroscopy measurement, the RMS charge radius was determined and reduced the uncertainty on $\delta_{C2} = 1.50(30)\%$ to 0.25% while confirming the mean value [16]. As a consequence, the Q_{EC} value contributes to the uncertainty of the $\mathcal{F}t$ at a similar amount as the nuclear structure dependent corrections. This implies two strong motivations to improve the Q_{EC}-value. Firstly, an error reduction on Q_{EC} would have a direct impact on the corrected $\mathcal{F}t$ whose uncertainty could be improved by 20%. Secondly, an improved ft-value would allow more stringent tests regarding the discrepancies between different models of the ISB corrections (Section 2.8). As mentioned before, ^{74}Rb, with its largest δ_C among all superallowed β emitters, would carry particular weight were it not limited by the current precision in its Q_{EC}-value. Considering the importance of the CKM matrix and the tension of some ISB models with unitarity, an error reduction in the ft-value of ^{74}Rb is crucial. For all of these reasons, a new measurement of the superllowed BR in ^{74}Rb has recently been performed at TRIUMF and its analysis is underway [109]. But since the uncertainty of the ft-value is dominated by the Q_{EC} it is most important to improve the precision of involved masses. Another dedicated measurement of ^{74}Kr in a Penning trap would likely lead to a more precise atomic mass. However, ^{74}Rb poses, due to its half-life of 65 ms, a real challenge to experiment. Its mass is known by a factor 2 less precisely than that of ^{74}Kr, although it has already been determined 3 times in a Penning trap. This indicates that an improved precision is unlikely to be reached due to limits of the technique. To understand its limitation better, it is important to consider the achievable precision of a mass measurement in a Penning trap which follows

$$\frac{\delta m}{m} \propto \frac{m}{qBT_{\text{rf}}\sqrt{N_{\text{ion}}}} \qquad (2.89)$$

[10], where $\delta m/m$ is the achievable relative precision in mass m. q is the ion's charge state utilized in the measurements, which are generally performed with SCI. B is the magnetic field strength of typically a few Tesla. The highest field strength used at Penning trap facilities to measure masses of radioactive nuclides is 9.4 T [110]. The requirement of very homogeneous fields makes even larger field

strengths very difficult to explore. The number of ions N_{ion} is limited by the available experimental time at radioactive beam facilities where radioactive nuclides are being produced (see Section 3.2). It is further constrained by the production yield at radioactive beam facilities and efficiency of the spectrometer. Finally, the precision is dependent on the measurement time T_{rf} on each individual ion. The range of possible T_{rf} is obviously restricted by a nuclide's half-life, which is indeed the limiting factor for the precision in the mass of ^{74}Rb.

Hence, an option for a more precise mass of ^{74}Rb is to develop experimental techniques which enable Penning trap mass measurements in higher charge states. Another approach would be a novel octupolar excitation scheme in Penning trap spectrometry [111, 112] which promises gain in experimental precision. However, this excitation is more sensitive to the initial conditions of the measurement and its theoretical foundation has been laid out only very recently [113]. On the other hand, Penning trap mass studies utilizing HCI have already been successfully pioneered with stable nuclides [11, 114]. In the realm of rare isotope science with Penning traps, HCI represent a thus far unexplored opportunity to improve the experimental precision further circumventing constraints imposed by short half-lives and lower yields when probing the limits of nuclear existence. However, in contrast to measurements with stable nuclides, the requirements of high efficiency and short measurement times are critical when working with radioactive ions. The experimental part of this work is focused on the very first mass measurement of HCI of radioactive, short-lived nuclides in a Penning trap including a successful mass measurement of ^{74}Rb^{+8}.

Chapter 3

Experimental Setup

3.1 Introduction and overview of the TITAN facility

The mass measurements described in this thesis are performed with TRIUMF's Ion Trap for Atomic and Nuclear science (TITAN), which is coupled to the radioactive beam facility ISAC at TRIUMF. Operational for online measurements since 2007, TITAN's measurement program had initially focused on mass measurements of so-called halo nuclei [115, 116]. The masses of ^{8}He [117, 118], ^{6}He [118], ^{11}Li [7], ^{11}Be [119], and ^{12}Be [120] have successfully been measured. The ground state of ^{12}Be is not a halo nucleus itself, but in its first excited 0^+-state a neutron halo-like structure might be formed [121]. The ability to carry out precision mass measurements, even for very-short lived nuclides with $T_{1/2} < 10$ ms distinguishes TITAN from other facilities and is due to TITAN's fast measurement preparation which does not require a preparation trap and uses a Lorentz steerer for beam injection into its Measurement Penning Trap (MPET)(see Section 3.7.7). In fact, the demonstration of the mass measurement of ^{11}Li with its half-life of 8.8 ms makes TITAN the fastest online Penning trap system worldwide. This is a critical feature for further exploration towards the limits of nuclear existence. Considering that the half-lives tend to get shorter further away from the valley of stability, this ability becomes increasingly important. Figure 3.1 illustrates the increased accessibility of short-lived nuclides at TITAN for masses up to $Z \leq 50$ and $N \leq 50$.

In the field of metrology, TITAN has helped to resolve a discrepancy in the mass of the stable nuclide ^{6}Li [124]. This measurement, with $\delta m/m = 4.4$ Parts-Per-Billion (PPB), has highlighted the achievable accuracy which is competitive with facilities dedicated to high precision mass measurements of stable nuclides. More recently, TITAN has performed measurements on ^{30,31}Na motivated by the so-called island of inversion [125, 126] and of $^{47-50}$K, $^{49-50}$Ca [1] and ^{51}K, ^{51,52}Ca

71
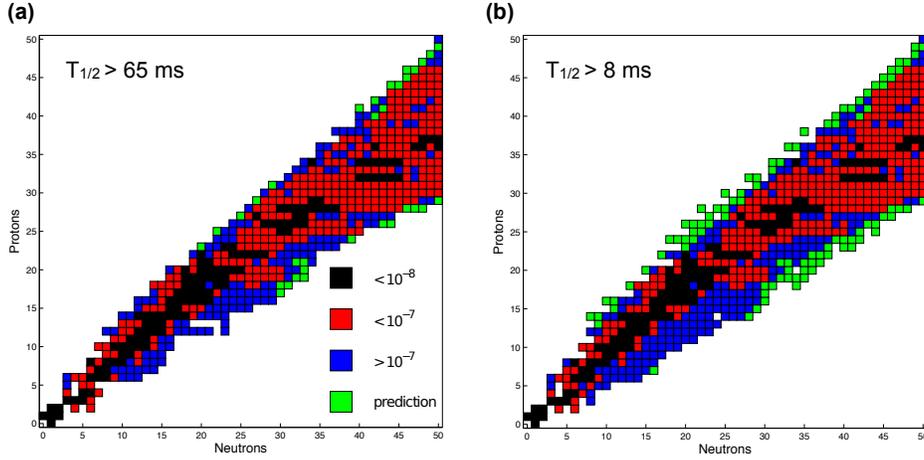
Figure 3.1: Lower section of the chart of nuclides with nuclides with half-lives larger than 65 ms (a) and 8 ms (b). Before TITAN's mass measurement of ^{11}Li, ^{74}Rb ($T_{1/2} = 65$ ms) used to be the shortest lived nuclide whose mass has been determined in a Penning trap [13]. The color-code reflects the relative mass uncertainty $\delta m/m$ of a nuclide. The mass data were taken from the 2011 preview of the atomic mass evaluation [122] and the half-lives are from [123].

[127]. The latter mass range is interesting due to predictions about shell closures at $N = 32$ and $N = 34$ [128, 129] to which the two-neutron separation energies $S_{2n} = -M(A, Z) + M(A - 2, Z) + 2m_n$ are sensitive. Theoretical models with only NN-forces fail to reproduce the experimental masses even when soft, momentum-evolved potentials are used (compare with Section 2.1.3). But when 3-body forces are added, the qualitative trend follows experiment [127, 129].

Up to now, TITAN measurements have been performed with Singly Charged Ions (SCI) as it is done at all other Penning trap setups [110][130][131][132][133] coupled to radioactive beam facilities. As the precision scales inversely with the charge state of the ion (Equation 2.89), the use of Highly Charged Ions (HCI) offers great gains for Penning trap mass measurements. Indeed, the Stockholm-Mainz-Ion-LEvitation-TRAP (SMILETRAP) has pioneered this approach for stable nuclides [11, 114]. In the realm of rare-isotope science, short half-lives and the need for high efficiency complicates the use of HCI in Penning trap mass spectrometry, and this path has so far not been exploited. In consequence, HCI represent an opportunity for new limits in the precision of Penning trap mass measurements. A second cornerstone of TITAN's scientific program is hence to set out to master the chal-
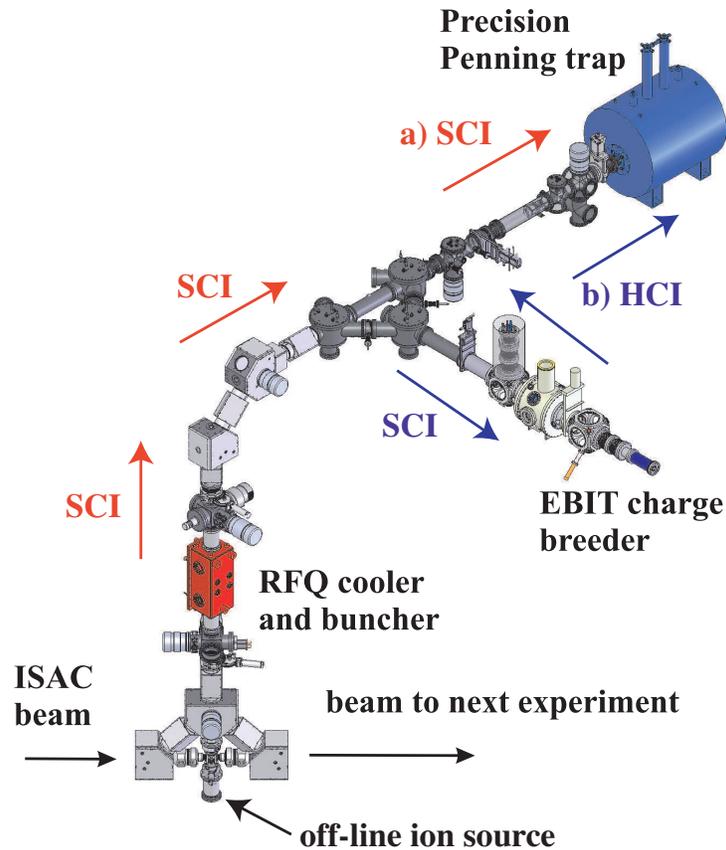
Figure 3.2: Schematic of the experimental setup of TRIUMF's Ion Trap for Atomic and Nuclear science (TITAN). The different paths for SCI (a) and HCI (b) are marked.

lenges of highly charged, radioactive nuclides to explore the advantages of HCI. A schematic overview of the TITAN facility is shown in Figure 3.2. The radioactive beam of SCI from ISAC is injected in a RFQ cooler and buncher [134, 135] which is floated just below ($\Delta V \approx 5 - 20$ V) the ISAC beam energy to decelerate and to trap the beam. Buffer gas cooling takes place through collisions with He or H_2 gas, which thermalize the ions to room temperature while an oscillating Radio-Frequency (RF) field provides radial confinement. The net result is an overall cooling of the 'hot' ISAC beam. In addition, a longitudinal electrostatic potential leads to a confinement which allows the continuous beam from ISAC to be accumulated in the RFQ. Ions are extracted from the RFQ by opening the con-

fining potential, and ion bunches are released. Beam extraction from the RFQ can proceed in the reverse or forward direction [97]. In the reverse mode, the beam is sent back into the ISAC beam line (as indicated in Figure 3.2 with 'beam to next experiment') where other experimental setups can take advantage of the cooled and bunched beam. Recent laser spectroscopy measurements of isotope shifts have benefited from this technique [16].

When the bunched beam from the RFQ is extracted in the forward direction, it can follow two paths within the TITAN setup. First, it can be transferred directly into the precision MPET. In this case, the mass measurement is carried out with SCI (see a in Figure 3.2). Alternatively (Figure 3.2b), the ion bunches can be sent into the EBIT charge breeder [2, 136]. In an EBIT, higher charge states are reached through electron-impact ionization by an intense electron beam. The design of the EBIT reaches electron beam energies up to 70 keV. As the electron binding energies increase with the number of removed electrons, such an electron beam energy in the EBIT allows removal of even deeply bound electrons of the ion. After the charge breeding, the HCI are extracted as pulses and are delivered to the MPET.

An unavoidable effect of the charge breeding in the EBIT is an increased energy spread which can negatively impact the capture efficiency at the MPET or the mass measurement itself (see Section 3.7.3). A Cooler Penning Trap (CPET) [137] [138] [139] is currently being built at TITAN to prepare the HCI for injection into the MPET by providing a cooling mechanism for highly charged ions. Because of the high charge state and the rapid charge exchange (compare with Equation 3.57 to be discussed later), buffer gas cooling with neutral atoms is not an option. Recently, sympathetic cooling of HCI in a laser-cooled plasma of singly charged ions (e.g. $^{24}Mg^+$) has been suggested as a fast cooling mechanism [140] [141] [142]. However, at TITAN's CPET, electron or proton cooling will be utilized because both techniques can be developed and studied based on the same trap setup. Moreover, electron cooling of protons has already been demonstrated in [143]. The self-cooling of electrons in a strong magnetic field due to synchrotron radiation offers simple availability of a cold electron gas. Simulations suggest [137] that during the time until the ions are cooled to $\approx 1eV/q$ only a few percent of the ions undergo recombination. Losses could then be minimized by separating the HCI from the electrons before recombination sets in. In proton cooling, recombination of HCI with the coolant is avoided. Due to short half-lives well below one second, the hot ion bunches from the EBIT will need to be trapped, cooled, and transferred to MPET quickly. Access to large amounts of cold protons, $N_p \sim 10^8$, on this time scale is more difficult because the larger proton mass hinders any self-cooling in the B-field. Once tested in an off-line setup with its own source of SCI [139], the CPET will be inserted into the TITAN beamline just in front of the MPET.

Apart from the time limitations imposed by the respective nuclide's half-life there

are no fundamental differences between stable and radioactive ions in terms of applying these techniques. Thus, a surface ion source is installed at TITAN which allows test and optimization of all individual components. Generally, it provides different beams of singly charged alkali metals. A recent test of a Ca source has also been successful. Hence, measurements can be prepared using ions from TITAN's ion source previous to ISAC beam delivery of radioactive beams. As an additional advantage systematic effects can be studied well in advance of an experiment by measuring well known masses of stable nuclides. As a result, major contributions to the systematic uncertainty can be investigated independently of the actual measurement.

This chapter will introduce the different stages of the beam formation and preparation necessary for the mass measurement.

3.2   ISAC: production and delivery of radioactive beam

Various techniques are established to produce beams of short-lived radioactive nuclides. Most common are fragmentation of a fast (typically 100s of MeV/u), heavy ion beam on a target of light nuclei (called in-flight fragmentation) [144] and the spallation, fission, and fragmentation of a heavy target by a driver beam of light nuclides. The second technique is known as Isotope Separator On-Line (ISOL). The ISAC facility [145] at TRIUMF falls into this category. It is driven by a proton beam from TRIUMF's cyclotron, which accelerates H^- to 500 MeV. When passing through stripper foils inside the cyclotron a fraction of a H^- bunch is converted to H^+ and extracted. The proton beam is delivered to ISAC where it impinges on a so-called production target. The ISAC facility receives up to 100 μA of proton beam which is currently the highest beam intensity on-target for any ISOL facility. Hence, the availability of beam powers with up to 50 kW in combination with thick, high power targets represents unique prerequisites to achieve the highest ISOL production yields. The products from the bombardment of the proton beam have to diffuse out of the target. Thus, target temperature is a critical parameter which is controlled by the energy loss of the proton beam and possibly by heating the target resistively. For high beam powers, targets require cooling to withstand deposited heat during the continuous proton bombardment. Once the products diffuse out of the target several ion sources [147] are available at ISAC to ionize the neutral atoms including a surface, laser [148], and Forced Electron Beam Induced Arc Discharge (FEBIAD) ion source. Surface ionization is accomplished by heating an ionizer tube and target to about 2000 ^{o}C. Following the Langmuir-Saha surface ionization theory (see its application for surface ion sources for instance in [149, 150]), elements with an ionization potential I_p lower than the work function ϕ of the surface, e.g. tungsten with $\phi = 4.6$ eV, can efficiently be ionized. Hence, a surface ion source is well
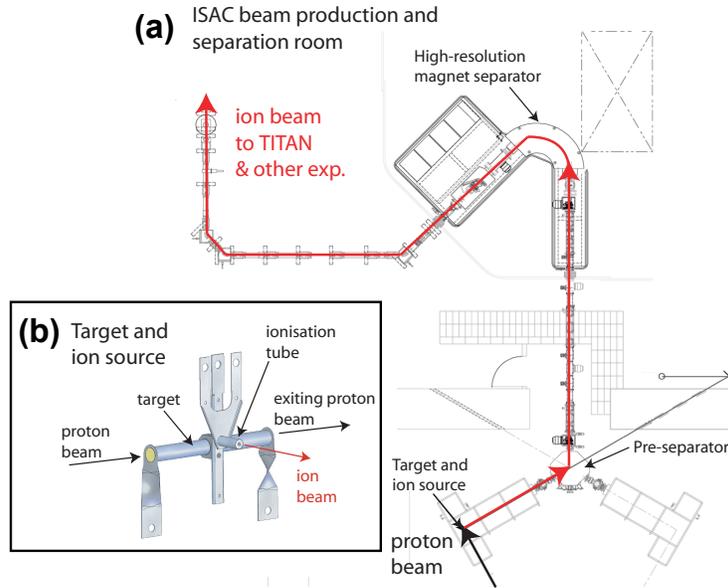
Figure 3.3: (a) Schematics of production, ionization, and separation of radioactive beams at ISAC. The inset (b) shows the target and ion source setup. Figure from [146].

suited for alkali elements such as the studied Rb isotopes ($I_p = 4.2$ keV), but noble gases are not accessible owing to the highest ionization potentials of all elements. The ions are electrostatically accelerated up to 60 keV beam energy. They pass a two-stage dipole magnet mass separator unit (pre- and main separator) which selects ions based on their mass-to-charge ratio. Nuclides with different mass numbers are easily separated due to the large mass differences. But different elements with the same mass number (i.e. isobars) can often be too close in mass to be resolved by the mass separator. Isobaric contamination in the beam delivered to the experiment has to be expected if a typical resolving power of $m/\delta m \approx 3000$ is surpassed. This could represent a problem for experiments such as the mass measurements at TITAN which require contamination-free beams of the nuclides of interest. Contaminants could affect the measurement or reduce the sensitivity. The schematics of production, ionization, and separation of the radioactive beam at ISAC are shown in Figure 3.3. The ISAC experimental halls (see Figure 3.4) are divided into three areas with distinct energy regimes. All measurements which are relevant for superallowed β-decays require low energy beams. Indeed, TRIUMF is in the unique position to measure all quantities to characterize a superallowed β-
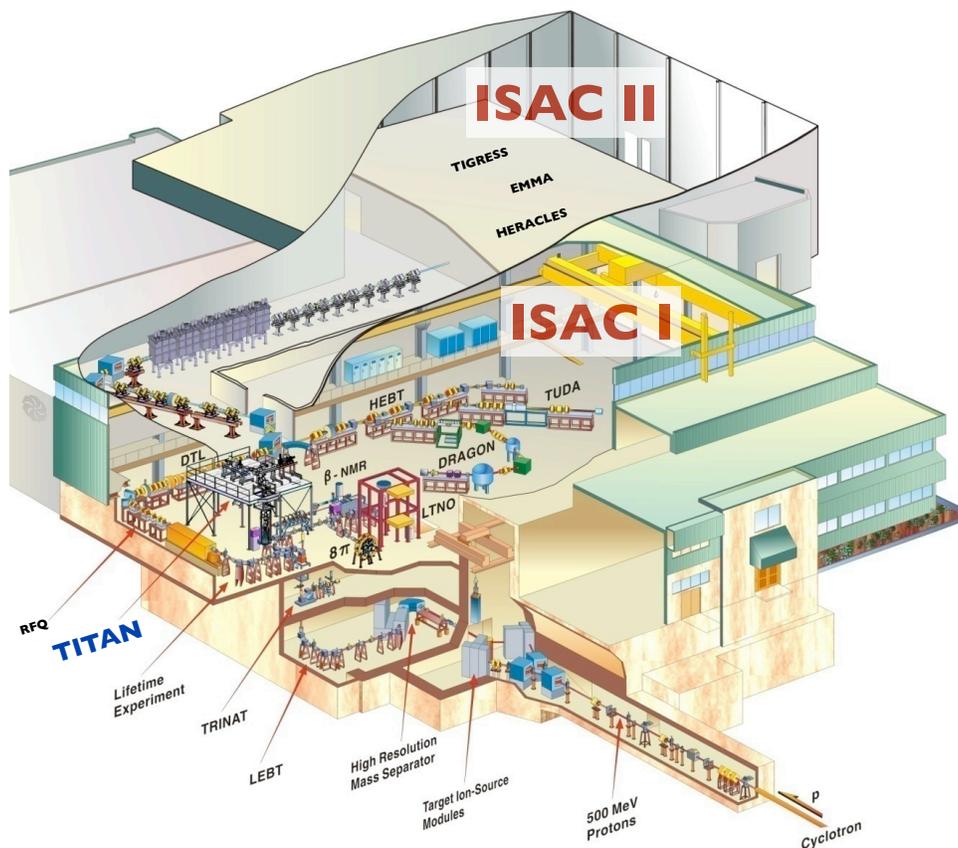
Figure 3.4: Schematics of the ISAC facility and the experimental facilities. ISAC experimental areas are distinguished by their respective beam energy. First, the low energy section with up to 60 keV is dedicated to ground state and decay properties investigated by trapping experiments, β-decay studies, or collinear laser spectroscopy work. An RFQ and a drift tube linac accelerate the radioactive ion beam up to 1.5 MeV per nucleon in the so-called mid-energy regime. There, the beam is used for reaction measurements important for nuclear astrophysics. Moving into the third energy regime, the ISAC-II superconducting linear accelerator brings the beam to 5-11 MeV/u for nuclear reactions at higher energy.
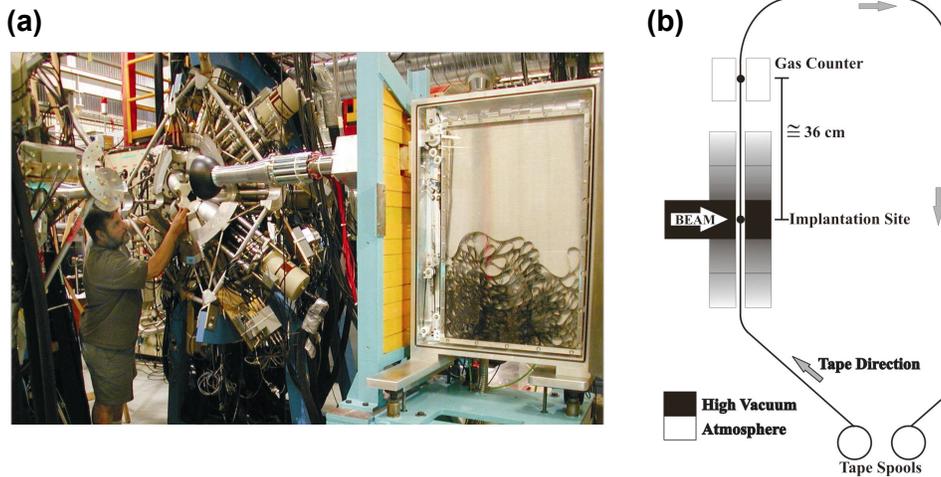
Figure 3.5: (a) Photo of the 8π facility. (b) Schematic of the gas proportional counter with tape station. Both from [153].

decay. BR are determined at the 8π γ-ray spectrometer [151] which consists of 20 Compton-suppressed HPGe detectors. It works in conjunction with a tape-station setup and β-particle counter such as the Scintillating Electron Positron Tagging Array (SCEPTAR) [152], see Figure 3.5. Half-lives of β-decays are measured at a tape station which transports the implanted sample into a gas proportional counter [154]. Finally, the Q_{EC}-value can be deduced from direct mass measurements at TITAN. If the superallowed decay branch populates an excited state in the daughter nucleus, its excitation energy can be precisely measured through the emitted γ-rays at the 8π facility.

3.2.1 Production and delivery of neutron-deficient Rb-beams

Different target materials produce different radioactive nuclides. Figure 3.6 compares various targets in their yields of Rb isotopes. This study aimed towards the proton dripline, i.e. the line where members of an isotopic chain become unbound when removing another neutron. These neutron-deficient Rb isotopes can be delivered in high quantities from ZrC and Nb targets. For the yields shown in Figure 3.6, ZrC targets were typically operated with a 35-75 μA proton beam, while Nb targets were bombarded by 98 μA of protons. The sudden drop for ^{74}Rb in the use of a ZrC target is likely caused by the short half-life of 65 ms (compared to 19 s for ^{75}Rb) and the lower proton beam intensity of 35 μA compared to the Nb-target
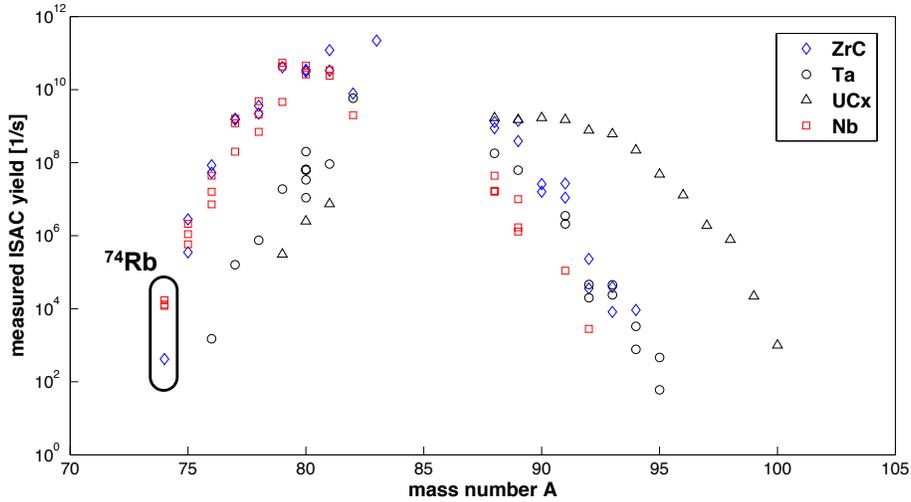
Figure 3.6: Measured yields of ground state Rb isotopes at ISAC for various targets. These are measured absolute numbers which are not normalized to the respective beam currents for different targets. Due to the regulator licence restrictions, the ISAC UCx target was only irradiated with a 2 μA proton beam which is a factor of 10-50 less than all other targets. Uranium targets owing to their large excess of neutrons are particularly suited for beams of neutron-rich nuclides but less favourable for the present studies. The gap at $A = 85 - 87$ is due to the stable ^{85,87}Rb as well as the long-lived ^{86}Rb with a half-life of 18.6 days. Data are taken from ISAC yield database [155].

[156][157][158]. This has led to the choice of a Nb-target for the present measurements.

As Rb is an alkali metal the studies presented in this thesis required the surface ion source. Unavoidably, this also ionized other elements such as Ga ($I_p = 6.0$ eV) or Sr ($I_p = 5.7$ eV), although at a lower ionization efficiency. Most other elements such as Kr ($I_p = 14.0$ eV) were not surface ionized due to their higher ionization potentials. The resolving powers $R = m/\delta m$ needed to separate isobaric Ga and Sr from the Rb beam were beyond the capabilities of the ISAC mass separator (see Table 3.1). ^{74}Rb could be separated with $R \approx 4300$ from the isomeric and ground states of ^{74}Ga which did not much exceed the performance of the mass separator. It was possible to fine tune the magnets of the mass separator to a more favourable ratio between contaminant and beam of interest at the cost of a lower intensity of

Table 3.1: Contamination, mass excess m.e., required resolving power R, and results of yield measurements [159] previous to the TITAN beamtime Nov. 20-24, 2010.

A	element	m.e. [keV]	R to ^{A}Rb	Yield [1/s]		
				Nov. 7	Nov 12	Nov 20
78	Ga	-63706.0(1.9)	22492			
	Rb	-66936.2(7.5)		$2.1 \cdot 10^9$		$1.6 \cdot 10^8$
	^{m}Rb	-66825.1(7.5)	653445	$4.4 \cdot 10^9$		$2.2 \cdot 10^9$
	Sr	-63173.9(7.5)	19312			
76	Ga	-66296.6(2.0)	-12167			
	Rb	-60478.1(1.2)		$4.4 \cdot 10^7$		$2.3 \cdot 10^7$
	Sr	-54248(35)	11363			
75	Ga	-68464.6(2.4)	-6212	$4.6 \cdot 10^5$		$2.0 \cdot 10^5$
	Rb	-57218.7(1.6)		$2.1 \cdot 10^6$		$1.1 \cdot 10^6$
	Sr	-46619(220)	6591			
74	Ga	-68049.6(3.7)	-4273	$3.1 \cdot 10^5$	$4.5 \cdot 10^5$	
	^{m}Ga	-67989.6(3.7)	-4289	$1.2 \cdot 10^3$	$2.4 \cdot 10^3$	
	Rb	-51917.0(3.7)		$1.7 \cdot 10^4$	$1.2 \cdot 10^4$	$6.4 \cdot 10^3$
	Sr	mass unknown				

^{74}Rb (see Section 4.1). Table 3.1 also lists the measured yields previous to this measurement. Ga was the dominant nuclide at $A = 74$, and for $A = 75$ a beam contamination of ~ 15 % was found. The yields of heavier Ga isotopes were not measured this time. But beam intensities for Ga (see Figure 3.7) typically become smaller with every added neutron for masses larger than ≈ 70. The Ga isotopes found were on the neutron-rich side in respect to stable Ga, and higher masses represent isotopes further away from stability. Hence, ^{76}Ga (or ^{78}Ga) was not expected to be a significant contamination for ^{76}Rb (or ^{78}Rb). Sr yields were not determined directly. Simulations of in-target production [159] indicated that on the neutron-deficient side Sr was about one order of magnitude less abundant than Rb and was dropping down to more than 2 orders of magnitude for $A = 74$. This trend was consistent with older yield measurements for ^{79,81}Sr (Figure 3.7).

Hence, contamination was an important factor to consider for the mass measurements of ^{74,75}Rb. Since Ga was a dominant component in the $A = 74$ beam, fine tuning of the mass separator and isobaric cleaning with ion-trap techniques at TITAN was required (see Section 3.7.6). It is interesting to note that the beam intensities from this target decreased over time (see Table 3.1) indicating deterio-
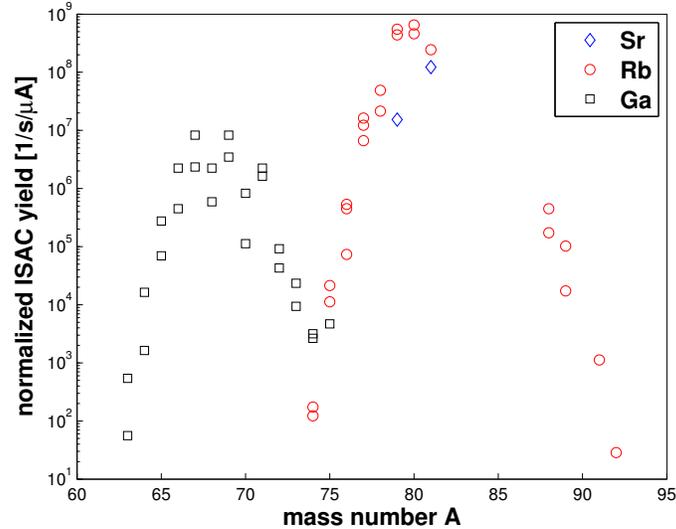
Figure 3.7: Measured yields of Ga, Rb, and Sr isotopes for three Nb-targets at ISAC. The yield is normalized to 1 μA proton beam. Data taken from [155].

ration due to irradiation. When ^{74}Rb was first delivered to TITAN its intensity had dropped by almost a factor of ≈ 2.5 in comparison to the target performance when it had been first irradiated by the proton beam.

3.3 TITAN's Radio-Frequency Quadrupole (RFQ) cooler and buncher

For the mass measurement, the ISAC beam with an energy up to 60 keV needs to be brought to quasi-rest and have a typical remaining kinetic energy of a few eV in the MPET. The formation of the radioactive beam introduces an energy spread of a few 10's of eV in the extraction process from the source as opposed to the measurement requirement of low energy spread. Moreover, ISAC delivers a continuous beam. Trap experiments on the contrary load the trap in pulsed beams, and usually no new particles are added during the measurement itself. To efficiently use the ISAC beam, it has to be accumulated and bunched.

All of these tasks are accomplished by a buffer gas filled RFQ cooler and buncher. Such devices are now widely used at radioactive beam facilities [5, 160, 161],

mostly for mass measurements of rare isotopes but increasingly also for collinear laser spectroscopy [16, 162, 163]. In order to stop the radioactive beam TITAN's RFQ [134, 135] is biased a few eV below beam energy. Care has to be taken during injection to match the acceptance of the RFQ to the emittance of the incoming beam. This is achieved by deceleration optics forming an electrostatic azimuthal quadrupole potential [134, 164]. This decelerates the ions in axial direction while maintaining the transverse emittance as the ions oscillate radially with a harmonic motion. TITAN's RFQ is designed for beam energies between 12 - 60 keV with a transverse emittance of up to 50 πmm mrad in $x - \theta_x$-space. The ions are cooled through collisions with a room-temperature buffer gas to thermal energies. Without additional forces, the ions could not be confined in an accumulation region during the collisional cooling process. Thus, the buffer gas cooling takes place in a linear Paul trap. A linear Paul trap is a 2D trap, hence without a longitudinal confinement as in a 3D hyperboloidal Paul trap [5]. In a linear Paul trap, the ions are trapped in longitudinal direction by an electrostatic potential (see Figure 3.8). It is applied by biasing 24 longitudinal segments at well defined DC voltages. The gradient is chosen to drag ions into the minimum of the potential. Since the Laplace equation does not have solutions with minima in all three dimensions for a source free volume, additional confinement is necessary. For this reason, the radial confinement is accomplished by a quadrupolar RF-field generated by four, pairwise connected longitudinally segmented rods. A cross-sectional view is given in Figure 3.9a and the respective electric potential in Figure 3.9b. The saddle of the quadrupole field results in a force on the ions towards the radial centre of the trap in one direction and outwards in the other direction. By switching the polarity of the applied voltage the ion can be confined radially when the combination of applied RF frequency, amplitude, and the ions' mass-to-charge ratio leads to stable trajectories in the trap. Radially, the ions follow along a harmonic macro-motion disturbed by a small micro-motion. The harmonic motion can be described by a so-called pseudo-potential [165] in comparison to the trap depth in a true harmonic potential. Traditionally, sinusoidal RF-fields are used in these devices. However, it can be shown [134] that a square wave driven RF field can increase the pseudo-potential by a factor of about 1.5. The square-wave drive is also referred to as digitally driven [166]. TITAN's RFQ operates with a square-wave RF with peak-to-peak amplitudes up to $V_{pp} = 400$ V in a frequency range of 0.2 to 1.4 MHz. Such a drive is a technical challenge for large capacitive loads as in the case of the TITAN RFQ with about 1500 pF. It is achieved by stacking fast switching, Metal-Oxide Semiconductor Field-Effect Transistors (MOSFET) in a push-pull configuration [134, 167]. The use of several MOSFETs reduces the power dissipation on each individual transistor. The RF is capacitively coupled to the individual electrodes (see Figure 3.9c) while the DC bias to create the longitudinal field gradient is delivered over a resis-
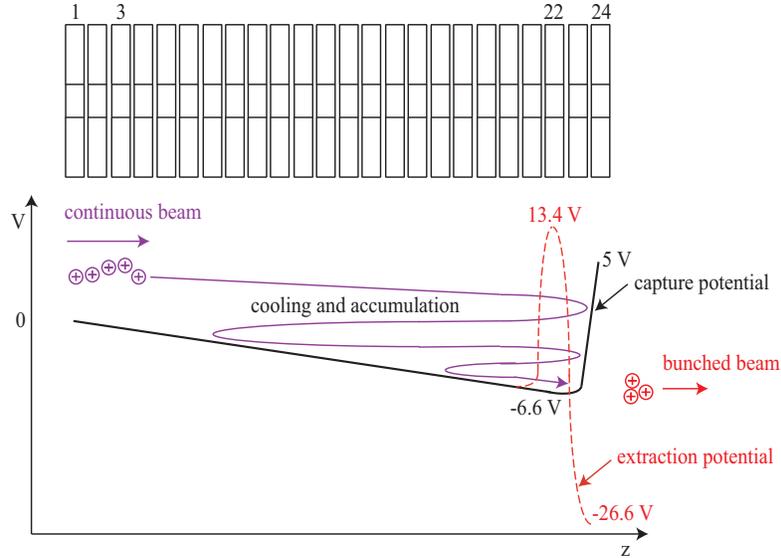
Figure 3.8: Top: Schematic of the longitudinal segmentation of TITAN's RFQ into 24 sections. The segment number is indicated at the top. Bottom: Schematic of the typically applied potential. The DC field drags the buffer gas cooled ions to the minimum of the trapping potential (solid line). The beam is extracted in ion bunches by switching the potentials of the electrodes 22 and 24 (dashed-line). Figure from [146].

.

tor which damps the RF to protect the DC power supplies.

An effective net buffer gas cooling in an RFQ takes place when the mass of the ion is larger than the coolant gas particles [165, 168]. In the presence of an RF-field for trapping, a drastic change in energy would disturb the ion's micro-motion significantly and bring the motion out of phase with the RF-field. Hence, if the mass of the coolant is larger than the ion's mass the energy of the ion is on average increased, an effect which is referred to as RF-heating [169]. In a buffer gas of lighter masses, little momentum is transferred per collision, and the disturbance of the micro-motion is less relevant. As a consequence the harmonic, macro-motion can be damped while keeping the micro-motion coherent to the external RF-field. The average, relative energy change per hard-sphere collision (Figure 3.10) follows [168]

$$< \epsilon >= \kappa \frac{1 - \kappa}{(1 + \kappa)^2} \tag{3.1}$$
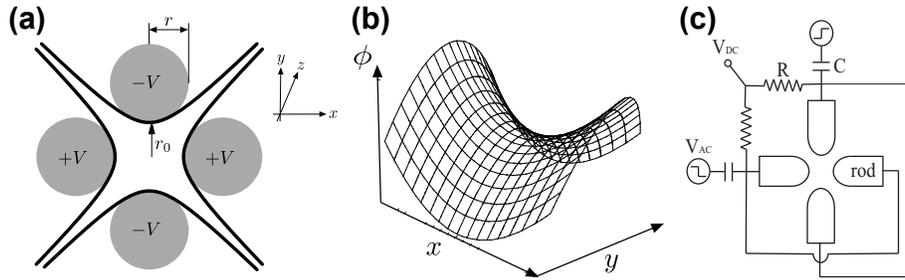
Figure 3.9: Schematic cross sectional view of electrode structure (a), which generates a radial quadrupole field (b). The polarity of the applied potentials in (a) is switched following a square-wave RF driver, which confines the ions radially. The coupling of the DC and RF components to the individual electrodes of a longitudinal segment is shown in (c). Figure (a) and (b) are from [134] and (c) from [146].
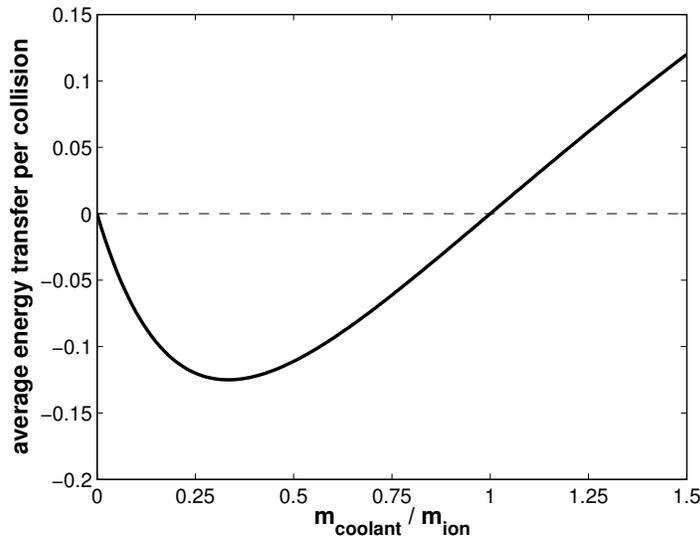
Figure 3.10: Average, relative energy change per hard-sphere collision between an ion trapped in an RFQ and a particle from the buffer gas [168].
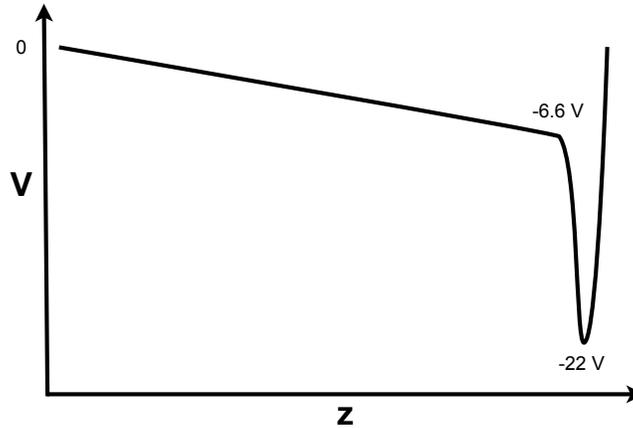
Figure 3.11: Schematic of RFQ DC potential during the neutron deficient Rb-mass measurements.

when $\kappa = m_{\mathrm{coolant}}/m_{\mathrm{ion}}$ is the mass ratio between coolant gas particle and ion. At TITAN, a He buffer gas is used at a pressure of order $\sim 1 \cdot 10^{-2}$ mbar. The choice of the buffer gas is also influenced by the charge exchange cross section as neutralized ions-of-interest are lost in this process by becoming neutral atoms. With the largest ionization energy, He is in this respect the optimal choice. However, due to resonant charge exchange reactions during radioactive He-isotope measurements, TITAN's RFQ can also be operated with H_2 as a buffer gas. Figure 3.10 suggests that a buffer gas of N_2 or Ne would have been even more favourable for $^{74-78}$Rb from a cooling kinematics point of view. He was used nevertheless as simulations of the TITAN RFQ [134, 135] showed that thermalization of the even heavier ^{133}Cs can be accomplished faster than typical accumulation times and suggested that the necessary condition for effective and efficient transport into the next unit of the TITAN system can be achieved.

Once the ions are thermalized in the RFQ, they can be extracted in an ion bunch from the RFQ by switching the segments neighbouring the minimum in potential (see Figure 3.8). In all segments for which the DC bias needs to be switched, the DC and RF-fields cannot be coupled to the electrode following Figure 3.9c. Such a setup would lead to a too long rise time when switching the DC voltage. Instead dedicated switch-boxes have been built at TRIUMF allowing the coupling of the RF-field as well as fast switching of the DC component. For mass measurements of singly charged ions the kicking strength of the extraction is typically $\Delta V = 20$ V around segment 23, the minimum of the trapping potential (Figure 3.8). A softer
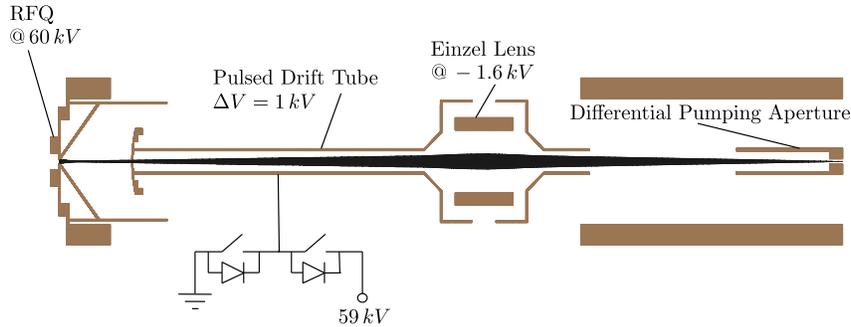
Figure 3.12: Extraction optics from the RFQ into a PLT which is floated to $U_{\mathrm{RFQ}} - \Delta V$. When the ion bunch is in the centre of the PLT it is switched to ground without affecting the ion bunch. The SCI leave the PLT with a kinetic energy of $e \cdot \Delta V$. Figure from [134].

kick would result in a smaller energy spread, but an increased pulse-width in time. Both effects are relevant for the trapping and mass measurement at MPET. For optimal performance for SCI, the pulse-width is artificially shortened to 300 - 1000 ns. This is achieved by only accepting a certain fraction of the phase space and eliminating ions in the low energy tail of the ion bunch. As a consequence, this reduces the overall measurement efficiency. For measurement of HCI, energy spread and pulse width are influenced mainly by the charge breeding process in the EBIT. In this work, the kicking strength was $\Delta V = 100$ V to achieve a smaller pulse width which allowed efficient trapping of the ion bunch in the EBIT. An additional modification of the RFQ DC settings was done by lowering the minimum of the potential (see Figure 3.11). This was motivated firstly by simulations of TITAN's RFQ [170] which showed good performance for this potential shape for heavier masses such as ^{133}Cs. Secondly, it allowed larger storage of ions at the segment with the potential minimum. Though it did not make a difference for measurements carried out with lower beam intensities such as ^{74}Rb, more ions per bunch simplified the setup of the ^{74}Rb measurement which was done with ^{85}Rb from TITAN's own ion source. Particularly to find a tuneable signal for injection, charge breeding, and extraction from the EBIT, large beam intensities were helpful.

3.3.1 A Pulsed Drift Tube (PLT) after the RFQ cooler and buncher

The kinetic energy of bunched beams along the TITAN beam lines connecting RFQ, EBIT, and MPET ranges between 1-2 keV. At these energies, electrostatic beam optics with moderate requirements on power supplies can be used (a few 100 V for
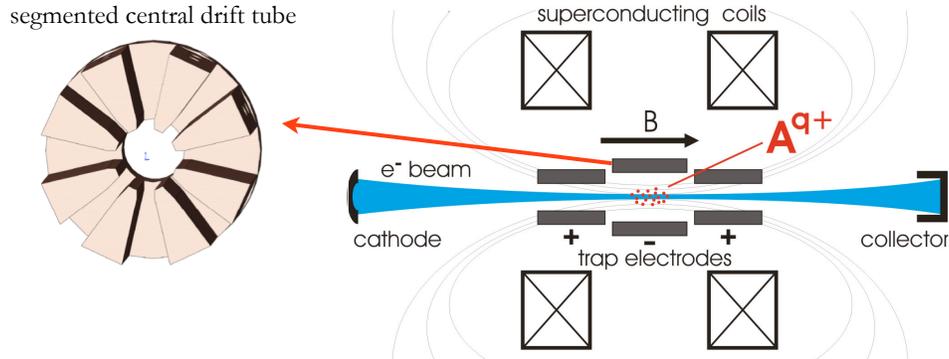
Figure 3.13: Right: Schematic of an EBIT with a magnetic field formed by Helmholtz coils. The ions are trapped in axial direction by an electrostatic field. Left: A cross sectional view of the central trapping electrode. It is segmented which provides direct visual access to the trapped HCI and allows monitoring of the charge breeding process. Moreover, the segmentation can be used for RF- cleaning (see Section 3.7.6).

steering and <5 keV for focusing). The beam can be brought to rest by floating a trap potential just below the beam energy. Ions in the RFQ are trapped, but at an electrostatic potential U_{RFQ} of a few 10 kV which is adjusted to stop the incoming ISAC beam. A Pulsed Drift Tube (PLT) is used as an 'elevator' to lower the ion bunch to ground potential [161]. As shown in Figure 3.12, the ion bunch is accelerated towards the PLT after extraction from the RFQ. The PLT is initially biased to $U_{\mathrm{RFQ}} - \Delta V$. When the ions reach the centre of the PLT it is switched quickly to ground potential. Due to the length and the injection hole of the PLT, the shape of the potential within the PLT itself is not affected by the fast switching, hence, avoiding any extra accelerating force on the ions. The ion bunch leaves the PLT while on ground potential with a kinetic energy of $e \cdot \Delta V$. In the presented measurements, ΔV was set to about 2 kV. Recent investigations of the setup of the PLT are summarized in Section A.1.

3.4 The electron beam ion trap for charge breeding of radioactive ions

The main function of the EBIT is to convert singly charged ions into multiple or Highly Charged Ions (HCI). The short half-lives and limited yield of radioactive
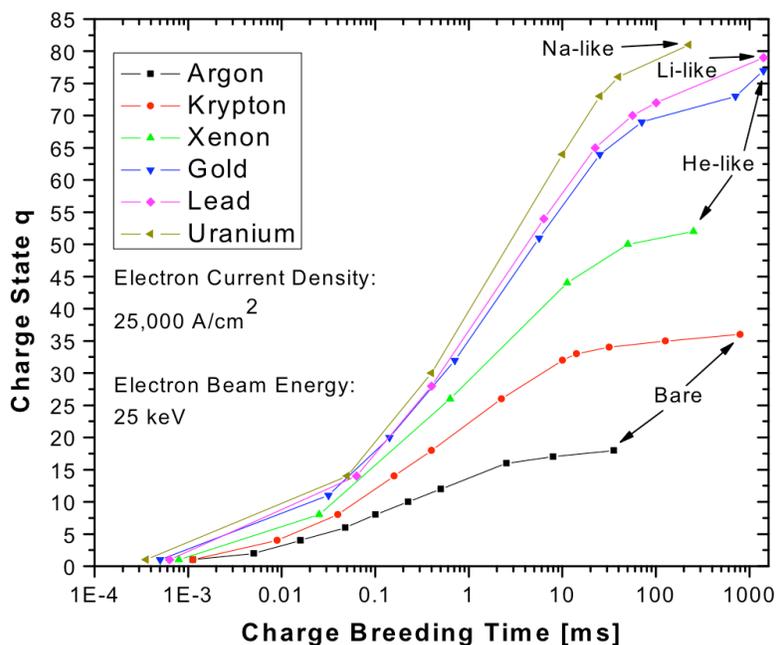
Figure 3.14: Simulation of breeding times in the TITAN EBIT to reach a certain charge state for various elements. Simulation and figure from [171].

nuclides requires the charge breeding process to be fast and efficient. Moreover, a charge state breeding process is desired which maintains a clean environment. Charge states of $q \approx 10 - 20+$ should be attainable in less than half of the nuclide's half-life while maintaining an overall breeding efficiency of a few percent. In an EBIT (see Figure 3.13), ions are trapped axially by an electrostatic potential applied to an EBIT's drift tube. The confinement in the radial direction is achieved by an intense electron beam and a strong magnetic field. Higher charge states are produced by electron impact ionization of the ions with the electron beam.

The TITAN EBIT [2, 136, 171] was designed and built in collaboration with the Max-Planck-Institut for Nuclear Physics (MPI-K) in Heidelberg and brought to TRIUMF in 2006. It is designed to operate with electron beam energies and currents of up to ~ 70 keV with 500 mA (and later 5 A), of which 400 mA at ~ 7 keV and 25 keV at 200 mA have been demonstrated experimentally [2]. In a magnetic field strength of 6 T the 70 keV, 500 mA electron beam is compressed to a density of 30,000A/cm^2. Simulations of the charge breeding in the TITAN EBIT [171]
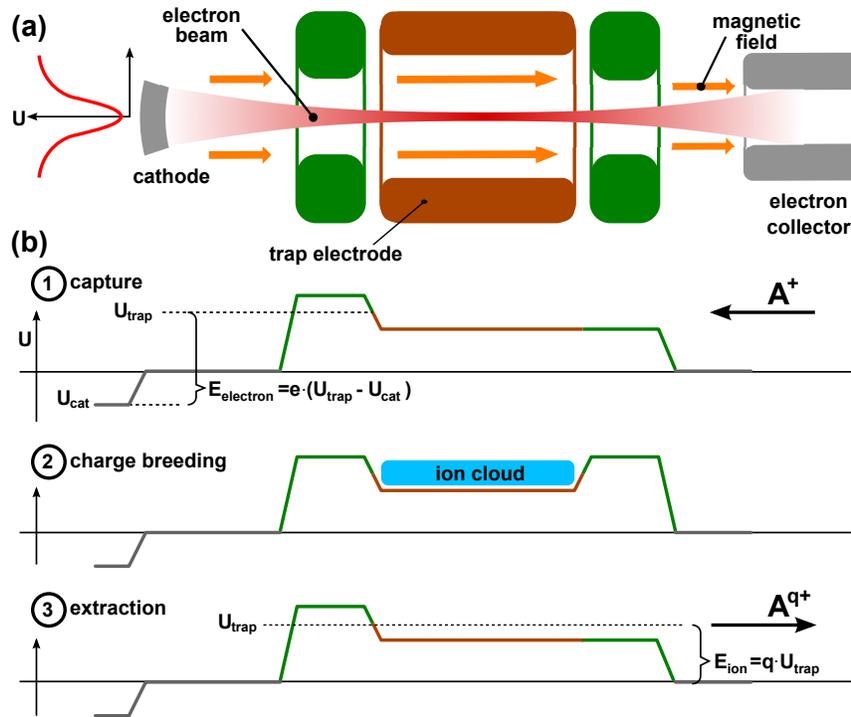
Figure 3.15: Schematic of the EBIT (a) and the injection, charge breeding, and extraction potentials (b).

confirm the rapid charge breeding process (Figure 3.14). In particular, high charge states of $q = 20+$ and more can be reached within tens of milliseconds which is hence compatible even for short-lived nuclides such as ^{74}Rb.

At TITAN, the ion bunch of SCI from the RFQ is injected into the EBIT where it is decelerated by floating the central drift tube to a potential U_trap slightly below the transfer beam energy (compare with Figure 3.15). The ion bunch is dynamically captured by switching the neighbouring drift tube to a higher potential which establishes the axial trapping potential. The electron beam energy is defined by the difference between U_trap and the bias voltage of the cathode of the electron gun U_cat, $E = e(U_\mathrm{trap} - U_\mathrm{cat})$. The charge breeding time is set by the time the ions are kept in the EBIT. Typical breeding times used so far range from 20 ms to 200 ms depending on half-life of the nuclide and desired charge state. Once this charge state is maximized in the abundance distribution, the beam is extracted from the same side of the EBIT as it had been injected (see Figure 3.15). Due to the higher charge state the total kinetic energy of the HCI is increased to $E_\mathrm{ion} = q \cdot U_\mathrm{trap}$ after

extraction. In our operation, the electron beam is continuously on, even during injection and extraction of the ion bunches.

The first charge breeding of radioactive beam for a mass measurement was achieved in fall 2009. ^{44}K^{1+} beam from ISAC was enhanced to a charge state $q = 4+$ in the EBIT, and its mass was determined in the MPET [1, 2]. This was done with a small electron beam current of less than 1 mA by only warming up the cathode but not applying any bias. The electron beam energy was ≈ 2 keV. Due to this low electron beam current 200 ms of breeding time were necessary to reach a sufficiently large $q = 4+$ abundance to perform a mass measurement. A Time-Of-Flight (TOF) spectrum of ion bunches extracted from the EBIT is displayed in Figure 3.16. Peaks at the charge states $q = 2-5+$ were readily distinguishable from charge bred residual gas. However, residual gas is always present in the EBIT despite the good vacuum conditions achieved by operating the trap's drift tube at 4 Kelvin. The long half-life of 22 min and the high ISAC yields of more than 10^7 ions / s for ^{44}K were favourable for this proof-of-principle measurement. In an attempt to perform a mass measurement with the ground state of the superallowed β emitter ^{38m}K during the same beamtime with ISAC yields of $\sim 10^5$ ions per second, no signs of charge bred ^{38}K extracted from the EBIT could be observed. Hence, despite the success it was concluded that significant improvements in breeding time, electron beam current, and efficiency would have to be accomplished in preparation for the first physics-motivated measurement, which should also be carried out in a higher charge state. Hence, for the radioactive beam measurement of neutron-deficient Rb isotopes in November 2010 the EBIT was operated with a beam current of 10 mA. The optimization of the charge breeding time is discussed in the next section.

3.4.1 Charge breeding time of Rb isotopes

The optimal charge breeding time for the Rb measurements was determined with stable ^{85}Rb, however, taking into account that the total breeding time should not exceed about a half of the half-life of ^{74}Rb (65 ms). For the purpose of charge breeding, isotopic differences were negligible, and it was considered to be identical to the radioactive Rb regarding the cross sections of electron impact ionization.

The relative abundances of the charge states were measured via TOF to a Multi Channel Plate (MCP), and the results are displayed in Figure 3.17. Two trends were apparent. First, with longer breeding time higher charge states were favoured over lower. Second, the higher the charge state the smaller was the maximum in abundance. The latter was due to the fact that more charge states were reached, and the total number of ions was spread over a wider range of charge states. In Figure 3.17, a plateau for $q = 8+$ was reached at ≈ 20 ms. For the measurement of ^{74}Rb in the same charge state, the ions were hence kept for 23 ms in the EBIT
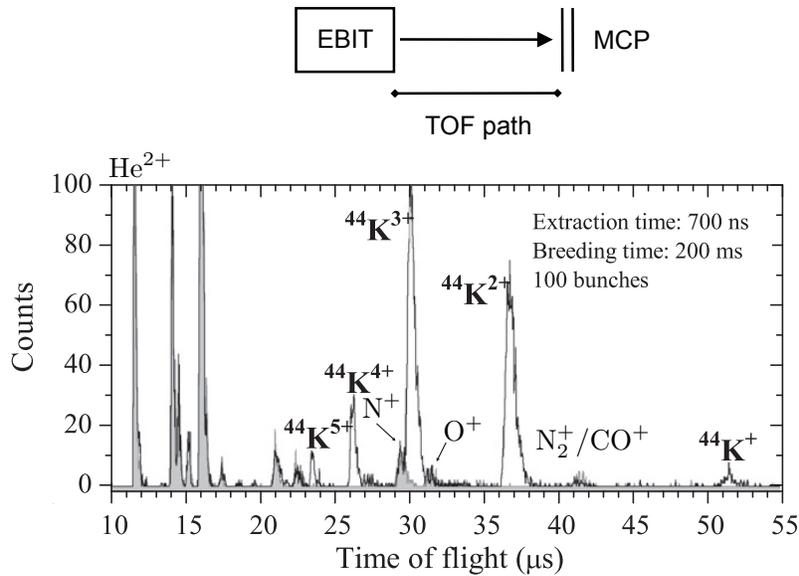
Figure 3.16: A Time-Of-Flight (TOF) spectrum of ions extracted from the EBIT. For the shaded distribution no ^{44}K$^+$ ions were injected into the EBIT. These TOF peaks correspond to charge-bred residual gas from the EBIT. Figure on the bottom modified from [2].

for charge breeding. In the cases of ^{75,76}Rb the breeding time was 35 ms for which $q = 9+$ was the most populated charge state. A TOF spectrum of charge bred ^{75}Rb is presented in Figure 3.18. Hints of $q = 12+$ ions can be seen in this spectrum. This charge state was used for a mass measurement of ^{76}Rb.

In future studies, it will be interesting to compare measurements of the charge breeding time with simulations such as the one in Figure 3.14. For the current measurement this was not possible as the breeding conditions (e.g. electron beam radius or overlap of the electron beam with the trapped ions) were, due to the time constraint of the online beamtime, not fully determined.

3.5 Beam transport

After cooling and bunching in the RFQ and charge breeding in the EBIT, the ions are delivered to the MPET. An illustration of the TITAN beamline is shown in Figure 3.19 which provides details about beam optics and diagnostic elements. However, minor components are omitted for clarity of the figure. The entire set of beam
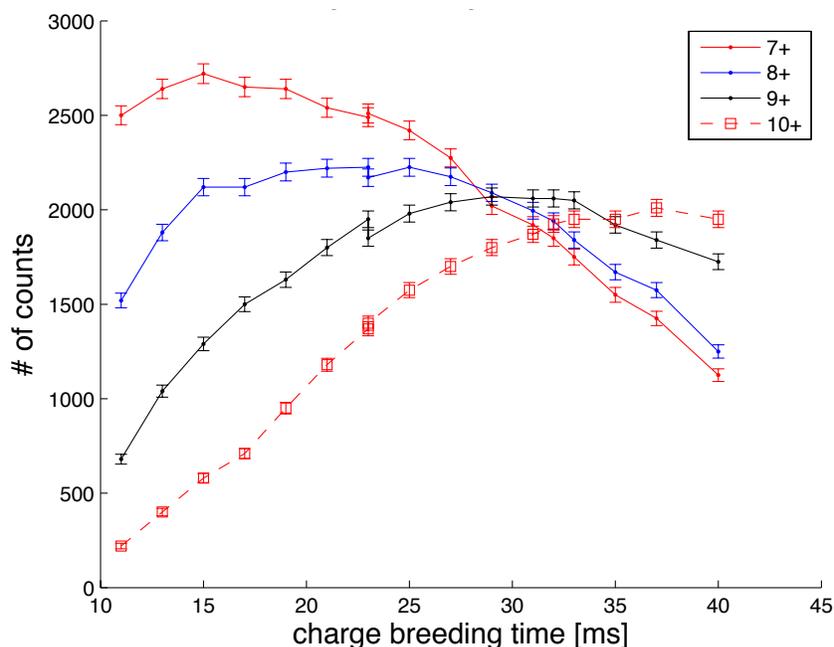
Figure 3.17: Measured number of ions of ^{85}Rb in various charge states for different charge breeding times in the EBIT with a 2.5 keV and 10 mA electron beam. The plotted number of counts for each breeding time is the sum of 200 extractions from the EBIT.

optics at TITAN is electrostatic. Here only those elements and devices are discussed which were relevant for the measurement.

After the ions were extracted from the RFQ, the PLT (Section 3.3.1) allowed for a adjustment of the kinetic energy to 2 keV. The ion bunch was transferred through a series of benders into the EBIT, where the charge breeding took place. A detailed description of the beam optimization for injection, trapping, and extraction in the EBIT is presented in Section A.3. A series of retractable MCP detectors were installed at critical positions along the beamline for beam diagnostics and were used for beam transport optimization. Three of them (MCP1, MCP3, and MCP4) were further equipped with phosphor screens which provided a visualization of the beam spot impinging upon the MCP. A more comprehensive explanation of the beam transport system and optics can be found in Section A.2.

After charge breeding in the EBIT, a bunch of the HCI was extracted from the EBIT and was bent by 90° into the MPET beamline. There, MCP0 was utilized for beam
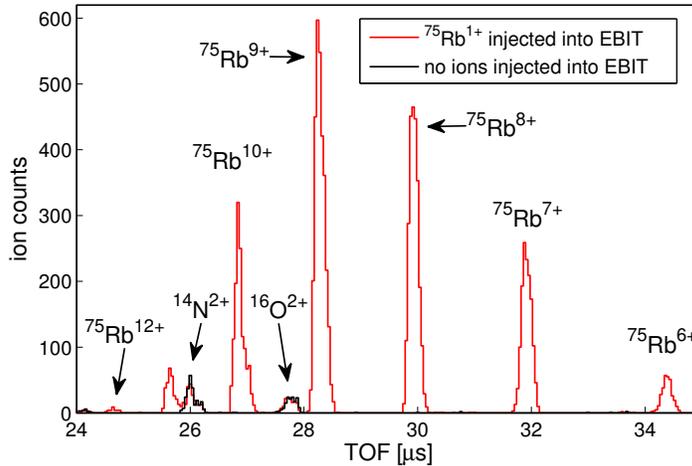
Figure 3.18: TOF spectrum of 500 ion bunches of radioactive ^{75}Rb extracted from the EBIT with an 800 ns extraction pulse after 35 ms of charge breeding with a 10 mA, 2.5 keV electron beam. ^{16}O^{2+} and ^{14}N^{2+} were due to ionized and further charge-bred residual gas in the EBIT.

optimization. MCP0 was operated in a single-ion counting mode by coupling the MCP's anode signal via a preamplifier to a Multi Channel Scaler (MCS). TOF spectra analogous to Figure 3.16 and Figure 3.18 were recorded. When the count-rate of ions in the TOF peak of interest was too high and led to signal pile-up, the beam intensity of ions sent into the RFQ was reduced. Through the single-ion-counting mode, different beam transport and EBIT settings could be compared quantitatively. An optimization software was developed to scan individual beamline parameters and to record the number of counts for specific peaks in the TOF spectrum in each setting. By maximizing the counts in the TOF peak associated with the desired charge state, this greatly improved the overall beam transfer efficiency and EBIT performance.

The resolving power of the TOF depended on the energy spread and the spatial extent of the ions in the EBIT. The distance between the two end caps in the EBIT is approximately 77 mm. If the trap were fully emptied, then the TOF peaks would have been smeared out entirely in the TOF spectrum. As the resolving of different m/q was essential for the mass measurement (see Section 3.6), the EBIT was only opened with an extraction pulse of a few hundred nanoseconds. The remaining HCI were dumped onto the beampipe a few milliseconds after the initial ion ex-
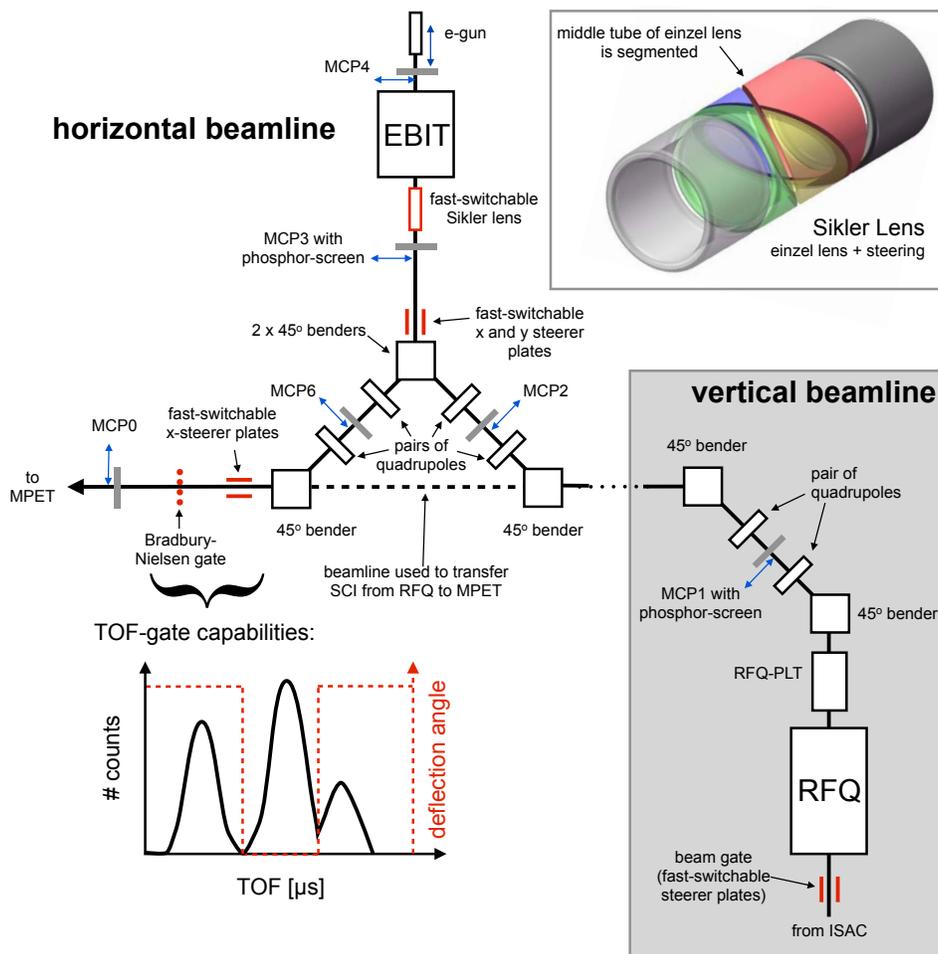
Figure 3.19: Layout of the TITAN transport beamline from the RFQ cooler and buncher to the EBIT and finally to the MPET. Only the elements which are mentioned in the text are displayed while omitting other einzel lenses and steerers. Elements displayed in red are controlled by fast HV switches. Devices with blue double arrows are retractable. The insert at the top right shows a schematic of a so-called Sikler lens. Figure of the Sikler lens taken from [172].

traction. Although this implied a significant reduction in efficiency, accumulation of short-lived nuclides in the EBIT was limited by the half-life. More importantly, ionized and further charge bred residual gas could have filled the trap hindering the injection and storage of new SCI. The trap was hence left open after emptying the EBIT of remaining HCI until the arrival of the new ion bunch.

3.6 A/q selection

The mass measurement in a Penning trap by the technique applied at TITAN (see Section 3.7.3) is ideally performed with ions of only one ion species in the trap at a time. Other contaminant ions reduce the measurement signal and might lead to a disturbance of the measurement result. Ions with different ratios of mass number A to charge state q differ in their TOF (see Figure 3.16). They can be rejected by a gate which only lets ions with a certain A/q pass.

In the past, this TOF gate was implemented by switching the applied voltage on one element of a steerer plate assembly which is located right after the switchyard (see Figure 3.19). The steerer assembly deflected the beam into the beam pipe except at a specified time, when the beam was directed along the beamline. The minimum gate width of the setup was $\sim 1.2\,\mu$s, which was in most cases sufficient to separate different mass numbers for singly charged ions. For example, this method was used in the mass measurement of ^{6}Li [124] to separate the two stable Li-isotopes with $A = 6$ and 7, which both were simultaneously injected into the RFQ from TITAN's surface ion source. With the capability of HCI, the spacing in TOF over a similar TOF distance was much tighter. Additionally, the EBIT produced background in the form of charge bred residual gas. For instance, ^{44}K^{3+}, N$^+$, and O$^+$ in Figure 3.16 were all within a window of 3 μs in TOF. Selecting a clean ion bunch of ^{44}K^{3+} would be impossible with a gate width of 1.2 μs. Therefore, a better TOF gate was necessary.

An investigation of the limiting factors of this TOF gate highlighted three shortcomings, an overly long cable between HV switch and steerer plate, strong voltage oscillation after the fast HV switch itself, and a large capacitance of ~ 70 pF. The first two issues were addressed by a reduced cable length and a new HV switch designed and built at TRIUMF. To reduce the capacitance for a TOF gate, a Bradbury Nielsen ion Gate (BNG) [173] was designed and tested [174] in a collaboration with the Enriched Xenon Observatory (EXO) [175] group at Stanford and TITAN.

Instead of deflector plates, a BNG consists of small, parallel wires arranged in a plane which is perpendicular to the propagation of the ions (see Figure 3.20). Every second wire is biased at the same voltage. If both sets of wires are at the same potential (normally on the beamline ground) the ion bunch can pass through the gate. However, any potential difference leads to a steering force and deflects the
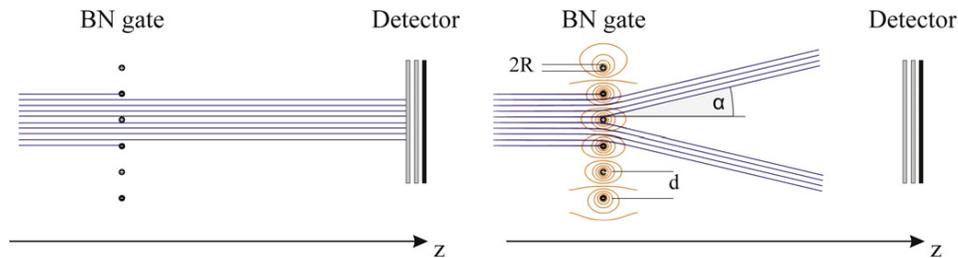
Figure 3.20: Concept of a Bradbury Nielsen ion Gate (BNG). The ion beam is passing through a set of wires perpendicular to the direction of the ion propagation. The wires are arranged in pairs such that to every second wire the same potential is applied. When both sets of wires are at the same potential (normally on beamline ground) the ions will pass the gate (figure on the left). A potential difference between the two wire sets, however, deflects the beam (figure on the right). Figures from [174].
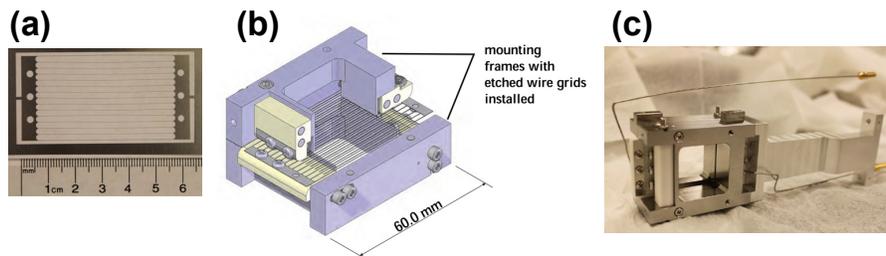
Figure 3.21: New design of BNG based on chemically etched wires. The etched wires (a), the schematic of the BNG (b), and the fully assembled BNG (c) are shown. Figures from [174].

beam. Hence, such a setup can be used as a TOF gate. The main advantage of a BNG over deflection plates is its reduced capacitance and hence faster switching time. Narrower TOF gates can be realized. Additionally, when the potentials on the wire pairs are equal but of opposite polarity, the field alterations due to the BNG are minimal and only extend spatially over lengths comparable to the wire spacing. So, the ions which pass the BNG first after the gate is opened are less influenced than in the case of deflector plates. As a drawback the transmission of an open BNG is not unity because of the physical barrier the wires themselves represent. The newly designed BNG [174] represents an advancement in the manufacturing

of such a gate. In previous designs the wires were stretched over a frame which is difficult to assemble and requires significant effort when changing to a different wire spacing. These complications are overcome by chemically etched wires to be used in the new BNG [174] as shown in Figure 3.21. A wire set is pictured in (a), two of which are individually mounted on its frame (b) to form the BNG wire structure.

The fully assembled BNG in (c) was inserted into the TITAN beamline downstream of the steerer plate assembly which had been used at the TOF gate in the past (see Figure 3.19). Its capacitance was ~ 20 pF, and the bias voltages of the full setup could be switched such that a 50 ns pulse width could be achieved. Typical widths of TOF peaks were much longer than 50 ns. Thus, the BNG performance was well suited for the purpose of a TOF gate. During the presented measurements, the TOF gate was opened between 300-500 ns to let the Rb charge state of choice pass the gate. For the wire sets in place, wires with a diameter of 51 μm were spaced 2.2 mm apart. This resulted in an approximate beam transmission of 95%. In this configuration, the advantages offered by the BNG outweighed the losses in efficiency.

3.7 The measurement Penning trap

3.7.1 Motion of charged particles in a Penning trap

In a homogeneous magnetic field B, the Lorentz force $\vec{F} = Q \cdot \vec{v} \times \vec{B}$ directs a charged particle of charge $Q = q \cdot e$ in a circular motion.[1] The angular frequency of this motion, called the cyclotron frequency, is

$$\omega_c = \frac{QB}{m}. \tag{3.2}$$

It is linear inversely proportional to the mass, the quantity of interest, but independent of the radius of the circular motion ρ. Considering an ion of charge state q, mass number A, and of radial energy $E_\rho = 1$ eV, the radius ρ is according to $E_\rho = m\omega_c^2 \cdot \rho^2/2$

$$\rho \approx 1.4 \cdot 10^{-4} \frac{\sqrt{A}}{q \cdot B[\text{T}]} \quad \text{m}. \tag{3.3}$$

Hence, even the heaviest atomic ions with $A^{q+} > 250^{1+}$ could be confined with a magnetic field strength of 2 T to $\rho \approx 1$ mm. However, such a magnetic field does not restrict the ion motion along the field direction. If the axial motion contributes

---

[1] If not otherwise stated, the description of the ion motion in Penning traps follows the references [5, 165, 176–178]
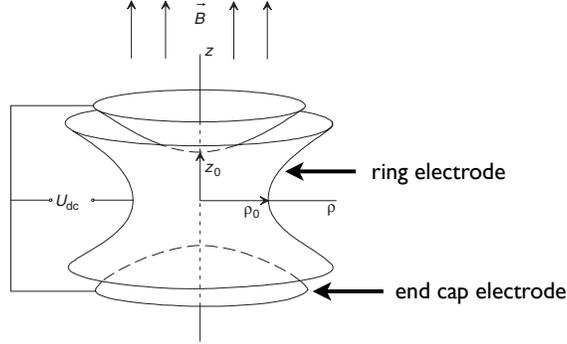
Figure 3.22: Schematics of a Penning trap. The hyperbolic shape of the electrodes generates the electrostatic quadrupole potential of Equation 3.4. Figure modified from [5].

to the energy with 1 eV, the axial velocity of $v_a \approx 1.4/\sqrt{A} \cdot 10^4$ m/s would move the ion very rapidly out of a measurement region. To trap the ion along the magnetic field axis, a weak electrostatic field is superimposed to form a Penning trap. For simplicity, this electrostatic potential is usually chosen to follow a quadrupole form,

$$V(\rho, z) = \frac{U}{2d_0^2}\left(z^2 - \frac{1}{2}\rho^2\right). \tag{3.4}$$

In the cylindrical symmetry, ρ is the radial coordinate, $\rho^2 = x^2 + y^2$. The homogeneous magnetic field shall be taken along the z-direction. The potential of a quadrupole field has been illustrated already in Figure 3.9. An accurate formation of such a potential can be realized for instance by shaping electrodes along equipotential surfaces. These are, according to Equation 3.4, two hyperboloids of revolutions (see Figure 3.22). The potential difference between the one-sheeted hyperboloid (the ring electrode) and the two-sheeted one (the two end caps) is given as

$$\Delta V = V(\rho = 0, z = z_0) - V(\rho = \rho_0, z = 0) = \frac{U}{2d_0^2}\left(z_0^2 + \frac{1}{2}\rho_0^2\right). \tag{3.5}$$

The characteristic trap dimension d_0 is defined by

$$d_0^2 = \frac{1}{2}\left(z_0^2 + \frac{1}{2}\rho_0^2\right) \tag{3.6}$$

98

such that the potential difference between the end caps and the ring electrode equals U. The classical equations of motion of a charged particle in the trap are

$$
\begin{aligned}
\ddot{x} &= \omega_c \dot{y} + \frac{1}{2}\omega_z^2 x \\
\ddot{y} &= -\omega_c \dot{x} + \frac{1}{2}\omega_z^2 y \\
\ddot{z} &= -\omega_z^2 z
\end{aligned}
\tag{3.7}
$$

of which the axial motion is completely decoupled from the radial motion and follows a harmonic motion with a frequency

$$
\omega_z = \sqrt{\frac{Q \cdot U}{m d_0^2}}.
\tag{3.8}
$$

Thus, $Q \cdot U > 0$ must hold to form a confining force in axial direction. The radial equations are most easily solved by combining the two coordinates x and y to the complex $u = x + iy$, which transforms the two coupled real differential equations into one complex,

$$
\ddot{u} = -i\omega_c \dot{u} + \frac{1}{2}\omega_z^2 u.
\tag{3.9}
$$

Its general solution $u = A^+ \exp(-i\omega_+ t) + A^- \exp(-i\omega_- t)$ is governed by the two angular eigenfrequencies[2]

$$
\omega_\pm = \frac{\omega_c}{2} \pm \sqrt{\frac{\omega_c^2}{4} - \frac{\omega_z^2}{2}}.
\tag{3.10}
$$

The angular frequencies are tied to each other by the following relationships.

$$
\begin{aligned}
\omega_c &= \omega_+ + \omega_- \\
\omega_c^2 &= \omega_+^2 + \omega_-^2 + \omega_z^2 \\
2\omega_+ \omega_- &= \omega_z^2.
\end{aligned}
\tag{3.11}
$$

For $\omega_c < \sqrt{2} \cdot \omega_z$, $\omega_\pm$ becomes complex which implies a real exponent in the exponential in u. Hence, the ion would not be confined radially. This condition for

---

[2]Angular (ω_x) and ordinary frequencies $\nu_x = \omega_x/(2\pi)$ are often interchanged in the following text. While formal treatments are more conveniently expressed by ω_x, the ordinary frequencies ν_x are preferred from an experimental viewpoint.

ion trapping translates to

$$\frac{|U[\mathrm{V}]|}{B[\mathrm{T}]} \lesssim 10^2 \cdot \frac{|q|}{A} \cdot (d_0[\mathrm{mm}])^2. \tag{3.12}$$

A confinement even within 1 mm^3 can be accomplished when employing a strong magnetic field in combination with a weak electrostatic potential. At the limit of the trapping condition, the two radial eigenfrequencies are identical, $\omega_+ = \omega_-$. Penning traps are usually operated well below this limit ($\omega_c \gg \sqrt{2} \cdot \omega_z$) to establish a hierarchy in all three eigenfrequencies

$$\omega_+ \gg \omega_z \gg \omega_-. \tag{3.13}$$

A Taylor expansion of Equation 3.10 under this condition allows the radial eigenfrequencies to be expressed as

$$\begin{aligned} \omega_+ &\approx \omega_c - \frac{\omega_z^2}{2\omega_c} \\ \omega_- &\approx \frac{\omega_z^2}{2\omega_c}. \end{aligned} \tag{3.14}$$

Because of these relationships, ω_+ is known as the reduced cyclotron frequency. Due to the influence of the superimposed electrostatic quadrupole field, the cyclotron motion in the magnetic field is slightly reduced in its angular frequency from ω_c in a pure magnetic field to ω_+ in the Penning trap. The radial eigenmotion at ω_- is best understood by considering a drift velocity $\vec{v}_d = \vec{E} \times \vec{B}/B^2$. Because of the cross product with $\vec{B}$, it is a radial vector but depends on the radial position $\vec{\rho}$. For a charged particle at velocity $\vec{v}_d$ in the Penning trap, the force in radial direction would vanish because $\vec{F} = Q \cdot (\vec{E} + \vec{v}_d \times \vec{B}) = QE_z\hat{z}$. Here, $\hat{z}$ is the unit vector along the z-axis. Analogously to the principle of a Wien velocity filter, the charged particle is unaffected by the electric and magnetic fields and the drift velocity $\vec{v}_d$ is unchanged. When we look more closely at $\vec{v}_d$

$$\vec{v}_d = \frac{\vec{E} \times \vec{B}}{B^2} = \frac{\omega_z^2}{2\omega_c}\vec{\rho} \times \hat{z} \approx \omega_-\vec{\rho} \times \hat{z}, \tag{3.15}$$

$\vec{v}_d$ can be identified as the velocity vector of the radial motion characterized by ω_-. Hence, its associated motion can be seen as an $E \times B$ drift motion. Again in analogy to the velocity filter, which works irrespective of the charged particle's
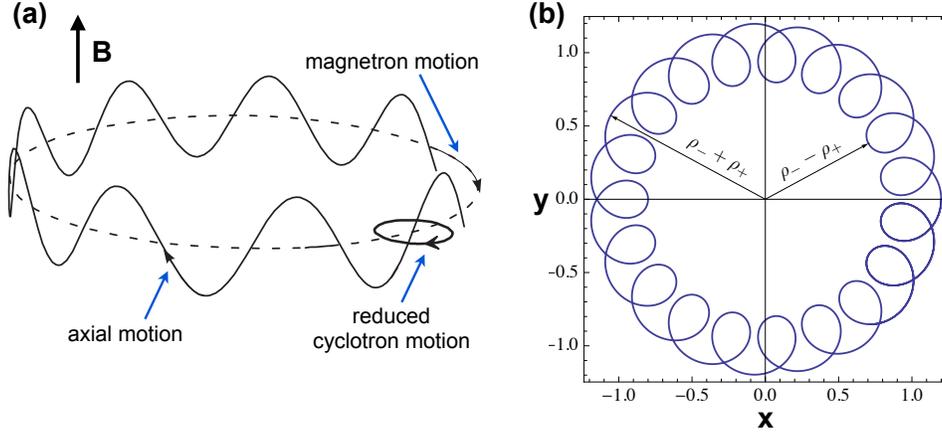
Figure 3.23: Schematics of the motion of a positively charged particle in a
Penning trap. The motion consists of three harmonic eigenmotions,
one in the axial direction with an angular frequency ω_z and two in
the radial directions with frequencies $\omega_\pm$. While (a) is an illustration
of the three dimensional motion, (b) is its projection onto the radial
plane. See text for details. Figures are modified from [131] and [146].

mass or charge, ω_- is (approximately) independent of m/q,

$$\omega_- \approx \frac{\omega_z^2}{2\omega_c} = \frac{U}{d_0^2 B}. \tag{3.16}$$

Strictly speaking, all of this is only true at one specific position $\vec{\rho}$ since $\vec{v}_d$ is a
function of $\vec{\rho}$. Hence, there has to be a non-vanishing time derivative on $\vec{v}_d$ in the
radial direction once the particle leaves the specific $\vec{\rho}$, where the statement of a
vanishing radial force is exact. The reason why it is a good approximation is due to
the fact that ω_- is small, and its associated radial eigenmotion known as magnetron
motion is slow.
The general motion in a Penning trap can be described as the combination of the
three eignmotions. An example of a trajectory of a positively charged particle is
shown in Figure 3.23. The total energy of the charged particle in the trap is

$$E = E_{\text{kin}} + E_{\text{pot}} = \frac{1}{2}mz_{\text{max}}^2 + m(\omega_+ - \omega_-) \cdot (\rho_+^2\omega_+ - \rho_-^2\omega_-) \tag{3.17}$$

101

where z_{max} and $\rho_{\pm}$ are the amplitudes and radii of each eigenmotion. The radial contributions to the total energy are

$$
\begin{aligned}
E_{\rho,\mathrm{kin}} &= \frac{1}{2}mv_{\rho}^2 = \frac{1}{2}m\left[\rho_+^2\omega_+^2 + \rho_-^2\omega_-^2 + 2\rho_+\rho_-\cos\left((\omega_+ - \omega_-)t + \phi_+ - \phi_-\right)\right] \\
E_{\rho,\mathrm{pot}} &= QV = -\frac{1}{4}m\omega_z^2\left[\rho_+^2 + \rho_-^2 + 2\rho_+\rho_-\cos\left((\omega_+ - \omega_-)t + \phi_+ - \phi_-\right)\right].
\end{aligned}
$$
(3.18)

Owing to the hierarchy of the involved frequencies ($\omega_+ \gg \omega_z \gg \omega_-$) the kinetic term associated with the reduced cyclotron motion dominates over the potential part. For the magnetron motion the opposite is true. The radial potential of the quadrupole field is negative. Hence, the larger the magnetron radius ρ_- the smaller its energy. The magnetron motion is strictly speaking unstable. While any dissipative energy loss damping the axial or reduced cyclotron motion forces the ions closer to the trap centre, a lower energy for the magnetron motion pushes the ions to larger and larger radii until the ions are lost from the trap, i.e. hit an electrode. The damping times in UHV are much longer than the ions are trapped for these experiments and, thus, the instability of the magnetron motion is irrelevant for any of the mass measurements at TITAN. Of key importance for the mass measurement technique employed at TITAN is that the energy of a cyclotron motion with radius $\rho_+ = \rho_0$ is significantly larger than a magnetron motion with the same radius $\rho_- = \rho_0$.

Quantum mechanical description

The motion of a charged particle in a Penning trap can be quantized [176, 178] by formulating the Hamiltonian in canonical coordinates and momenta and replacing the classical Poisson brackets by the quantum-mechanical commutator relations. The Hamiltonian can be expressed by means of annihilation and creation operators or equivalently by the number operator $\hat{n} = a^+a$ for the three eigenmotions.

$$
H = \hbar\omega_z(\hat{n}_z + \frac{1}{2}) + \hbar\omega_+(\hat{n}_+ + \frac{1}{2}) - \hbar\omega_-(\hat{n}_- + \frac{1}{2})
$$
(3.19)

Among these three harmonic oscillators, the magnetron motion is inverted, i.e. the larger the quantum number n_- the smaller the energy. This is reflected in the previous discussion for the classical magnetron motion of lower energy for larger magnetron radii. TITAN's MPET is at room temperature. Assuming that the ions were in thermal equilibrium with their surrounding, their energy would be $E = k_BT \approx 25$ meV. Since ω_+ is the largest of the three eigenfrequencies, we

expect the reduced cyclotron motion to be in quantum states

$$n_+ \approx \frac{E}{\hbar\omega_+} > \frac{E}{\hbar\omega_c} \approx \frac{A}{q \cdot B[\mathrm{T}]} \cdot 6 \cdot 10^4. \qquad (3.20)$$

The typical energy spread of ions extracted from the RFQ is in the range of a few eV. Hence, the classical description of the ion motion in the Penning trap will be sufficient for our purposes. However, the quantum mechanical treatment of creation and annihilation operators can provide an intuitive explanation of ion excitation by means of RF fields [113, 178], which will be discussed later.

3.7.2 The Fourier-transform ion-cyclotron-resonance method

To determine the mass of an ion in a Penning trap, the cyclotron frequency ω_c is to be measured. However, ω_c is not an eigenfrequency of any eigen motion and cannot be measured directly. Penning traps for stable nuclides often take advantage of $\omega_c^2 = \omega_+^2 + \omega_-^2 + \omega_z^2$ (Equation 3.11), a relation known as the Brown-Gabrielse invariance theorem [176]. In the technique called Fourier-Transform Ion-Cyclotron-Resonance (FT-ICR) [179], the image currents induced by the motion of the ions in electrodes of the Penning trap are detected. In a Fourier analysis of these signals the three eigenfrequencies can be determined and by utilizing the Brown-Gabrielse invariance theorem ω_c, is obtained. Variations of this approach can achieve very high precision. For instance TITAN's mass measurement of ^{6}Li [124] has been confirmed and improved by such a measurement at Florida State University (FSU) [180] by over one order of magnitude to ≈ 0.2 PPB. Moreover, mass comparisons of singly charged molecules and atoms with relative accuracies below 10^{-11} have been reported [181, 182]. Despite its appeal by means of the achievable precision, the FT-ICR method is generally not applicable for radioactive nuclides because of its extended measurement time which is in conflict with short half-lives. The exception to this statement is found for mass measurements of super-heavy elements or other special cases (e.g. the double magic nuclide ^{100}Sn), where half-lives in the order of seconds are combined with very low production yields ($\sim$1 ion per minute or less). To take full advantage of few low numbers of ions available, the non-destructive character of the FT-ICR method might be advantageous over the destructive Time-Of-Flight Ion-Cyclotron-Resonance (TOF-ICR) technique discussed next. FT-ICR Penning traps for longer-lived, but ultra low yield nuclides are currently being built (e.g. [183]). To date, however, all Penning trap mass spectrometers at radioactive ion beam facilities utilize the TOF-ICR method.

3.7.3 Quadrupole excitations and the time-of-flight ion-cyclotron-resonance method

In the TOF-ICR [184, 185] the cyclotron frequency ω_c is determined by coupling the two radial frequencies $\omega_+ + \omega_- = \omega_c$ through the application of an external azimuthal quadrupole RF- field,

$$V_{\mathrm{rf}} = -\frac{V_{0,\mathrm{rf}}}{2a^2} \cos\left(\omega_{\mathrm{rf}}t + \phi_{\mathrm{rf}}\right)x \cdot y. \tag{3.21}$$

$V_{0,\mathrm{rf}}$ is the amplitude of the RF-field at a radius a. The angular frequency and phase of the RF-field are ω_{rf} and ϕ_{rf}, respectively. Under the influence of such an RF-field magnetron motion is converted into reduced cyclotron motion and *vice versa*. Details of the general, classical ion motion and the technique are derived in [185]. In our measurement the ions are prepared on a pure magnetron orbit at the beginning of the measurement, $\rho_-(t = 0) = \rho_0$ and $\rho_+(t = 0) = 0$. The axial motion is minimized. Since it is irrelevant for the measurement principle it is ignored for the moment. Assuming these initial conditions, the amplitudes of the radial motions evolve owing to the RF-field according to

$$
\begin{aligned}
\rho_-(t) &= \rho_0\left(\cos(\omega_B t) + \frac{1}{2}\frac{i(\omega_{\mathrm{rf}} - \omega_c)}{\omega_B}\sin\left(\omega_B t\right)\right)\cdot e^{i\frac{1}{2}(\omega_{\mathrm{rf}}-\omega_c)t} \\
\rho_+(t) &= -\frac{1}{2}\frac{\rho_0 k_0 e^{-i\Delta\phi}}{\omega_B}\sin\left(\omega_B t\right)\cdot e^{i\frac{1}{2}(\omega_{\mathrm{rf}}-\omega_c)t}
\end{aligned}
\tag{3.22}
$$

with

$$
\begin{aligned}
\omega_B &= \frac{1}{2}\sqrt{(\omega_{\mathrm{rf}} - \omega_c)^2 + k_0^2} \tag{3.23} \\
k_0 &= \frac{V_{0,\mathrm{rf}}}{2a^2}\frac{Q}{m}\frac{1}{\omega_+ - \omega_-}. \tag{3.24}
\end{aligned}
$$

$\Delta\phi$ is the difference between the phases of the RF, the magnetron and the reduced cyclotron motion. For simplicity, we set all phases to zero. It is important to note that phase independent results are only obtained for the initial conditions of $\rho_-(t = 0) = \rho_0$ and $\rho_+(t = 0) = 0$ [178]. In the case when $\omega_{\mathrm{rf}} = \omega_c$, the amplitudes turn into

$$
\begin{aligned}
\rho_-(t) &= \rho_0 \cos\left(\frac{k_0 t}{2}\right) \\
\rho_+(t) &= \rho_0 \sin\left(\frac{k_0 t}{2}\right). \tag{3.25}
\end{aligned}
$$

The quadrupole RF-field results in a beating between the two radial eigenmotions. For those times when there is a pure reduced cyclotron or pure magnetron motion, the ion revolves along the same circular radius, $\rho_{+,\mathrm{max}} = \rho_{-,\mathrm{max}} = \rho_0$. Considering the absolute values $|\rho_\pm|$, the period of one full conversion from and back to pure magnetron motion is

$$T = \frac{2\pi}{k_0} = \frac{\pi a^2}{V_{0,\mathrm{rf}}} \frac{m}{Q} \cdot (\omega_+ - \omega_-) = \frac{\pi a^2 B}{V_{0,\mathrm{rf}}} \sqrt{1 - \frac{2\omega_z^2}{\omega_c^2}}. \qquad (3.26)$$

Assuming the hierarchy in the angular frequencies, the last expression can be expanded to

$$T \approx \frac{\pi a^2 B}{V_{0,\mathrm{rf}}} \left(1 - \frac{\omega_z^2}{\omega_c^2}\right) = \frac{\pi a^2 B}{V_{0,\mathrm{rf}}} \left(1 - \frac{mU}{QB^2 d_0^2}\right). \qquad (3.27)$$

Thus, the period is mass and charge independent except for the small term

$$\frac{mU}{QB^2 d_0^2} = 10^{-4} \frac{A \cdot U[\mathrm{V}]}{q(B[\mathrm{T}] \cdot d_0[\mathrm{cm}])^2}. \qquad (3.28)$$

In order to convert an initially pure magnetron motion into pure cyclotron motion, the product of RF-amplitude and the time T_{rf}, which the RF-field is applied for, has to be a certain constant:

$$k_0 = \frac{\pi}{T_{\mathrm{rf}}} \Rightarrow V_{0,\mathrm{rf}} \cdot T_{\mathrm{rf}} = const. \qquad (3.29)$$

Since $\omega_+ \gg \omega_-$, the radial (kinetic) energy is dominated by the reduced cyclotron motion, $E_\rho \approx m/2 \cdot \rho_+^2 \omega_+^2$. A conversion between the two radial energies leads to a drastic change in kinetic energy, i.e. a gain from starting in pure magnetron motion. For the product $V_{0,\mathrm{rf}} \cdot T_{\mathrm{rf}}$ at which the initial magnetron motion is fully converted into reduced cyclotron motion, the radial energy is maximal. Hence, the radial energy is an indication for the degree of conversion between the radial motions. In general, the radial energy is, according to Equation 3.25, proportional to

$$E_\rho \propto \frac{\sin^2(\omega_B T_{\mathrm{rf}})}{\omega_B^2}. \qquad (3.30)$$

For $k_0 \cdot T_{\mathrm{rf}} = \pi$ (one full conversion when $\omega_{\mathrm{rf}} = \omega_c$) one obtains

$$E_\rho = E_0 \frac{\sin^2\left(\pi/2 \cdot \sqrt{1 + (2\Delta\nu_{\mathrm{rf}} T_{\mathrm{rf}})^2}\right)}{1 + (2\Delta\nu_{\mathrm{rf}} T_{\mathrm{rf}})^2} \qquad (3.31)$$

when introducing the detuning frequency $\Delta\nu_{\mathrm{rf}} = (\omega_{\mathrm{rf}} - \omega_c)/(2\pi)$. Figure 3.24a

(a)

(b)
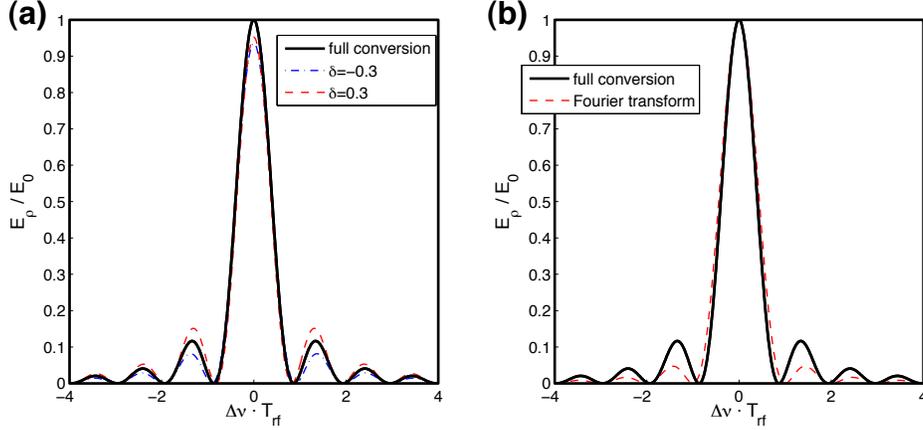
Figure 3.24: Calculated radial energy of an ion after the application of a quadrupole RF- field for a time $T_{\mathrm{rf}} = \pi/k_0$ at an angular frequency $\omega_{\mathrm{rf}} = \omega_c + 2\pi\Delta\nu$. (a) The full conversion is compared to an under-converted ($\delta = -0.3$) and an over-converted ($\delta = 0.3$) case. (b) The shape of the E_ρ- function is compared to the Fourier transform of a pulse of a scalar wave of the same duration.

displays the radial energy after the RF-field is applied as a function of the detuning function and T_{rf}. A pronounced maximum is found for $\Delta\nu_{\mathrm{rf}} = 0$, hence $\omega_{\mathrm{rf}} = \omega_c$, because the initial magnetron motion is fully converted into reduced cyclotron motion. For all other $\Delta\nu_{\mathrm{rf}}$ some magnetron motion remains. Hence, for $\Delta\nu_{\mathrm{rf}} \neq 0$ the reduced cyclotron motion has not reached its full amplitude $\rho_+ = \rho_0$, and the radial energy is smaller. Consequently, the frequency of the RF-quadrupole field causes a resonance at the true cyclotron frequency ω_c, which can be detected by the change in energy of the ion in the Penning trap.

Figure 3.24a motivates the following measurement principle. Ions from an ion species whose mass is to be determined are injected into the Penning trap and prepared with initial magnetron motion. Then, a quadrupole RF-field is applied at a certain frequency ω_{rf} for a time T_{rf}. At the end of the RF-field the energy of the ion is determined. Repeating these steps for several ω_{rf}, a resonance curve as a function of ω_{rf} is obtain from which ω_c of the ion, and thus its mass, can be calculated, when B and q are known.

Before discussing how E_r is measured experimentally, a few more details about the ion excitation with an azimuthal quadrupole RF-field are mentioned. The excitation time T_{rf} enters into the shape of the energy distribution twice (Equation 3.30),

firstly through $\Delta\nu \cdot T_{\text{rf}}$ and secondly via k_0 in ω_B because the product of $k_0 \cdot T_{\text{rf}}$ dictates the amount of conversion when $\omega_{\text{rf}} = \omega_c$. Experimentally, this is tuned by an optimal value of $V_{0,\text{rf}} \cdot T_{\text{rf}}$ (Equation 3.29). According to Equation 3.28, this condition is only approximately mass and charge independent. If we introduce a deviation δ from the exact condition $k_0 \cdot T_{\text{rf}} = \pi \cdot (1+\delta)^{1/2}$, then, the radial energy of Equation 3.31 is modified to

$$E_\rho = E_0(1+\delta) \cdot \frac{\sin^2\left(\pi/2 \cdot \sqrt{1+\delta+(2\Delta\nu_{\text{rf}}T_{\text{rf}})^2}\right)}{1+\delta+(2\Delta\nu_{\text{rf}}T_{\text{rf}})^2}. \tag{3.32}$$

The radial energies with $\delta = \pm 0.3$ are also shown in Figure 3.24a. As the ion motion is either under- or overconverted, the amplitude of the cyclotron motion is not maximized for $\Delta\nu_{\text{rf}} = 0$. Instead, some magnetron motion is present. In consequence, the radial energy at $\Delta\nu_{\text{rf}} = 0$ is reduced. However, the detuning frequency $\Delta\nu_{\text{rf}}$ enters into E_ρ in quadrature and the maximum at $\Delta\nu_{\text{rf}} = 0$ persists. Hence, slight deviations of the condition for full conversion $k_0 \cdot T_{\text{rf}} = \pi \cdot (1+\delta)^{1/2}$ might cause a reduction in the measurement signal, but do not affect the position of the resonance at $\omega_{\text{rf}} = \omega_c$. The m/Q dependence at the $\sim 10^{-4}$ level in $k_0 \cdot T_{\text{rf}}$ is orders of magnitude larger than the aimed precision for the mass measurement, but does not matter for a measurement of ω_c. This is a general feature of this measurement technique. Not everything in the setup has to be controlled or measured at the accuracy level of the mass measurement itself. Critical for the mass measurement is the accuracy in the determination of ω_c only.

The cases of $\delta = \pm 0.3$ in Figure 3.24 are extreme cases to illustrate the behaviour. In reality, δ is much closer to zero, and the reduction in E_ρ for $\omega_{\text{rf}} = \omega_c$ is negligible for the measurement sensitivity.

The over-conversion with $\delta = 0.3$ cannot only be seen in a smaller radial energy at $\Delta\nu = 0$, but also in the maxima on either side of the main maximum (Figure 3.24). In the scenario of an over-conversion their heights are increased compared to the full conversion. For under-conversion the opposite holds. The reason for these additional maxima or so-called side-bands is due to the square-wave pattern of the amplitude of the quadrupole RF- field, $V_{0,\text{rf}} = V_{A,\text{rf}} \cdot \Theta(t) \cdot \Theta(T_{\text{rf}} - t)$. $\Theta(t)$ is the Heaviside step function in time t. A Fourier transform of a scalar wave $s = \exp(-i\omega_0 t + \phi) \cdot \Theta(t) \cdot \Theta(T_{\text{rf}} - t)$ for example results in an intensity profile in frequency space of

$$I(\omega) = |\tilde{S}(\omega)|^2 = \frac{\sin^2\left(\pi/2\Delta_\nu T_{\text{rf}}\right)}{(\Delta\nu T_{\text{rf}})^2} \tag{3.33}$$

with $\Delta\nu = (\omega - \omega_0)/(2\pi)$, whose analogy to Equation 3.31 is apparent. It is plotted normalized to the radial energy profile in Figure 3.24b. The width of the energy profile is in fact narrower than the Fourier transform of the scalar wave. When expanding Equation 3.31 in a Taylor series, an approximation of the line width of

$$\Delta\nu(\text{FWHM}) \approx \frac{0.8}{T_{\text{rf}}} \tag{3.34}$$

is found. Hence, the longer the observation time the more narrow the line profile and the more precise the measurement.

Quantum mechanical description

In [178][3], the RF-quadrupole field Equation 3.21 is quantized by the previously introduced creation and annihilation operators of the radial motions.

$$Q \cdot V_{\text{rf}} \propto e^{-i(\omega_{\text{rf}}t + \phi_{\text{rf}})} \cdot \left(a_+^{+2} + a_-^2 + 2a_+^+ a_- \right) + h.c. \tag{3.35}$$

The first term is responsible for the creation of two quanta of reduced cyclotron motion when a photon with an energy $\hbar\omega_{\text{rf}} \approx 2\hbar\omega_+$ from the RF- field is absorbed. Analogously, the second term could remove two quanta of the magnetron motion. Since the magnetron motion is an inverted, harmonic motion this requires additional energy which is due to an absorbed photon of $E = \hbar\omega_{\text{rf}} \approx 2\hbar\omega_-$. Finally, the last term is responsible for the conversion of magnetron motion into reduced cyclotron motion as one of the latter quanta is annihilated while a former quantum is created. A photon of the RF- field of energy $E = \hbar\omega_{\text{rf}} \approx \hbar\omega_c$ is absorbed. This is the part of the quadrupole excitation which is used for the mass measurement. Thus, the formalism provides an intuitive understanding of the quadrupole RF- field and how it leads to a conversion between the two radial eigenmotions. Furthermore, energy conservation through the creation and annihilation of respective quanta from the undisturbed Hamiltonian Equation 3.19 and the relation $\omega_c = \omega_+ + \omega_-$ explains why the resonance of the quadrupole excitation occurs at $\omega_{\text{rf}} \approx \omega_c$.

The measurement of E_ρ via TOF

The previous sections outlined how an azimuthal quadrupole RF-field induces a resonant net gain in energy for $\omega_{\text{rf}} \approx \omega_c$, which allows the determination of $\omega_c = QB/m$. The measurement of the radial energy to map out the resonance has yet to

---

[3]Note that the $x - y$ coordinate system of [178] is rotated by 45° compared to [185] and Equation 3.21.
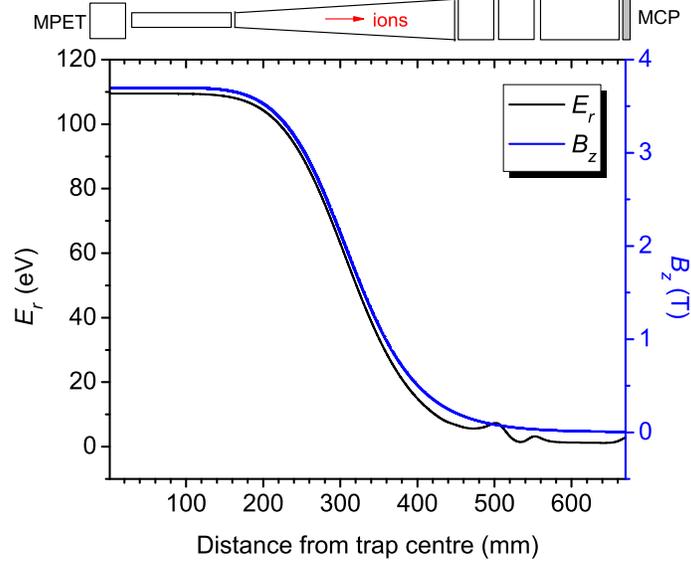
Figure 3.25: Radial energy (black) and magnetic field (blue) along the ion extraction path. The top shows a schematic of the ion optic components. After the extraction of the ion bunch from TITAN's MPET, radial energy is converted in the magnetic field gradient into axial energy. Thus, the TOF from MPET to a MCP detector provides a measure of the radial energy of the ions in MPET. Figure from [146].

be explained. This is done by a Time-Of-Flight (TOF) measurement of the excited ion extracted from the Penning trap to an MCP detector. Along the extraction path (Figure 3.25), the ions are transported from the strong and homogeneous magnetic field at the trap to the (quasi-) field-free region where the MCP detector is located. While in the homogeneous magnetic field, the circulation of an ion around the magnetic field axis generates a magnetic moment $\vec{\mu}$. Hence, the radial energy E_ρ can be expressed as an interaction of the magnetic field with the magnetic moment.

$$E_\rho = U = \vec{\mu} \cdot \vec{B} \tag{3.36}$$

which defines the magnetic moment as

$$\vec{\mu} = \frac{E_\rho(\omega_{\mathrm{rf}})}{B} \cdot \hat{z}. \tag{3.37}$$

It was established above that the radial energy, and thus the magnetic moment as well, depends on the angular frequency of the external quadrupole RF- field. Once in the magnetic field gradient, an axial force given by

$$\vec{F}(\omega_{\mathrm{rf}}, z) = -\nabla\big(\vec{\mu}(\omega_{\mathrm{rf}}) \cdot \vec{B}\big) = -\frac{E_\rho(\omega_{\mathrm{rf}})}{B}\partial_z B_z \hat{z} \qquad (3.38)$$

transforms the radial energy of the ion into axial energy (Figure 3.25), which is measured by the TOF of the ion from the trap to the detection MCP. The analytic expression for the TOF to the MCP detector is [185]

$$T(\omega_{\mathrm{rf}}) = \int_{z_0}^{z_1} dz \left(\frac{m}{2 \mid E_0 - Q \cdot V(z) - \mu(\omega_{\mathrm{rf}}) \cdot B(z) \mid}\right)^{\frac{1}{2}} \qquad (3.39)$$

where E_0 is the initial (axial) energy. $V(z)$ and $B(z)$ are the electric potential and the magnetic field along the TOF path.

The sequence for a measurement, then, is as follows. Each ion bunch is injected into the Penning trap and prepared with pure magnetron motion. A quadruple RF- field is applied at ν_{rf} near ν_c. After the RF-excitation, the gain in radial energy is measured by the TOF to a detector outside of the magnetic field. When plotted as a function of the applied RF- frequency, a TOF resonance is obtained like in Figure 3.26. The maximized radial energy for $\nu_{\mathrm{rf}} = \nu_c$ is seen as a minimum in TOF. The axial energy and its spread of the ions when injected into MPET as well as background counts at the MCP can reduce the signal-to-baseline ratio, i.e. the difference between the observed minimum and the maximum in the TOF resonance in comparison to the uncertainty in the TOF. This ratio can be improved by collecting data in the form of multiple ion bunches at each ν_{rf}. In practice, one chooses a frequency scanning range $\nu_s \leq \nu_c \leq \nu_e$ before a measurement run. A frequency scan over this frequency range consists of n ion bunches (typically 41 or 21 at TITAN). For each ion bunch, a different $\nu_{\mathrm{rf}} = \nu_s + i \cdot (\nu_e - \nu_s)/(n - 1)$ with $i = 0, 1, ..., (n - 1)$ is applied, and the corresponding TOF is measured. A measurement run is composed of several frequency scans (refer also to Figure A.7). Based on these data, the averaged TOF of ions from the MPET to the MCP detector is calculated as a function of the applied ν_{rf}.

Damping of the ion motion

Interaction of the charged particles with the residual gas in the Penning trap can lead to a damping of the ion motion [185]. The damping arises from the polarization of the residual gas atoms in the presence of the ion(s). The averaged damping
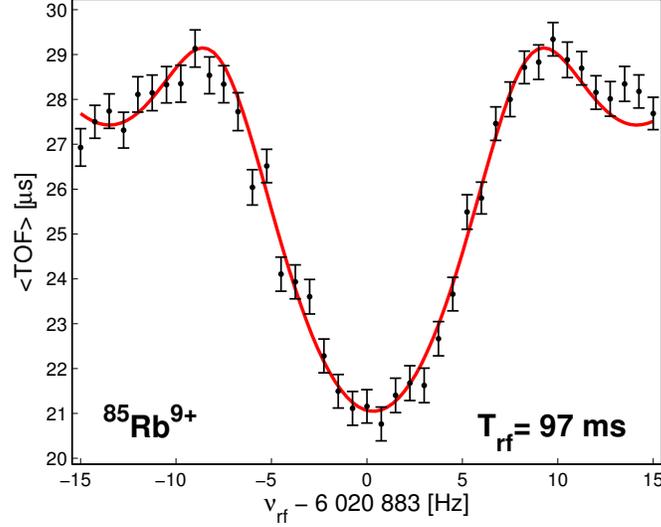
Figure 3.26: Example for a measurement of a resonance curve for the TOF-ICR method. Ion bunches of stable ^{85}Rb^{+9} are injected in the TITAN MPET, where for each ion bunch a fixed quadrupole RF- frequency $\nu_{\rm rf}$ is applied for a time $T_{\rm rf} = 97$ ms. The conversion of initial magnetron into reduced cyclotron motion is measured via TOF when an ion bunch is extracted from the MPET after the application of the RF- field. The minimum in TOF corresponds to the true cyclotron frequency $\nu_c = 1/(2\pi) \cdot mB/Q$. The fit (solid red line) is based on the theoretical line-shape Equation 3.39 as derived in [185].

force on an ion motion can be described by

$$\vec{F} = -\delta \cdot m \cdot \vec{v}. \tag{3.40}$$

The damping parameter δ is expressed as

$$\delta = \frac{Q}{m} \frac{1}{M_{\rm ion}} \frac{p/p_N}{T/T_N} \tag{3.41}$$

in relation to a normal pressure p_N and temperature T_N. The damping is proportional to Q/m and will thus play a larger role for HCI. The reduced ion mobility $M_{\rm ion}$ is a coefficient which depends on ion species and the residual gas [186]. $M_{\rm ion}$

can be determined from the drift velocity of ions through a certain gas (at p_N and T_N). The drift velocity is a result of the balance in forces between an applied electric field E and the damping and hence

$$v_d = M_{\text{ion}} \cdot E. \tag{3.42}$$

As mentioned earlier, a damping force will reduce the amplitude of the cyclotron motion, but increase the magnetron motion. The effect of the damping is folded into the theoretical resonance line shape in [185]. The maximal radial energy is reduced by the damping which results in a less pronounced TOF minimum. Additionally, the width of the resonance is broadened. The expression of the damping parameter in Equation 3.41 indicates which experimental conditions have to be addressed in order to minimize damping. An improved base pressure in the vacuum system not only makes the influence of damping less severe, but also reduces charge exchange between HCI and the neutral atoms from the residual gas. A good vacuum system is consequently a prerequisite for mass measurements of HCI to minimize damping and charge exchange (see Section 3.7.8).

The measurements (mostly with $q = 8, 9+$) of this work did not exhibit signs which could be unambiguously linked to damping. But cyclotron resonances during a later experiment with neutron-rich Rb and Sr- isotopes with $q = 15+$ [187] were broader than the expected width based on Equation 3.34. Although it is not entirely resolved yet whether this is caused by damping, the inclusion of the damping into the fitting function can compensate for the wider resonance. Hence, a fitting function including damping was always employed for the present analysis (Section 4.2).

Achievable measurement precision

Following Equation 3.34, the width in the resonance is inversely proportional to the time T_{rf} of the RF-application. The (mass) resolving power R can be formulated to be

$$R = \frac{\Delta m}{m} = \frac{\Delta \nu}{\nu_c} \propto \frac{1}{\nu_c \cdot T_{\text{rf}}}. \tag{3.43}$$

Inserting the expression for the cyclotron frequency $\nu_c = 1/(2\pi) \cdot QB/m$, one obtains

$$R \propto \frac{m}{Q \cdot B \cdot T_{\text{rf}}} \tag{3.44}$$

for the resolving power. Finally, the achievable precision $\delta m/m$ is improved by statistics, hence the number of ions in the measurement N_{ions}.

$$\frac{\delta m}{m} \propto \frac{R}{\sqrt{N_{\mathrm{ions}}}} \propto \frac{m}{Q \cdot B \cdot T_{\mathrm{rf}} \sqrt{N_{\mathrm{ions}}}}. \tag{3.45}$$

This is Equation 2.89 whose implications have been discussed in Section 2.9. The proportionality constant between the achievable precision and $m/(Q \cdot B \cdot T_{\mathrm{rf}} \sqrt{N_{\mathrm{ions}}})$ is a quality factor of the resonance which is trap-dependent. The individual parameters depend on various aspects. In the area of radioactive ion research, the number of ions, owing to the radioactive decay, is also a function of the excitation time and the nuclide's half-life, $N_{\mathrm{ions}} = N_0 \cdot \exp\left[-T_{\mathrm{rf}} \ln 2 / T_{1/2}\right]$. The depth of the trap U ($U = 35.75$ V in the present work) is for SCI in most cases low enough that ions would leave the trap due to the recoil following a β-decay. For HCI, the energy required for an ion to be expelled from the trap axially can be much larger because of the charge state dependence of the effective trap potential, $E = Q \cdot U$. In this case, the daughter may remain trapped although with a much higher axial energy. Assuming that the number of surviving ions after the RF-excitation period in a measurement run is large enough to unambiguously record a TOF resonance, the best precision is achieved with an excitation time of $T_{\mathrm{rf}} = 2 \cdot T_{1/2} / \ln 2 \approx 2.9 \cdot T_{1/2}$.

3.7.4 The Ramsey excitation scheme

A variation of the quadrupole excitation is the Ramsey method of separated oscillatory fields. The original idea is from N.F. Ramsey [188] [189] [190] who proposed the technique for the molecular-beam magnetic resonance method. It was first introduced to Penning trap mass spectrometry in 1992 [191]. Penning trap measurements based on the same concept have been performed [114, 192], but for the TOF-ICR technique it took until 2007 when a sound theoretical foundation was established [178, 193]. Other studies of the same approach are published in [194–196]. [197] discusses the effect of damping on the Ramsey technique. The basic idea of the Ramsey method of separated oscillatory fields is to apply the RF-field in well defined pulses instead of continuously. Figure 3.27 illustrates different excitations schemes that are typically applied in Ramsey TOF-ICR methods. As described in Section 3.7.3, during a normal quadrupole excitation the ions are driven by a continuous RF-field for the whole excitation time $T_{\mathrm{rf}} = \tau$,

$$V_{\mathrm{rf}} \propto A_1 \cos(\omega_{\mathrm{rf}} \cdot t + \phi_{\mathrm{rf}}) \cdot \Theta(t) \cdot \Theta(\tau - t). \tag{3.46}$$
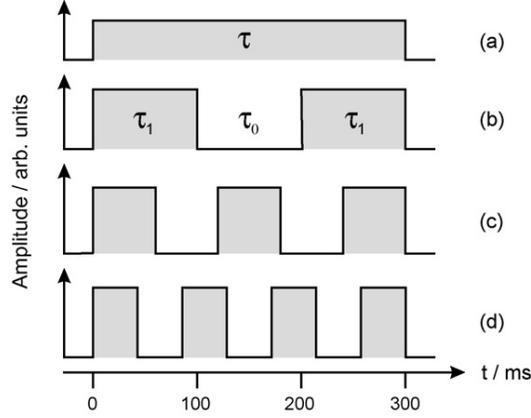
Figure 3.27: Amplitudes of the quadrupole excitation in a conventional excitation scheme as discussed in Section 3.7.3 (a) compared the amplitudes in Ramsey excitation schemes. (b) represents a two-pulse mode in which the RF- field is applied in two pulses of duration τ_1 which are separated by a waiting period of time τ_0. (c) and (d) are three- and four- pulse excitations. Figure from [194].

For a two-pulse Ramsey scheme, the RF-field is only applied in two pulses each of duration τ_1. The pulses are separated by a waiting period τ_0 with a summed duration of $T_{rf} = 2 \cdot \tau_1 + \tau_0$ (see Figure 3.27b).

$$V_{rf,2-pulses} \propto A_2 \cos(\omega_{rf} \cdot t + \phi_{rf}) \cdot \left[\Theta(t) \cdot \Theta(\tau_1 - t) + \Theta(t - T_{rf} + \tau_1) \cdot \Theta(T_{rf} - t) \right].$$
(3.47)

To understand why the Ramsey technique is an appealing extension to the normal quadrupole excitation it is helpful to consider the Fourier transform of the RF-fields. In Section 3.7.3, we have already seen the close relationship between the Fourier transform and the exact description of the ion motion under the influence of the RF-field. Figure 3.28 compares Equation 3.46 and Equation 3.47 by means of the amplitudes, the actual RF-field, and the respective Fourier transform. From the perspective of precision experiments the most important advantage between the two excitation schemes is the reduction in the line width which facilitates a significant gain in experimental precision. To see this narrower line width better, the extreme case of $\tau_1 = T_{rf}/1000$ is contrasted to the normal quadrupole excitation in Figure 3.29. In order to obtain the same strength in the intensity profile the

normal quad. **Ramsey**

(a) A rf vs time

(b) V rf vs time

(c) $|I(\omega)|$ vs $\Delta\nu$
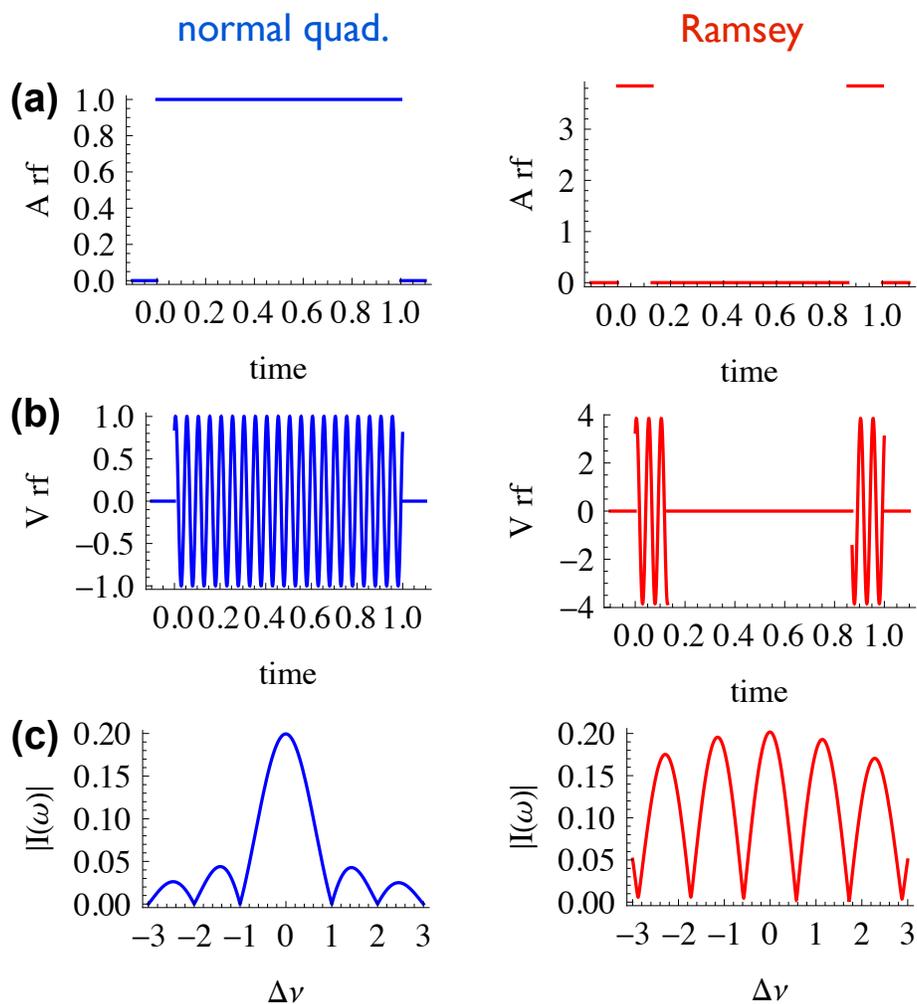
Figure 3.28: Comparison of a one-pulse excitation scheme ('normal quad.') compared to a two-pulse Ramsey excitation ('Ramsey'). In (a), the amplitudes of the respective excitation are displayed over time. The actual applied RF-fields following Equation 3.46 and Equation 3.47 are shown in (b). Finally, the Fourier transforms of each case are plotted in (c) as a function of $\Delta\nu = (\omega - \omega_{\mathrm{rf}})/(2\pi)$. The magnitude of the amplitude for the Ramsey excitation is adjusted such that the intensities in frequency space $|\, I(\omega = \omega_{\mathrm{rf}})\,|$ are the same for both excitation modes.
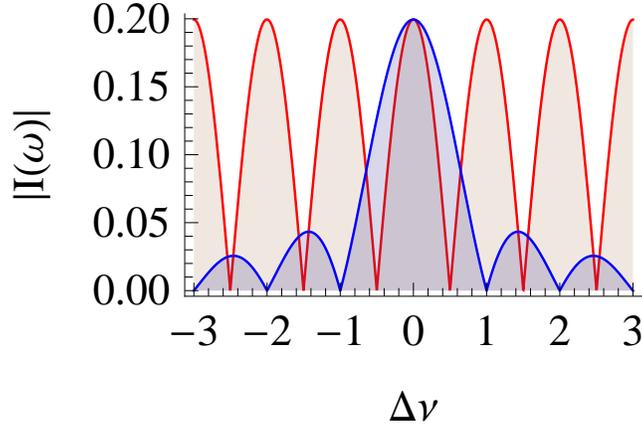
Figure 3.29: Direct comparison of a Fourier transform of a regular one-pulse excitation with a duration of T_{rf} to a two-pulse Ramsey excitation with a pulse width of each RF-pulse of $\tau_1 = T_{rf}/1000$, but with the same total $T_{rf} = 2 \cdot \tau_1 + \tau_0$.

amplitude A_2 of the Ramsey excitation has to be scaled to A_1 according to

$$A_2 = A_1 \cdot \frac{T_{rf}}{2 \cdot \tau_1}. \tag{3.48}$$

Hence, the shaded areas in Figure 3.27 have to be equal for each scheme. Strongly enhanced side maxima are a distinct feature of the Ramsey method. Indeed, in Figure 3.29 the side maxima are indistinguishable from the main maximum at $\Delta\nu = 0$. In practise, this implies that the main maximum is typically first identified with the continous quadrupole excitation, and only then the measurement technique is adapted to the Ramsey method.

Studies of the application of the Ramsey technique for TOF-ICR have shown that the two pulse excitation scheme offers the largest gain in precision [194] and it was used throughout the present measurement. The smaller τ_1, the more narrow is the line width although the scaling law of the amplitude Equation 3.48 limits the minimal practical duration of τ_1. The exact model of the line shape in TOF-ICR is derived in [178] and was used for the fit of all recorded resonance spectra. In addition, our fitting function has been modified to consider damping as explained in [197].

3.7.5   Determination of atomic masses and Q_{EC}-values

In order to extract the mass from the measurement of the cyclotron frequency, one has to consider that the magnetic field strength is not known precisely enough, undergoes fluctuations, and decays with the residual resistance of the superconducting magnet. Hence, a simple inversion to mass from Equation 3.2 is not possible. Instead the magnetic field is calibrated by measuring ν_c of an ion species with a well known mass. From there, a frequency ratio

$$R = \frac{\nu_{c,r}}{\nu_c} = \frac{q_r}{q} \cdot \frac{m_{\mathrm{ion}}}{m_{r,\mathrm{ion}}} \tag{3.49}$$

between ion of interest and the reference ion (labeled with r in the subscript) is obtained. The atomic mass of the ion of interest is calculated by

$$m = \frac{q}{q_r} \cdot R \cdot (m_r - q_r \cdot m_e + B_{e,r}) + q \cdot m_e - B_e. \tag{3.50}$$

Here, m_r is the atomic mass of the reference ion, m_e is the mass of the electron, and the $B_{e,x}$ are the total binding energies of the q_x removed electrons. Following the convention of the Atomic Mass Evaluation (AME) [198, 199], the atomic masses of nuclides are expressed as the mass excess $m.e. = m - A \cdot m(^{12}\mathrm{C})/12$ and keV is used as the unit of mass. When ions of the parent (p) and daughter (d) nuclide involved in a β- decay are available during an experimental campaign, the Q_{EC}-value can be determined to

$$Q_{\mathrm{EC}} = \left(\frac{\nu_{c,d}}{\nu_{c,p}} \cdot \frac{q_p}{q_d} - 1\right) \cdot (m_d - q_d \cdot m_e + B_{e,d}) + m_e \cdot (q_p - q_d) - B_{e,p} + B_{e,d}. \tag{3.51}$$

Since $\nu_{c,d}/\nu_{c,p} \cdot q_p/q_d \approx 1$, the uncertainty on the Q_{EC}-value due to the atomic mass of the daughter nuclide is suppressed and does not need to be known in the literature to the same precision as for their direct mass measurements.

Measurements of ν_c for the ion of interest are performed between determinations of $\nu_{c,r}$ of the reference ion. As indicated in Figure 3.30, the cyclotron frequency for the reference ion is linearly interpolated to the mid-time of the measurement run for the ion of interest and a frequency ratio $R = \tilde{\nu}_{c,r}/\nu_c$ is used for the evaluation of Equation 3.50 or Equation 3.51. The difference in time between two consecutive reference measurements has to be short enough to minimize non-linear field fluctuations. At TITAN, this time is typically ≈ 1 h at a field decay of ≈ 0.25 PPB/h [124].

The access to ions with different charge states of the same nuclide for mass measurements at TITAN would in principle allow an absolute atomic mass determina-
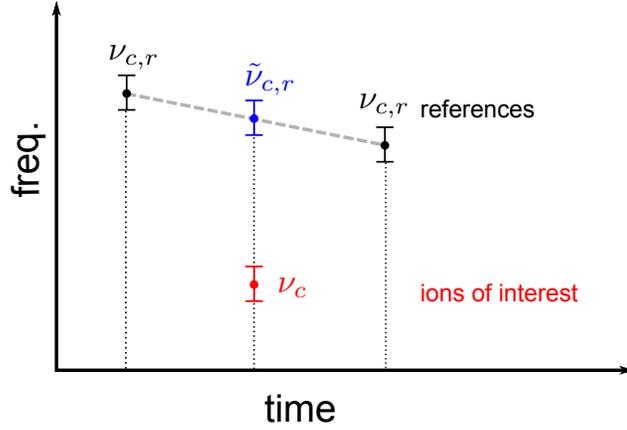
Figure 3.30: Schematic of the linear interpolation of reference measurements for the determination of the frequency ratio $R = \tilde{\nu}_{c,r}/\nu_c$.

tion according to

$$m = \frac{\frac{q_1}{q_2} \cdot R(-q_2 \cdot m_e + B_{e,2}) + q_1 \cdot m_e - B_{e,1}}{1 - \frac{q_1}{q_2} \cdot R} \tag{3.52}$$

without the need for a reference ion species. The frequency ratio $R = \nu_{c,2}/\nu_{c,1}$ taken is here between charge states q_2 and q_1 of the same nuclide. In practice, this approach is not feasible because the denominator is close to 0 and inflates the partial uncertainty on the mass dramatically

$$\sigma_{m,R} = \frac{m/R - q_1 \cdot m_e + B_{e,1}}{1 - \frac{q_1}{q_2} \cdot R} \cdot \sigma_R \approx \frac{m}{1 - \frac{q_1}{q_2} \cdot R} \cdot \frac{\sigma_R}{R} \tag{3.53}$$

in comparison to the uncertainty in the measured frequency ratio σ_R. Hence, in contrast to Equation 3.50, the relative precision of the frequency ratio does not translate to the relative precision in the mass.

Determination of electron binding energies

In the evaluation of Equation 3.50, electron binding energies are taken from the literature (e.g. [200] for HCI of Rb). For conventional Penning trap mass measurements of radioactive nuclides with SCI, these are only a few eV. B_e is in this case negligible compared to the measurement uncertainty. In the context of HCI,

the total electron binding energies can be much more influential and can be in the range of a few keV or more. Often, their uncertainties can account for several tens of eV and/or are based on theoretical calculations only. Although this is not the case for the present studies, these uncertainties could be a limiting factor for future mass measurements at higher charge states q of higher precision. In such a scenario, differences between binding energies for different charge state of the same element could be measured directly. Since

$$\sigma_{\Delta B_e} \approx m_{\text{ion}}\frac{\sigma_R}{R} \approx A\frac{\sigma_R}{R} \cdot 10^9 \text{ eV} \tag{3.54}$$

uncertainties of ~ 10 eV and below would be in reach provided that systematic errors can be kept under control. The contribution to the uncertainties due to the atomic mass itself is again suppressed by a term $(1 - q_1/q_2 \cdot R)$, which is close to zero. This is particularly true as these measurements could be done with stable isotopes whose atomic masses are generally much better known.

3.7.6 Dipole excitations

Each individual eigenmotion can be excited by an electric dipole RF-field with a frequency equal to the respective eigenfrequency. For the excitation of the axial motion the dipole field is applied between the two end cap electrodes. Since the axial motion is mostly irrelevant for the TOF-ICR technique, an axial RF-field is rarely employed. For excitations of the radial eigenmotions the ring electrode can be segmented. As this electrode is often split in (at least) 4 radial segments for the quadrupole excitation, the dipole field is applied to two opposing segments. Figure 3.31 compares the application of quadrupole and dipole RF-fields. With the mass measurement program at TITAN, a dipole excitation is routinely used to push unwanted, contaminating ion species to a larger radius or out of the trap altogether. Here, one takes advantage of the mass and charge dependency of the reduced cyclotron frequency ω_+. Exact knowledge of ω_+ is not necessary because the more power is driven into the system at the approximate ω_+ the more frequencies in the Fourier transform carry sufficient intensity to drive an ion out of the trap. This cleaning method of contamination can be very effective, but each contaminating species has to be identified such that a dipole excitation on its individual ω_+ can be carried out. When working with overwhelming, unidentified contamination other separation techniques such as the sideband cooling technique in a buffer-gas filled purification Penning trap [131, 201] or the Stored Waveform Inverse Fourier Transform (SWIFT) ion excitation [202] for advanced dipole cleaning are more appropriate. Both cannot currently be applied at TITAN. For contamination suppression a multi-reflection time-of-flight apparatus [203] is planned to be inserted

119
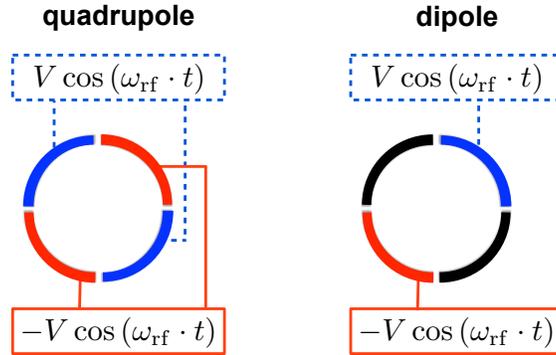
Figure 3.31: Schematic of a cross sectional view of a segmented ring electrode which can be used to apply an azimuthal quadrupole or dipole field on top of the DC trapping potential.

into the setup in 2012. It will be able to separate the ions of interest from isobaric contaminations in the ISAC beam such as the unwanted ^{74}Ga ions next to ^{74}Rb in the present work.

3.7.7   TITAN's MPET setup

The Penning trap structure dedicated to the high precision mass measurements at TITAN is mounted in the bore of a superconducting magnet. The field strength of 3.7 T is comparable to other Penning trap facilities at radioactive beam facilities although most of those employ larger field strengths. But the unique feature of HCI at TITAN can boost the precision according to Equation 3.45 to a level above the one attainable even with the current strongest magnet field of 9.4 T at the Low-Energy Beam and Ion Trap facility (LEBIT) [110] at the National Superconducting Cyclotron Laboratory (NSCL) .

The trap setup as well as neighbouring beam optics for extraction and injection are shown in Figure 3.32 all of which are mounted on the same support structure. It is installed in a vacuum tube in the inside of the magnet's bore. To minimize magnetic field inhomogeneities, all material used for the trap support structure and even for the vacuum tube is chosen to be non-magnetic. The main components of the injection path in Figure 3.32 are a PLT and a Lorentz steerer. The purpose of the PLT is to remove the majority of the kinetic energy from the ions. It is biased below the transport energy of the ions. When the ions are in the centre of the PLT at time t_{PLT}, it is switched to a bias voltage below the Penning trap. The ions can enter the trap through a hole in the end cap electrode of the trap (see Figure 3.33).
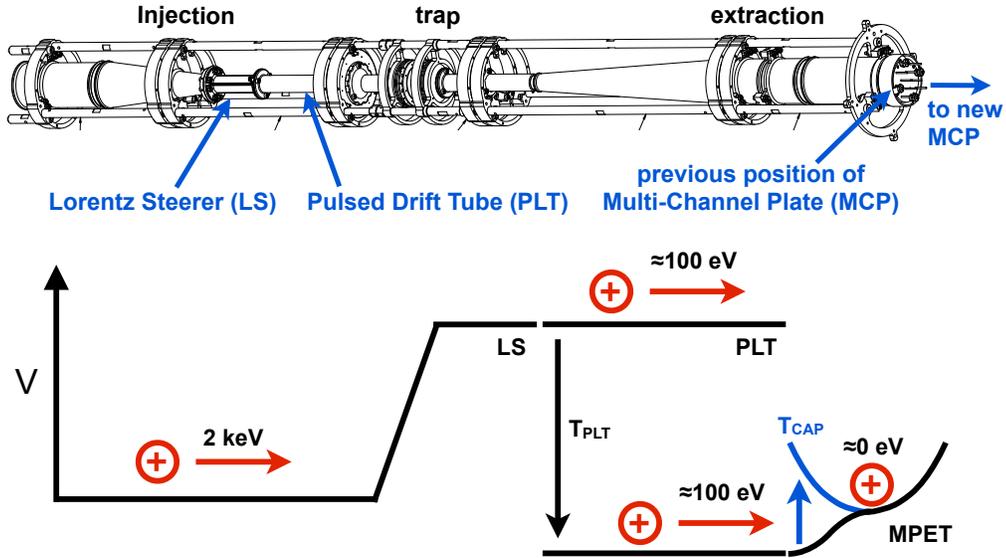
Figure 3.32: Top: Technical drawing of the injection, trap, and extraction setup of TITAN's Measurement Penning Trap (MPET) structure. The whole structure is located inside a titanium vacuum tube placed in the bore of the superconducting magnet. The figure at the bottom explains the electrostatic potentials on axis (not to scale) and timings for the dynamic capture of ions in the MPET.

The bias voltage of this end cap is lowered during injection. The energy difference between the PLT and the trap centre is adjusted such that the ions are at rest when the ions reach the trap. At this time, t_{cap}, the potential at the end cap electrode is raised and the ions are dynamically captured. Potentials and timings of the capture process are illustrated in the bottom of Figure 3.32.

The Lorentz steerer [204] is an electrostatic steerer setup in the presence of the magnetic field. The $\vec{E} \times \vec{B}$ drift motion allows the ion bunch to be steered off-axis. This prepares the ions in the initial magnetron motion. Due to the Lorentz steerer, the radial displacement of the ions is equal to [204]

$$\rho = \frac{E}{B} \cdot t = v_{\mathrm{drift}} \cdot t. \tag{3.55}$$

Hence, the axial velocity of the ions while passing through the Lorentz steerer should be small and its potential along the axis is the same as the potential of the
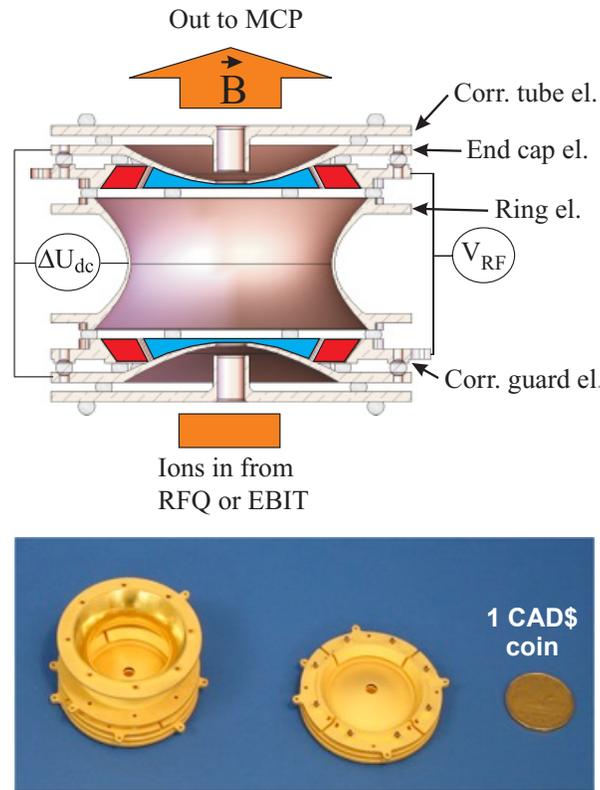
Figure 3.33: Schematics and picture of TITAN's MPET electrodes. The Canadian dollar coin (with a diameter of 26.5 mm) is given for scale (bottom). Figures from [146].

PLT before it is pulsed down. In this configuration the ions lose most of their kinetic energy before entering the Lorentz steerer (see Figure 3.32). The Lorentz steerer is composed of a segmented, cylindrical tube which creates a dipole field when biased following Figure 3.34. The radial displacement is proportional to the Lorentz steering strength ΔV_{LS} and the time it takes the ions to pass through the Lorentz steerer (Equation 3.55). The latter time depends on m/Q since every ion species is accelerated by the same electric potential difference after the thermalization in the RFQ or the EBIT. Since, $t \propto \sqrt{m/Q}$ ion species with smaller m/Q ratios need a stronger Lorentz steering strength ΔV_{LS} to be positioned to the same initial magnetron radius. Since for a full conversion the initial magnetron radius and the final cyclotron motion are identical in size (see Equation 3.25) a larger ρ_0 will result in a larger gain in energy during the RF-excitation in the MPET. The maximal ρ_0 is
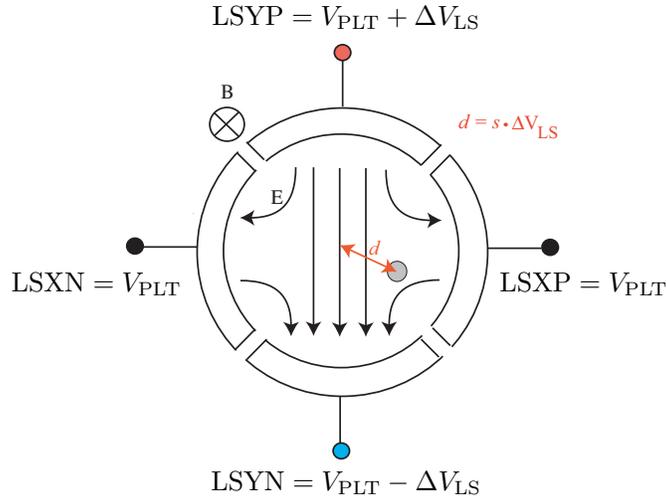
Figure 3.34: Cross sectional schematices of the Lorentz steerer. Figure modified from [146].

constrained by the radius of the injection hole in the end cap of MPET and similar sized holes in the PLT. The functionality of the Lorentz steerer described so far assumes injection of the ions into the magnetic field along its axis. The Lorentz steerer can also be used to correct for off-axis injection following the procedure in [204]. Most other Penning trap facilities operate without a Lorentz steerer and the initial magnetron motion is induced by a dipole excitation on the (almost) mass- or charge-independent magnetron frequency ν_-. The duration of this excitation is on the order of a few 10's of ms and is consequently a limiting factor for measurements of short-lived nuclides. In contrast, the preparation by the Lorentz steerer takes place during the injection itself and comes without any loss in time.

The measurement Penning trap

The mass measurement itself takes place in a precision Penning trap. Schematics and a picture of this MPET are displayed in Figure 3.33. Its characteristic trap dimension is $d_0 \approx 11.21$ mm. The trap electrodes are made of ultra pure oxygen-free copper. They are silver and gold plated to impede localized oxidation which could result in field distortions and to optimize conductivity. The hole for injection and extraction in each end cap electrode as well as the finite size of the electrode cause higher order anharmonicities and deviations from the harmonic potential of an ideal Penning trap. To correct for these imperfections, in particular for the field

Table 3.2: Nominal frequencies of an ion with mass $A = 74$ and charge $q = 8+$ in TITAN's MPET with $B = 3.7$ T and the trapping potential $U = 35.75$ V.

ν_c	6.142 MHz
ν_+	6.136 MHz
ν_z	274.1 kHz
ν_-	6.123 kHz

in the trapping volume at the trap centre, correction-tube electrodes are placed next to the entrance and exit hole in the end caps. Correction guard (or octopole) electrodes are inserted into the space between the ring and the end cap electrodes. The trap compensation procedure to obtain a potential closest to the ideal case is discussed in detail in [205].

For the present measurements, a trapping potential between the end cap and the ring electrodes of $U = 35.75$ V has been used. Nominal frequencies of an ion with $A^{q+} = 74^{8+}$ are listed in Table 3.2. The azimuthal (dipole and quadrupole) RF-fields (Figure 3.31) are most commonly applied to segments of the ring electrode. In the TITAN setup the guard electrodes are segmented instead of the ring electrode to avoid distortions in the harmonic field due to the splitting of the ring electrode. This improvement, however, requires larger RF-amplitudes to reach equal field strengths at the position of the ions and hence the need for RF-amplifiers.

At the end of the RF-excitation phase, the extraction end cap is lowered and ions are extracted from the MPET. During the extraction path the radial energy is converted into longitudinal energy as discussed earlier (Figure 3.25) and the TOF from the ion extraction to the arrival of the ions at the MCP detector is measured. Timings of the measurement process are either controlled by the MPET Programmable Pulse Generator (PPG) (e.g. PLT, RF, etc.) or by a slow control unit (essentially all DC bias potentials for the Penning trap) which are operated by the MIDAS control and data acquisition system [206]. The TOF measurement itself is integrated into the MIDAS system by a time-to-digital converter based on the timing of the MCP detection signal.

3.7.8 MPET vacuum system

The quality of the vacuum in the Penning trap is important due to increased damping and charge exchange for higher pressures. Requirements on the residual gas density are more severe when dealing with HCI compared to SCI. The MPET was designed as a room temperature trap system. Considering the success of Penning

trap mass measurements of stable HCI at SMILETRAP, which also operates at room-temperature [114], it was concluded that cryogenic temperatures were unnecessary at TITAN's MPET. The SMILETRAP group reports a pressure estimate in their Penning trap of less than $6.4(3.6) \cdot 10^{-12}$ mbar. This estimate is based on a measured charge exchange rate in comparison to charge exchange cross sections from the literature (in this case from [207]). When keeping ^{76}Ge^{22+} for 3.7 s in the trap only $\lesssim 9$ % of the initial ions underwent charge exchange.

An empirical scaling law [208] of the cross section for charge exchange of ions with energies below 25 keV/A in a neutral gas gives

$$\sigma^{QX}[\text{cm}^2] = 1.43 \cdot 10^{-12} q^{1.17} \cdot I_p^{-2.76}[\text{eV}], \qquad (3.56)$$

where I_p is the ionization potential of the neutral atom or molecule. Hence, the probability for an ion to pick up an electron from the residual gas in an infinitesimal time interval dt is

$$P \propto \frac{\sigma^{QX} p v_{\text{ion}}}{k_B T} \cdot dt \propto \frac{q^{1.17} p v_{\text{ion}}}{k_B T} \cdot dt. \qquad (3.57)$$

Charge exchange during the TOF-ICR measurement is consequently intensified for HCI due to two reasons. Firstly, the charge exchange cross section is proportional to the charge state q and, secondly, the reduced cyclotron frequency is increased for HCI leading to a larger ion velocity v_{ion} with $\nu_c = \nu_{\text{rf}}$.

The pressure in the MPET section before working with charge-bred ions (earlier than summer 2009) was determined to be $\approx 2 \cdot 10^{-9}$ mbar[4]. Previous to the mass measurement of ^{44}K^{4+} [1] an ion pump in the MPET vacuum section was baked at $\approx 200^o$ C which led to a vacuum pressure of $\approx 8 \cdot 10^{-10}$ mbar. However, as illustrated in Figure 3.35 for data with ^{39}K^{4+}, strong signs of charge exchange were observed. A peak of H$_2^+$ appeared in the TOF spectra when storing the ions longer in the MPET. H$_2$ was the most abundant residual gas as determined by a residual gas analyzer. Additionally, the tail of the TOF peak of ^{39}K^{4+} extended to longer TOF which is indicative of ^{39}K in lower charge states. As soon as an ion changes its initial charge, it has a different cyclotron frequency and is subsequently insensitive to the applied RF-field. Thus, the charge exchange affects the quality of the TOF resonance severely as seen in Figure 3.35 and Table 3.3.

In order to successfully work with HCI the quality of the vacuum had to be improved further. This was achieved by multiple efforts including baking the whole

---

[4]Please note that this is not necessarily the pressure in the trap itself. The pressure was measured with an ion gauge which is in the same cross as a turbo molecular pump. All pressures in the MPET vacuum section were, if not otherwise stated, measured at the same position and are at least a sign of relative improvements.
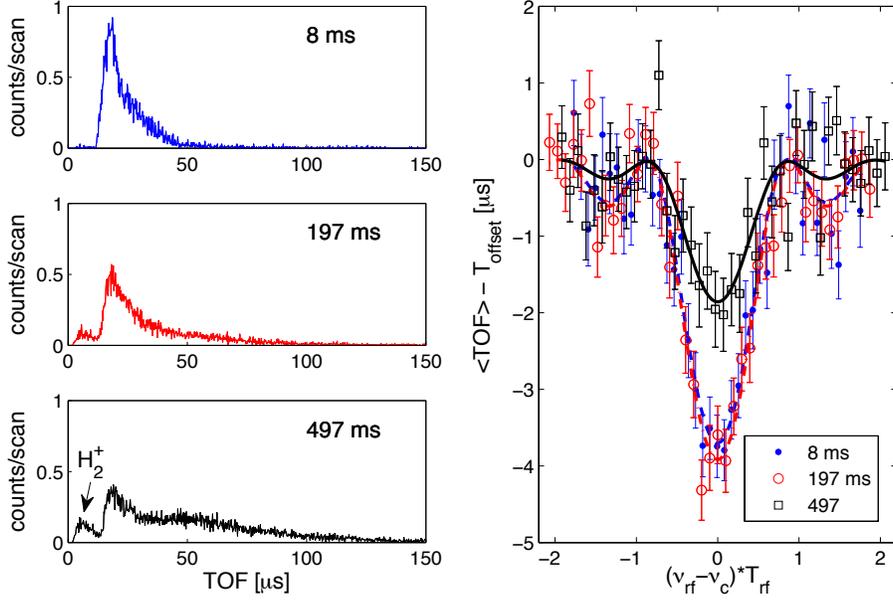
Figure 3.35: TOF spectra of ion bunches of $^{39}\mathrm{K}^{4+}$ measured with $T_{\mathrm{rf}} = 8$ ms, 197 ms, and 497 ms irrespective of the applied ν_{rf} (left part of the figure). The counts are normalized to the number of frequency scans for each measurement run. The ions were extracted from the MPET right after the application of the RF-field. The strong peak of $^{39}\mathrm{K}^{4+}$ in the TOF spectrum for $T_{\mathrm{rf}} = 8$ ms is reduced for longer excitation times. Instead a rise in counts of H_2^+ and in the tail of the initial TOF peak is observed, which corresponds to $^{39}\mathrm{K}^{3+,2+,1+}$. The charge exchange reduces the quality of the resonance as seen in the plot on the right.

Table 3.3: Uncertainty in the cyclotron frequency ν_c of $^{39}\mathrm{K}^{4+}$ for different excitation times T_{rf}. The last column lists the expected uncertainty based on $\Delta\nu$ for $T_{\mathrm{rf}} = 8$ ms and scaled to the larger T_{rf} using Equation 3.45. Figure 3.35 shows the TOF-ICR of these measurement runs.

T_{rf} [ms]	frequency scans	$\Delta\nu$ [Hz]	expected $\Delta\nu$ [Hz]
8	100	2.607	
197	200	0.096	0.074
497	199	0.094	0.030

setup at temperatures above 200° C and a hardware upgrade to the vacuum system. An example for the bake-out setup and for residual gas measurements of the MPET vacuum tube is shown in Figure 3.36. A more detailed description of the baking procedures and the modifications of the vacuum system are summarized in Section A.5. In the final setup, the pressure during the mass measurement of the neutron deficient Rb was $\approx 6 \cdot 10^{-11}$ mbar. When the ion pump was tested and fully operational at a later time, the pressure was further reduced and eventually went below the limit of the ion gauge ($\approx 2 \cdot 10^{-11}$ mbar).

During the course of the modifications of the MPET vacuum system prior to the Rb-mass measurements, the MCP detector for the TOF measurement was moved further away from the MPET and a Daly detector [209, 210] was added. A detector in addition to the primary MCP detector provided an immediate alternative detection system for the TOF measurement in case of a detector failure. Details can be found in Section A.5. Finally, the MPET support structure and wiring system were modified for better reliability of the electrical connections and simplified maintenance (see documentation in [211]).
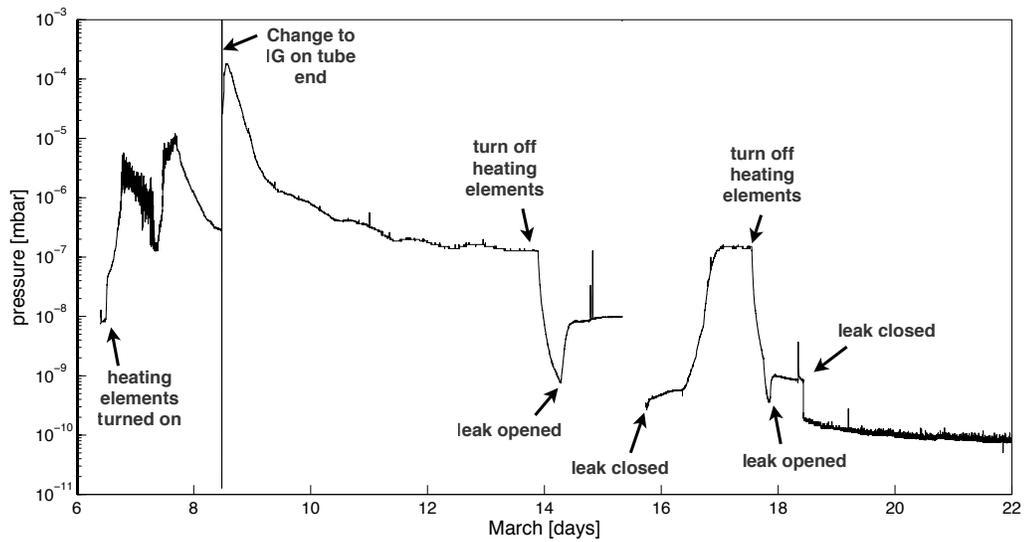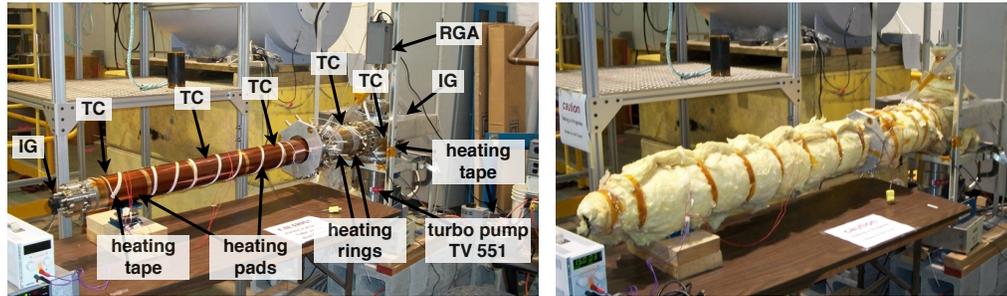
Figure 3.36: Top: Pictures of the baking setup for the vacuum tube with the trap structure, injection and extraction optics. The baking was monitored by two ion gauges (IG), a set of thermocouples (TC), and a residual gas analyzer (RGA). Several heating elements were mounted on the tube and the cross with the turbo molecular pump. The development of the pressure during and after the baking is shown in the plot at the bottom. A vacuum leak opened twice during a cool-down phase and was closed by tightening the bolts on the CF flange.

Chapter 4

Measurement and Analysis

Neutron-deficient Rb nuclides represent a very appealing isotopic chain for the first Penning trap mass measurements of HCI at a radioactive beam facility. The half-lives of $^{75-78}$Rb range from tens of seconds to minutes. Radioactive decay does not need to be considered for those cases because the typical measurement times with a single ion bunch at TITAN are much shorter than the respective half-lives. In combination with the high yields (Table 3.1) for nuclides closer to the valley of stability, this allows for optimal experimental conditions while approaching the measurement of ^{74}Rb. The relatively well known masses of ^{75,76}Rb with uncertainties of 1.6 and 1.2 keV [14], respectively, provide immediate benchmarks for the accuracy of the new measurement approach. Both nuclides have been measured at the ISOLTRAP facility and are considered to be very reliable. The strong physics motivation and the necessity for a new method with improved precision (Section 2.9) make ^{74}Rb itself most interesting among neutron deficient Rb isotopes. Its short half-life of 65 ms further gives insight about the feasibility of the technique with respect to the lowest lifetimes measurable with Penning trap mass spectrometers. Moderate yields of a few thousand ions per second highlight the relationship between loss in efficiency due to the additional step of charge breeding in contrast to the gain in precision due to the higher charge state.

Finally, a long lived isomeric state (with a half-life of 5.7 min) is known for ^{78}Rb, which lies only 111.19(22) keV above the ground state [212]. This corresponds to a resolving power of $R \approx 6.5 \cdot 10^5$. Although isomer and ground state have been resolved before in a Penning trap [213], the case can illustrate the potential of HCI for isomer research in Penning traps. This approach is particularly well suited for low lying isomers with half-lives of 100's of ms.

This chapter will provide details about the mass measurement and its analysis of highly charged $^{74-76,78m,78}$Rb as well as ^{74}Ga. The latter was a contaminant in the

$A = 74$ beam from ISAC. Systematic uncertainties will be discussed which also include measurements involving stable nuclides with well known masses as a cross check.

4.1 Measurement summary

The experimental facility was prepared previous to beam delivery from ISAC with a beam of stable ^{85,87}Rb from TITAN's own surface ion source (see Chapter 3). A study to benchmark systematic uncertainties was carried out during this time. The ion-optic tune from ISAC to TITAN was established with a 20 keV ISAC beam of stable ^{69}Ga. Its intensity of ≈ 160 pA made the beam detectable on Faraday cups and allowed for better tuning of the beam into the RFQ and adjustments of RFQ parameters. During this process the RFQ was operated in a DC mode, i.e. ions were passing through the RFQ without being trapped longitudinally. A DC transfer efficiency of ≈ 75 % was reached which compared well with the RFQ's typical performance [134]. Once optimized, the only parameters to be adjusted for different masses were mass dependent parameters such as beam transport timings and in some cases RF-frequency and amplitude or buffer gas settings in the RFQ. The rest of the TITAN beamline remained unchanged because the transfer beam energy was controlled by the PLT after the RFQ. Hence, modifications were not required in comparison to the preparation tune. Complementary to the ISAC beam, stable beam of ^{85}Rb or ^{87}Rb could be delivered from TRIUMF's Off-Line Ion Source (OLIS) [214] at the same beam energy as the ISAC beam. Access to an ion species with well known mass was necessary to calibrate the magnetic field in MPET to the required level of precision (see Section 3.7.5). Determining the Q_{EC}- value of ^{74}Rb directly as outlined by Equation 3.51 was not possible because ^{74}Rb and its daughter nuclide ^{74}Kr could not be delivered due to different chemical properties and would have required different target- ion source combinations. The stable Rb beam from OLIS was preferable over TITAN's own offline source because OLIS could provide dipole-magnet based mass separated and consequently contamination free ^{85}Rb or ^{87}Rb beam. In contrast, the beam from TITAN's offline source was a combination of various alkali metals. Although the RFQ provided a mass selectivity, its resolving power was not high enough to separate the two stable isotopes of Rb. ^{85}Rb and ^{87}Rb could only be distinguished in TOF after extraction from the RFQ or EBIT. In the aim for the most identical experimental conditions for reference ions and radioactive ion of interest, OLIS was the better alternative even for stable Rb beam. An initial plan to deliver stable ^{74}Ge from OLIS could not be realized this time. Providing a reference ion of the same mass number as ^{74}Rb would have reduced systematic uncertainties (see Section 4.3) and ^{74}Ge's atomic mass with a precision of 0.2 PPB [215] is very well known.
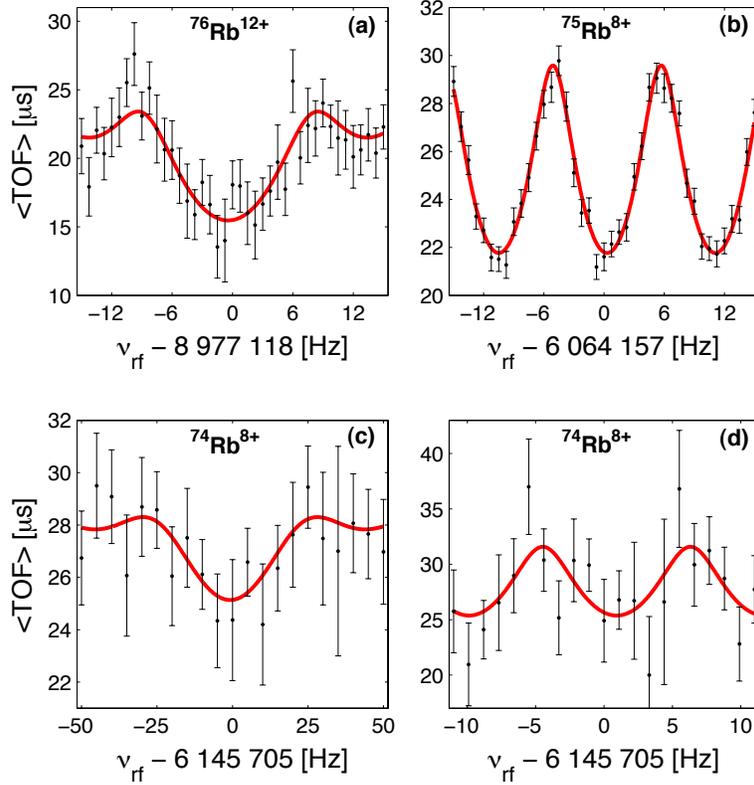
Figure 4.1: Time-of-flight ion-cyclotron resonances for Rb-isotopes in charge state $q = 8+$ and $q = 12+$. During (a) and (c) the RF- field was continuously applied for $T_{\mathrm{rf}} = 97$ ms and 30 ms, respectively, and a Ramsey excitation scheme with 6-85-6 ms was utilized in (b) and (d). The solid (red) lines represent the fit to the theoretical line shapes [178, 185].

The measurements of radioactive Rb isotopes were performed with charge states $q = 8+$ and $q = 12+$. The magnetic field was calibrated by measurements of $^{85}\mathrm{Rb}^{9+}$. The charge state $q = 9+$ was chosen as the reference to minimize the difference in m/q between the radioactive $q = 8+$ ions and the reference ions because a number of systematic effects are proportional to this difference (see Section 4.3). Typical resonances of radioactive Rb isotopes are displayed in Figure 4.1. Both, conventional quadrupole and Ramsey excitations were applied in the course of the measurement. $^{74}\mathrm{Ga}$ was the dominat contribution to the $A = 74$ beam and its mass was also determined in a set of measurements. The required resolving power be-
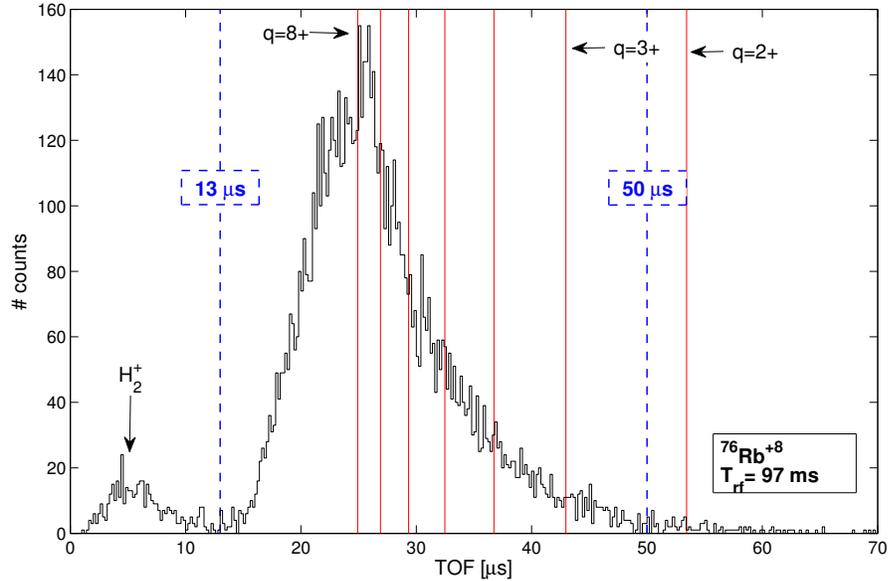
Figure 4.2: A TOF histogram of detected ions after they were released from the MPET. In addition to ^{76}Rb^{8+}, a peak corresponding to H$_2^+$ was observed, which was due to charge exchange in the MPET between the stored HCI and the residual gas. See text for details.

tween ^{74}Rb and ^{74}Ga was slightly above the performance of the resolving power of the ISAC mass separator. Nevertheless, it could be fine tuned to a more favourable ratio between the two components of the beam at the expense of a lower absolute ^{74}Rb yield. For the purpose of this fine adjustment, singly charged $A = 74$ beam was brought directly into MPET by bypassing the EBIT entirely (compare with Figure 3.19). In consecutive measurement runs the dipole cleaning (Section 3.7.6) was applied at the mass selective reduced cyclotron frequency ν_+ for ^{74}Rb$^+$ and ^{74}Ga$^+$. The number of ions lost because of the dipole RF-field at the respective ν_+ was interpreted as an indicator for the number of ions in the beam for Rb or Ga. The ISAC mass separator magnet and slits were adjusted until ^{74}Rb represented the majority in the beam. Then, the mass measurement continued with HCI.

Figure 4.2 is a TOF histogram of all detected ions during a measurement run of ^{76}Rb^{8+} irrespective of the applied RF- frequency ν_{rf}. The main peak in the TOF histogram corresponded to ^{76}Rb^{8+} ions which were initially injected into the MPET.
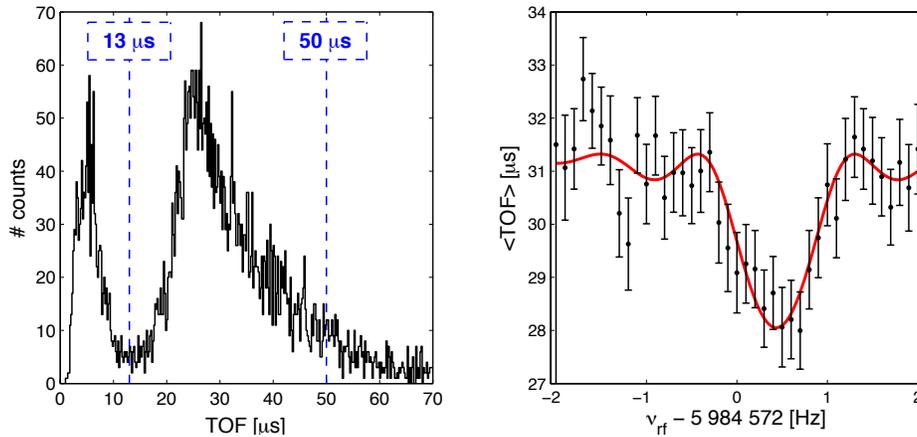
Figure 4.3: TOF histogram (left) and TOF resonance (right) for ^{76}Rb^{8+} with an excitation time of $T_{\text{rf}} = 997$ ms. In comparison to Figure 4.2 the peak corresponding to H$_2^+$ (at ≈ 5 μs) was more prominent.

An additional peak at a TOF of ≈ 5 μs was due to charge exchange of the stored HCI with residual gas in the MPET. Previous work established that it represented H$_2^+$ ions as the application of a dipole excitation at ν_+ of H$_2^+$ removed this peak. For longer storage times of the HCI in the MPET larger peaks associated with charge exchange appeared. This indicated that despite the improvements in the vacuum quality of the MPET (Section 3.7.8) charge exchange could not be avoided entirely. However, for an excitation time of $T_{\text{rf}} = 97$ ms the fraction of ions which underwent charge exchange remained at an acceptable level (Figure 4.2); the number of counts in the H$_2^+$ peak was only $\approx 5\%$ of all detected signals. Hence, the majority of the online mass measurement was carried out with the excitation time $T_{\text{rf}} = 97$ ms. This corresponded to a 10 Hz repetition rate, i.e. the rate at which ions were extracted from the RFQ. In fact, the HCI could be held much longer in the MPET and a measurement with a quadrupole time of $T_{\text{rf}} = 997$ ms was performed as well (hence at a 1 Hz repetition rate). Although the charge exchange was a more severe problem in this case, a TOF- resonance of ^{76}Rb^{8+} could be recorded (see Figure 4.3).

As these measurements are carried out with only a few ions (typically 1-5) in the trap at a time to minimize frequency shifts by ion-ion interactions (compare Section 4.2.1), the ISAC beam of ^{76}Rb had to be attenuated to reduce the number of ions in MPET to the desired level.

A TRIUMF site-wide power-outage at the end of the ^{74}Ga mass determination trig-

133

gered a turbo pump failure in the EBIT, which required the reconditioning of the electron beam and a re-tuning of the beam transfer from the EBIT to the MPET previous to the ^{74}Rb mass measurement. As a consequence, another set of measurements to cross check the accuracy of the setup had to be performed between ^{74}Rb measurement runs, since the comprehensive systematic tests performed before the power-outage could not reliably be applied to the data obtained after the reconditioning.

Finally, the ground and isomeric state of ^{78}Rb were studied in the MPET. As the energy difference between the two states is only 111.2 keV it represented an interesting case to demonstrate the improved resolving power for low lying isomeric states when working with HCI. In order to show the relationship between high charge state and excitation time in the resolving power, the measurements were performed with $T_{\mathrm{rf}} = 97$ ms and $T_{\mathrm{rf}} = 197$ ms.

4.2 Analysis

The analysis of the data was separated into two main parts. First, the cyclotron frequency ν_c was determined for each measurement run by fitting the resonance data with Equation 3.39 and the theoretical line shapes [178, 185]. In the second part, individual frequency ratios (Equation 3.49) were summarized to weighted averages from which the atomic mass was determined (Equation 3.50).

4.2.1 Determination of the cyclotron frequency ν_c

Following Section 3.7.3, the raw data recorded during a measurement of a cyclotron resonance consisted of TOF measurements of ions which were released from the MPET at a certain RF- frequency ν_{rf}. Hence, for each ion bunch the number of counts at the MCP detector, their respective TOF, and the applied ν_{rf} was stored. As discussed in Section 3.7.3 the amount of damping was a free parameter in the fitting function. To obtain ν_c the analysis procedure described below was followed.

Data selection

H_2^+ originating from charge exchange did not respond to the RF-excitation due to its different (mass dependent) cyclotron frequency which was outside the ν_{rf}-scanning range. Hence, the counts of ions at the MPET MCP detector associated with H_2^+ (compare to the TOF histograms of Figure 4.2 and Figure 4.3) would have reduced the quality of the actual resonance of a Rb- isotope. The peak in the TOF spectrum corresponding to H_2^+ was excluded from the analysis. Analogously,

HCI which had picked up an electron from the residual gas while stored in the MPET were subsequently insensitive to the RF- excitation. Consequently, the TOF- range which was considered in the analysis was fixed by the TOF- distribution for very short excitation times ($T_{\rm rf} \approx 10$ ms) for which charge exchange was negligible. Hence, only counts in the TOF-range of 13-50 μs were selected for the analysis. In the measurement of ^{76}Rb^{12+} it was extended to 10-50 μs. The considered range is indicated in TOF histograms of Figure 4.2 and Figure 4.3 by labeled vertical lines. As shown in Figure 4.2 other charge states resulting from charge exchange could have fallen into the same TOF range. Ambiguities related to this choice of the considered TOF- range and potential systematic effects are described in Section 4.3.7.

The cut on the data also excluded a large fraction of background counts which were recorded without a fixed time relation to the release of ions from the MPET. At the mostly used repetition rate of 10 Hz, the number of these background counts after 50 μs in the recorded TOF window (which spanned over 0-200 μs) was a few 10's per hour of measurement.

An additional selection criterion was applied to each ion bunch as a whole. To minimize potential shifts in ν_c due to the interactions between ions stored in the MPET at the same time, only ion bunches with 1-5 detected ions per bunch were processed in the analysis. These shifts were observed experimentally (e.g. in [213]) when ions of different ion species were simultaneously kept in the trap.

TOF uncertainty

In order to obtain the measured TOF-resonance (such as in Figure 4.1) the raw data had to be sorted according to the RF-frequency applied to each trapped ion bunch. After the cut on the TOF range was made the mean TOF, $\overline{T}_k$, was calculated for ion bunches with the same applied $\nu_{\rm rf,k}$. In previous work, the variance on $\overline{T}_k$ was obtained by considering the width of the TOF distribution irrespective of $\nu_{\rm rf,k}$

$$\sigma^2(\overline{T}) = \frac{\sum_{i=1}^{N}(T_i - \overline{T})^2}{N - 1},\tag{4.1}$$

where N was the number of ions in the selected TOF- range, T_i was the TOF of each ion, and $\overline{T} = (\sum_{i=1}^{N} T_i)/N$. The variance on $\overline{T}_k$ was assigned according to

$$\sigma^2(\overline{T}_k) = \frac{\sigma^2(\overline{T})}{N_k}\tag{4.2}$$

with N_k being the total number of counted ions at $\nu_{\rm rf,k}$. This procedure is called the sum-statistics method. Recently, it has been pointed out [216] that from a statistical

point of view the approach was not exact because it assumed T_i to be independent of $\nu_{\mathrm{rf},k}$. This is opposed to the measurement principle of ν_c itself. In fact, for measurement runs with a sufficient number of ion counts per ν_{rf}, the sum-statistics is too conservative and overestimates the uncertainty.

Although the correct statistical treatment was tested, the present analysis continued to use the sum-statistics method. This was motivated by two reasons. First, for measurement runs with very few counts for a given RF-frequency $\nu_{\mathrm{rf},k}$ the sum statistics approach was considered to be more appropriate [216]. The second reason is related to possible line shape distortions when working with HCI, e.g. due to charge exchange (compare for instance with the discussion on damping in Section 3.7.3). When the correct statistical treatment was utilized, the typical χ^2 was larger than what was expected from the degrees of freedom in the fit. This situation would require the inflation of the uncertainties on the fit parameters in order to account for potential line shape distortions. However, when the sum-statistics method was applied, the distribution of χ^2 in the line-shape fits followed the statistical expectation (see Figure 4.4). Hence, in order to take full advantage of the correct statistical treatment of the data in future work, the measured line shapes have to be investigated.

Count class analysis

To address previously mentioned potential shifts in ν_c due to ion-ion interaction, a so-called count-class [217] analysis was performed. In this method, data from a measurement run were grouped according to the number of detected ions per ion bunch, usually into three groups. The resonance of each group was fitted separately to determine a cyclotron frequency. Trends in the cyclotron frequency as a function of detected ions per ion bunch could be investigated and ν_c was extrapolated to the case of a single ion stored in the Penning trap. Considering the detector efficiency of the MCP, this corresponds to $\epsilon = 0.6 \pm 0.2$ detected ions [118]. Due to charge exchange of HCI, ions in different charge states could be present in the trap even when a contaminant free beam had been captured in the MPET. Hence, a count-class analysis was performed for all online measurements provided that a run had sufficient number of counts (typically a few thousand) to separate the data into three classes.

4.2.2 Determination of the frequency ratio

The frequency ratio $R = \nu_{c,r}/\nu_c$ between the ion of interest (ν_c) and the reference ion ($\nu_{c,r}$) was calculated by linearly interpolating the $\nu_{c,r}$ to the mid- time of the measurement run to determine ν_c as discussed in Section 3.7.5 (compare
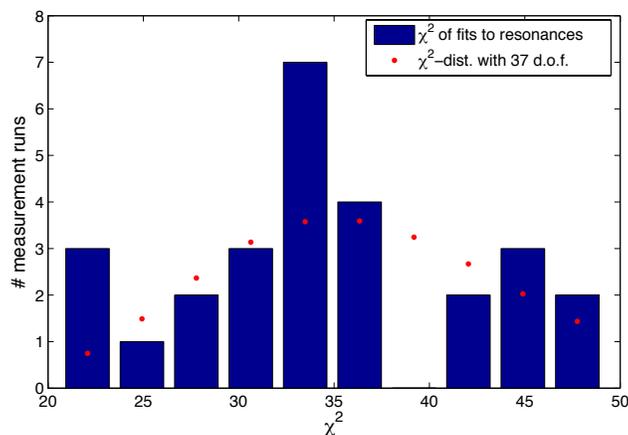
Figure 4.4: A histogram of χ^2 from fits of the theoretical line shape to experimental resonances is compared to the expectation of the statistical χ^2-distribution. Each fit was based on 41 data points in a resonance and 4 free parameters (ν_c, the initial ρ_-, the TOF-offset, and the damping parameter), hence 37 degrees of freedom. For the resonance data, the sum-statistics method was used for the determination of the uncertainty of the TOF-measurements. The experimental data is a measurement set of ^{87}Rb^{9+} versus ^{85}Rb^{9+} which was performed previous to the online measurement.

with Figure 3.30). As a measure to maximize the use of available radioactive beam reference measurements were shared between consecutive measurement runs of the ion of interest (see Figure 4.5). Consequently, these frequency ratios were not statistically independent. These correlations due to shared reference measurements have so far not been considered in the literature. However, owing to the potential of HCI for the precision of mass measurement, correlations between frequency ratios were accounted for in the present work. The derivation of the complete covariance matrix to reflect these correlations is done in Appendix B.

4.2.3   Analysis software

For the present analysis, a new software package was developed which automated most of the analysis and allowed efficient investigations of the results as a function of various fitting settings. It consisted of a resonance fitting program [218], a sorting code to coordinate the fitting of individual measurement runs and to extract (averaged) frequency ratios and masses, and several plotting routines. As a cross
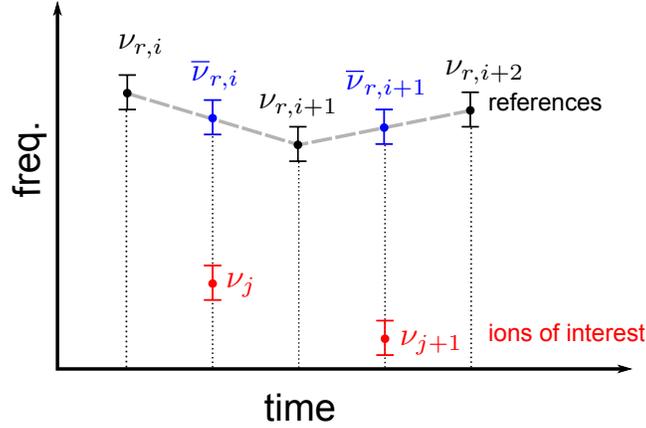
Figure 4.5: Origin of correlations between measured frequency ratios. The reference ion's cyclotron frequency is linearly interpolated to the mid-time of a measurement run of the ion of interest. When the same reference measurement (e.g. $\nu_{r,i+1}$ in this plot) is used for the interpolation of ν_r to two measurement runs (ν_j and ν_{j+1}), these two frequency ratios are statistically correlated.

check, a large part of the analysis was also performed with previously established software packages such as EValuation and Analysis (EVA) [219] for fitting the theoretical resonance line shapes to the TOF data and Simple Online Mass Analysis (SOMA) [220] for the calculation of frequency ratios and masses.

4.2.4 Analysis results

^{76}**Rb**

The data for ^{76}Rb were separated into four groups. Three sets of measurements were carried out in the conventional quadrupole excitation. This set consisted of three groups: firstly, measurements of ^{76}Rb^{8+} with an excitation time of $T_{\mathrm{rf}} = 97$ ms, secondly, two measurement runs with Rb-ions in a higher charge state (^{76}Rb^{12+} with $T_{\mathrm{rf}} = 97$ ms), and finally ^{76}Rb^{8+} resonances with an extended excitation time of $T_{\mathrm{rf}} = 997$ ms. All reference measurements to calibrate the magnetic field were based on ions of ^{85}Rb^{9+} with an excitation time of $T_{\mathrm{rf}} = 97$ ms. The last set consisted of measurements with the Ramsey excitation mode. Two RF pulses were applied for $\tau_1 = 6$ ms interrupted by a waiting period $\tau_0 = 85$ ms
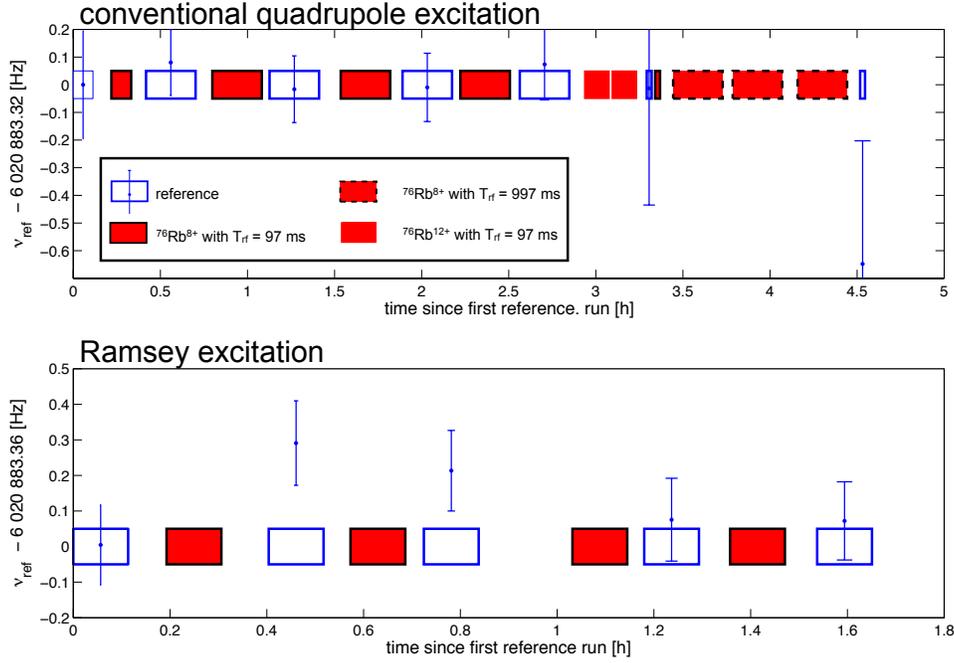
Figure 4.6: The time and durations of measurements for reference ions ^{85}Rb^{9+} and for radioactive ^{76}Rb ions in charge state $q = 8+$ and $12+$ are indicated by rectangles. For the reference ions the measured cyclotron frequency is shown on the vertical axis.

(which is labeled 6-85-6 ms in Figure 4.1) adding again to a total measurement time of $T_{\mathrm{rf}} = 97$ ms.

The relative time and durations of individual measurement runs for ^{76}Rb and its references are shown in Figure 4.6. The scatter of the reference measurements are also displayed. Measurements with $T_{\mathrm{rf}} = 97$ ms of ^{76}Rb^{8+} were always alternated with calibrations with ^{85}Rb^{9+} as these were the main data of the ^{76}Rb mass determination. The supplementary data sets of $T_{\mathrm{rf}} = 997$ ms excitations or in charge state $q = 12+$ were each performed between two reference measurements.

In Figure 4.7a, the error contributions to the frequency ratios for individual ^{76}Rb^{8+} measurements due the cyclotron frequency of ^{76}Rb^{8+} and of the (interpolated) reference are shown. The individual frequency ratios themselves are plotted in Figure 4.7b together with the weighted averages for each set. The latter's uncertainty also includes the correlations due to shared reference measurements.

The effect of taking correlations into account was studied in Figure 4.8. In (a),

139
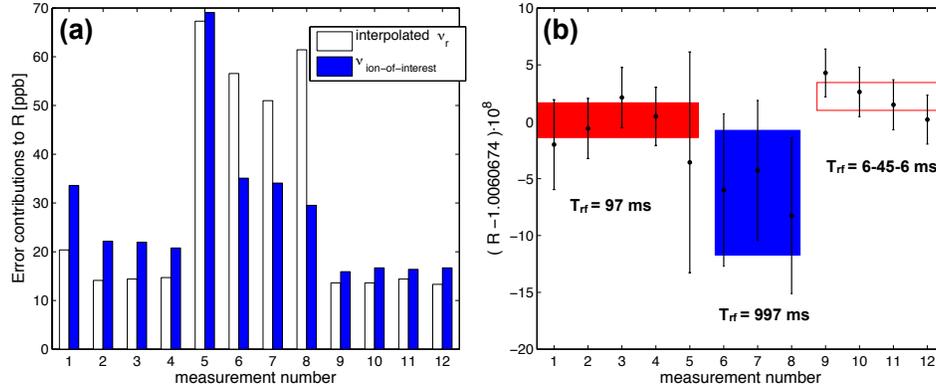
Figure 4.7: Measurements of ^{76}Rb^{8+}. All reference measurements of ^{85}Rb^{9+} were performed with a conventional excitation of $T_{\mathrm{rf}} = 97$ ms or with a Ramsey scheme of 6-85-6 ms, while ^{76}Rb^{8+} was split into sets of measurements with $T_{\mathrm{rf}} = 97$ ms and $T_{\mathrm{rf}} = 997$ ms in the conventional excitation and of a Ramsey scheme with 6-45-6 ms.
(a) contributions to the frequency ratio R due the uncertainty in the cyclotron frequency of the reference ion and the ion of interest.
(b) Individual R. The shaded areas represent the weighted average with uncertainties including correlations between the individual R.

all measurements of the ion of interest were separated by reference data. Due to correlations, the central value shifted by $\approx 8\,\%$ of the statistical uncertainty, which itself was increased by about a tenth of its value. Figure 4.8b was the special case that all three measurements shared both references, i.e. the three runs were taken in between two references (compare also to Figure B.1). Here, the correlations substantially inflated the uncertainty. As these three measurement runs were very close in time (see Figure 4.6), an alternative approach was to add their data together and to fit the resonance. This should implicitly take all correlations between the individual runs into account. As seen in Figure 4.8b, this result was indeed almost identical to the analysis of the individual runs demonstrating the importance to consider the correlations for this case. Table 4.1 summarizes all measurements of ^{76}Rb.

^{75}Rb

All data for ^{75}Rb were taken in charge state $q = 8+$ and with the Ramsey excitation method. As mentioned in Section 3.7.4, the side-minima in Ramsey schemes
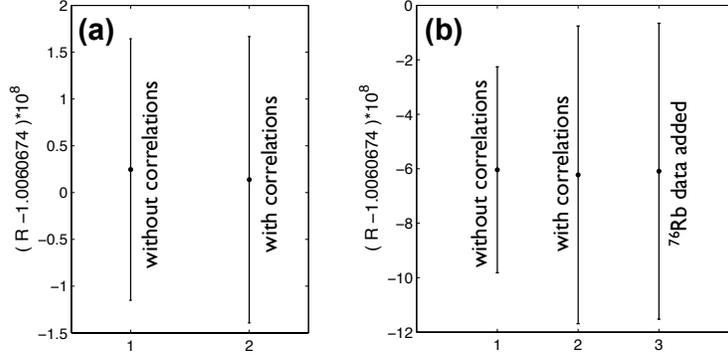
Figure 4.8: Implications of correlations due to shared references studied with $^{76}\text{Rb}^{8+}$ measurement runs.

(a) The weighted average for R of the data with a conventional $T_{\text{rf}} = 97$ ms excitation is displayed with and without taking correlations into account. With correlations the central value is shifted by ≈ 8 % of the uncertainty σ. σ itself is increased by $\approx \sigma/10$.

(b) Same as (a) but for the $T_{\text{rf}} = 997$ ms data. According to Figure 4.6 this is a special case, because all three runs share both references. When the data of the three runs are added together and analysed (3), its central value and uncertainty is essentially identical to (2), where correlations are taken into account between the three individual measurement runs.

Table 4.1: Averaged frequency ratios (with correlations) of $^{76}\text{Rb}^{q+}$ with respect to $^{85}\text{Rb}^{9+}$ ions. The table lists the charge state q, the excitation mode, the excitation time, the number of measurements per set, and the resulting frequency ratio R. Except for $q = 12+$, R are based on a count-class analysis and the given errors are statistical uncertainties. The count rate for $^{76}\text{Rb}^{12+}$ was too low to perform a count-class analysis with the recorded data.

q of ^{76}Rb	excitation mode	T_{rf} [ms]	# measurements	R
8^+	conventional	97	5	1.006067401(15)
12^+	conventional	97	2	0.670692259(23)
8^+	conventional	997	3	1.006067338(55)
8^+	Ramsey	6-85-6	4	1.006067422(12)
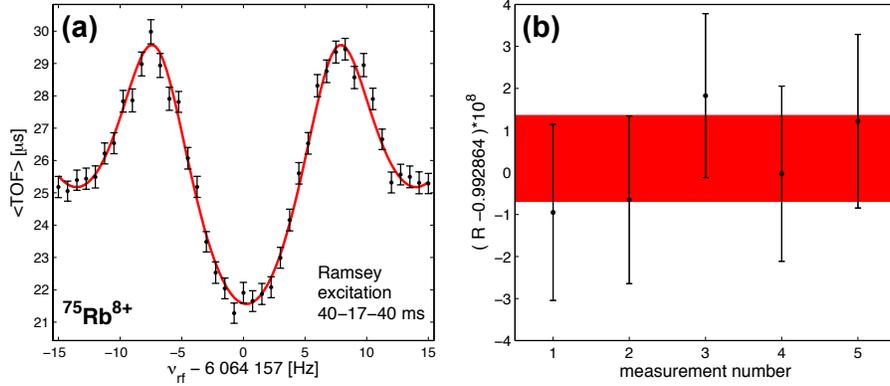
Figure 4.9: Measurement of $^{75}\mathrm{Rb}^{8+}$. The position of the main minimum corresponding to the cyclotron frequency of $^{75}\mathrm{Rb}^{8+}$ was determined with a Ramsey scheme of 40-17-40 ms such as (a) which had less pronounced side minima. In (a), these side minima are close to the edges of the frequency scanning region. Individual frequency ratios for measurements of $^{75}\mathrm{Rb}^{8+}$ with respect to $^{85}\mathrm{Rb}^{9+}$ with a Ramsey excitation of 6-85-6 ms are shown in (b). The error band corresponds to the weighted average with correlations considered.

are indistinguishable from the main minima when the application time τ_1 is much shorter than the waiting period τ_0. In order to determine the position of the main minimum which corresponded to ν_c of $^{75}\mathrm{Rb}$, a Ramsey scheme of 40-17-40 ms was employed in which the side maxima were much less pronounced [178]. An example of such a measurement run is shown in Figure 4.9a. Once the main minimum was unambiguously identified, the data taking was continued with the more precise 6-85-6 ms excitation scheme. A count-class analysis of ν_c of $^{75}\mathrm{Rb}^{8+}$ did not reveal frequency shifts due to potential contamination of $^{75}\mathrm{Ga}^{8+}$ (see Table 3.1). Assuming a linear dependence of ν_c on the number of detected ions, the weighted average of the slope was $k = 0.01 \pm 0.03$ Hz/(# detected ions), consistent with zero.

The individual frequency ratios of the $^{75}\mathrm{Rb}$ data set are displayed in Figure 4.9b. Table 4.2 contrasts the averaged frequency ratio with and without correlations due to shared reference measurements. The central value was relatively insensitive to the correlations, but the uncertainty was increased by $\approx 12\%$.

Table 4.2: Weighted average for the frequency ratio $R = \nu_r/\nu$ of $^{75}\text{Rb}^{8+}$ and $^{85}\text{Rb}^{9+}$. The table lists the resulting weighted average with and without correlations. Between all measurements of $^{75}\text{Rb}^{8+}$, a reference of $^{85}\text{Rb}^{9+}$ was taken. The period between the mid-time of two reference runs was typically 25 min. The uncertainties are statistical only.

averaging method	R
without correlations	0.9928640032(91)
with correlations	0.9928640034(102)
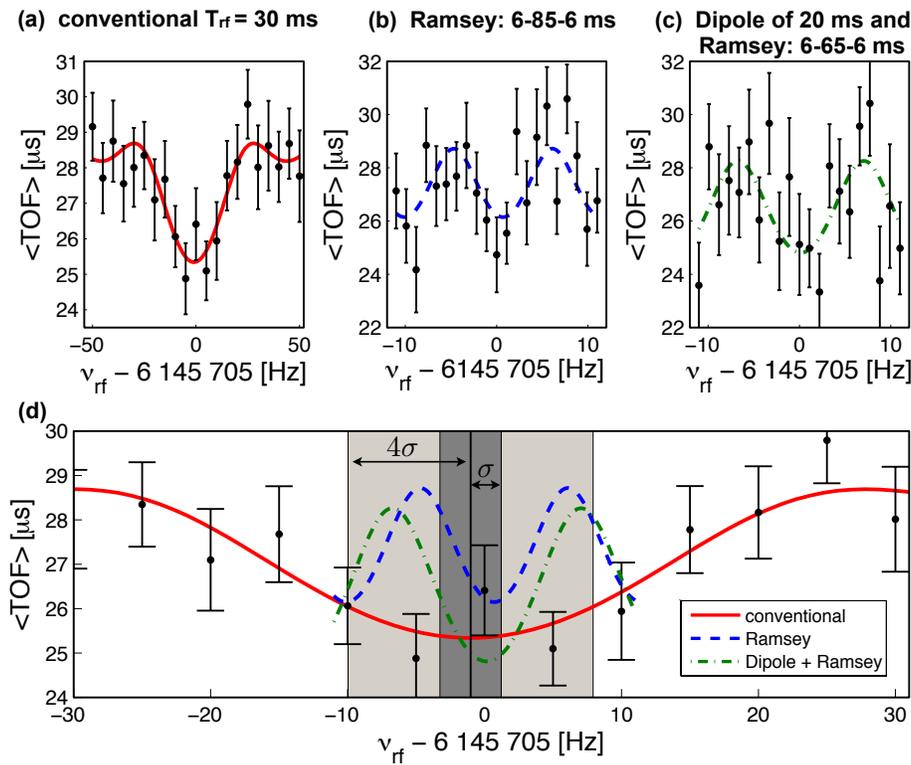
Figure 4.10: Main TOF minimum for $^{74}\text{Rb}^{8+}$. (a)-(c) are the TOF resonances and fits when all runs of one measurement setting are added. In (d) it is confirmed that the main minimum in TOF corresponding to ν_c of $^{74}\text{Rb}^{8+}$ was determined correctly. The statistical uncertainties on ν_c for (b) and (c) were < 0.7 Hz. See text for details.

^{74}Rb

Measurement and analysis of ^{74}Rb^{8+} differed from the previous cases because of the significantly reduced yield and the ^{74}Ga contamination. Hence, measurements of ^{74}Rb^{8+} could last up to ≈ 5 h before a new reference was taken. This spread between reference measurements was longer than the normally aimed 1 h separation, but in comparison to the achieved precision systematic shifts due to non linearities in the magnetic field decay were negligible (see Section 4.3.5).

In order to determine the cyclotron frequency of ^{74}Rb^{8+} sufficiently well before switching to the more precise Ramsey method, a data set were taken with a conventional quadrupole RF- field. The low count-rate and the limited availability of radioactive beam from ISAC required an adaption of the previously used strategy for the other Rb-isotopes, where a precise enough ν_c could be determined within an hour or less. For ^{74}Rb^{8+}, a shorter excitation time of $T_{\rm rf} = 30$ ms reduced ion losses due to radioactive decay. Then, data was taken and added together until the statistical uncertainty on ν_c of ^{74}Rb^{8+} was smaller than a fourth of the difference between the sidebands and the main TOF minimum of a Ramsey excitation with 6-85-6 ms (compare with Figure 4.10). Although references were recored in between, this required the addition of measurement runs which were more than 5 hours separated in time. The linear field decay of the superconducting magnet had been determined in an extensive study to be < 0.25 PPB/h [124]. Prior to the radioactive beam of Rb a separate verification was carried out by a measurement, however, at lower precision. The decay was confirmed to be smaller than < 1 PPB/h. Hence, to determine ν_c within ~ 3 Hz when adding all data was considered sufficiently reliable.

Afterwards, measurements utilizing the Ramsey method were carried out in two configurations, starting first with 6-85-6 ms excitations. In a second set, a dipole RF- field was applied for the first 20 ms of the ion storage time in MPET. With its frequency at ν_+ of ^{74}Ga^{8+}, the RF- field mass selectively drove remaining contaminating ions to a larger radius or out of the trap. This avoided ion-ion interaction between ^{74}Ga and ^{74}Rb. More importantly for low count rates, contaminating ions driven to a larger radius could not pass through the extraction hole in the end cap electrode. Hence, detected signals on the MCP detector due to ^{74}Ga could no longer add to the background and the sensitivity of the measurement was increased. After the period with the dipole RF-field, a Ramsey excitation of 6-65-6 ms was applied.

Individual frequency ratios and their partial uncertainties due to reference ions and ions of interest are shown in Figure 4.11. Data in (b) are grouped according to the three measurement settings. The low count rate excluded a count-class analysis and all detected ions were considered in the analysis. For the same reason, it
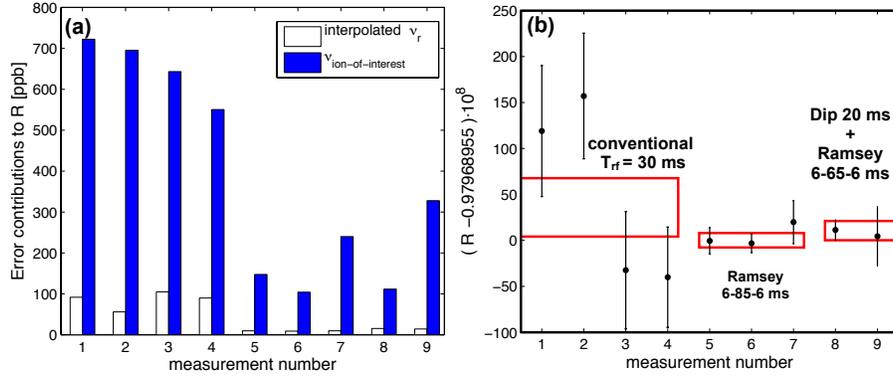
Figure 4.11: Frequency ratios $R = \nu_r/\nu$ of measurements of $^{74}Rb^{8+}$ with $^{85}Rb^{9+}$ as the reference ion. The contributions to the uncertainty of R due to reference measurements is small (a).

Table 4.3: Results for $R = \nu_r/\nu$ of measurements of $^{74}Rb^{8+}$ with $^{85}Rb^{9+}$ as the reference. Since the count rate was too low for a count-class analysis, the data were analyzed once for ion bunches with 1 detected ion and a second time with 1-5 detected ions. The statistical uncertainty is given in brackets.

setting [ms]	analysis	R	difference
Ramsey 6-85-6	1 ion	0.979689548(79)	
	1-5 ions	0.979689552(79)	5% of σ
Dip.+Ramsey 6-65-6	1 ion	0.979689619(108)	
	1-5 ions	0.979689656(104)	35% of σ

was rare that two or more ions were injected simultaneously into the MPET. Thus, ion-ion interaction with contaminating ions of ^{74}Ga was very unlikely to have an effect on the frequency ratio. However, to be conservative a second analysis was performed considering only ion bunches with one detected ion. The results of both analyses are shown in Table 4.3. The difference in the frequency ratio between the two analyses was added in quadrature to the statistical uncertainty.

^{74}Ga

The results of the four measurement runs with $^{74}Ga^{8+}$ are plotted in Figure 4.12. Although the number of ions was slightly higher for ^{74}Ga it was not possible to
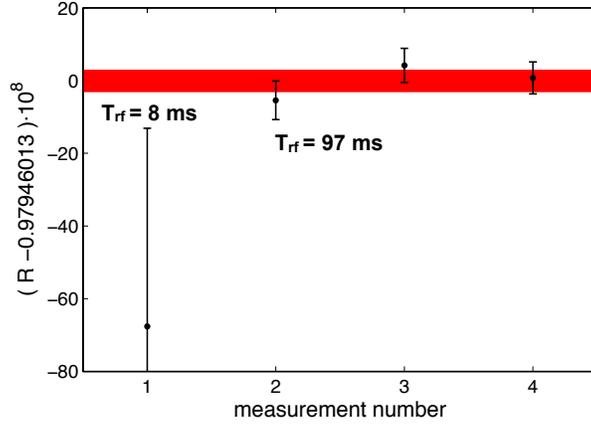
Figure 4.12: Measurements of the frequency ratio $R = \nu_r/\nu$ for ^{74}Ga^{8+} with ^{85}Rb^{9+} as the reference.

Table 4.4: Results for $R = \nu_r/\nu$ of measurements of ^{74}Ga^{8+} with ^{85}Rb^{9+} as the reference. Since the count rate was too low for a count-class analysis, the data were analyzed once for ion bunches with 1 detected ion and a second time with 1-5 detected ions. The statistical uncertainty is given in brackets.

analysis	R	difference
1 ion	0.979460108(47)	
1-5 ions	0.979460129(29)	72 % of σ

process the data using a count class analysis. To be conservative, the result was compared to an analysis which considered only ion bunches with one detected ion. The statistical uncertainties for the two analyses differed by a factor ≈ 1.6 in contrast to ^{74}Rb where both were almost identical (Table 4.3). This was a consequence of the higher count rate, i.e. there were more ion bunches with two detected ions per bunch. Hence, the statistical correlations between the two were smaller.
As listed in Table 3.1, the isomer of ^{74}Ga was presented in the ISAC beam at a ratio of $\approx 1 : 190$ compared to the ground state. Considering the low probability of having more than one ion per ion bunch in the trap, shifts in ν_c are unlikely. Furthermore, due to the high charge state, the isomer would have been fully resolved and no weighting of ground state and isomer according to their respective yield as introduced in [107] and done in [14] was required.

Table 4.5: Differences in mass number A, m/q, and q/m for ion species studied in this work in comparison to the reference ion $^{86}\text{Rb}^{9+}$

nuclides	q	ΔA	$\Delta(m/q)$	$\Delta(q/m) \cdot 100$
^{78}Rb	8	7	-0.31	0.33
^{76}Rb	8	9	-0.06	0.06
	12	9	3.11	-5.20
^{75}Rb	8	10	0.07	-0.08
$^{74}\text{Rb},^{74}\text{Ga}$	8	11	0.19	-0.22

4.3 Systematic uncertainties

For any measurement with a statistical uncertainty of ~ 10 PPB as in the present studies, systematic errors have to be well understood. Moreover, the accuracy of the setup has to be at the same level or below in order to take full advantage of the achieved precision. General systematic uncertainties are discussed for the TITAN MPET in [146, 205] and apply for both HCI and SCI. These are briefly discussed first while specific systematic effects for HCI and the present studies will be described later. As a general remark, the majority of the systematic uncertainties depend on the difference in m/q (or q/m) between the reference ion and the ion of interest which we define as $\Delta(m/q) = m_r/q_r - m/q$. This is a consequence of the determination of the mass by means of a frequency ratio R, where many systematic shifts on the frequency measurement cancel out in R. Because of the $\Delta(m/q)$ dependence, it is desirable to have access to a reference ion with a similar mass-to-charge ratio. For SCI, ions from elements with the same mass number A are not always available and $\Delta(m/q) = \Delta A \approx 10$ or larger is not uncommon. As a specific charge state can be selected when working with HCI, $\Delta(m/q)$ can be minimized even for larger mass differences. Hence, the use of HCI not only leads to more precise but also more accurate measurements provided that effects unique to HCI are understood. As shown in Table 4.5 for differences in the presented measurement, $\Delta(m/q)$ are 1-2 orders of magnitude smaller than ΔA and reduce the respective systematic errors accordingly. In the following, all systematic effects will be studied in terms of relative shifts in the frequency ratio,

$$\frac{\Delta R}{R} = \frac{R_{\text{measured}} - R_{\text{ideal}}}{R_{\text{ideal}}}. \tag{4.3}$$

4.3.1 Spatial magnetic field inhomogeneities

In a real Penning trap the magnetic field is not perfectly homogeneous due to the finite size of the magnet, field distortion caused by the trap material, etc. The associated induced frequency shifts are [177]

$$\Delta\nu_c = \beta_2 \Big[(z^2 - \rho_+^2) - \frac{\nu_-}{\nu_c}(\rho_+^2 + \rho_-^2) \Big] \tag{4.4}$$

where β_2 is the coefficient of the quadrupole component in the magnetic field which is the lowest order contribution to the field distortion. z, ρ_+, and ρ_- are the previously introduced (Section 3.7) amplitudes or radii of the axial and radial eigenmotions. At TITAN this effect is estimated to be [205]

$$\left| \frac{\Delta R}{R} \right| < 4.3 \cdot 10^{-11} \Delta(m/q), \tag{4.5}$$

when a trap potential of 35.75 V is considered.

4.3.2 Harmonic distortion and misalignment of the magnetic field axis

A non-vanishing angle θ between the axes of the magnetic and electric field and an elliptical distortion of the ring electrode (parameterized by the finite asymmetry parameter ϵ) lead to a frequency shift [221] [222][223] of

$$\Delta\nu_c = \Big(\frac{9}{4}\theta^2 - \frac{1}{2}\epsilon^2 \Big) \cdot \nu_-. \tag{4.6}$$

For TITAN this translates to [205]

$$\left| \frac{\Delta R}{R} \right| < 4.3 \cdot 10^{-10} \Delta(m/q), \tag{4.7}$$

again taking the used trap potential into account.

4.3.3 Non-harmonic imperfections of the trapping potential

The deviations from the ideal electric potential arise due to the truncation of infinite hyperboloids and the holes for injection and extraction in the end cap electrodes. The potentials on the tube and guard correction electrodes have been carefully adjusted [205] to achieve minimal deviations of the field in the trapping region. After confirming the trapping potential with well known masses, shifts in the frequency

ratio are assigned to be lower than [205]

$$\left|\frac{\Delta R}{R}\right| < 3.6 \cdot 10^{-10} \Delta(m/q). \tag{4.8}$$

4.3.4 Relativistic effects

Due to their high angular frequencies and thus larger velocities inside the Penning trap, relativistic effects have to be considered for HCI and light SCI. In TITAN's MPET, an ion of $^{74}\text{Rb}^{8+}$ has a velocity of $v/c \approx 2.6 \cdot 10^{-4}$ on a reduced cyclotron motion with a radius $\rho_+ = 2$ mm. Therefore, the relativistic γ factor deviates from the non-relativistic limit by $1 - \gamma \approx 33 \cdot 10^{-9}$ and the cyclotron frequency would be affected at a similar level. Relativistic effects on the frequency ratio have been studied in detail during the relative mass measurement of $^6\text{Li}^+$ to $^7\text{Li}^+$ [124]. By controlling the initial magnetron radius with different Lorentz steerer strengths (Section 3.7.7) and hence the velocity, the relativistic shifts could be investigated and corrected.

The limited availability of radioactive beam did not allow similar measurements to be performed directly. However, by considering the studies in [124] an estimate for $\Delta R/R$ due to relativistic effects could be obtained. The extension of the description in [124] for the Lorentz steerer configuration of the present work results in

$$\left|\frac{\Delta R}{R}\right| = \frac{a}{2} \cdot \Delta V_{\text{LS}}^2 \cdot \Delta(q/m) \tag{4.9}$$

where a is the proportionality constant independent of the Lorentz steerer strength ΔV_{LS}, m, or q. Here, both ion species (ion of interest and reference) are assumed to pass through the Lorentz steerer with the same steering strength as was the case during the present measurements. Based on [124], one obtains

$$\left|\frac{\Delta R}{R}\right| = 6.3 \cdot 10^{-8} \cdot \Delta(q/m) \tag{4.10}$$

when a value of $\Delta V_{\text{LS}} \approx 30$ V is used for the present work. This appears to be large in comparison to previous systematic errors, but as shown in Table 4.5 all $\Delta(q/m)$ are two orders of magnitude smaller than $\Delta(m/q)$.

4.3.5 Magnetic field stability

In addition to the linear field decay, temperature or pressure fluctuations in the LHe dewar of a superconducting magnet can cause non-linear field fluctuations. For this

reason the dewar is pressure stabilized. In [124], the stability of the magnetic field and its remaining short time ($\approx$ 10 min) to long time ($\approx$ 4 h) deviations from the linear field decay have been investigated. Its associated uncertainty is 0.04(11) PPB/h. For all measurements of this work except for ^{74}Rb reference measurements were at most 1 h apart. This leads to an upper limit for the systematic error of $\Delta R/R = 0.2$ PPB. In the case of ^{74}Rb, the measurement periods usually lasted $\approx$ 2.5 h although for one measurement run references were $\approx$ 5 h apart. Given the poorer statistical uncertainty of the ^{74}Rb measurement non-linear field fluctuations are negligible.

4.3.6 Image charges

As charged particles induce image or mirror charges on the surface of a conductor, there is an additional interaction between the stored ions and the Penning trap electrodes, which is more influential for HCI. This effect was studied in [224] for FT-ICR measurements. It was found that the reduced cyclotron frequency ν_+ and the magnetron frequency ν_- were shifted due to image charges. Since the shifts were of equal absolute value, but of opposite sign, the cyclotron frequency $\nu_c = \nu_+ + \nu_-$ itself remained unchanged. Following the quantum mechanical explanation of the quadrupole excitation in the TOF-ICR technique (Section 3.7.3), the photons of the RF-field would require the same energy to induce a conversion of an ion's magnetron to reduced cyclotron motion even when ν_+ and ν_- have changed, but $\nu_c = \nu_+ + \nu_-$ has not.
Additionally, the size of the effect scales with the trap dimension as d^{-3} reducing its impact at TITAN's MPET which is about a factor of 10 larger than the trap in [224]. SMILETRAP with a similar trap dimension and operating with the TOF-ICR technique reports negligible influences of mirror charges [114].

4.3.7 Ambiguity in the TOF-range selection

As discussed in Section 4.2.1 charge exchange led to different charge states in the MPET which could not be separated in TOF between the extraction at the trap and the MCP detector. Lower charge states besides the initial one could thus fit into the TOF- range which was selected for the analysis (see Figure 4.2). Similarly, the peaks corresponding to the HCI and H_2^+ overlapped in their tails. To investigate potential shifts in R due to ambiguities in the TOF- range the lower and upper limit was varied in an independent analysis from the initially fixed ranges (13-50 μs for $q = 8-9+$ ions). As the number of ions was reduced with narrower TOF intervals, a count class analysis was generally not performed.
Figure 4.13 provides an example of such a consistency check in which the lower
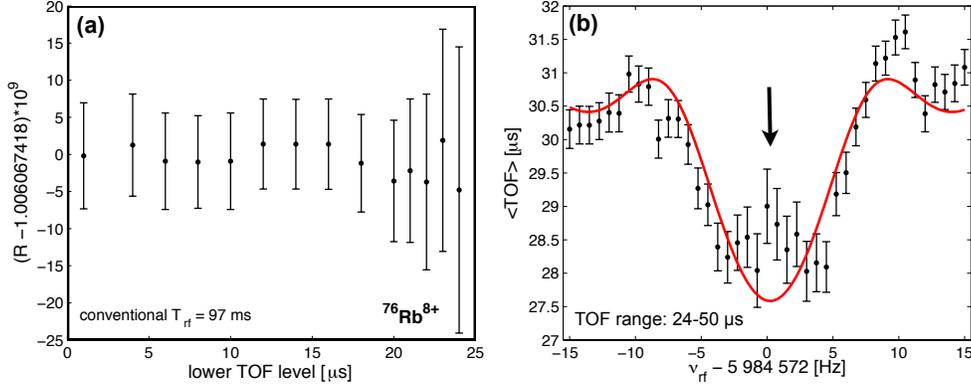
Figure 4.13: Dependency of the frequency ratio $R = \nu_r/\nu$ of ^{76}Rb^{8+} to ^{85}Rb^{9+} on the lower limit of the selected TOF- range (a). The data are from the measurement runs with the conventional excitation of $T_{\mathrm{rf}} = 97$ ms. Note that the uncertainties are not independent but highly correlated because they are based on very similar data. With increasing lower limit one starts to cut into the ion distribution for ions on resonance. As a consequence, the averaged TOF for ions with an RF- field of $\nu_{\mathrm{rf}} = \nu_c$ becomes larger as indicated by the arrow in (b).

limit of the TOF- range was varied and the impact on the frequency ratio R was investigated. Since there was no trend observable in this case, no additional systematic uncertainty had to be added. A dependency of R on the TOF selection was observed in other cases. In some of those, a count-class analysis resolved the shift because its result was independent of the TOF- range. Figure 4.14 falls into this category. However, for other cases even the results of the count-class analysis followed a trend over the TOF- range selection. For measurements with too few counts a TOF-range dependent count-class could not be performed. Hence, whenever a trend could not be resolved, a systematic uncertainty corresponding to the maximal shift in the central value of R with respect to the main analysis range (13-50 μs) was added in quadrature as a systematic uncertainty.

The measurement runs of ^{74}Rb had so few ions that the TOF-range dependency could not be reliably studied. However, the respective shifts found for ^{74}Ga were added as a systematic error. It was added in quadrature to the weighted average of each measurement set and not to the overall weighted average because the size of the effect itself depended on the available statistics. Moreover, trends due to the TOF-selection showed different behaviours in different measurement settings even for the same nuclide (e.g. Figure 4.13 and Figure 4.14b which were both
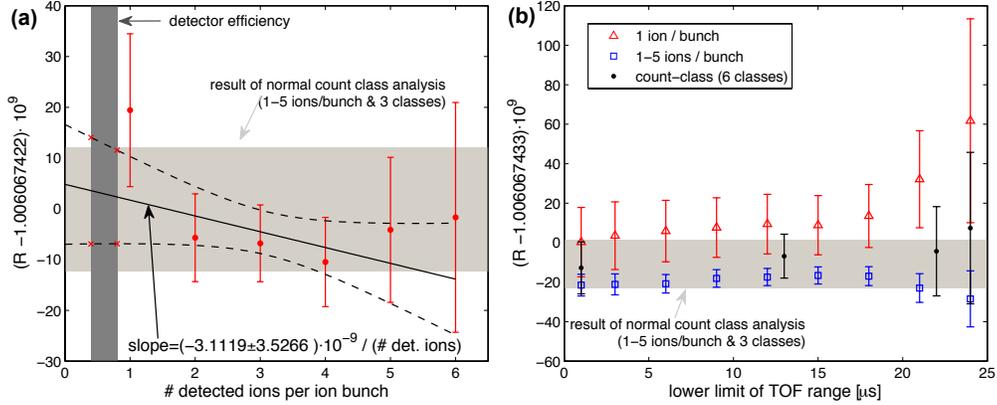
Figure 4.14: Dependency of the frequency ratio $R = \nu_r/\nu$ of ^{76}Rb^{8+} to ^{85}Rb^{9+} on the lower limit of the selected TOF- range (b). The data are from the measurement runs with the Ramsey excitation. With increasing lower limit the analyses with 1 ion and 1-5 ions per ion bunch drift away from the result of the main analysis, i.e. a count-class analysis with data from 13-50 μs, (shaded area). However, a more advanced count-class analysis does not follow these deviations. This analysis was performed with 6 classes with a selection of 1-6 detected ions (i.e. each count number is its own class) and instead of extrapolating ν_c, the extrapolation to a single ion stored in the Penning trap was done for the frequency ratio R. The actual number of stored ions is related to the detected ions by the MCP detector efficiency. An example is shown in (a) for a TOF- range of 13-50 μs.

^{76}Rb^{8+} versus ^{85}Rb^{9+}). This might be related to the probability for charge exchange which depends on the velocity of the ion (see Equation 3.57). Thus, the charge state distribution could indeed be different between Ramsey and conventional excitations even when the total time spent in the trap is the same. Hence, different measurement settings were also interpreted as benchmarks of the influences of charge exchange and of the TOF- range selection.

4.3.8 Remaining uncertainties and independent accuracy checks

In order to address remaining uncertainties, mass measurements involving ^{85}Rb$^{10+,8+}$ and ^{87}Rb^{9+} with ^{85}Rb^{9+} as the reference ions were performed prior to and during the measurement campaign of neutron deficient Rb- isotopes. In all of these
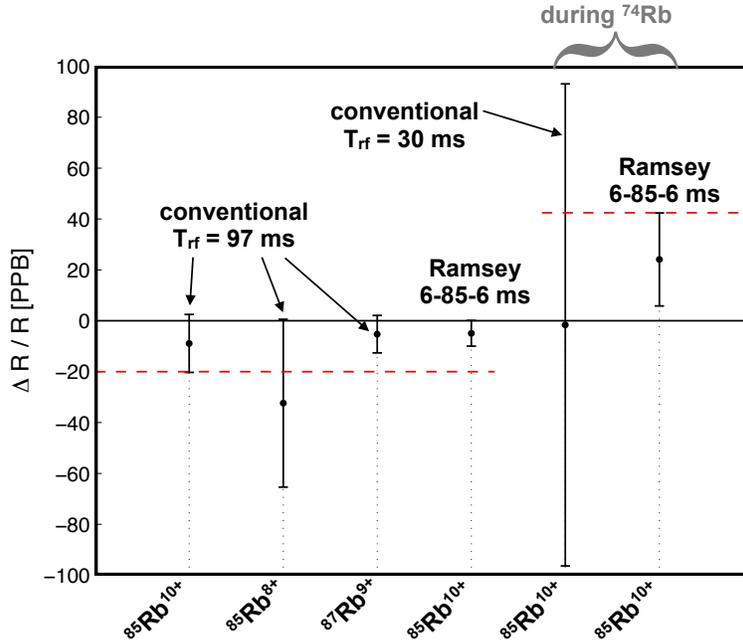
Figure 4.15: Measurements to check the accuracy of the measurement setup. The dashed, red lines represent the upper limit on remaining systematic uncertainties which was assigned to the frequency ratios of the online measurement. See text for details.

cases $\Delta(m/q)$ and $\Delta(q/m)$ were larger in their absolute values than the respective quantities in the measurement of $^{74-76}$Rb^{8+}, except for ^{87}Rb^{9+} versus ^{85}Rb^{9+} in comparison to the ^{78}Rb measurement. Hence, according to the previous discussions on systematic errors any remaining uncertainty due to m/q dependent shifts in R should be even smaller.

At a 10 Hz repetition rate, different configurations were tested which were later also used during the online experiment. The differences ΔR between the measured and the expected frequency ratio based on the literature [122, 200] are plotted in Figure 4.15. The last two sets correspond to consistency checks during the ^{74}Rb measurement itself which was required due to a power outage related turbo pump failure and the subsequent reconditioning of the electron beam in the EBIT and a retuning of the beam into the MPET. The data were analyzed with the same TOF range as used in the main analysis (13-50 μs). No deviations from the expectation were observed. The uncertainty on the data point for ^{85}Rb^{8+} was larger because

of unidentified contamination, possibly from charge bred residual gas in the EBIT. This significantly reduced the quality of the resonance.

To be conservative, an upper limit of 20.0 PPB was assigned for measurements of ^{75,76}Rb^{8+} and ^{74}Ga^{8+} corresponding to a maximal deviation at the 1 σ level of any accuracy check prior to the online experiment (see Figure 4.15). ^{85}Rb^{8+} was not considered for this constraint because of its limitation due to contamination. The benchmark of the $T_{\mathrm{rf}} = 30$ ms measurement was almost an order of magnitude more precise than the ^{74}Rb^{8+} measurement itself. Finally, the Ramsey excitation was also tested between measurements of ^{74}Rb^{8+}, and an upper limit of 42.4 PPB was assigned as a systematic error. Since no measurements were carried out to confirm the accuracy with $\Delta(m/q)$ or charge states similar to the measurement set of ^{76}Rb^{12+} its remaining systematic uncertainty could not be reliably estimated. The ^{76}Rb^{12+} data set was hence disregarded for the mass determination of ^{76}Rb although its result is in agreement with the other measurement sets.

As a concluding remark it should be noted that all uncertainties in Figure 4.15 were entirely of a statistical nature, and not inflated by any other known systematic uncertainty. These errors could be understood as cumulative uncertainties covering all other effects, including TOF range dependences. Hence, it could be argued that only these upper limits would be a sufficient estimate for all systematic uncertainties. The fact that they were added as a separate source of systematic errors was due to a conservative approach considered adequate for the first HCI mass measurement at TITAN. However, considering the modifications and improvements done on the MPET setup in preparation for these measurements (Section 3.7.8, Section A.5), it is possible that some limits on systematic uncertainties studied in [124, 205] have changed since then. This justified this conservative approach.

4.4 Results

The error budgets are shown in Table 4.6 and Table 4.7. The weighted average for ^{76}Rb does not include the measurements with ^{76}Rb^{12+} or the ^{76}Rb^{8+} with $T_{\mathrm{rf}} = 997$ ms. Although in agreement with the major data sets, they are not considered because of the potentially larger systematic uncertainty (^{76}Rb^{12+}, see discussion above) or a different repetition rate for the measurement of ion of interest and the reference ion ($T_{\mathrm{rf}} = 997$ ms), which had caused systematic uncertainties in the past, likely due to slightly different ion energies (see discussion in Section A.1).

As seen in Table 4.6, the major contributions to the total error are the statistical (Section 4.2.4), the TOF range dependence (Section 4.3.7), and the upper limit from the independent measurements to benchmark the accuracy of the setup for HCI (Section 4.3.8). For ^{74}Ga and ^{74}Rb where no count-class analysis could be

Table 4.6: Error budget for the frequency ratio of the measurements of $^{75-76}$Rb in PPB.

uncertainty	$^{76}\text{Rb}^{8+}$			$^{75}\text{Rb}^{8+}$
	conventional	Ramsey	total	
Statistical (count class)	15.212	12.152		10.295
Lower TOF Range	0.000	0.000		4.656
Upper TOF Range	0.000	0.000		9.835
Previous Combined			9.495	
B-Field Inhomogeneities			0.002	0.003
Harmonic Distortions			0.024	0.030
Trap Potential			0.020	0.025
Relativistic Effects			0.039	0.049
B-Field Stability			0.200	0.200
Accuracy Check			20.000	20.000
Total			22.140	24.989

Table 4.7: Error budget for the frequency ratio of the measurements of ^{74}Ga and ^{74}Rb in PPB.

uncertainty	$^{74}\text{Ga}^{8+}$	$^{74}\text{Rb}^{8+}$			
		conv. 30 ms	Ram. 6-85-6 ms	Dip. 20 ms + Ram. 6-65-6 ms	total
Statistical	29.446	324.238	80.537	106.625	
Lower TOF Range	39.418	39.418	39.418	39.418	
Upper TOF Range	44.618	44.618	44.618	44.618	
Difference 1 and 1-5 Ions	21.440	24.913	4.027	37.319	
Previous Combined					76.690
Magnetic Field Inhomogeneities	0.008				0.008
Harmonic Distortions	0.084				0.084
Trap Potential	0.070				0.070
Relativistic Effects	0.140				0.140
B-Field Stability	0.200				0.750
Accuracy Check	20.000				42.400
Total	72.604				87.634

155

Table 4.8: Mean frequency ratios $\overline{R}$ of $^{76,75,74}\mathrm{Rb}^{8+}$ and $^{74}\mathrm{Ga}^{8+}$ with respect to $^{85}\mathrm{Rb}^{9+}$. Where applicable, the ratio and error are the result of a count-class analysis. The last column represents the extracted atomic mass given in the form of the mass excess. Uncertainties are displayed as (statistical) and {stat. + systematics}.

species	excitation [ms]	$\overline{R} = \nu_c^{\mathrm{ref}}/\nu_c^{\mathrm{meas}}$	#meas	m.e. [keV]
$^{76}\mathrm{Rb}^{8+}$	97 (conventional)	1.006067401(15)	5	
	6-85-6 (Ramsey)	1.006067422(12)	4	
	previous combined	1.006067414{22}		-60481.0{1.6}
$^{75}\mathrm{Rb}^{8+}$	6-85-6 (Ramsey)	0.992864003(10){25}	5	-57218.7{1.7}
$^{74}\mathrm{Rb}^{8+}$	30 (conventional)	0.979689909(318){324}	4	
	6-85-6 (Ramsey)	0.979689552(79){98}	3	
	20(dip)6-65-6(Ram)	0.97968966(10){13}	2	
	previous combined	0.979689609{86}		-51916.5{6.0}
$^{74}\mathrm{Ga}^{8+}$	8 & 97 (conventional)	0.979460129(29){71}	4	-68049.7{5.0}

performed an additional, significant uncertainty was added in the form of the difference between one ion and 1-5 ions per ion bunch. With the measured $\overline{R}$, the atomic masses of the respective nuclides are calculated following Equation 3.50 in Table 4.8 taking into account the total electron binding energies (0.5, 0.7, and 1.6 keV for $\mathrm{Rb}^{8,9,12+}$[200], respectively, as well as 0.6 keV for Ga^{8+}[225]). Partial uncertainties for the mass of $^{74}\mathrm{Rb}$ are presented in Table 4.9. These results are in agreement with ISOLTRAP's measurements [14, 226] (see Figure 4.16). Due to the use of HCI and the Ramsey excitation they are comparable in precision despite the significantly shorter measurement time ($<$22 h for $^{74}\mathrm{Rb}$).

156

Table 4.9: Leading partial uncertainties in the present measurements of the mass of ^{74}Rb in keV. The calculation for each partial uncertainty was carried out considering independence of the other sources, i.e the latter were set to zero. As some sources of uncertainties are specific to each of the three data sets, they were added in quadrature for each set before the weighted average of the sets was made and the global systematic uncertainties were added (again in quadrature). Hence, adding the partial uncertainties of this table in quadrature would lead to a smaller total uncertainty than in Table 4.8.

	partial uncertainty [keV]
Statistical	4.3
Accuracy Check	2.9
TOF Range	2.4
Difference 1 and 1-5 Ions	0.3
B-field Stability	0.1
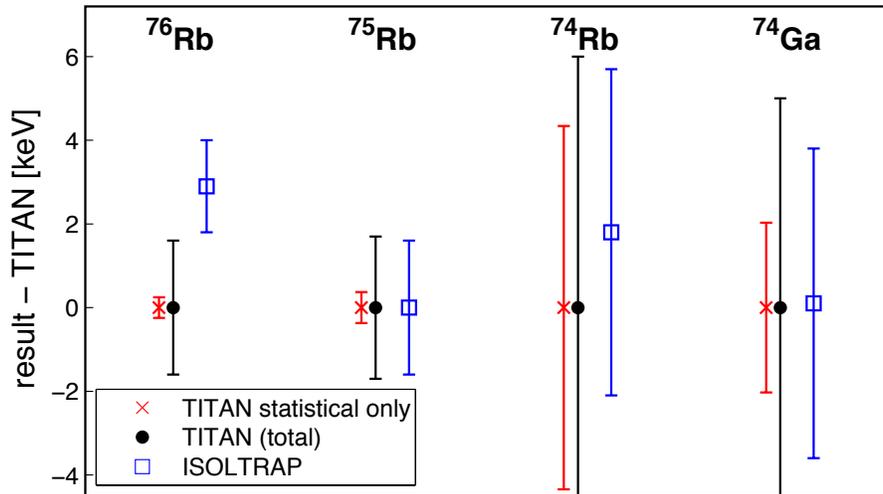
Figure 4.16: Atomic masses of ^{76,75,74}Rb and ^{74}Ga in comparison to their respective ISOLTRAP measurements [14, 226]. Statistical uncertainties are based on fits of ion bunches with 1-5 detected ions but without a count-class analysis.

Chapter 5

Discussion

The implications of the first Penning trap mass measurements with HCI of rare isotopes is summarized along four topics. First, the impact of the present measurements on the primary motivation of this work is discussed, which are the Q_{EC}-value of ^{74}Rb and the isospin symmetry corrections δ_C necessary for the extraction of V_{ud} from superallowed β-decays. Then, the results are considered as part of a new Atomic Mass Evaluation (AME) [199]. A perspective of HCI for mass measurements of radioactive HCI in Penning traps is given. Finally, the potential to resolve low-lying isomers with HCI is discussed on the basis of the ^{78m,78}Rb data of this work.

5.1   The Q_{EC}-and ft-value of ^{74}Rb

When the mass measurements of ^{74}Rb [14] and ^{74}Kr [106] by the ISOLTRAP collaboration are combined with the present work, a Q_{EC}-value for ^{74}Rb of 10 416.8(3.9) keV is obtained (see Table 5.1), an improvement of $\approx 12\%$. This implies a statistical rate function of $f = 47\,283(94)$ [75] and together with the recent improvements in δ_C due to the laser spectroscopy work [16] translates to a corrected $\mathcal{F}t$-value of

Table 5.1: Mass excess (m.e.) of ^{74}Rb and ^{74}Kr required to deduce the Q_{EC}-value of ^{74}Rb from direct mass measurements.

Quantity	ISOLTRAP [keV]	TITAN [keV]	all data [keV]
m.e. (^{74}Rb)	-51 914.7(3.9) [14]	-51 916.5(6.0)	-51 915.2(3.3)
m.e. (^{74}Kr)	-62 332.0(2.1) [106]		-62 332.0(2.1)
Q_{EC}-value			10 416.8(3.9)
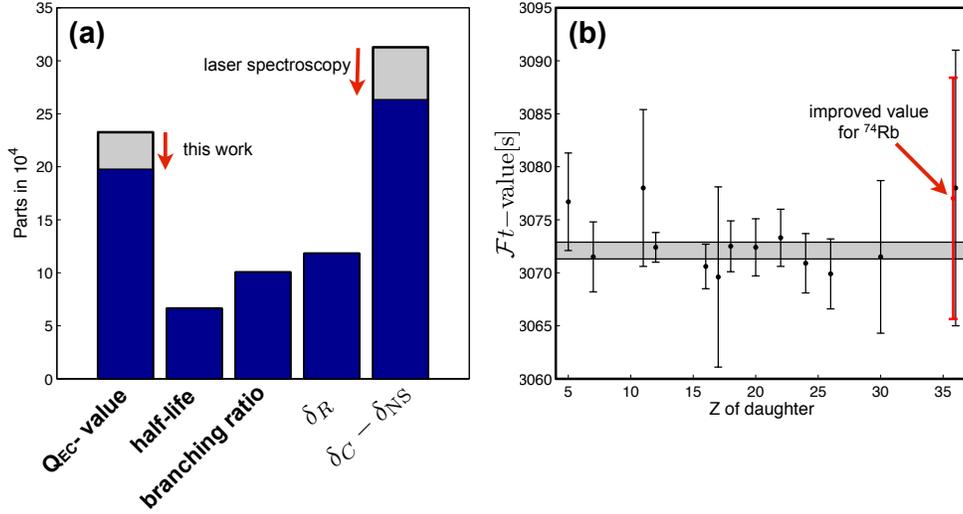
Figure 5.1: Improvements in the $\mathcal{F}t$-value of ^{74}Rb due to laser spectroscopy [16] and this work. (a) shows the partial contributions to the uncertainty of the $\mathcal{F}t$-value of ^{74}Rb. In (b) it is compared to the data of the most recent survey of superallowed β-decays [15].

3 077(11) s, when considering δ_C based on shell model calculations with Saxon-Woods radial wave-functions [15]. A summary of the improvements is given in Figure 5.1a in terms of the partial contributions to the $\mathcal{F}t$-value of ^{74}Rb. This represents a modest gain in precision with respect to the global situation of $\mathcal{F}t$-values (see Figure 5.1b). The feasibility of Penning trap mass spectrometry of radioactive HCI has been demonstrated with this work. Hence, a direct measurement of the Q_{EC}- value with this method would substantially reduce the uncertainty of the $\mathcal{F}t$-value of ^{74}Rb.

In light of the improvement for ^{74}Rb through the present mass measurement and the laser spectroscopy work, a new variation of experimental tests of the isospin-symmetry breaking ISB corrections, δ_c, is introduced based upon the following reasoning. Out of the 13 precise superallowed $\mathcal{F}t$-values ^{74}Rb and ^{62}Ga have significantly larger ISB corrections due to the approximate $\delta_c \sim Z^2$ dependence (see Figure 2.20). Both nuclides belong to the fp-shell which, due to the larger model space, is computationally more difficult than for the lighter superallowed β-emitters. Moreover, the effective interactions in the shell model become less reliable (see discussion and references in [16]). Hence, the new test of models of δ_C aims to benchmark the consistency of a set of δ_c calculations for ^{74}Rb and ^{62}Ga. Assuming that for the lighter cases with $Z \leq 28$ the δ_c-calculations are more reli-
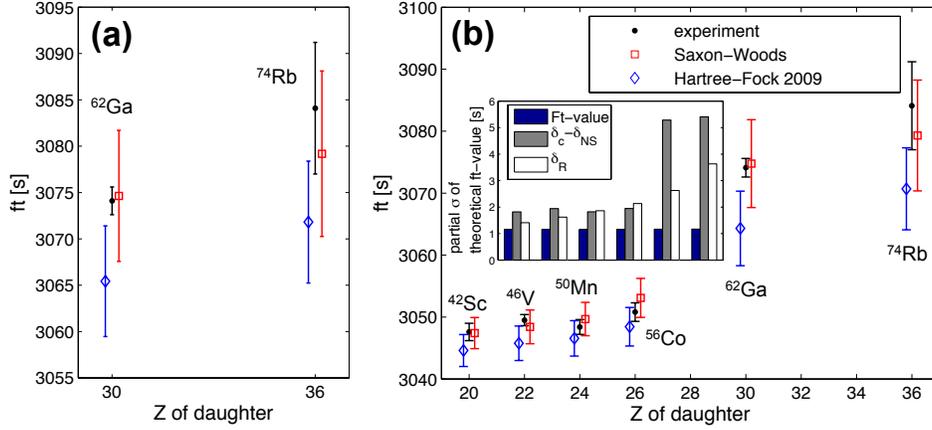
Figure 5.2: Test of the ISB correction term δ_C for the heavier superallowed
β-decays. The insert in (b) shows the error contributions to these six
theoretical ft-values for δ_C from the shell model with Hartree-Fock
radial wave-functions. Out of the three error contributions, statistical
uncertainties enter only in $\overline{\mathcal{F}t}$. See text for details.

able, the weighted average $\overline{\mathcal{F}t}$ is extracted from a set of δ_c from the other 11 precise
superallowed cases. Then, Equation 2.86 is employed to calculate an ft-value for
^{74}Rb and ^{62}Ga, which can be compared to the experimental value. Similarly, as
for other comparisons mentioned in Section 2.8, such a test can only point out in-
consistencies. However, as $\overline{\mathcal{F}t}$ is calculated from different data than the cases to be
tested, the experimental and 'theoretical' ft-values are truely independent.

In Figure 5.2a, the test is presented for the δ_C-calculations which are currently
considered in the survey of superallowed β-decays. These are the shell model cal-
culations based on Saxon-Woods [73] and Hartree-Fock [15] radial wave functions.
They appear based on other tests (e.g. Table 2.4) as the most consistent calculations
which have published δ_C for all 13 cases. Noting that the uncertainties for the 'the-
oretical' ft-values are only partly of statistical origin (see insert of Figure 5.2b),
the agreement between the experimental ft-values and the ones extracted from the
Saxon-Woods model of δ_C is better than the values from the Hartree-Fock calcula-
tion (see Figure 5.2a). The latter are, in both cases, below the experimental value.
Since the ft-value of ^{74}Rb is dominated by the Q_{EC}-value, a new more precise
mass measurement of ^{74}Rb and ^{74}Kr has a strong potential for the discrimination
between different models of δ_C.

In Figure 5.2b, the same test for models of δ_c is extended to the full fp-shell, which

Table 5.2: Mass excess for measured nuclides.

nuclide	this work [keV]	mass evaluation [keV]
^{76}Rb	-60481.0(1.6)	-60479.1(0.9)
^{75}Rb	-57218.7(1.7)	-57218.7(1.2)
^{74}Rb	-51916.5(6.0)	-51916.0(3.0)
^{74}Ga	-68049.7(5.0)	-68049.6(3.0)

means that $\overline{\mathcal{F}t}$ is estimated from the lightest seven of the precise superallowed cases (^{10}C to ^{38m}K). When the ft-values of the other six cases are calculated based on their δ_C and $\overline{\mathcal{F}t}$, the ISB corrections δ_C from Hartree-Fock calculations tend to underestimate the experimental ft-values. In all six cases, their values are lower than the experimental ones, three of which differ by more than one full standard deviation. ft-values estimated with δ_C based on Saxon-Woods radial wave functions perform well covering the full experimental uncertainty by their own error bands. ^{54}Co is a minor exception to this statement. Experimentally, the uncertainty in the ft-value of ^{74}Rb limits the impact of this test. However, a more substantial comparison of models for δ_C including a precise ft-value of ^{74}Rb is within reach owing to the advent of Penning trap mass measurements of radioactive HCI.

5.2 The Atomic Mass Evaluation (AME)

The wealth of experimental data of mass measurements is reviewed in the AME [199]. The data are processed to establish the mass of individual nuclides by taking into account all measured relations between different nuclides. For example in Penning trap mass spectrometry the relationship is the frequency ratio between the ion species. A complete atomic mass evaluation has been performed including the present results based on the procedures in [199], with the addition of the electron binding energies to the evaluation formulas. They had been neglected in previous evaluations because for SCI the electron binding energies are only a few eV and insignificant compared to the experimental precision of most nuclides' masses. As discussed in Section 3.7.5, the total electron binding energies for HCI can be a few keV or more and have to be considered.

The previous mass evaluation [199] included a mass value for ^{74}Rb determined from the $\mathcal{F}t$-value of other superallowed β emitters and ^{74}Rb's half-life and branching ratio [100]. The present evaluation did the same with an updated Q_{EC}-value estimate of 10413.8(7.0) keV [75] based on [15]. For the discussion of superallowed decays, this estimate was not considered. The results of the evaluation for

161

all measured nuclides is shown in Table 5.2.

5.3 General considerations for Penning trap mass measurements with radioactive HCI

All techniques required for a Penning trap mass measurement with HCI as demonstrated in this work are universally applicable to any nuclide provided that the additional step of charge breeding can be accomplished in a time period such that the number of remaining HCI after radioactive decays is sufficient for the mass measurements. The feasibility has been shown for ^{74}Rb with a half-life of only 65 ms. An increased electron beam current reduces the breeding time such that in principle the method is extendable to even shorter half-lives. Hence, the presented measurement opens the field to a new level of precision over a wide range of the nuclear chart.

In the pioneering work at SMILETRAP Penning trap mass measurements on stable nuclides have been performed in even higher charge states ($q > 40+$) [11, 114, 227]. Simulations (see Figure 3.14) suggest that similar charge states are reachable in tens of ms breeding times and hence suitable for even short-lived nuclides. The combination of HCI and the Ramsey excitation scheme opens a new class of on-line mass measurements with potentially up to 2 orders of magnitude improved precision versus conventional SCI-TOF-ICR spectroscopy.

Very high precision is essential for fundamental symmetries studies, such as presented here for the superallowed β emitter ^{74}Rb. For nuclear structure and nuclear astrophysics, where the experimental precision is already sufficient, this novel technique will reduce the measurement time and thus allow one to map the nuclear mass landscape more quickly. In addition, the same precision can be achieved for lower production yields and/or shorter half-lives.

Due to the $\sqrt{N_{\mathrm{ions}}} \cdot q$ dependence in the precision (see Equation 3.45), HCI are favourable over SCI as long as the loss in efficiency caused by the charge breeding is smaller than q^2. The total number of ions is affected by the breeding in three ways:

- non-unity efficiency for the chosen charge state due to the charge-state distribution (see Figure 3.18),

- increased energy spread of the extracted charge bred ions which reduces transport and trapping efficiency at MPET, and

- loss of ions due to the radioactive decay in the EBIT. Thus, a balance between the desired charge state and the breeding time has to be found. For example,

for the ^{74}Rb measurement, ions were trapped for 23 ms in the EBIT ($\sim 0.35 \cdot T_{1/2}$), and the breeding was done in parallel with a measurement in MPET.

However, Penning trap mass measurements are performed with only a few ions (1-5) at a time (see Section 4.2.1). For instance, a measurement with SCI of ^{75,76}Rb would have required beam attenuation to achieve the small number of trapped ions. Hence, the lower efficiency due to the charge breeding to ^{75,76}Rb^{+8} could be compensated by reducing this beam attenuation.

The problem of an increased emittance will be addressed at TITAN with the integration of the Cooler Penning Trap (CPET) (see Section 3.1). However, as the cooling time is expected to be in the order of a few 100's of ms [137], a compromise between the advantages of cold HCI and losses due to radioactive decay has to be found here, too.

In the present studies, the number of ^{74}Rb ions delivered from ISAC to TITAN was a few 1000 ions per second providing information about the minimal required yields to perform mass measurements of HCI. Several developments are foreseen at TITAN to improve the overall efficiency further and to charge breed nuclides with even lower production yields.

5.4 Resolving low-lying isomeric states with HCI

Isomeric states in nuclei (or nuclear isomers) are excited, metastable states in atomic nuclei. They are interesting to study because of their implications for nuclear structure [228, 229] or nuclear astrophysics where they can affect nucleosynthesis processes [230]. As discussed for Equation 3.34, the width of a resonance $\Delta\nu \sim 1/T_{\mathrm{rf}}$ is solely governed by the duration T_{rf} of the RF-field, but is independent of q, m, or B. Thus, if two nuclides are very close in mass and brought into the Penning trap with the same charge state, the two resonance shapes cannot be separated if the resolving power of (Equation 3.44)

$$R = \frac{\Delta\nu}{\nu} \propto \frac{m}{q \cdot B \cdot T_{\mathrm{rf}}} \tag{5.1}$$

is surpassed. This is especially the case for energetically low-lying isomers which can be difficult to resolve from the ground state of the nuclide. Since conventional Penning trap mass spectrometry utilizes SCI, the way to increase resolving power (Equation 5.1) is to extend the measurement time T_{rf}. However, this approach is constrained by the half-lives of the isomer or ground state which hinders access to low-lying, short-lived isomers.[1] The same limitation applies to the newly devel-

---

[1]Note that the term 'short-lived' is ambiguous in the present context. While an isomer's half-life of few tens of ms is considered as long-lived in isomer research, it is short-lived for Penning trap
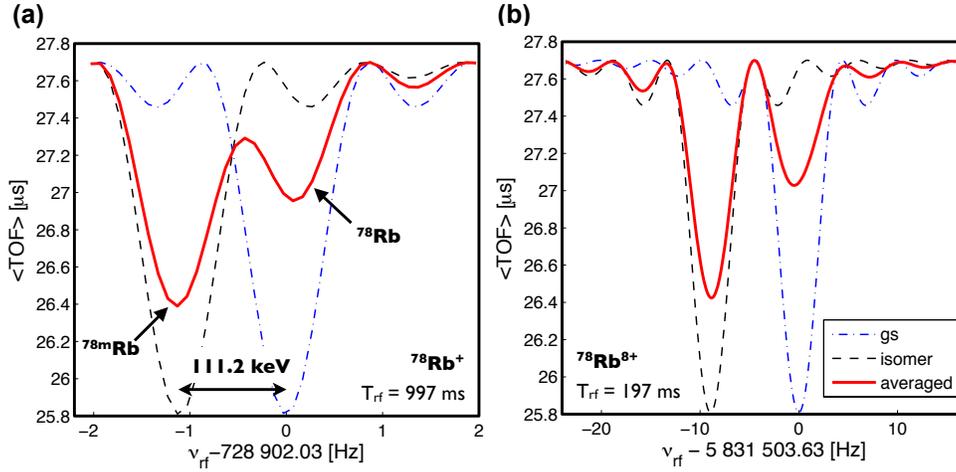
Figure 5.3: Resolving the low-lying isomeric state of ^{78}Rb at 111.2 keV from the ground state with a long excitation time (a) or with HCI (b). The solid (red) line represents the combined line shape assuming a ratio of 2:1 between isomer and ground state. See text for details.

oped Ramsey dipole cleaning [216]. Even though this technique allows isomeric cleaning previous to a mass measurement, it lasts upwards of one hundred milliseconds. The introduction of HCI improves the resolving power by increasing the ion's cyclotron frequency ν_c and hence the absolute difference in ν_c between isomer and ground state.

Figure 5.3 illustrates the principle for ^{78m,78}Rb which requires a resolving power of $R \approx 6.5 \cdot 10^5$. This is either achieved by a longer excitation time (Figure 5.3a) or by a higher charge state (Figure 5.3b). The isomer and ground state have been resolved in [213] with SCI and an excitation time of $T_{rf} = 900$ ms (in a 6 T magnetic field). The present work demonstrates the advantages of HCI, which allows one to use much shorter excitation times while still separating both long-lived states of ^{78}Rb. Typical resonances of ^{78m,78}Rb^{8+} are shown in Figure 5.4. For the long half-lives of the ground and isomeric states of several minutes in ^{78}Rb both methods are equivalent. However, for similar cases with shorter half-lives only HCI are able to provide the required resolving power. Figure 5.5 provides a view of the extended accessibility to known short-lived isomers when working with HCI. Hence, a wide new area is open for study and discovery of new isomers. This perspective, however, ignores that every element has a maximal attainable charge

---

mass spectroscopy. In the following, we refer to half-lives of 10's to a few 100's of ms as short-lived.
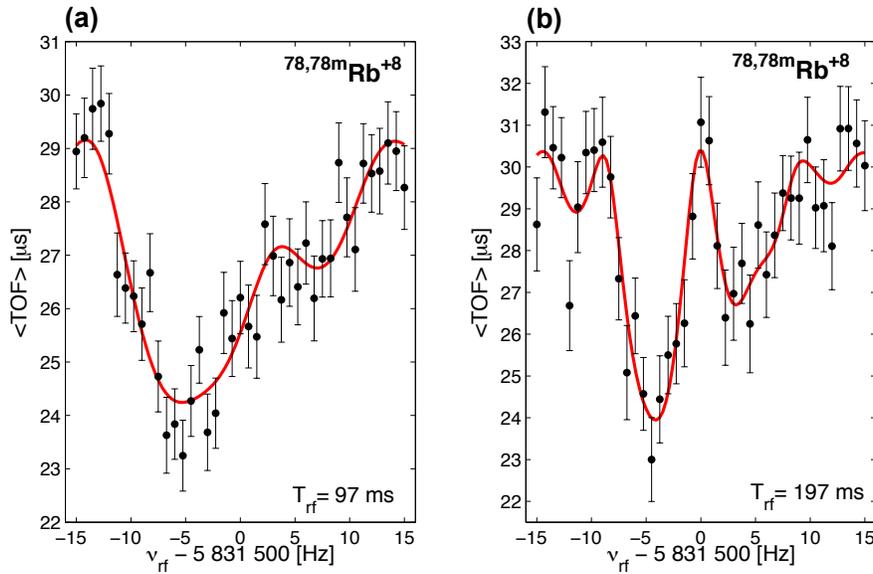
Figure 5.4: Improved resolving power for low lying isomers with HCI. The long lived isomer and ground state of ^{78}Rb are separated by 111.2 keV. This corresponds to a resolving power of $R \approx 6.5 \cdot 10^5$. As seen in comparison between the two figures, a longer excitation time increases the resolving power, and so does the higher charge state (see Figure 5.3).

state $q = Z$. Thus, the known isomers are shown in Figure 5.6 in light of the theoretically required charge state to resolve isomer and ground state. For comparison it also displays the charge state of the conventional method $q = 1+$ and for HCI with a limit imposed by $q = Z$. The figure illustrates again that with HCI many new cases can be addressed. Moreover, isomers which cannot be resolved because they would require $q > Z$ mostly have half-lives of less than 5 ms. Those cases are unlikely to be available in sufficient amounts at ISOL or at low energy branches of today's fragmentation facilities and thus represent a more general limit for experimental studies.

In summary, HCI at Penning trap spectrometers provide an intriguing new method to study low-lying isomers with half-lives of 10's to a few 100's of ms which could otherwise not be resolved with SCI. This feature is critical for the study, confirmation, or discovery of nuclear isomers. A first application of this technique could be ^{80}Ga for which recent laser spectroscopy has found a low-lying isomer [231]. Its half-life is expected to be > 200 ms, but its existence has not been observed in
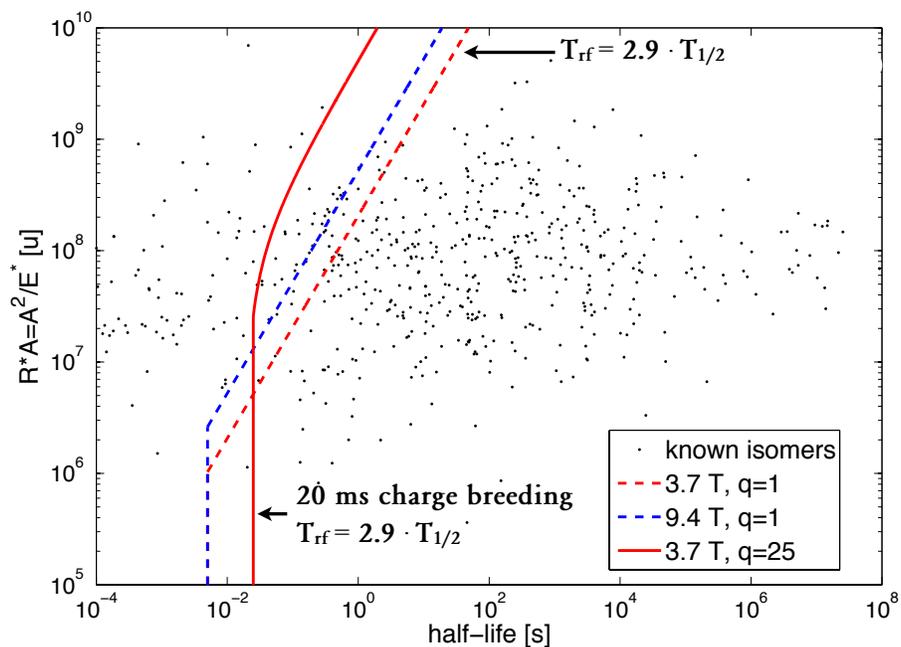
Figure 5.5: Known nuclear isomers. The required resolving power R to separate isomer and ground state due to their mass difference E^* is plotted over the half-life of the isomer. R is multiplied by the mass number A to eliminate the mass dependency of R. The lines indicate the achievable R for different magnetic field strengths and charge states. All cases to the right of the lines can be resolved. Data from [123].

Penning trap mass measurements [232]. This suggests that the excitation energy of the isomer is of order of 50 keV [231].
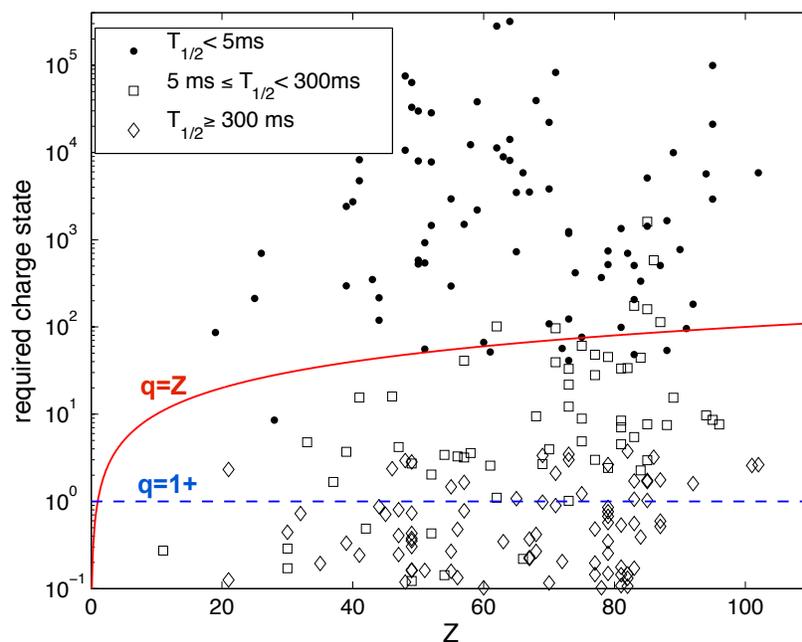
Figure 5.6: Theoretically required charge state to resolve the isomer from the ground state given their mass difference and the isomers' half-life. A magnetic field strength of 3.7 T and an excitation time of $T_{\mathrm{rf}} = 2.9 \cdot T_{1/2}$ is assumed. The solid (red) line corresponds to bare ions, hence, the maximally possible charge state. Every isomer underneath the line can be resolved from the ground state provided that the respective charge state can be reached in a breeding time smaller than the half-life.

Chapter 6

Summary and Outlook

Ever since its discovery a hundred years ago [233], the atomic nucleus has been an intriguing object of research. A field, which had started with the scattering of α- and β-particles on a gold foil, has expanded over the last century to study properties of thousands of different nuclides, of which only ≈ 250 are considered to be stable against nuclear decay. The world-wide emergence of next-generation facilities such as the RadioIsotope Beam Factory (RIBF) (Japan), the Facility for Rare Isotope Beams (FRIB) (USA), the Facility for Antiproton and Ion Research (FAIR) (Europe), or the Advanced Rare IsotopE Laboratory (ARIEL) (Canada) will provide over the next years wider experimental access to the ~ 8000 nuclides thought to exist [144]. However, the enlarged availability of exotic nuclides has to be accompanied by equivalent advances in experimental techniques to address the many outstanding questions regarding nuclear structure, nuclear astrophysics, or fundamental symmetries. For the latter, the atomic nucleus is seen as a probe for particle physics phenomenon.

As an aspect of novel experimental methods, this thesis has explored the use of radioactive Highly Charged Ions (HCI) for Penning trap mass spectrometry. In combination with new measurement schemes such as the Ramsey excitation, introduced to the field only recently, HCI open a new class of online mass measurements with potentially up to 2 orders of magnitude improved precision compared to the conventional Time-Of-Flight Ion-Cyclotron-Resonance (TOF-ICR) technique with Singly Charged Ions (SCI).

In this work, the first Penning trap mass measurements of radioactive HCI have been performed at TRIUMF's Ion Trap for Atomic and Nuclear science (TITAN). For these measurements, ions of neutron-deficient Rb isotopes were prepared in an Electron Beam Ion Trap (EBIT) in charge states $q = 8+$ to $12+$ prior to their injection into the Measurement Penning Trap (MPET). Among the studied nuclides,

168

^{74}Rb has a half-life of only 65 ms. The measurements demonstrated the applicability of the technique even to such short-lived radioisotopes. Indeed, the short half-life of ^{74}Rb had in the past been the limiting factor for high precision measurements of its mass and consequently of its β-decay transition energy or Q-value. ^{74}Rb is one of 13 superallowed β-emitters which combined provide currently the most precise determination of V_{ud} of the Cabibbo-Kobayashi-Maskawa (CKM) quark mixing matrix. The Q-value is in addition to half-life and Branching Ratio (BR) an experimental input value to obtain the ft-value of a superallowed β-decay from which V_{ud} is extracted. In recent years, the study of superallowed β-decays has focused on theoretical isospin-symmetry breaking (ISB) corrections, δ_C, which need to be applied to the ft-values to determine V_{ud}. Calculations of δ_C in different models show systematic discrepancies which is critical to resolve. In this theoretical debate, accurate and precise experimental data are of crucial importance to accentuate inconsistencies, which ultimately helps to discriminate between existing models.

A weighted average of existing data with the present measurement led to an improved Q_{EC}-value of 10 416.8(3.9) keV for ^{74}Rb. The Q_{EC}-value was employed in a new test to benchmark δ_C calculated in different models. Among the two models which are considered in the latest survey of superallowed β-decays [15], this test showed inconsistencies when the δ_C-corrections were taken from recent shell model calculations with Hartree-Fock radial wave-functions. However, the presented test would be more stringent if the uncertainty in Q_{EC}-value of ^{74}Rb was further improved as it currently dominates the uncertainty in its ft-value.

Since the present work demonstrated the feasibility of Penning trap mass measurements of short-lived nuclides with HCI, a new measurement of ^{74}Rb and its daughter, ^{74}Kr, is planned at TITAN with charge states up to $q \approx 30+$, reachable by a more intense electron beam ($I_e = 400$ mA) in the EBIT. Such a new measurement could provide knowledge of ^{74}Rb's Q_{EC}-value within 0.5 keV. Uncertainties of half-life or branching ratio (BR) would then surpass the Q_{EC}-value's contribution to the ft-value's error, stimulating new BR measurements. At this level of experimental precision the uncertainty of the statistical rate function f of ^{74}Rb would be dominated by theory and not by the Q_{EC}-value [74, 75]. Perhaps most importantly, more stringent comparisons of conflicting theoretical models of δ_C similar to [18] or the test presented in this work could challenge perceived consistencies between a set of δ_C-calculations, experimental results, and the Conserved Vector Current (CVC) hypothesis. Here, ^{74}Rb, with its largest δ_C among all superallowed β emitters, would carry particular weight were it not limited by the current precision in its Q_{EC}-value.

In addition to ^{74}Rb, the masses of ^{75,76}Rb as well as ^{74}Ga were measured in the present studies. The results are in agreement with the literature [14] lending further

evidence to the accuracy of the technique and the experimental facility. However, to take full advantage of HCI, it will be necessary to gain further improved control over systematic effects. Work is underway to improve vacuum conditions of the MPET further and avoid uncertainties associated with charge exchange of HCI with residual gas. It has been demonstrated prior to this work that m/q dependent shifts at TITAN for SCI are at the level of a few Parts-Per-Billion (PPB) [124, 205] and this work supports the expectation that the same accuracy can be achieved with HCI.

Finally, the potential to resolve low-lying isomers with HCI in a Penning trap was explored with ^{78m,78}Rb. The studied ^{78m}Rb isomer is only 111.2 keV heavier than the ground state. Despite a required resolving power of $R \approx 6.5 \cdot 10^5$, isomer and ground state could be well separated even with short storage times for a single ion of 100 to 200 ms. At another facility utilizing SCI, this had only been achieved by longer storage times on the order of 1 s [213]. The conventional method is hence not applicable for shorter-lived isomers, but they have now become accessible with HCI.

In summary, Penning trap mass measurements of highly-charged, short-lived nuclides have been performed for the first time. This opens the door to unrivalled precision with gains of 1-2 orders of magnitude depending on the charge state and excitation scheme. This is essential for fundamental symmetries studies, such as discussed here for the superallowed β emitter ^{74}Rb. A new measurement of its Q_{EC}-value is planned at TITAN aiming for precision of ~ 0.5 keV and utilizing a charge state $q \approx 30+$. For nuclear structure and nuclear astrophysics, where the experimental precision is already sufficient, this novel technique will reduce the (total) measurement time and thus allows one to map the nuclear mass landscape more quickly. In addition, the same precision can be achieved for lower production yields and/or shorter half-lives. Moreover, HCI provide opportunities for unprecedented resolving power to identify and resolve isomers in a Penning trap. This approach is particularly powerful for low-lying isomers with half-lives in the order of 10's to 100's of milliseconds, which up to now could not be resolved by the conventional method utilizing SCI. At this time, TITAN is unique in providing the possibility for high charge states in Penning trap mass spectroscopy of radionuclides.

Bibliography

[1] A. Lapierre, M. Brodeur, T. Brunner, S. Ettenauer, P. Finlay, A. T. Gallant, V. V. Simon, P. Delheij, D. Lunney, R. Ringle, H. Savajols, and J. Dilling. Penning-trap mass measurements of the neutron-rich K and Ca isotopes: Resurgence of the $N = 28$ shell strength. *Phys. Rev. C*, 85:024317, 2012. Available from: http://link.aps.org/doi/10.1103/PhysRevC.85.024317. → pages 71, 90, 125

[2] A. Lapierre, M. Brodeur, T. Brunner, S. Ettenauer, A.T. Gallant, V. Simon, M. Good, M.W. Froese, J.R. Crespo López-Urrutia, P. Delheij, S. Epp, R. Ringle, S. Schwarz, J. Ullrich, and J. Dilling. The TITAN EBIT charge breeder for mass measurements on highly charged short-lived isotopes-First online operation. *Nuclear Instruments and Methods in Physics Research Section A: Accelerators, Spectrometers, Detectors and Associated Equipment*, 624:54 – 64, 2010. Available from: http://www.sciencedirect.com/science/article/pii/S0168900210020231. → pages 74, 88, 90, 91, 209, 211

[3] G. Bollen, P. Dabkiewicz, P. Egelhof, T. Hilberath, H. Kalinowsky, F. Kern, H. Schnatz, L. Schweikhard, H. Stolzenberg, R. Moore, H. Kluge, G. Temmer, and G. Ulm. First absolute mass measurements of short-lived isotopes. *Hyperfine Interactions*, 38:793–802, 1987. Available from: http://dx.doi.org/10.1007/BF02394875. → pages 1

[4] H. Stolzenberg, St. Becker, G. Bollen, F. Kern, H.-J. Kluge, Th. Otto, G. Savard, L. Schweikhard, G. Audi, and R. B. Moore. Accurate mass determination of short-lived isotopes by a tandem penning-trap mass spectrometer. *Phys. Rev. Lett.*, 65:3104–3107, 1990. doi:10.1103/PhysRevLett.65.3104. → pages 1

[5] Klaus Blaum. High-accuracy mass spectrometry with stored ions. *Physics Reports*, 425:1 – 78, 2006. Available from:

http://www.sciencedirect.com/science/article/pii/S0370157305004643. →
pages 1, 81, 82, 97, 98

[6] K Blaum, M Block, R B Cakirli, S Eliseev, M Kowalska, S Kreim, Y A
Litvinov, Sz Nagy, W Nörtershäuser, and D T Yordanov. Measurements of
ground-state properties for nuclear structure studies by precision mass and
laser spectroscopy. *Journal of Physics: Conference Series*, 312:092001,
2011. Available from: http://stacks.iop.org/1742-6596/312/i=9/a=092001.
→ pages 1

[7] M. Smith, M. Brodeur, T. Brunner, S. Ettenauer, A Lapierre, R. Ringle,
V. L. Ryjkov, F. Ames, P. Bricault, G. W. F. Drake, P. Delheij, D. Lunney,
F. Sarazin, and J. Dilling. First Penning-Trap Mass Measurement of the
Exotic Halo Nucleus ^{11}Li. *Phys. Rev. Lett.*, 101:202501, 2008. Available
from: http://link.aps.org/doi/10.1103/PhysRevLett.101.202501. → pages 1,
68, 71

[8] M. Block et al. Direct mass measurements above uranium bridge the gap to
the island of stability. *Nature*, 463:785, 2010. → pages 1

[9] M. Dworschak, M. Block, D. Ackermann, G. Audi, K. Blaum, C. Droese,
S. Eliseev, T. Fleckenstein, E. Haettner, F. Herfurth, F. P. Heßberger,
S. Hofmann, J. Ketelaer, J. Ketter, H.-J. Kluge, G. Marx, M. Mazzocco,
Yu. N. Novikov, W. R. Plaß, A. Popeko, S. Rahaman, D. Rodríguez,
C. Scheidenberger, L. Schweikhard, P. G. Thirolf, G. K. Vorobyev,
M. Wang, and C. Weber. Penning trap mass measurements on nobelium
isotopes. *Phys. Rev. C*, 81:064312, 2010.
`doi:10.1103/PhysRevC.81.064312.` → pages 1

[10] G. Bollen. Mass measurements of short-lived nuclides with ion traps.
Nuclear Physics A, 693:3 – 18, 2001. Available from:
http://www.sciencedirect.com/science/article/pii/S0375947401003530. →
pages 1, 69

[11] C. Carlberg, T. Fritioff, and I. Bergström. Determination of the ^{133}Cs and
Proton Mass Ratio Using Highly Charged Ions. *Phys. Rev. Lett.*,
83:4506–4509, 1999. Available from:
http://link.aps.org/doi/10.1103/PhysRevLett.83.4506. → pages 1, 70, 72,
162

[12] F. Herfurth, A. Kellerbauer, F. Ames, G. Audi, D. Beck, K. Blaum,
G. Bollen, O. Engels, H.-J. Kluge, D. Lunney, R.B. Moore, M. Oinonen,

E. Sauvan, C. Scheidenberger, S. Schwarz, G. Sikler, and C. Weber. Accurate mass measurements of very short-lived nuclei. *The European Physical Journal A - Hadrons and Nuclei*, 15:17–20, 2002. Available from: http://dx.doi.org/10.1140/epja/i2001-10216-x. → pages 2, 68

[13] A. Kellerbauer, G. Audi, D. Beck, K. Blaum, G. Bollen, B. A. Brown, P. Delahaye, C. Guénaut, F. Herfurth, H.-J. Kluge, D. Lunney, S. Schwarz, L. Schweikhard, and C. Yazidjian. Direct Mass Measurements on the Superallowed Emitter ^{74}Rb and Its Daughter ^{74}Kr: Isospin-Symmetry-Breaking Correction for Standard-Model Tests. *Phys. Rev. Lett.*, 93:072502, 2004. Available from: http://link.aps.org/doi/10.1103/PhysRevLett.93.072502. → pages 68, 72

[14] A. Kellerbauer, G. Audi, D. Beck, K. Blaum, G. Bollen, C. Guénaut, F. Herfurth, A. Herlert, H.-J. Kluge, D. Lunney, S. Schwarz, L. Schweikhard, C. Weber, and C. Yazidjian. High-precision masses of neutron-deficient rubidium isotopes using a Penning trap mass spectrometer. *Phys. Rev. C*, 76:045504, 2007. Available from: http://link.aps.org/doi/10.1103/PhysRevC.76.045504. → pages 2, 68, 129, 146, 156, 157, 158, 169

[15] J. C. Hardy and I. S. Towner. Superallowed $0^+ \to 0^+$ nuclear β decays: A new survey with precision tests of the conserved vector current hypothesis and the standard model. *Phys. Rev. C*, 79:055502, 2009. → pages 2, 21, 24, 41, 43, 44, 45, 46, 50, 51, 54, 59, 60, 61, 63, 64, 66, 68, 159, 160, 161, 169

[16] E. Mané, A. Voss, J. A. Behr, J. Billowes, T. Brunner, F. Buchinger, J. E. Crawford, J. Dilling, S. Ettenauer, C. D. P. Levy, O. Shelbaya, and M. R. Pearson. First Experimental Determination of the Charge Radius of ^{74}Rb and Its Application in Tests of the Unitarity of the Cabibbo-Kobayashi-Maskawa Matrix. *Phys. Rev. Lett.*, 107:212502, 2011. Available from: http://link.aps.org/doi/10.1103/PhysRevLett.107.212502. → pages 2, 45, 63, 66, 69, 74, 82, 158, 159

[17] G.F. Grinyer, C.E. Svensson, and B.A. Brown. Extraction of V_{ud} from superallowed Fermi decay by the Wilkinson techniques. *Nuclear Instruments and Methods in Physics Research Section A: Accelerators, Spectrometers, Detectors and Associated Equipment*, 622:236 – 245, 2010. Available from: http://www.sciencedirect.com/science/article/pii/S0168900210014555. → pages 2, 65

[18] I. S. Towner and J. C. Hardy. Comparative tests of isospin-symmetry-breaking corrections to superallowed $0^+ \rightarrow 0^+$ nuclear β decay. *Phys. Rev. C*, 82:065501, 2010. Available from: http://link.aps.org/doi/10.1103/PhysRevC.82.065501. $\rightarrow$ pages 2, 65, 169

[19] J. Dilling, R. Baartman, P. Bricault, M. Brodeur, L. Blomeley, F. Buchinger, J. Crawford, J.R. Crespo López-Urrutia, P. Delheij, M. Froese, G.P. Gwinner, Z. Ke, J.K.P. Lee, R.B. Moore, V. Ryjkov, G. Sikler, M. Smith, J. Ullrich, and J. Vaz. Mass measurements on highly charged radioactive ions, a new approach to high precision with TITAN. *International Journal of Mass Spectrometry*, 251:198 – 203, 2006. Available from: http://www.sciencedirect.com/science/article/pii/S1387380606000777, `doi:DOI:10.1016/j.ijms.2006.01.044.` $\rightarrow$ pages 2

[20] G.L. Fogli, E. Lisi, A. Marrone, and A. Palazzo. Global analysis of three-flavor neutrino masses and mixings. *Progress in Particle and Nuclear Physics*, 57:742 – 795, 2006. Available from: http://www.sciencedirect.com/science/article/pii/S0146641005000980. $\rightarrow$ pages 4

[21] Cliff Burgess and Guy Moore. *The Standard Model- A Primer*. Cambridge University Press, 2007. $\rightarrow$ pages 5

[22] Walter Greiner and Berndt Müller. *Gauge Theory of Weak Interactions*. Springer-Verlag, 2nd edition, 1996. $\rightarrow$ pages 5, 29

[23] Michael E. Peskin and Daniel V. Schroeder. *An Introduction to Quantum Field Theory*. Westview Press, 1995. $\rightarrow$ pages 5, 11, 26, 28

[24] Walter Greiner and Joachim a. Maruhn. *Nuclear Models*. Springer-Verlag, 1996. $\rightarrow$ pages 5

[25] Peter Renton. *Electroweak Interactions: An Introduction to the Physics of Quarks and Leptons*. 1990. $\rightarrow$ pages 5

[26] I S Towner and J C Hardy. The evaluation of V_{ud} and its impact on the unitarity of the Cabibbo–Kobayashi–Maskawa quark-mixing matrix. *Reports on Progress in Physics*, 73:046301, 2010. Available from: http://stacks.iop.org/0034-4885/73/i=4/a=046301. $\rightarrow$ pages 5, 19, 20, 24, 38

[27] D.H. Wilkinson, editor. *Isospin in Nuclear Physics*. 1969. $\rightarrow$ pages 5

[28] K. Grotz and H. V. Klapdor. *The weak interaction in nuclear, particle, and astrophysics*. Taylor & Francis, 1990. → pages 5

[29] K. Nakamura et al. Particle data group. *J. Phys. G*, 37:075021, 2010. → pages 9, 20, 21, 23, 31, 32, 61

[30] R. B. Wiringa, V. G. J. Stoks, and R. Schiavilla. Accurate nucleon-nucleon potential with charge-independence breaking. *Phys. Rev. C*, 51:38–51, 1995. Available from: http://link.aps.org/doi/10.1103/PhysRevC.51.38. → pages 10

[31] R. Machleidt. High-precision, charge-dependent Bonn nucleon-nucleon potential. *Phys. Rev. C*, 63:024001, 2001. Available from: http://link.aps.org/doi/10.1103/PhysRevC.63.024001. → pages 10

[32] V. G. J. Stoks, R. A. M. Klomp, C. P. F. Terheggen, and J. J. de Swart. Construction of high-quality *NN* potential models. *Phys. Rev. C*, 49:2950–2962, 1994. Available from: http://link.aps.org/doi/10.1103/PhysRevC.49.2950. → pages 10

[33] B. S. Pudliner, V. R. Pandharipande, J. Carlson, and R. B. Wiringa. Quantum Monte Carlo Calculations of $A \leq 6$ Nuclei. *Phys. Rev. Lett.*, 74:4396–4399, 1995. Available from: http://link.aps.org/doi/10.1103/PhysRevLett.74.4396. → pages 10

[34] Steven C. Pieper, V. R. Pandharipande, R. B. Wiringa, and J. Carlson. Realistic models of pion-exchange three-nucleon interactions. *Phys. Rev. C*, 64:014001, 2001. Available from: http://link.aps.org/doi/10.1103/PhysRevC.64.014001. → pages 10

[35] Evgeny Epelbaum. Few-nucleon forces and systems in chiral effective field theory. *Progress in Particle and Nuclear Physics*, 57:654 – 741, 2006. Available from: http://www.sciencedirect.com/science/article/pii/S0146641005001018. → pages 11

[36] E. Epelbaum, H.-W. Hammer, and Ulf-G. Meißner. Modern theory of nuclear forces. *Rev. Mod. Phys.*, 81:1773–1825, 2009. → pages 11, 13

[37] S.K. Bogner, R.J. Furnstahl, and A. Schwenk. From low-momentum interactions to nuclear structure. *Progress in Particle and Nuclear Physics*, 65:94 – 147, 2010. Available from: http://www.sciencedirect.com/science/article/pii/S0146641010000347. → pages 12, 13, 14

[38] Robert Roth, Thomas Neff, and Hans Feldmeier. Nuclear structure in the framework of the Unitary Correlation Operator Method. *Progress in Particle and Nuclear Physics*, 65:50 – 93, 2010. Available from: http://www.sciencedirect.com/science/article/pii/S0146641010000335. → pages 14

[39] G.F. Bertsch, D.J. Dean, and W. Nazarewicz. Computing atomic nuclei. *SciDAC Rev.*, 6:42, 2007. → pages 14

[40] J. Menéndez, D. Gazit, and A. Schwenk. Chiral Two-Body Currents in Nuclei: Gamow-Teller Transitions and Neutrinoless Double-Beta Decay. *Phys. Rev. Lett.*, 107:062501, 2011. → pages 15

[41] W. Satuła, J. Dobaczewski, W. Nazarewicz, and M. Rafalski. Microscopic Calculations of Isospin-Breaking Corrections to Superallowed Beta Decay. *Phys. Rev. Lett.*, 106:132502, 2011. → pages 15, 54, 55, 60

[42] Riccardo de Sangro. Ckm physics. XXXVII International Meeting on Fundamental Physics, Banasque, Feb. 9-13 2009, 2009. → pages 19

[43] A. Sher, R. Appel, G. S. Atoyan, B. Bassalleck, D. R. Bergman, N. Cheung, S. Dhawan, H. Do, J. Egger, S. Eilerts, H. Fischer, W. Herold, V. V. Issakov, H. Kaspar, D. E. Kraus, D. M. Lazarus, P. Lichard, J. Lowe, J. Lozano, H. Ma, W. Majid, S. Pislak, A. A. Poblaguev, P. Rehak, Aleksey Sher, J. A. Thompson, P. Truöl, and M. E. Zeller. High statistics measurement of the $k^+ \to \pi^0 e^+ \nu$ (k_{e3}^+) branching ratio. *Phys. Rev. Lett.*, 91:261802, 2003. → pages 20

[44] T. Alexopoulos et al. Measurements of K_L branching fractions and the CP violation parameter $|\eta_{+-}|$. *Phys. Rev. D*, 70:092006, 2004. Available from: http://prd.aps.org/abstract/PRD/v70/i9/e092006. → pages 20

[45] T. Alexopoulos et al. A Determination of the Cabibbo-Kobayashi-Maskawa Parameter $|V_{us}|$ Using K_L Decays. *Phys. Rev. Lett.*, 93:181802, 2004. → pages 20

[46] F. Ambrosino et al. Measurements of the absolute branching ratios for the dominant K_L decays, the K_L lifetime, and V_{us} with the KLOE detector. *Physics Letters B*, 632:43 – 50, 2006. Available from: http://www.sciencedirect.com/science/article/pii/S0370269305014942. → pages 20

[47] F. Ambrosino et al. Study of the branching ratio and charge asymmetry for the decay $KS \rightarrow \pi e \nu$ with the KLOE detector. *Physics Letters B*, 636:173 – 182, 2006. Available from: http://www.sciencedirect.com/science/article/pii/S0370269306003807. → pages 20

[48] A. Lai et al. Measurement of the branching ratio of the decay KL→ $\pi^{\pm} e^{\mp} \nu$ and extraction of the CKM parameter V_{us}. *Physics Letters B*, 602:41 – 51, 2004. Available from: http://www.sciencedirect.com/science/article/pii/S0370269304013954. → pages 20

[49] V. I. Romanovsky et al. Measurement of k_{e3}^- branching ratio. *arXiv.org*, (0704.2052v2 [hep-ex]), 2007. → pages 20

[50] P. A. Boyle, A. Jüttner, R. D. Kenway, C. T. Sachrajda, S. Sasaki, A. Soni, R. J. Tweedie, and J. M. Zanotti. K_{l3} Semileptonic Form Factor from $(2 + 1)$-Flavor Lattice QCD. *Phys. Rev. Lett.*, 100:141601, 2008. → pages 20

[51] P. Boyle, J. Flynn, A. Jüttner, C. Kelly, C. Maynard, H. de Lima, C. Sachrajda, and J. Zanotti. K form factors with reduced model dependence. *The European Physical Journal C - Particles and Fields*, 69:159–167, 2010. 10.1140/epjc/s10052-010-1405-4. Available from: http://dx.doi.org/10.1140/epjc/s10052-010-1405-4. → pages 20, 21

[52] V. Lubicz, F. Mescia, S. Simula, and C. Tarantino. $K \rightarrow \pi l \nu$ semileptonic form factors from two-flavor lattice QCD. *Phys. Rev. D*, 80:111502, 2009. → pages 20

[53] E. Follana, C. T. H. Davies, G. P. Lepage, and J. Shigemitsu. High-Precision Determination of the π, K, D, and D_s Decay Constants from Lattice QCD. *Phys. Rev. Lett.*, 100:062002, 2008. → pages 21

[54] M. Antonelli, V. Cirigliano, G. Isidori, F. Mescia, M. Moulson, H. Neufeld, E. Passemar, M. Palutan, B. Sciascia, M. Sozzi, R. Wanke, and O. Yushchenko. An evaluation of V_{us} and precise tests of the Standard Model from world data on leptonic and semileptonic kaon decays. *The European Physical Journal C - Particles and Fields*, 69:399–424, 2010. 10.1140/epjc/s10052-010-1406-3. Available from: http://dx.doi.org/10.1140/epjc/s10052-010-1406-3. → pages 21, 22

[55] B. Aubert et al. *Phys. Rev. Lett.*, 105:051602, 2010. → pages 21

177

[56] M. Antonelli et al. Flavor physics in the quark sector. *Physics Reports*, 494:197 – 414, 2010. Available from: http://www.sciencedirect.com/science/article/pii/S037015731000133X. → pages 21, 23

[57] William J. Marciano. Fermi constants and "new physics". *Phys. Rev. D*, 60:093006, 1999. → pages 23

[58] W. J. Marciano and A. Sirlin. Constraint on additional neutral gauge bosons from electroweak radiative corrections. *Phys. Rev. D*, 35:1672–1676, 1987. → pages 24

[59] M.J. Ramsey-Musolf and S. Su. Low-energy precision tests of supersymmetry. *Physics Reports*, 456:1 – 88, 2008. Available from: http://www.sciencedirect.com/science/article/pii/S0370157307003894. → pages 24

[60] Nathal Severijns, Marcus Beck, and Oscar Naviliat-Cuncic. Tests of the standard electroweak model in nuclear beta decay. *Rev. Mod. Phys.*, 78:991–1040, 2006. Available from: http://link.aps.org/doi/10.1103/RevModPhys.78.991. → pages 24, 30

[61] R. P. Feynman and M. Gell-Mann. Theory of the Fermi Interaction. *Phys. Rev.*, 109:193–198, 1958. Available from: http://link.aps.org/doi/10.1103/PhysRev.109.193. → pages 29

[62] A. Serebrov, V. Varlamov, A. Kharitonov, A. Fomin, Yu. Pokotilovski, P. Geltenbort, J. Butterworth, I. Krasnoschekova, M. Lasakov, R. Tal'daev, A. Vassiljev, and O. Zherebtsov. Measurement of the neutron lifetime using a gravitational trap and a low-temperature Fomblin coating. *Physics Letters B*, 605:72 – 78, 2005. Available from: http://www.sciencedirect.com/science/article/pii/S0370269304015552. → pages 31, 38

[63] S Arzumanov, L Bondarenko, S Chernyavsky, W Drexel, A Fomin, P Geltenbort, V Morozov, Yu Panin, J Pendlebury, and K Schreckenbach. Neutron life time value measured by storing ultracold neutrons with detection of inelastically scattered neutrons. *Physics Letters B*, 483:15 – 22, 2000. Available from: http://www.sciencedirect.com/science/article/pii/S0370269300005797. → pages 31

[64] A. Pichlmaier, V. Varlamov, K. Schreckenbach, and P. Geltenbort. Neutron lifetime measurement with the ucn trap-in-trap mambo ii. *Physics Letters B*, 693(3):221 – 226, 2010. Available from: http://www.sciencedirect.com/science/article/pii/S0370269310009792. → pages 31

[65] A. P. Serebrov and A. K. Fomin. Neutron lifetime from a new evaluation of ultracold neutron storage experiments. *Phys. Rev. C*, 82:035501, 2010. Available from: http://link.aps.org/doi/10.1103/PhysRevC.82.035501, doi:10.1103/PhysRevC.82.035501. → pages 31

[66] Fred E. Wietfeldt and Geoffrey L. Greene. *Colloquium* : The neutron lifetime. *Rev. Mod. Phys.*, 83:1173–1192, 2011. Available from: http://link.aps.org/doi/10.1103/RevModPhys.83.1173. → pages 31

[67] W. Bambynek, H. Behrens, M. H. Chen, B. Crasemann, M. L. Fitzpatrick, K. W. D. Ledingham, H. Genz, M. Mutterer, and R. L. Intemann. Orbital electron capture by the nucleus. *Rev. Mod. Phys.*, 49:77–221, 1977. Available from: http://link.aps.org/doi/10.1103/RevModPhys.49.77. → pages 37

[68] O. Naviliat-Cuncic and N. Severijns. Test of the Conserved Vector Current Hypothesis in $T = 1/2$ Mirror Transitions and New Determination of $|V_{ud}|$. *Phys. Rev. Lett.*, 102:142302, 2009. Available from: http://link.aps.org/doi/10.1103/PhysRevLett.102.142302. → pages 37

[69] H. Abele, M. Astruc Hoffmann, S. Baeßler, D. Dubbers, F. Glück, U. Müller, V. Nesvizhevsky, J. Reich, and O. Zimmer. Is the Unitarity of the Quark-Mixing CKM Matrix Violated in Neutron β-Decay? *Phys. Rev. Lett.*, 88:211801, 2002. Available from: http://link.aps.org/doi/10.1103/PhysRevLett.88.211801. → pages 38

[70] S. Weinberg and S. B. Treiman. Electromagnetic corrections to isotopic spin conservation. *Phys. Rev.*, 116:465–468, 1959. Available from: http://link.aps.org/doi/10.1103/PhysRev.116.465. → pages 39

[71] M. Bhattacharya, D. Melconian, A. Komives, S. Triambak, A. Garcia, E. G. Adelberger, B. A. Brown, M. W. Cooper, T. Glasmacher, V. Guimaraes, P. F. Mantica, A. M. Oros-Peusquens, J. I. Prisciandaro, M. Steiner, H. E. Swanson, S. L. Tabor, and M. Wiedeking. *ft* value of the $0^+ \to 0^+$ β^+ decay of ^{32}Ar: A measurement of isospin symmetry breaking in a superallowed decay. *Phys. Rev. C*, 77:065503, 2008. Available from: http://link.aps.org/doi/10.1103/PhysRevC.77.065503. → pages 39, 50

179

[72] I. S. Towner and J. C. Hardy. Calculated corrections to superallowed Fermi β decay: New evaluation of the nuclear-structure-dependent terms. *Phys. Rev. C*, 66:035501, 2002. Available from: http://link.aps.org/doi/10.1103/PhysRevC.66.035501. → pages 40, 42, 45, 47, 48, 49, 62

[73] I. S. Towner and J. C. Hardy. Improved calculation of the isospin-symmetry-breaking corrections to superallowed Fermi β decay. *Phys. Rev. C*, 77:025501, 2008. Available from: http://link.aps.org/doi/10.1103/PhysRevC.77.025501. → pages 40, 43, 45, 47, 48, 50, 51, 52, 53, 55, 60, 62, 64, 160

[74] J. C. Hardy and I. S. Towner. Superallowed $0^+ \rightarrow 0^+$ nuclear β decays: A critical survey with tests of the conserved vector current hypothesis and the standard model. *Phys. Rev. C*, 71:055501, 2005. Available from: http://link.aps.org/doi/10.1103/PhysRevC.71.055501. → pages 41, 44, 46, 59, 169

[75] I. S. Towner. private communications, 2011. → pages 41, 158, 161, 169

[76] A. Sirlin. General Properties of the Electromagnetic Corrections to the Beta Decay of a Physical Nucleon. *Phys. Rev.*, 164:1767–1775, 1967. Available from: http://link.aps.org/doi/10.1103/PhysRev.164.1767. → pages 41

[77] A. Sirlin. Current algebra formulation of radiative corrections in gauge theories and the universality of the weak interactions. *Rev. Mod. Phys.*, 50:573–605, 1978. Available from: http://link.aps.org/doi/10.1103/RevModPhys.50.573. → pages 41, 42

[78] W. J. Marciano and A. Sirlin. Radiative corrections to β decay and the possibility of a fourth generation. *Phys. Rev. Lett.*, 56:22–25, 1986. Available from: http://link.aps.org/doi/10.1103/PhysRevLett.56.22. → pages 41

[79] Andrzej Czarnecki, William J. Marciano, and Alberto Sirlin. Precision measurements and CKM unitarity. *Phys. Rev. D*, 70:093006, 2004. Available from: http://link.aps.org/doi/10.1103/PhysRevD.70.093006. → pages 41

[80] William J. Marciano and Alberto Sirlin. Improved Calculation of Electroweak Radiative Corrections and the Value of V_{ud}. *Phys. Rev. Lett.*, 96:032002, 2006. Available from:

http://link.aps.org/doi/10.1103/PhysRevLett.96.032002. → pages 41, 42, 43, 44, 45, 50

[81] E. Blucher et al. Status of the Cabibbo Angle. arXiv:hep-ph/0512039v1, 2005. → pages 45

[82] W. E. Ormand and B. A. Brown. Corrections to the Fermi Matrix Element for Superallowed β Decay. *Phys. Rev. Lett.*, 62:866–869, 1989. Available from: http://link.aps.org/doi/10.1103/PhysRevLett.62.866. → pages 45, 49

[83] W. E. Ormand and B. A. Brown. Isospin-mixing corrections for *fp*-shell Fermi transitions. *Phys. Rev. C*, 52:2455–2460, 1995. Available from: http://link.aps.org/doi/10.1103/PhysRevC.52.2455. → pages 45, 49, 50, 60

[84] P. Finlay, S. Ettenauer, G. C. Ball, J. R. Leslie, C. E. Svensson, C. Andreoiu, R. A. E. Austin, D. Bandyopadhyay, D. S. Cross, G. Demand, M. Djongolov, P. E. Garrett, K. L. Green, G. F. Grinyer, G. Hackman, K. G. Leach, C. J. Pearson, A. A. Phillips, C. S. Sumithrarachchi, S. Triambak, and S. J Williams. High-Precision Half-Life Measurement for the Superallowed β^+ Emitter ^{26m}Al. *Phys. Rev. Lett.*, 106:032501, 2011. → pages 45, 63

[85] N. Auerbach. Coulomb corrections to superallowed β decay in nuclei. *Phys. Rev. C*, 79:035502, 2009. Available from: http://link.aps.org/doi/10.1103/PhysRevC.79.035502. → pages 46, 50, 51, 52, 60, 65

[86] J Britz, A Pape, and M.S Antony. Coefficients of the isobaric mass equation and their correlations with various nuclear parameters. *Atomic Data and Nuclear Data Tables*, 69:125 – 159, 1998. Available from: http://www.sciencedirect.com/science/article/pii/S0092640X98907732. → pages 48

[87] W.E. Ormand. *Isospin-symmetry violation in light nuclei*. PhD thesis, Michigan State University, 1986. → pages 49

[88] W.E. Ormand and B.A. Brown. Calculated isospin-mixing corrections to Fermi β-decays in 1s0d-shell nuclei with emphasis on A = 34. *Nuclear Physics A*, 440:274 – 300, 1985. Available from: http://www.sciencedirect.com/science/article/pii/0375947485903410. → pages 49

[89] I. S. Towner. private communcations, 2009. → pages 50

181

[90] G. A. Miller and A. Schwenk. Isospin-symmetry-breaking corrections to superallowed Fermi β decay: Formalism and schematic models. *Phys. Rev. C*, 78:035501, 2008. Available from: http://link.aps.org/doi/10.1103/PhysRevC.78.035501. → pages 52, 58

[91] Haozhao Liang, Nguyen Van Giai, and Jie Meng. Isospin corrections for superallowed Fermi β decay in self-consistent relativistic random-phase approximation approaches. *Phys. Rev. C*, 79:064316, 2009. Available from: http://link.aps.org/doi/10.1103/PhysRevC.79.064316. → pages 53, 54, 60, 61

[92] Haozhao Liang, Nguyen Van Giai, and Jie Meng. Isospin symmetry-breaking corrections for superallowed β decay in relativistic RPA approaches. *Journal of Physics: Conference Series*, 205:012028, 2010. Available from: http://stacks.iop.org/1742-6596/205/i=1/a=012028. → pages 54

[93] E. Caurier, P. Navrátil, W. E. Ormand, and J. P. Vary. *Ab initio* shell model for $A = 10$ nuclei. *Phys. Rev. C*, 66:024314, 2002. Available from: http://link.aps.org/doi/10.1103/PhysRevC.66.024314. → pages 56, 57

[94] R. Machleidt. High-precision, charge-dependent Bonn nucleon-nucleon potential. *Phys. Rev. C*, 63:024001, 2001. Available from: http://link.aps.org/doi/10.1103/PhysRevC.63.024001. → pages 57

[95] G. A. Miller and A. Schwenk. Isospin-symmetry-breaking corrections to superallowed Fermi β decay: Radial excitations. *Phys. Rev. C*, 80:064319, 2009. Available from: http://link.aps.org/doi/10.1103/PhysRevC.80.064319. → pages 58

[96] H. Liang and N. Van Giai. personal communications, 2011. → pages 61

[97] E. Mane, J. Behr, J. Billowes, T. Brunner, M. Brodeur, F. Buchinger, J. Crawford, J. Dilling, S. Ettenauer, C. Levy, A. Voss, and M. Pearson. Collinear laser spectroscopy with reverse-extracted bunched beams at TRIUMF. *Hyperfine Interactions*, 199:357–363, 2011. 10.1007/s10751-011-0331-7. Available from: http://dx.doi.org/10.1007/s10751-011-0331-7. → pages 63, 74

[98] B. Hyland, C. E. Svensson, G. C. Ball, J. R. Leslie, T. Achtzehn, D. Albers, C. Andreoiu, P. Bricault, R. Churchman, D. Cross, M. Dombsky, P. Finlay, P. E. Garrett, C. Geppert, G. F. Grinyer, G. Hackman, V. Hanemaayer, J. Lassen, J. P. Lavoie, D. Melconian, A. C. Morton, C. J. Pearson, M. R.

Pearson, A. A. Phillips, M. A. Schumaker, M. B. Smith, I. S. Towner, J. J. Valiente-Dobón, K. Wendt, and E. F. Zganjar. Precision Branching Ratio Measurement for the Superallowed β^+ Emitter ^{62}Ga and Isospin-Symmetry-Breaking Corrections in $A \geq 62$ Nuclei. *Phys. Rev. Lett.*, 97:102501, 2006. Available from: http://link.aps.org/doi/10.1103/PhysRevLett.97.102501. $\rightarrow$ pages 63

[99] K. G. Leach, C. E. Svensson, G. C. Ball, J. R. Leslie, R. A. E. Austin, D. Bandyopadhyay, C. Barton, E. Bassiachvilli, S. Ettenauer, P. Finlay, P. E. Garrett, G. F. Grinyer, G. Hackman, D. Melconian, A. C. Morton, S. Mythili, O. Newman, C. J. Pearson, M. R. Pearson, A. A. Phillips, H. Savajols, M. A. Schumaker, and J. Wong. Internal γ Decay and the Superallowed Branching Ratio for the β^+ Emitter ^{38}K^m. *Phys. Rev. Lett.*, 100:192504, 2008. Available from: http://link.aps.org/doi/10.1103/PhysRevLett.100.192504. $\rightarrow$ pages 63

[100] A. Piechaczek, E. F. Zganjar, G. C. Ball, P. Bricault, J. M. D'Auria, J. C. Hardy, D. F. Hodgson, V. Iacob, P. Klages, W. D. Kulp, J. R. Leslie, M. Lipoglavsek, J. A. Macdonald, H.-B. Mak, D. M. Moltz, G. Savard, J. von Schwarzenberg, C. E. Svensson, I. S. Towner, and J. L. Wood. High precision branching ratio measurement for the superallowed β decay of ^{74}Rb : A prerequisite for exacting tests of the standard model. *Phys. Rev. C*, 67:051305, 2003. Available from: http://link.aps.org/doi/10.1103/PhysRevC.67.051305. $\rightarrow$ pages 66, 67, 161

[101] M Oinonen et al. Non-analog β decay of ^{74}Rb. *Physics Letters B*, 511:145 – 150, 2001. Available from: http://www.sciencedirect.com/science/article/pii/S0370269301006463. $\rightarrow$ pages 68

[102] G. C. Ball, S. Bishop, J. A. Behr, G. C. Boisvert, P. Bricault, J. Cerny, J. M. D'Auria, M. Dombsky, J. C. Hardy, V. Iacob, J. R. Leslie, T. Lindner, J. A. Macdonald, H.-B. Mak, D. M. Moltz, J. Powell, G. Savard, and I. S. Towner. Precise Half-Life Measurement for the Superallowed $0^+ \rightarrow 0^+$ β Emitter ^{74}Rb: First Results from the New Radioactive Beam Facility (ISAC) at TRIUMF. *Phys. Rev. Lett.*, 86:1454–1457, 2001. Available from: http://link.aps.org/doi/10.1103/PhysRevLett.86.1454. $\rightarrow$ pages 68

[103] M. Mukherjee, D. Beck, K. Blaum, G. Bollen, P. Delahaye, J. Dilling, S. George, C. Guénaut, F. Herfurth, A. Herlert, A. Kellerbauer, H. Kluge, U. Köster, D. Lunney, S. Schwarz, L. Schweikhard, and C. Yazidjian. Mass measurements and evaluation around A = 22. *The European Physical*

183

Journal A - Hadrons and Nuclei, 35:31–37, 2008.
10.1140/epja/i2007-10523-2. Available from:
http://dx.doi.org/10.1140/epja/i2007-10523-2. $\rightarrow$ pages 68

[104] G. Savard, F. Buchinger, J. A. Clark, J. E. Crawford, S. Gulick, J. C. Hardy,
A. A. Hecht, J. K. P. Lee, A. F. Levand, N. D. Scielzo, H. Sharma, K. S.
Sharma, I. Tanihata, A. C. C. Villari, and Y. Wang. Q Value of the
Superallowed Decay of ^{46}V and Its Influence on V_{ud} and the Unitarity of
the Cabibbo-Kobayashi-Maskawa Matrix. *Phys. Rev. Lett.*, 95:102501,
2005. Available from:
http://link.aps.org/doi/10.1103/PhysRevLett.95.102501. $\rightarrow$ pages 68

[105] T. Eronen, D. Gorelov, J. Hakala, J. C. Hardy, A. Jokinen, A. Kankainen,
V. S. Kolhinen, I. D. Moore, H. Penttilä, M. Reponen, J. Rissanen,
A. Saastamoinen, and J. Äystö. Q_{EC} values of the superallowed β emitters
^{10}C, ^{34}Ar, ^{38}Ca, and ^{46}V. *Phys. Rev. C*, 83:055501, 2011. Available from:
http://link.aps.org/doi/10.1103/PhysRevC.83.055501. $\rightarrow$ pages 68

[106] D. Rodriguez, V. S. Kolhinen, G. Audi, J. Äystö, D. Beck, K. Blaum,
G. Bollen, F. Herfurth, A. Jokinen, A. Kellerbauer, H. J. Kluge,
M. Oinonen, H. Schatz, E. Sauvan, and S. Schwarz. Mass Measurement on
the rp-Process Waiting Point ^{72}Kr. *Phys. Rev. Lett.*, 93:161104, 2004.
Available from: http://link.aps.org/doi/10.1103/PhysRevLett.93.161104.
$\rightarrow$ pages 68, 158

[107] G. Audi, M. Epherre, C. Thibault, A.H. Wapstra, and K. Bos. Masses of
Rb, Cs and Fr isotopes. *Nuclear Physics A*, 378:443 – 460, 1982. Available
from:
http://www.sciencedirect.com/science/article/pii/0375947482904596. $\rightarrow$
pages 68, 146

[108] D. Lunney, N. Vieira, G. Audi, C. Gaulard, M. de Saint Simon, and
C. Thibault. Mass measurements of the shortest-lived nuclides a la mistral.
International Journal of Mass Spectrometry, 251:286 – 292, 2006.
Available from:
http://www.sciencedirect.com/science/article/pii/S1387380606001138. $\rightarrow$
pages 68

[109] Ryan Dunlop, Carl Svensson, Gordon Ball, et al. private communication,
2010. $\rightarrow$ pages 69

[110] R. Ringle, G. Bollen, A. Prinke, J. Savory, P. Schury, S. Schwarz, and
T. Sun. The LEBIT 9.4 T Penning trap mass spectrometer. *Nuclear*

Instruments and Methods in Physics Research Section A: Accelerators, Spectrometers, Detectors and Associated Equipment, 604:536 – 547, 2009. Available from: http://www.sciencedirect.com/science/article/pii/S0168900209006901. → pages 69, 72, 120

[111] R. Ringle, G. Bollen, P. Schury, S. Schwarz, and T. Sun. Octupolar excitation of ion motion in a penning trap: A study performed at lebit. *International Journal of Mass Spectrometry*, 262:33 – 44, 2007. Available from: http://www.sciencedirect.com/science/article/pii/S1387380606004738. → pages 70

[112] S. Eliseev, M. Block, A. Chaudhuri, F. Herfurth, H.-J. Kluge, A. Martin, C. Rauth, and G. Vorobjev. Octupolar excitation of ions stored in a Penning trap mass spectrometer: A study performed at SHIPTRAP. *International Journal of Mass Spectrometry*, 262:45 – 50, 2007. Available from: http://www.sciencedirect.com/science/article/pii/S1387380606004623. → pages 70

[113] S. Eliseev, C. Roux, K. Blaum, M. Block, C. Droese, F. Herfurth, M. Kretzschmar, M. I. Krivoruchenko, E. Minaya Ramirez, Yu. N. Novikov, L. Schweikhard, V. M. Shabaev, F. Šimkovic, I. I. Tupitsyn, K. Zuber, and N. A. Zubova. Octupolar-Excitation Penning-Trap Mass Spectrometry for Q-Value Measurement of Double-Electron Capture in ^{164}Er. *Phys. Rev. Lett.*, 107:152501, 2011. Available from: http://link.aps.org/doi/10.1103/PhysRevLett.107.152501. → pages 70, 103

[114] I. Bergstrom, C. Carlberg, T. Fritioff, G. Douysset, J. Schonfelder, and R. Schuch. SMILETRAP: A Penning trap facility for precision mass measurements using highly charged ions. *Nuclear Instruments and Methods in Physics Research Section A: Accelerators, Spectrometers, Detectors and Associated Equipment*, 487:618 – 651, 2002. Available from: http://www.sciencedirect.com/science/article/pii/S0168900201021787. → pages 70, 72, 113, 125, 150, 162

[115] A. S. Jensen, K. Riisager, D. V. Fedorov, and E. Garrido. Structure and reactions of quantum halos. *Rev. Mod. Phys.*, 76:215–261, 2004. Available from: http://link.aps.org/doi/10.1103/RevModPhys.76.215. → pages 71

[116] Björn Jonson. Light dripline nuclei. *Physics Reports*, 389:1 – 59, 2004. Available from: http://www.sciencedirect.com/science/article/pii/S0370157303003259. → pages 71

[117] V. L. Ryjkov, M. Brodeur, T. Brunner, M. Smith, R. Ringle, A. Lapierre, F. Ames, P. Bricault, M. Dombsky, P. Delheij, D. Lunney, M. R. Pearson, and J. Dilling. Direct Mass Measurement of the Four-Neutron Halo Nuclide ^{8}He. *Phys. Rev. Lett.*, 101:012501, 2008. Available from: http://link.aps.org/doi/10.1103/PhysRevLett.101.012501. → pages 71

[118] M. Brodeur et al. First direct mass-measurement of the two-neutron halo nucleus ^{6}He and improved mass for the four-neutron halo ^{8}He. *arXiv:1107.1684*, 2011. → pages 71, 136

[119] R. Ringle, M. Brodeur, T. Brunner, S. Ettenauer, M. Smith, A. Lapierre, V.L. Ryjkov, P. Delheij, G.W.F. Drake, J. Lassen, D. Lunney, and J. Dilling. High-precision Penning trap mass measurements of ^{9,10}Be and the one-neutron halo nuclide ^{11}Be. *Physics Letters B*, 675:170 – 174, 2009. Available from: http://www.sciencedirect.com/science/article/pii/S0370269309004067. → pages 71, 203

[120] S. Ettenauer, M. Brodeur, T. Brunner, A. T. Gallant, A. Lapierre, R. Ringle, M. R. Pearson, P. Delheij, J. Lassen, D. Lunney, and J. Dilling. Precision ground state mass of ^{12}Be and an isobaric multiplet mass equation (IMME) extrapolation for 2^+ and 0_2^+ states in the $T = 2$, $A = 12$ multiplet. *Phys. Rev. C*, 81:024314, 2010. Available from: http://link.aps.org/doi/10.1103/PhysRevC.81.024314. → pages 71

[121] R. Kanungo, A.T. Gallant, M. Uchida, C. Andreoiu, R.A.E. Austin, D. Bandyopadhyay, G.C. Ball, J.A. Becker, A.J. Boston, H.C. Boston, B.A. Brown, L. Buchmann, S.J. Colosimo, R.M. Clark, D. Cline, D.S. Cross, H. Dare, B. Davids, T.E. Drake, M. Djongolov, P. Finlay, N. Galinski, P.E. Garrett, A.B. Garnsworthy, K.L. Green, S. Grist, G. Hackman, L.J. Harkness, A.B. Hayes, D. Howell, A.M. Hurst, H.B. Jeppesen, K.G. Leach, A.O. Macchiavelli, D. Oxley, C.J. Pearson, B. Pietras, A.A. Phillips, S.V. Rigby, C. Ruiz, G. Ruprecht, F. Sarazin, M.A. Schumaker, A.C. Shotter, C.S. Sumitharachchi, C.E. Svensson, I. Tanihata, S. Triambak, C. Unsworth, S.J. Williams, P. Walden, J. Wong, and C.Y. Wu. Structure of states in ^{12}Be via the ^{11}Be(d,p) reaction. *Physics Letters B*, 682:391 – 395, 2010. Available from:

http://www.sciencedirect.com/science/article/pii/S0370269309013586. $\rightarrow$ pages 71

[122] G. Audi and W. Meng. Preview of atomic mass evaluation. private communication, April 2011, 2011. Available from: http://amdc.in2p3.fr/masstables/Ame2011int/filel.html. $\rightarrow$ pages 72, 153

[123] J. K. Tuli. Nuclear wallet cards, 2005. Available from: http://www.nndc.bnl.gov/wallet/ [cited Arpil 2011]. $\rightarrow$ pages 72, 166

[124] M. Brodeur, T. Brunner, C. Champagne, S. Ettenauer, M. Smith, A. Lapierre, R. Ringle, V. L. Ryjkov, G. Audi, P. Delheij, D. Lunney, and J. Dilling. New mass measurement of ^{6}Li and ppb-level systematic studies of the Penning trap mass spectrometer TITAN. *Phys. Rev. C*, 80:044318, 2009. Available from: http://link.aps.org/doi/10.1103/PhysRevC.80.044318. $\rightarrow$ pages 71, 95, 103, 117, 144, 149, 150, 154, 170

[125] C. Thibault, R. Klapisch, C. Rigaud, A. M. Poskanzer, R. Prieels, L. Lessard, and W. Reisdorf. Direct measurement of the masses of ^{11}Li and $^{26-32}$Na with an on-line mass spectrometer. *Phys. Rev. C*, 12:644–657, 1975. Available from: http://link.aps.org/doi/10.1103/PhysRevC.12.644. $\rightarrow$ pages 71

[126] E. K. Warburton, J. A. Becker, and B. A. Brown. Mass systematics for *A* =29˘44 nuclei: The deformed *A* $\sim$32 region. *Phys. Rev. C*, 41:1147–1166, 1990. Available from: http://link.aps.org/doi/10.1103/PhysRevC.41.1147, doi:10.1103/PhysRevC.41.1147. $\rightarrow$ pages 71

[127] A. T. Gallant et al. in preparation. $\rightarrow$ pages 72

[128] M. Honma, T. Otsuka, B. A. Brown, and T. Mizusaki. Effective interaction for pf-shell nuclei. *Phys. Rev. C*, 65:061301, 2002. Available from: http://link.aps.org/doi/10.1103/PhysRevC.65.061301. $\rightarrow$ pages 72

[129] Jason D. Holt, Takaharu Otsuka, Achim Schwenk, and Toshio Suzuki. Three-body forces and shell structure in calcium isotopes. *arXiv:1009.5984v2*, 2011. $\rightarrow$ pages 72

[130] M. Block, D. Ackermann, K. Blaum, A. Chaudhuri, Z. Di, S. Eliseev, R. Ferrer, D. Habs, F. Herfurth, F. P. Heßberger, S. Hofmann, H.-J. Kluge, G. Maero, A. Martín, G. Marx, M. Mazzocco, M. Mukherjee, J. B. Neumayr, W. R. Plaß, W. Quint, S. Rahaman, C. Rauth, D. Rodríguez,

C. Scheidenberger, L. Schweikhard, P. G. Thirolf, G. Vorobjev, and C. Weber. Towards direct mass measurements of nobelium at SHIPTRAP. *The European Physical Journal D - Atomic, Molecular, Optical and Plasma Physics*, 45:39–45, 2007. Available from: http://dx.doi.org/10.1140/epjd/e2007-00189-2. → pages 72

[131] M. Mukherjee, D. Beck, K. Blaum, G. Bollen, J. Dilling, S. George, F. Herfurth, A. Herlert, A. Kellerbauer, H. Kluge, S. Schwarz, L. Schweikhard, and C. Yazidjian. ISOLTRAP: An on-line Penning trap for mass spectrometry on short-lived nuclides. *The European Physical Journal A - Hadrons and Nuclei*, 35:1–29, 2008. Available from: http://dx.doi.org/10.1140/epja/i2007-10528-9. → pages 72, 101, 119

[132] J. Clark, R.C. Barber, C. Boudreau, F. Buchinger, J.E. Crawford, S. Gulick, J.C. Hardy, A. Heinz, J.K.P. Lee, R.B. Moore, G. Savard, D. Seweryniak, K.S. Sharma, G. Sprouse, J. Vaz, J.C. Wang, and Z. Zhou. Improvements in the injection system of the Canadian Penning trap mass spectrometer. *Nuclear Instruments and Methods in Physics Research Section B: Beam Interactions with Materials and Atoms*, 204:487 – 491, 2003. Available from: http://www.sciencedirect.com/science/article/pii/S0168583X02021171. → pages 72

[133] V.-V. Elomaa, T. Eronen, J. Hakala, A. Jokinen, A. Kankainen, I.D. Moore, S. Rahaman, J. Rissanen, C. Weber, and J. Äystö. Systematic studies of the accuracy of the Penning trap mass spectrometer JYFLTRAP. *Nuclear Instruments and Methods in Physics Research Section A: Accelerators, Spectrometers, Detectors and Associated Equipment*, 612:97 – 102, 2009. Available from: http://www.sciencedirect.com/science/article/pii/S0168900209017215. → pages 72

[134] T. Brunner et al. TITAN's Digital RFQ Ion Beam Cooler and Buncher, Operation and Performance. *arXiv:1107.2187*, 2011. → pages 73, 82, 84, 85, 86, 130

[135] Mathew Smith, Laura Blomeley, Paul Delheij, and Jens Dilling. First tests of the TITAN digital RFQ beam cooler and buncher. *Hyperfine Interactions*, 173:171–180, 2006. 10.1007/s10751-007-9554-z. Available from: http://dx.doi.org/10.1007/s10751-007-9554-z. → pages 73, 82, 85

[136] M. Froese, C. Champagne, J. Crespo LÃpez-Urrutia, S. Epp, G. Gwinner, A. Lapierre, J. Pfister, G. Sikler, J. Ullrich, and J. Dilling. A high-current electron beam ion trap as an on-line charge breeder for the high precision mass measurement TITAN experiment. *Hyperfine Interactions*, 173:85–92, 2006. 10.1007/s10751-007-9546-z. Available from: http://dx.doi.org/10.1007/s10751-007-9546-z. → pages 74, 88

[137] Z. Ke, W. Shi, G. Gwinner, K. Sharma, S. Toews, J. Dilling, and V. Ryjkov. A cooler ion trap for the TITAN on-line trapping facility at TRIUMF. *Hyperfine Interactions*, 173:103–111, 2006. Available from: http://dx.doi.org/10.1007/s10751-007-9548-x. → pages 74, 163

[138] V. Simon, P. Delheij, J. Dilling, Z. Ke, W. Shi, and G. Gwinner. Cooling of short-lived, radioactive, highly charged ions with the TITAN cooler Penning trap. *Hyperfine Interactions*, 199:151–159, 2011. 10.1007/s10751-011-0309-5. Available from: http://dx.doi.org/10.1007/s10751-011-0309-5. → pages 74

[139] V V Simon, U Chowdhury, P Delheij, J Dilling, B Eberhardt, and G Gwinner. A cooler Penning trap for the TITAN on-line trapping facility. *Journal of Physics: Conference Series*, 312:052024, 2011. Available from: http://stacks.iop.org/1742-6596/312/i=5/a=052024. → pages 74

[140] M. Bussmann, U. Schramm, and D. Habs. Simulating strongly coupled plasmas at low temperatures. *AIP Conference Proceedings*, 862:221–231, 2006. Available from: http://link.aip.org/link/?APC/862/221/1. → pages 74

[141] M. Bussmann, U. Schramm, D. Habs, V.S. Kolhinen, and J. Szerypo. Stopping highly charged ions in a laser-cooled one component plasma of ions. *International Journal of Mass Spectrometry*, 251:179 – 189, 2006. Available from: http://www.sciencedirect.com/science/article/pii/S138738060600073X. → pages 74

[142] Radu Cazan, Christopher Geppert, Wilfried Nörtershäuser, and Rodolfo Sánchez. Towards sympathetic cooling of trapped ions with laser-cooled Mg^+ ions for mass spectrometry and laser spectroscopy. *Hyperfine Interactions*, 196:177–189, 2010. Available from: http://dx.doi.org/10.1007/s10751-009-0144-0. → pages 74

[143] D. S. Hall and G. Gabrielse. Electron Cooling of Protons in a Nested Penning Trap. *Phys. Rev. Lett.*, 77:1962–1965, 1996. Available from: http://link.aps.org/doi/10.1103/PhysRevLett.77.1962. → pages 74

189

[144] B R Fulton. Present and Future RIB Facilities. *Journal of Physics: Conference Series*, 312:052001, 2011. Available from: http://stacks.iop.org/1742-6596/312/i=5/a=052001. → pages 75, 168

[145] M. Dombsky, D. Bishop, P. Bricault, D. Dale, A. Hurst, K. Jayamanna, R. Keitel, M. Olivo, P. Schmor, and G. Stanford. Commissioning and initial operation of a radioactive beam ion source at ISAC. *Rev. Sci. Instrum.*, 71:978–980, 2000. → pages 75

[146] Maxime Brodeur. *First direct mass measurement of the two and four neutron halos ^{6}He and ^{8}He using the TITAN Penning trap mass spectrometer*. PhD thesis, University of British Columbia, 2010. → pages 76, 83, 84, 101, 109, 122, 123, 147

[147] Pierre Bricault, Friedhelm Ames, Tobias Achtzehn, Marik Dombsky, Francis Labrecque, Jens Lassen, Jean-Phillipe Lavoie, and Nathalie Lecesne. An overview on TRIUMF's developments on ion source for radioactive beams (invited). *Rev. Sci. Instrum.*, 79:02A908, 2008. → pages 75

[148] J. Lassen, P. Bricault, M. Dombsky, J. Lavoie, Ch. Geppert, and K. Wendt. Resonant Ionization Laser Ion Source Project at TRIUMF. *Hyperfine Interactions*, 162:69–75, 2005. 10.1007/s10751-005-9212-2. Available from: http://dx.doi.org/10.1007/s10751-005-9212-2. → pages 75

[149] G.D. Alton. Ion sources for accelerators in materials research. *Nuclear Instruments and Methods in Physics Research Section B: Beam Interactions with Materials and Atoms*, 73:221 – 288, 1993. Available from: http://www.sciencedirect.com/science/article/pii/0168583X9395738Q. → pages 75

[150] G.D. Alton. Sources of low-charge-state positive-ion beams. In F.B. Dunning and Randall G. Hulet, editors, *Atomic, Molecular, and Optical Physics: Charged Particles*, volume 29, Part A of *Methods in Experimental Physics*, pages 69 – 168. Academic Press, 1995. Available from: http://www.sciencedirect.com/science/article/pii/S0076695X08606547. → pages 75

[151] C.E. Svensson, R.A.E. Austin, G.C. Ball, P. Finlay, P.E. Garrett, G.F. Grinyer, G.S. Hackman, C.J. Osborne, F. Sarazin, H.C. Scraggs, M.B. Smith, and J.C. Waddington. Radioactive beam experiments with large gamma-ray detector arrays. *Nuclear Instruments and Methods in Physics*

Research Section B: Beam Interactions with Materials and Atoms, 204:660 – 665, 2003. Available from: http://www.sciencedirect.com/science/article/pii/S0168583X0202147X. → pages 78

[152] G C Ball, T Achtzehn, D Albers, J S Al Khalili, C Andreoiu, A Andreyev, S F Ashley, R A E Austin, J A Becker, P Bricault, S Chan, R S Chakrawarthy, R Churchman, H Coombes, E S Cunningham, J Daoud, M Dombsky, T E Drake, B Eshpeter, P Finlay, P E Garrett, C Geppert, G F Grinyer, G Hackman, V Hanemaayer, B Hyland, G A Jones, K A Koopmans, W D Kulp, J Lassen, J P Lavoie, J R Leslie, Y Litvinov, J A Macdonald, C Mattoon, D Melconian, A C Morton, C J Osborne, C J Pearson, M Pearson, A A Phillips, J J Ressler, F Sarazin, M A Schumaker, J Schwarzenberg, H C Scraggs, M B Smith, C E Svensson, J J Valiente-Dobon, J C Waddington, P M Walker, K Wendt, S J Williams, J L Wood, and E F Zganjar. High-resolution γ-ray spectroscopy: a versatile tool for nuclear β-decay studies at TRIUMF-ISAC. *Journal of Physics G: Nuclear and Particle Physics*, 31:S1491, 2005. Available from: http://stacks.iop.org/0954-3899/31/i=10/a=019. → pages 78

[153] Geoff Grinyer. *High-Precision Half-Life Measurements for Superallowed Fermi Beta Decays*. PhD thesis, University of Guelph, 2007. → pages 78

[154] V.T Koslowsky, E Hagberg, J.C Hardy, G Savard, H Schmeing, K.S Sharma, and X.J Sun. The half-lives of 42Sc, 46V, 50Mn and 54Co. *Nuclear Instruments and Methods in Physics Research Section A: Accelerators, Spectrometers, Detectors and Associated Equipment*, 401:289 – 298, 1997. Available from: http://www.sciencedirect.com/science/article/pii/S0168900297010176. → pages 78

[155] Marik Dombsky. ISAC yields, 2011. Available from: http://www.triumf.info/facility/research_fac/yield.php. → pages 79, 81

[156] M. Dombsky, P. Bricault, P. Schmor, and M. Lane. ISAC target operation with high proton currents. *Nuclear Instruments and Methods in Physics Research Section B: Beam Interactions with Materials and Atoms*, 204:191 – 196, 2003. Available from: http://www.sciencedirect.com/science/article/pii/S0168583X0201902X. → pages 79

[157] Dienes G. J. and Damask A. C. *J. Appl. Phys.*, 29:1716, 1958. → pages 79

[158] Sizman R. *J. Nucl. Mater.*, 69 & 70:386, 1978. → pages 79

[159] Marik Dombsky. private communications and ISAC electronic logbook. →
pages 80

[160] A. Kellerbauer, T. Kim, R.B. Moore, and P. Varfalvy. Buffer gas cooling of
ion beams. *Nuclear Instruments and Methods in Physics Research Section
A: Accelerators, Spectrometers, Detectors and Associated Equipment*,
469:276 – 285, 2001. Available from:
http://www.sciencedirect.com/science/article/pii/S0168900201002868. →
pages 81

[161] F Herfurth, J Dilling, A Kellerbauer, G Bollen, S Henry, H.-J Kluge,
E Lamour, D Lunney, R.B Moore, C Scheidenberger, S Schwarz, G Sikler,
and J Szerypo. A linear radiofrequency ion trap for accumulation,
bunching, and emittance improvement of radioactive ion beams. *Nuclear
Instruments and Methods in Physics Research Section A: Accelerators,
Spectrometers, Detectors and Associated Equipment*, 469:254 – 275, 2001.
Available from:
http://www.sciencedirect.com/science/article/pii/S0168900201001681. →
pages 81, 87

[162] A. Nieminen, P. Campbell, J. Billowes, D. H. Forest, J. A. R. Griffith,
J. Huikari, A. Jokinen, I. D. Moore, R. Moore, G. Tungate, and J. Äystö.
On-line ion cooling and bunching for collinear laser spectroscopy. *Phys.
Rev. Lett.*, 88:094801, 2002. Available from:
http://link.aps.org/doi/10.1103/PhysRevLett.88.094801. → pages 82

[163] E. Mané, J. Billowes, K. Blaum, P. Campbell, B. Cheal, P. Delahaye,
K. Flanagan, D. Forest, H. Franberg, C. Geppert, T. Giles, A. Jokinen,
M. Kowalska, R. Neugart, G. Neyens, Nörtershäuser W., I. Podadera,
G. Tungate, P. Vingerhoets, and D. Yordanov. An ion cooler-buncher for
high-sensitivity collinear laser spectroscopy at ISOLDE. *The European
Physical Journal A - Hadrons and Nuclei*, 42:503–507, 2009. Available
from: http://dx.doi.org/10.1140/epja/i2009-10828-0. → pages 82

[164] R.B. Moore, O. Gianfrancesco, R. Lumbo, and S. Schwarz. The use of
high RFQ fields to manipulate ions. *International Journal of Mass
Spectrometry*, 251:190 – 197, 2006. Available from:
http://www.sciencedirect.com/science/article/pii/S1387380606000819. →
pages 82

[165] F. G. Major, V. N. Gheorghe, and G. Werth. *Charged Particle Traps*. Springer, 2005. → pages 82, 83, 97

[166] Li Ding, Michael Sudakov, and Sumio Kumashiro. A simulation study of the digital ion trap mass spectrometer. *International Journal of Mass Spectrometry*, 221:117 – 138, 2002. Available from: http://www.sciencedirect.com/science/article/pii/S1387380602009211. → pages 82

[167] M.J. Barnes and G.D. Wait. A 25 kv, 75 khz, kicker for measurement of muon lifetime. In *Pulsed Power Conference, 2003. Digest of Technical Papers. PPC-2003. 14th IEEE International*, volume 2, pages 1407 – 1410 Vol.2, 2003. doi:10.1109/PPC.2003.1278079. → pages 82

[168] Stefan Schwarz. *Trapped Charged Particles and Fundamental Interactions*, chapter Simulations for Ion Traps- Buffer Gas Cooling. Lecture Notes in Physics. Springer, 2008. → pages 83, 84

[169] F. G. Major and H. G. Dehmelt. Exchange-Collision Technique for the rf Spectroscopy of Stored Ions. *Phys. Rev.*, 170:91–107, 1968. Available from: http://link.aps.org/doi/10.1103/PhysRev.170.91. → pages 83

[170] Mathew Jonathon Smith. A Square-Wave-Driven Radiofrequency Quadrupole Cooler and Buncher for TITAN. Master's thesis, University of British Columbia, 2005. → pages 86

[171] Michael W. Froese. The TITAN Electron Beam Ion Trap: Assembly, Characterization, and First Tests. Master's thesis, University of Manitoba, 2006. → pages 88

[172] M. C. Simon. *Photoionisation hochgeladener Ionen durch weiche Röntgenstrahlung in einer Elektronenstrahl-Ionenfalle*. PhD thesis, Ruprecht-Karls-Universität Heidelberg, 2010. → pages 94

[173] Norris E. Bradbury and Russell A. Nielsen. Absolute values of the electron mobility in hydrogen. *Phys. Rev.*, 49:388–393, 1936. Available from: http://link.aps.org/doi/10.1103/PhysRev.49.388. → pages 95

[174] T. Brunner, A.R. Mueller, K. O'Sullivan, M.C. Simon, M. Kossick, S. Ettenauer, A.T. Gallant, E. Mané, D. Bishop, M. Good, G. Gratta, and J. Dilling. A large Bradbury Nielsen ion gate with flexible wire spacing based on photo-etched stainless steel grids and its characterization applying symmetric and asymmetric potentials. *International Journal of Mass*

193

Spectrometry, 309:97 – 103, 2012. Available from:
http://www.sciencedirect.com/science/article/pii/S1387380611003770. →
pages 95, 96, 97

[175] N. Ackerman et al. Observation of Two-Neutrino Double-Beta Decay in
^{136}Xe with the EXO-200 Detector. *Phys. Rev. Lett.*, 107:212501, 2011.
Available from: http://link.aps.org/doi/10.1103/PhysRevLett.107.212501.
→ pages 95

[176] Lowell S. Brown and Gerald Gabrielse. Geonium theory: Physics of a
single electron or ion in a Penning trap. *Rev. Mod. Phys.*, 58:233–311,
1986. Available from: http://link.aps.org/doi/10.1103/RevModPhys.58.233.
→ pages 97, 102, 103

[177] G. Bollen, R. B. Moore, G. Savard, and H. Stolzenberg. The accuracy of
heavy-ion mass measurements using time of flight-ion cyclotron resonance
in a Penning trap. *J. Appl. Phys.*, 68:4355–4374, 1990. Available from:
http://dx.doi.org/10.1063/1.346185. → pages 148

[178] Martin and Kretzschmar. The Ramsey method in high-precision mass
spectrometry with Penning traps: Theoretical foundations. *International
Journal of Mass Spectrometry*, 264:122 – 145, 2007. Available from:
http://www.sciencedirect.com/science/article/pii/S1387380607001649. →
pages 97, 102, 103, 104, 108, 113, 116, 131, 134, 142

[179] Alan G. Marshall, Christopher L. Hendrickson, and George S. Jackson.
Fourier transform ion cyclotron resonance mass spectrometry: A primer.
Mass Spectrometry Reviews, 17:1–35, 1998. Available from:
http://dx.doi.org/10.1002/(SICI)1098-2787(1998)17:1⟨1::
AID-MAS1⟩3.0.CO;2-K. → pages 103

[180] Brianna J. Mount, Matthew Redshaw, and Edmund G. Myers. Atomic
masses of ^{6}Li,^{23}Na,^{39,41}K,^{85,87}Rb, and ^{133}Cs. *Phys. Rev. A*, 82:042513,
2010. Available from:
http://link.aps.org/doi/10.1103/PhysRevA.82.042513. → pages 103

[181] Simon Rainville, James K. Thompson, and David E. Pritchard. An ion
balance for ultra-high-precision atomic mass measurements. *Science*,
303:334–338, 2004. Available from:
http://www.sciencemag.org/content/303/5656/334.abstract. → pages 103

[182] Simon Rainville, James K. Thompson, Edmund G. Myers, John M. Brown,
Maynard S. Dewey, Ernest G. Kessler, Richard D. Deslattes, Hans G.

Borner, Michael Jentschel, Paolo Mutti, and David E. Pritchard. World Year of Physics: A direct test of $E = mc^2$. *Nature*, 438:1096–1097, 2005. Available from: http://dx.doi.org/10.1038/4381096a. → pages 103

[183] J. Ketelaer, K. Blaum, M. Block, K. Eberhardt, M. Eibach, R. Ferrer, S. George, F. Herfurth, J. Ketter, Sz. Nagy, J. Repp, L. Schweikhard, C. Smorra, S. Sturm, and S. Ulmer. Recent developments in ion detection techniques for Penning trap mass spectrometry at TRIGA-TRAP. *The European Physical Journal A - Hadrons and Nuclei*, 42:311–317, 2009. Available from: http://dx.doi.org/10.1140/epja/i2008-10711-6. → pages 103

[184] G. Gräff, H. Kalinowsky, and J. Traut. A direct determination of the proton electron mass ratio. *Zeitschrift für Physik A Hadrons and Nuclei*, 297:35–39, 1980. 10.1007/BF01414243. Available from: http://dx.doi.org/10.1007/BF01414243. → pages 104

[185] M. König, G. Bollen, H.-J. Kluge, T. Otto, and J. Szerypo. Quadrupole excitation of stored ion motion at the true cyclotron frequency. *International Journal of Mass Spectrometry and Ion Processes*, 142:95 – 116, 1995. Available from: http://www.sciencedirect.com/science/article/pii/016811769504146C. → pages 104, 108, 110, 111, 112, 131, 134

[186] E. W. McDaniel and E. A. Mason. *The Mobility and Diffusion of Ions in Gases*. John Wiley and Sons, 1973. → pages 111

[187] V. V. Simon et al. Penning trap mass spectrometry of highly charged, radioactive neutron-rich Rb and Sr isotopes in the vicinity of $A \approx 100$. *in preparation*. → pages 112

[188] Norman F. Ramsey. A new molecular beam resonance method. *Phys. Rev.*, 76:996–996, 1949. Available from: http://link.aps.org/doi/10.1103/PhysRev.76.996. → pages 113

[189] Norman F. Ramsey. A molecular beam resonance method with separated oscillating fields. *Phys. Rev.*, 78:695–699, 1950. Available from: http://link.aps.org/doi/10.1103/PhysRev.78.695. → pages 113

[190] Norman F. Ramsey. Experiments with separated oscillatory fields and hydrogen masers. *Rev. Mod. Phys.*, 62:541–552, 1990. Available from: http://link.aps.org/doi/10.1103/RevModPhys.62.541. → pages 113

[191] G. Bollen, H.-J. Kluge, T. Otto, G. Savard, and H. Stolzenberg. Ramsey technique applied in a Penning trap mass spectrometer. *Nuclear Instruments and Methods in Physics Research Section B: Beam Interactions with Materials and Atoms*, 70:490 – 493, 1992. Available from: http://www.sciencedirect.com/science/article/pii/0168583X9295971S. → pages 113

[192] Vasant Natarajan, Kevin R. Boyce, Frank DiFilippo, and David E. Pritchard. Precision Penning trap comparison of nondoublets: Atomic masses of H, D, and the neutron. *Phys. Rev. Lett.*, 71:1998–2001, 1993. Available from: http://link.aps.org/doi/10.1103/PhysRevLett.71.1998. → pages 113

[193] S. George, S. Baruah, B. Blank, K. Blaum, M. Breitenfeldt, U. Hager, F. Herfurth, A. Herlert, A. Kellerbauer, H.-J. Kluge, M. Kretzschmar, D. Lunney, R. Savreux, S. Schwarz, L. Schweikhard, and C. Yazidjian. Ramsey Method of Separated Oscillatory Fields for High-Precision Penning Trap Mass Spectrometry. *Phys. Rev. Lett.*, 98:162501, 2007. Available from: http://link.aps.org/doi/10.1103/PhysRevLett.98.162501. → pages 113

[194] S. George, K. Blaum, F. Herfurth, A. Herlert, M. Kretzschmar, S. Nagy, S. Schwarz, L. Schweikhard, and C. Yazidjian. The Ramsey method in high-precision mass spectrometry with Penning traps: Experimental results. *International Journal of Mass Spectrometry*, 264:110 – 121, 2007. Available from: http://www.sciencedirect.com/science/article/pii/S1387380607001662. → pages 113, 114, 116

[195] M Suhonen, I BergstrÃm, T Fritioff, Sz Nagy, A Solders, and R Schuch. High-frequency Ramsey excitation in a Penning trap. *Journal of Instrumentation*, 2:P06003, 2007. Available from: http://stacks.iop.org/1748-0221/2/i=06/a=P06003. → pages

[196] M. Eibach, T. Beyer, K. Blaum, M. Block, K. Eberhardt, F. Herfurth, J. Ketelaer, Sz. Nagy, D. Neidherr, W. NÃrtershÃuser, and C. Smorra. First investigation of phase-shifted Ramsey excitation in Penning trap mass spectrometry. *International Journal of Mass Spectrometry*, 303:27 – 30, 2011. Available from: http://www.sciencedirect.com/science/article/pii/S1387380610004665. → pages 113

[197] S. George, K. Blaum, M. Block, M. Breitenfeldt, M. Dworschak,
F. Herfurth, A. Herlert, M. Kowalska, M. Kretzschmar, E. Minaya Ramirez,
D. Neidherr, S. Schwarz, and L. Schweikhard. Damping effects in Penning
trap mass spectrometry. *International Journal of Mass Spectrometry*,
299:102 – 112, 2011. Available from:
http://www.sciencedirect.com/science/article/pii/S1387380610003635. →
pages 113, 116

[198] A.H. Wapstra, G. Audi, and C. Thibault. The Ame2003 atomic mass
evaluation: (I). Evaluation of input data, adjustment procedures. *Nuclear
Physics A*, 729:129 – 336, 2003. Available from:
http://www.sciencedirect.com/science/article/pii/S0375947403018086. →
pages 117

[199] G. Audi, A.H. Wapstra, and C. Thibault. The Ame2003 atomic mass
evaluation: (II). Tables, graphs and references. *Nuclear Physics A*, 729:337
– 676, 2003. Available from:
http://www.sciencedirect.com/science/article/pii/S0375947403018098. →
pages 117, 158, 161

[200] J. E. Sansonetti. Wavelengths, Transition Probabilities, and Energy Levels
for the Spectra of Rubidium (RbI through RbXXXVII). 35:301–421, 2006.
Available from: http://dx.doi.org/10.1063/1.2035727. → pages 118, 153,
156

[201] G. Savard, St. Becker, G. Bollen, H.-J. Kluge, R.B. Moore, Th. Otto,
L. Schweikhard, H. Stolzenberg, and U. Wiess. A new cooling technique
for heavy ions in a Penning trap. *Physics Letters A*, 158:247 – 252, 1991.
Available from:
http://www.sciencedirect.com/science/article/pii/0375960191910082. →
pages 119

[202] Shenheng Guan and Alan G. Marshall. Stored waveform inverse Fourier
transform (SWIFT) ion excitation in trapped-ion mass spectometry: Theory
and applications. *International Journal of Mass Spectrometry and Ion
Processes*, 157-158:5 – 37, 1996. Available from:
http://www.sciencedirect.com/science/article/pii/S0168117696044618. →
pages 119

[203] Wolfgang R. Plass, Timo Dickel, Ulrich Czok, Hans Geissel, Martin
Petrick, Katrin Reinheimer, Christoph Scheidenberger, and Mikhail
I.Yavor. Isobar separation by time-of-flight mass spectrometry for

low-energy radioactive ion beam facilities. *Nuclear Instruments and Methods in Physics Research Section B: Beam Interactions with Materials and Atoms*, 266:4560 – 4564, 2008. Available from: http://www.sciencedirect.com/science/article/pii/S0168583X08007763. → pages 119

[204] R. Ringle, G. Bollen, A. Prinke, J. Savory, P. Schury, S. Schwarz, and T. Sun. A "Lorentz" steerer for ion injection into a Penning trap. *International Journal of Mass Spectrometry*, 263:38 – 44, 2007. Available from: http://www.sciencedirect.com/science/article/pii/S1387380606005781. → pages 121, 123

[205] M. Brodeur, V.L. Ryjkov, T. Brunner, S. Ettenauer, A. T. Gallant, V. Simon, M. Smith, A. Lapierre, R. Ringle, P. Delheij, M. Good, D. Lunney, and J. Dilling. Verifying the accuracy of the TITAN Penning-trap mass spectrometer. *International Journal of Mass Spectrometry, accepted for publication*, 2011. → pages 124, 147, 148, 149, 154, 170

[206] Stefan Ritt, Pierre Amaudruz, Konstantin Olchanski, et al. MIDAS-Maximum Integrated Data Acquisition System. Available from: http://midas.psi.ch/htmldoc/index.html. → pages 124

[207] B. R. Beck, J. Steiger, G. Weinberg, D. A. Church, J. McDonald, and D. Schneider. Measurement of charge exchange between h_2 and low-energy ions with charge states $35 \leq\, \leq 80$. *Phys. Rev. Lett.*, 77:1735–1738, 1996. Available from: http://link.aps.org/doi/10.1103/PhysRevLett.77.1735. → pages 125

[208] Alfred Müller and Erhard Salzborn. Scaling of cross sections for multiple electron transfer to highly charged ions colliding with atoms and molecules. *Physics Letters A*, 62:391 – 394, 1977. Available from: http://www.sciencedirect.com/science/article/pii/0375960177906727. → pages 125

[209] N. R. Daly. Scintillation type mass spectrometer ion detector. *Review of Scientific Instruments*, 31:264–267, 1960. Available from: http://link.aip.org/link/?RSI/31/264/1. → pages 127, 216

[210] Cecilia Leung. A 2-Way Daly-Type Beam Diagnostic System for TITAN EBIT (report of summer student term in the TITAN group), 2007. Available from: https://titan.triumf.ca/intern/documents/REPORT-Cecilia-expanded-TITAN-plus-MCP.pdf. → pages 127, 216

[211] Stephan Ettenauer. Documentation of MPET repair, modification, and upgrade 2010. Available from: https://titan.triumf.ca/intern/MPETrepair2010.shtml. → pages 127, 215

[212] Ameenah R. Farhan and Balraj Singh. Nuclear Data Sheets for A = 78. *Nuclear Data Sheets*, 110:1917 – 2080, 2009. Available from: http://www.sciencedirect.com/science/article/pii/S0090375209000696. → pages 129

[213] G. Bollen, H.-J. Kluge, M. König, T. Otto, G. Savard, H. Stolzenberg, R. B. Moore, G. Rouleau, G. Audi, and ISOLDE Collaboration. Resolution of nuclear ground and isomeric states by a Penning trap mass spectrometer. *Phys. Rev. C*, 46:R2140–R2143, 1992. Available from: http://link.aps.org/doi/10.1103/PhysRevC.46.R2140. → pages 129, 135, 164, 170

[214] K. Jayamanna, F. Ames, G. Cojocaru, R. Baartman, P. Bricault, R. Dube, R. Laxdal, M. Marchetto, M. MacDonald, P. Schmor, G. Wight, and D. Yuan. Off-line ion source terminal for ISAC at TRIUMF. *Review of Scientific Instruments*, 79:02C711, 2008. Available from: http://link.aip.org/link/?RSI/79/02C711/1. → pages 130

[215] Brianna J. Mount, Matthew Redshaw, and Edmund G. Myers. Double-β-decay Q values of ^{74}Se and ^{76}Ge. *Phys. Rev. C*, 81:032501, 2010. Available from: http://link.aps.org/doi/10.1103/PhysRevC.81.032501. → pages 130

[216] Tommi Eronen. *High Precision Q_{EC} Value Measurements of superallowed $0^+ \rightarrow 0^+$ Beta Decays with JYFLTRAP*. PhD thesis, University of Jyväskylä, 2008. → pages 135, 136, 164

[217] A. Kellerbauer, K. Blaum, G. Bollen, F. Herfurth, H.-J. Kluge, M. Kuckein, E. Sauvan, C. Scheidenberger, and L. Schweikhard. From direct to absolute mass measurements: A study of the accuracy of ISOLTRAP. *The European Physical Journal D - Atomic, Molecular, Optical and Plasma Physics*, 22:53–64, 2003. Available from: http://dx.doi.org/10.1140/epjd/e2002-00222-0. → pages 136

[218] A. T. Gallant. personal communications 2011. → pages 137

[219] Stefan Schwarz. Eva 6.013.2. → pages 138

[220] Ryan Ringle. Soma [online]. Available from:
http://www-ap.gsi.de/conferences/DataAnalysis/R_Ringle.pdf. → pages
138

[221] Lowell S. Brown and Gerald Gabrielse. Precision spectroscopy of a
charged particle in an imperfect Penning trap. *Phys. Rev. A*, 25:2423–2425,
1982. Available from: http://link.aps.org/doi/10.1103/PhysRevA.25.2423.
→ pages 148

[222] G. Gabrielse. Why Is Sideband Mass Spectrometry Possible with Ions in a
Penning Trap? *Phys. Rev. Lett.*, 102:172501, 2009. Available from:
http://link.aps.org/doi/10.1103/PhysRevLett.102.172501. → pages 148

[223] G. Gabrielse. The true cyclotron frequency for particles and ions in a
Penning trap. *International Journal of Mass Spectrometry*, 279:107 – 112,
2009. Available from:
http://www.sciencedirect.com/science/article/pii/S1387380608004247. →
pages 148

[224] R. S. Van Dyck, F. L. Moore, D. L. Farnham, and P. B. Schwinberg.
Number dependency in the compensated Penning trap. *Phys. Rev. A*,
40:6308–6313, 1989. Available from:
http://link.aps.org/doi/10.1103/PhysRevA.40.6308. → pages 150

[225] T. Shirai, J. Reader, A. E. Kramida, and J. Sugar. Spectral Data for
Gallium: Ga I through Ga XXXI. *Journal of Physical and Chemical
Reference Data*, 36:509–615, 2007. Available from:
http://link.aip.org/link/?JPR/36/509/1. → pages 156

[226] C. Guénaut, G. Audi, D. Beck, K. Blaum, G. Bollen, P. Delahaye,
F. Herfurth, A. Kellerbauer, H.-J. Kluge, J. Libert, D. Lunney, S. Schwarz,
L. Schweikhard, and C. Yazidjian. High-precision mass measurements of
nickel, copper, and gallium isotopes and the purported shell closure at
$N = 40$. *Phys. Rev. C*, 75:044303, 2007. Available from:
http://link.aps.org/doi/10.1103/PhysRevC.75.044303. → pages 156, 157

[227] T. Fritioff, H. Bluhme, R. Schuch, I. Bergström, and M. Björkhage.
Shedding light on the mercury mass discrepancy by weighing hg^{52+} ions in
a penning trap. *Nuclear Physics A*, 723:3 – 12, 2003. Available from:
http://www.sciencedirect.com/science/article/pii/S0375947403012284. →
pages 162

[228] Philip M. Walker and James J. Carroll. Ups and Downs of Nuclear Isomers. *Physics Today*, 58:39–44, 2005. Available from: http://link.aip.org/link/?PTO/58/39/1, doi:10.1063/1.1996473. → pages 163

[229] Philip Walker and George Dracoulis. Energy traps in atomic nuclei. *Nature*, 399:35, 1999. → pages 163

[230] Ani Aprahamian and Yang Sun. Nuclear physics: Long live isomer research. *Nature Physics*, 1:81, 2005. → pages 163

[231] B. Cheal, J. Billowes, M. L. Bissell, K. Blaum, F. C. Charlwood, K. T. Flanagan, D. H. Forest, S. Fritzsche, Ch. Geppert, A. Jokinen, M. Kowalska, A. Krieger, J. Krämer, E. Mané, I. D. Moore, R. Neugart, G. Neyens, W. Nörtershäuser, M. M. Rajabali, M. Schug, H. H. Stroke, P. Vingerhoets, D. T. Yordanov, and M. Žáková. Discovery of a long-lived low-lying isomeric state in ^{80}Ga. *Phys. Rev. C*, 82:051302, 2010. Available from: http://link.aps.org/doi/10.1103/PhysRevC.82.051302. → pages 165, 166

[232] J. Hakala, S. Rahaman, V.-V. Elomaa, T. Eronen, U. Hager, A. Jokinen, A. Kankainen, I. D. Moore, H. Penttilä, S. Rinta-Antila, J. Rissanen, A. Saastamoinen, T. Sonoda, C. Weber, and J. Äystö. Evolution of the $N = 50$ Shell Gap Energy towards ^{78}Ni. *Phys. Rev. Lett.*, 101:052502, 2008. Available from: http://link.aps.org/doi/10.1103/PhysRevLett.101.052502. → pages 166

[233] E. Rutherford. The scattering of α and β particles by matter and the structure of the atom. *Philosophical Magazine Series 6*, 21:669–688, 1911. Available from: http://www.tandfonline.com/doi/abs/10.1080/14786440508637080. → pages 168

[234] Rick Baartman. private communications, 2010. → pages 207

[235] M. C. Simon, J. C. Bale, U. Chowdhury, B. Eberhardt, S. Ettenauer, F. Jang, A. T. Gallant, A. Lennarz, M. Luichtl, T. Ma, D. Robertson, V. V. Simon, C. Andreoiu, T. Brunner, A. Chaudhuri, J. R. Crespo Lopez-Urrutia, P. Delheij, D. Frekers, A. Grossheim, G. Gwinner, A. Kwiatkowski, A. Lapierre, E. Mane, M. R. Pearson, R. Ringle, B. E. Schultz, and J. Dilling. The on-line charge breeding program at TITAN for precision mass measurements. In *Conference Proceeding of the 14th International Conference on Ion Sources (ICIS)*, 2011, to be published. → pages 210

[236] P Mandal, G Sikler, and M Mukherjee. Simulation study and analysis of a compact einzel lens-deflector for low energy ion beam. *Journal of Instrumentation*, 6:P02004, 2011. Available from: http://stacks.iop.org/1748-0221/6/i=02/a=P02004. → pages 210

[237] Mel Good. UHV Cleaning and Assembling Procedures. Available from: https://titan.triumf.ca/intern/documents/TRIUMF%20UHV%20Cleaning%20&%20Assembly%20%20Procedure.pdf. → pages 217

[238] Damien Robertson. An Improved Vacuum System for Storing Highly Charged Ions in a Penning Trap (report of summer student term in the TITAN group), 2011. → pages 218

Appendix A

Further Details about the Experimental Setup

A.1 Investigations regarding the PLT after the RFQ

As the Radio-Frequency Quadrupole (RFQ) is floated to a potential U_{RFQ} of a few 10's of kV with respect to the rest of the beamline at TRIUMF's Ion Trap for Atomic and Nuclear science (TITAN), a Pulsed Drift Tube (PLT) is used in order to set the transport beam energy of the ion bunches to $E_{\mathrm{kin}} = 1 - 2$ keV (Section 3.3.1). The Singly Charged Ions (SCI) are extracted from the RFQ and accelerated into the RFQ which is initially biased to $U_{\mathrm{RFQ}} - E_{\mathrm{kin}}/e$. When the ions are in the centre of the PLT, it is switched to ground potential and the ions leave the PLT with a kinetic energy of E_{kin}.

The rate (called repetition rate) at which the ions are being extracted from the RFQ is adapted to the half-life of the studied nuclides and ranges from 100 Hz to 1 Hz. While the setting of the PLT bias voltage $(U_{\mathrm{RFQ}} - E_{\mathrm{kin}}/e)$ should be independent of the repetition rate, it was observed [119] that it needs to be adjusted by a few volts depending on the repetition rate. Additionally, unreliability and failures of the HV switch motivated a new investigation into the PLT setup.

The fast switching of the PLT after the RFQ is done by two Metal-Oxide Semiconductor Field-Effect Transistors (MOSFET)s in a push-pull circuit (HTS 201-01-GSM manufactured by Behlke). This HV switch operates with voltage differences of up to 20 kV and rise times below 100 ns. The circuit and setup of the HV switch is shown in Figure A.1. Due to problems with the switch in the past, the serial resistors at the inputs of the switch had already been increased from the recommended 33 Ω to 100 Ω to limit cross currents between the +HV and the -HV leads.
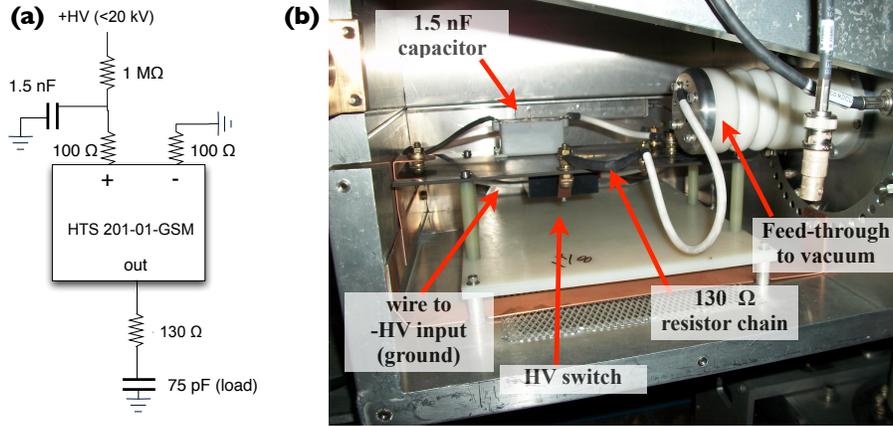
Figure A.1: HV switch setup to bring the PLT from maximal 20 keV to ground potential.(a) is the a circuit diagram and (b) a photo of the setup.

Together with the capacitive load of 75 pF in the form of the PLT and a 130 Ω resistor at the HV switch output, this increased the fall time when switching from 20 kV to ground potential to ~ 200 ns. The rise time when switching from ground potential back to HV is less critical as there are no ions in the PLT. When switching to +HV, instantaneous charge is provided by a 1.5 nF capacitor which is recharged by a HV power supply with a maximal current of 1.8 mA. A 1 MΩ resistor is inserted between the power supply and the rest of the circuit to limit the current well below the 1.8 mA maximum of the power supply. Assuming an ideal HV switch and power supply, the switching from ground back to +HV of the PLT can be described by a doubled RC circuit shown in Figure A.2. At time $t = 0$ there is no charge on the PLT, but the capacitor C_2 is fully charged, $Q_2(t = 0) = -C_2/V$. The circuit is governed by two time constants,

$$\lambda_{1,2} = \frac{-\left(R(C_1 + C_2) + R_1 C_1\right)\left[1 \pm \sqrt{1 - \frac{4RR_1 C_2 C_2}{(R(C_1+C_2)+R_1 C_1)^2}}\right]}{2RR_1 C_1 C_2}. \tag{A.1}$$
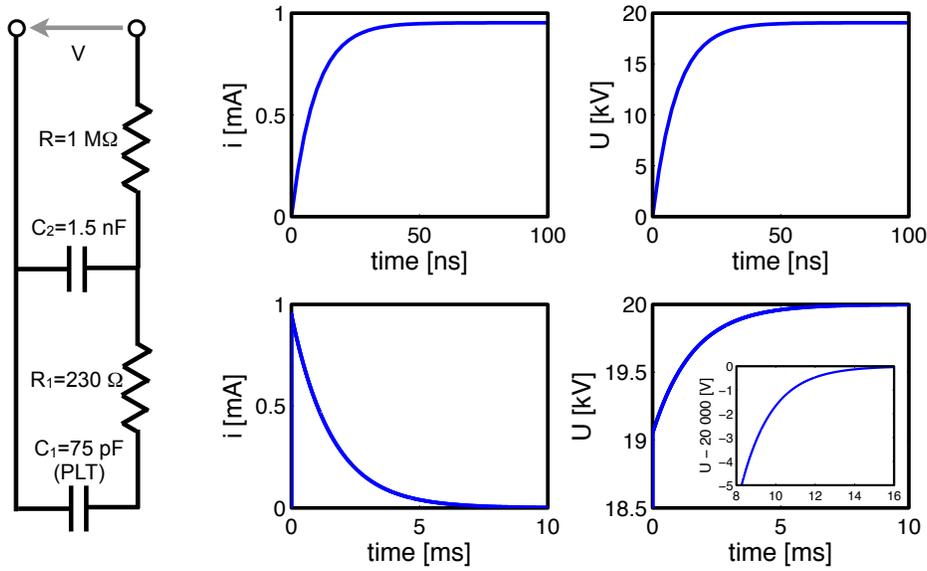
Figure A.2: Circuit diagram representing the switching from ground potential to 20 kV (on the left) (+HV branch in Figure A.1) . The graphs on the right show the current drawn from the power supply and the voltage at the PLT. While the plots in the first row show changes in the first 100 ns, the row of plots at the bottom illustrate the long term (10 ms) behaviour.

For $R_1 C_1 << R C_2$, the square root can be expanded and one obtains to lowest order

$$\lambda_1^{-1} \approx R C_2 (1 + \frac{C_1}{C_2}) \tag{A.2}$$

$$\lambda_2^{-1} \approx R_1 C_1 (1 + \frac{C_1}{C_2}). \tag{A.3}$$

$$\tag{A.4}$$

These are the time constants of each individual RC circuit modified by the ratio of the two capacitors which is the consequence of the coupling between the two RC circuits. The switching from ground to +20 kV of the PLT has hence a fast component which represents the instantaneous charge provided by the larger capacitance and the re-charging of C_2 which is slower due to the current limiting resistor R. As shown in Figure A.2 the fast component brings the PLT to about 19 kV within just
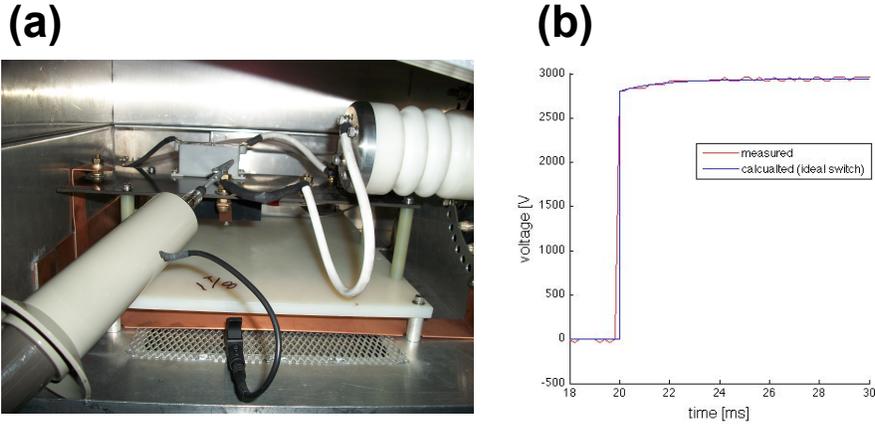
Figure A.3: Performance test of the PLT's HV switch circuit with a high volt-
age probe (a). The measured signals are compared to calculations as-
suming an ideal switch in (b). The test has been done for switching
from ground potential to 3 kV.

50 ns. Then the slow time constant starts to dominate as new charge has to be pro-
vided by the power supply to charge up C_2 and hence also C_1, the PLT. The second
part takes several milliseconds. As seen in the insert on the bottom-right of Fig-
ure A.2, after 10 ms the voltage at the PLT is still 2 V short of the 20 kV. A change
in the ion's mean kinetic energy by 2 eV or larger can indeed make a difference for
trapping at the Measurement Penning Trap (MPET). Hence, repetition rates of 100
Hz or faster will certainly be different in the optimal trapping conditions owing to
the PLT which is not charged up completely, when ions are extracted from the RFQ.

Measurements have been carried out to validate the assumption of an ideal switch.
The performance of the switch circuit was measured with a Tektronix P6015A 40
kV pk pulse scope probe which was brought into the circuit directly after the HV
switch. The test was performed at a 10 Hz repetition rate with an 80 % duty cycle.
Figure A.3 shows good agreement between measurement and calculation and con-
firms the description above.
In conclusion, repetition rates of 100 Hz and faster of ion extraction from the RFQ
lead in the current setup indeed to differences in the kinetic energy of ions for dif-
ferent repetition rates. Hence, for faster operation when switching to +20kV, the
current limiting resistor of 1 MΩ could be reduced because the maximal current
drawn from the power supply is about 1 mA in the present setup (see Figure A.2).

The power supply could provide currents up to 1.8 mA. However, these investigations cannot explain the observed differences in optimal measurement settings for repetition rates of 50 Hz to 5 Hz.

In the course of the investigations the 1 MΩ resistor at the output of the HV switch was identified as a cause for damage of HV switches in the past. A HV rated resistor was inserted into the setup replacing the old unreliable one. Since then the HV switch has worked properly.

A.2   More details on the beam transport

A basic description of the transport of ion bunches between different traps (i.e. RFQ, Electron Beam Ion Trap (EBIT), and MPET) has been provided in Section 3.5. This section explains further details about the beam transport setup at the TITAN facility as used during the present measurements.

Upstream of the RFQ a pair of steerer plates (labeled as 'beam gate' in Figure 3.19) adjusted the beam direction after the Isotope Separator and ACcelerator (ISAC) beam was bent by 90° from the horizontal ISAC beamline into the vertically mounted RFQ beamline. In order to control the injection of continuous beam into the RFQ, the bias voltage of the pair of steerer plates could be switched to deflect the beam and no ions could further reach the RFQ (Figure A.4). This was useful to set a well-defined cooling time in the RFQ. Without an interruption of the beam injection, new ions could collide with already thermalized ions. Furthermore, the energy distribution of the ions in the RFQ at the time of beam extraction could be wider because a fraction of the ions would not yet have been in thermal equilibrium with the buffer gas. Depending on the incoming beam intensity, the gate was typically closed 1-10 ms prior to the ion extraction from the RFQ. Ions arriving during this time were lost. Hence, for low yields the gate was not applied at all as the loss of ions was more critical for the measurement than a potential larger energy spread.

After the ions were extracted from the RFQ, the PLT allowed one to set the kinetic energy to 2 keV. Two electrostatic 45° benders directed the ion bunch from the vertical to the horizontal TITAN beamline. A pair of quadrupoles corrected for the beam aberration caused by the benders such that the beam spot on the horizontal beamline was again circular. For better diagnostics, a Multi Channel Plate (MCP) detector was installed after the first 45° (labeled MCP1 in Figure 3.19). MCP1 was equipped with a phosphor screen attached to the anode. The phosophor screen converted the secondary electrons from the MCP plates into visible light. Thus, at sufficiently large number of ions in the ion bunch an image of the beam spot was created which was read by a digital camera. After optimizing on beam intensity, the quadrupole lens was adjusted to gain a shape of the beam image at MCP1 according to the transfer matrix calculations of the TITAN beamline [234].
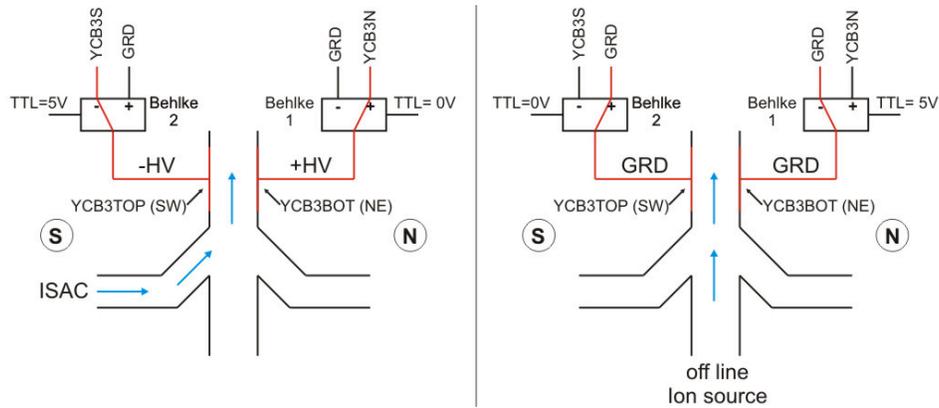
Figure A.4: Schematic of the beam gate in front of the RFQ for controlled injection times of ions from either ISAC or TITAN's ion source. Either the ISAC beam or the ion source is blocked completely by a source cup or a gate valve. By switching the bias voltage of steerer plates YCB3TOP and YCB3BOT, the steerer plates act as a beam gate. In the configuration pictured on the left the ISAC is injected into RFQ, while for the case on the right only a beam sent from TITAN's ion source can pass.

In the horizontal beamline, the further path of the ion bunch was guided by a switchyard. For mass measurements of SCI the beam could pass straight towards the MPET. When aiming for Highly Charged Ions (HCI), the beam of SCI was bent by another 90° into the EBIT beamline. Between two 45° turns, there was a quadrupole lens and MCP2 could be inserted for diagnostics. MCP2 had no phosphor screen, but it could be used for maximizing beam intensity. For better beam diagnostics, a new MCP was added to the beamline in front of the EBIT (MCP3). Its installation included a phosphor screen which was read out analogously to MCP1. The pair of quadrupoles in the first 90 degree bend in the switchyard were set to achieve a circular beam spot on MCP3. The procedure of the optimization of the EBIT is presented in Section A.3, which involved MCP6 as the main diagnostics tool. Once the ions were prepared to a high charge state in the EBIT, the ion bunch was released from the EBIT and sent back to the switchyard. There, two subsequent 45° benders guided the beam into the MPET beamline, where MCP0 served for transport optimization (as already explained in Section 3.5).

All preparations were done with beam from TITAN's surface ion source which provided the stable Rb-isotopes in their natural abundances of 72% of ^{85}Rb and 28%

of ^{87}Rb. The whole setup could be adapted to other masses by scaling all timings such as the EBIT trapping time or the time when the PLT after the RFQ had to be brought to ground potential. Independently of the mass, any ion species reached the same energy through the collision with the buffer gas in the RFQ and was re-accelerated by the same electrostatic potential. Hence, a certain timing for an ion with mass number A_1 is related to the calibration mass A_2 by $t_1 = t_2 \cdot \sqrt{A_2/A_1}$ with t_1 referenced to the RFQ extraction trigger. Analogously, any timing of HCI sent from the EBIT followed the same equation when A_i was substituted by A_i/q_i with q_i being the charge state. This relationship was also used for identifying m/q in Time-Of-Flight (TOF) spectra such as Figure 3.16. For better reliability of the scaling law, the preparation previous to the measurement was done with a m/q close to the one of the measurement itself. Particularly, with HCI of elements with larger atomic number Z the integer changes in q in m/q became smaller and a charge state in close proximity to the desired m/q could always be found.

A.3   Optimization of EBIT injection, trapping, and extraction

In its application to rare isotopes, the efficiency of the charge breeding is of prime concern. Good overlap of the electron beam with the trapped ions is equally important as minimal losses during the injection and extraction of ions in the EBIT. Here, the optimization of the EBIT injection and extraction is described as it was done in preparation of the present studies.

A preliminary injection tune into the EBIT was achieved without an electron beam or an applied trapping potential. The electron gun was retracted and provided space to insert MCP4 (see Figure 3.19) which was equipped with a phosphor screen. The optics elements along the EBIT beamline as well as the last benders influenced the injection trajectory. Ideally, the ion and electron beam should each be injected along the magnetic axis of the EBIT. In an off-axis injection, the ions circled around the field axis. In principle, these trajectories should be visible on the phosphor screen of MCP4 in the form of a ring as described in [2], while on-axis injection should result in a point. However, this method was found to be not accurate enough and was further complicated by that fact that the injection was different without and with electron beam. Once a preliminary injection setting was found with the help of MCP4, the electron beam was turned on and provisional voltages were applied to the EBIT drift tubes (see Figure A.5). The central drift tube, where ions would be trapped later, was slightly below the beam energy to remove most of the ions' kinetic energy. The injection was then fine-tuned in three steps.

First, the trap was kept closed all the time. Thus, the ion bunch could not enter into
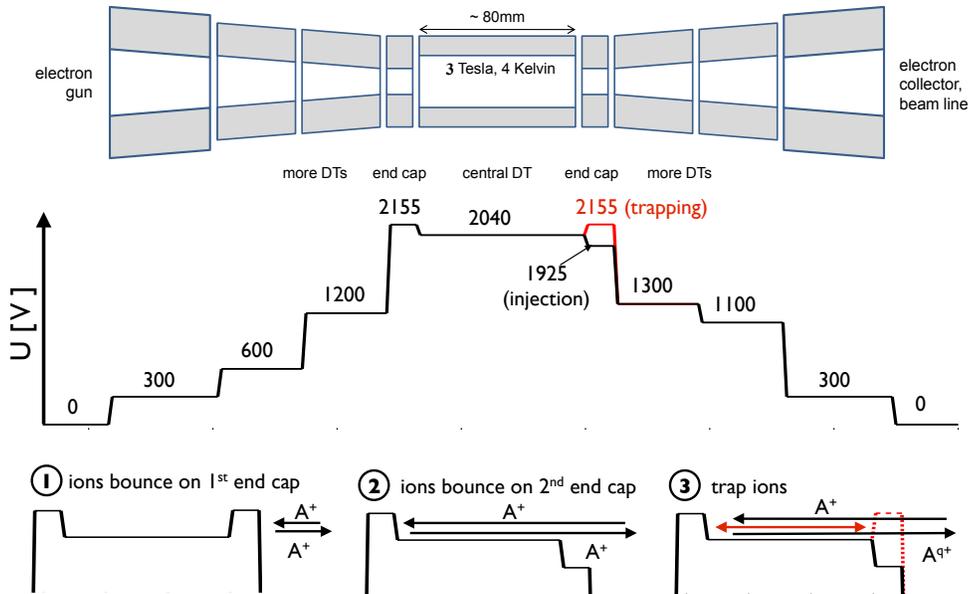
Figure A.5: Schematic of the EBIT drift tubes (top) and their potentials (bottom) for injection and trapping during the charge breeding of neutron-deficient Rb- isotopes. The procedure for the optimization of the ion injection is shown in (1) to (3). Electrode structure modified from [235].

the trap region, but was reflected at the drift tube which was used as the end cap on the electron collector side (Figure A.5(1)). In this manner the ion beam spent little time interacting with the electron beam which simplified the tuning procedure and virtually all ions remained singly charged. While the ions were in the EBIT region, voltages applied to x-steerers next to the switchyard in the EBIT beamline were switched in their polarity such that the reflected ion beam entered into a 45° bender to turn the beam onto MCP6 (see Figure 3.19). Hence, MCP6 could be used for diagnostics of the injection. Critical components of the EBIT setup were two Sikler lenses [236]. As the last optic elements before and the first (and only) in the magnetic field, their capability for x- and y- steering as well as focusing in the same compact unit was advantageous. A sketch of a Sikler lens is presented as an insert of Figure 3.19.

In the second step, the potential on the first end cap of the EBIT was lowered and the ion beam was reflected at the second end cap electrode (Figure A.5(2)). The interaction time of ions passing through the electron beam was still too short to make electron-impact ionization of the ions significant. Once a good signal of the

reflected ion bunch was seen on MCP6, the ions could be trapped in a last step (Figure A.5(3)). The optimal moment to close the trap was considered to be the time when the ions were reflected on the second end cap. Because of the equal path length from MCP2 to the EBIT and from there to MCP6 (compare Figure 3.19), this time could be inferred from $t_{\mathrm{capture}} = (t_{\mathrm{MCP6}} - t_{\mathrm{MCP2}})/2$. Here, t_{MCPi} was the TOF from the extraction from the RFQ to the respective MCP. The last optimization of injection was done by trapping the ions in the EBIT. Initially, they were trapped for a few milliseconds but after each optimization round, increasingly longer. For breeding times only lower charge states were populated by the charge breeding.

Injection and extraction setup were in such an opimization mode dependent from each other and could only be improved together. In principle, one would expect that the settings for injection and extraction along the EBIT beamline should (apart from the x-steerer next to the switchyard) be identical as the beam optics should be independent of m/q. However, in practice steering settings for injection and extraction drifted apart. This was likely due to the re-thermalization of the ion bunch in the EBIT to a different energy [2] and the presence of residual magnetic fields. During the preparation, each optical element along the EBIT beamline was once controlled by a HV switch to provide different optics parameters for injection and extraction. For those elements which showed significant differences between injection and extraction the HV switch was kept in the setup. In the end, these elements were the Sikler lens in front of the EBIT as well as the vertical steerer right next to the switchyard. Hence, at this position both x- and y-steerers were switched to their optimal EBIT injection and extraction values.

Since the influence of the electron beam on the injection was found to be important, it was necessary to start with a small electron beam current of 1-2 mA. When optimal settings had been found, the beam current was increased further in small steps and the three tuning steps described above were repeated. During the online-measurement, the EBIT was operating at an electron beam current of 10 mA. As the space charge potential of the electron beam modified the electrical force experienced by the ions, the potential of the drift tubes had to be readjusted with each increase of the electron beam. The final applied potentials are shown in Figure A.5.[1]

The magnetic field of 3 T was used at the EBIT throughout the entire measurement. A higher field would compress the electron beam more and higher electron densities would result in faster charge breeding assuming good overlap between electron beam and ions. However, a smaller electron beam size also made it more difficult to find this geometrical overlap. A field of 3 T was considered a good compromise

---

[1]After the described measurements, the procedure has been changed. Owing to more experience with the setup the optimization now usually starts with the desired electron beam current.
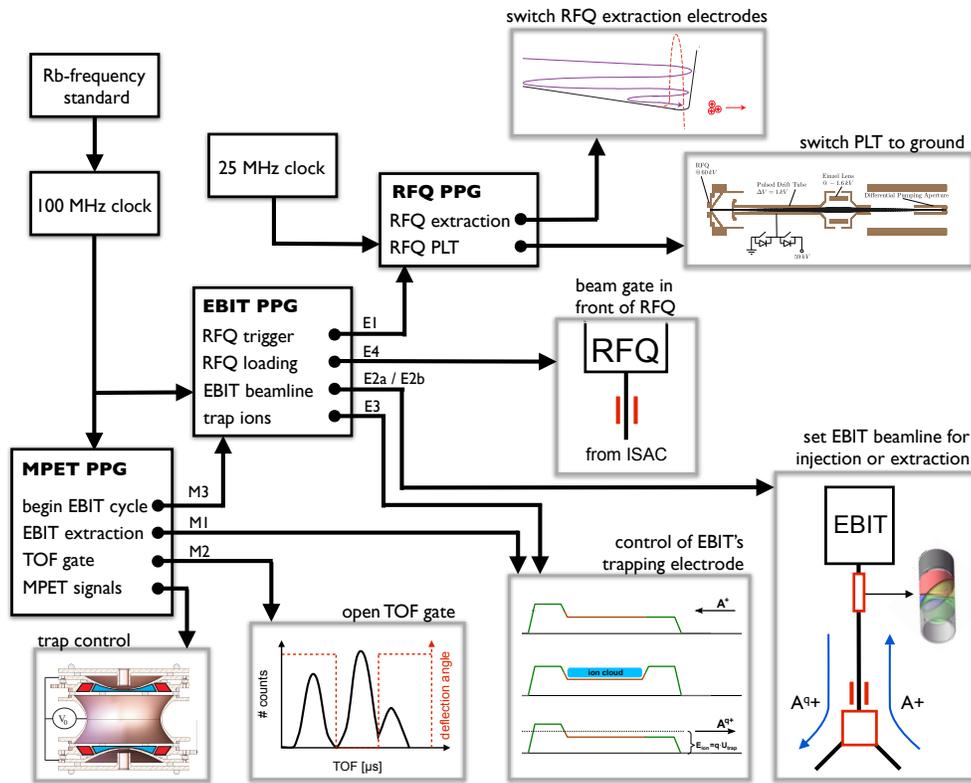
Figure A.6: Hierarchy of experimental control with Programmable Pulse Generators (PPGS).

between these conflicting interests.

A.4 Measurement control system

The architecture of the experimental control system is explained in Figure A.6. Its core is three Programmable Pulse Generators (PPGS) which each regulate the main time-dependent functionalities of the RFQ, EBIT, and MPET. The MPET PPG acts as the master PPG. It provides an external trigger to the EBIT PPG which on its own triggers the RFQ PPG. As discussed in Section 3.7.3, the mass measurement in MPET involves Radio-Frequency (RF)-scans in order to map a resonance around the ion's cyclotron frequency $\nu_c = 1/(2\pi) \cdot qB/m$. For each ion bunch one fixed frequency is applied. At TITAN, one frequency scan ramps over 41 or 21 frequency
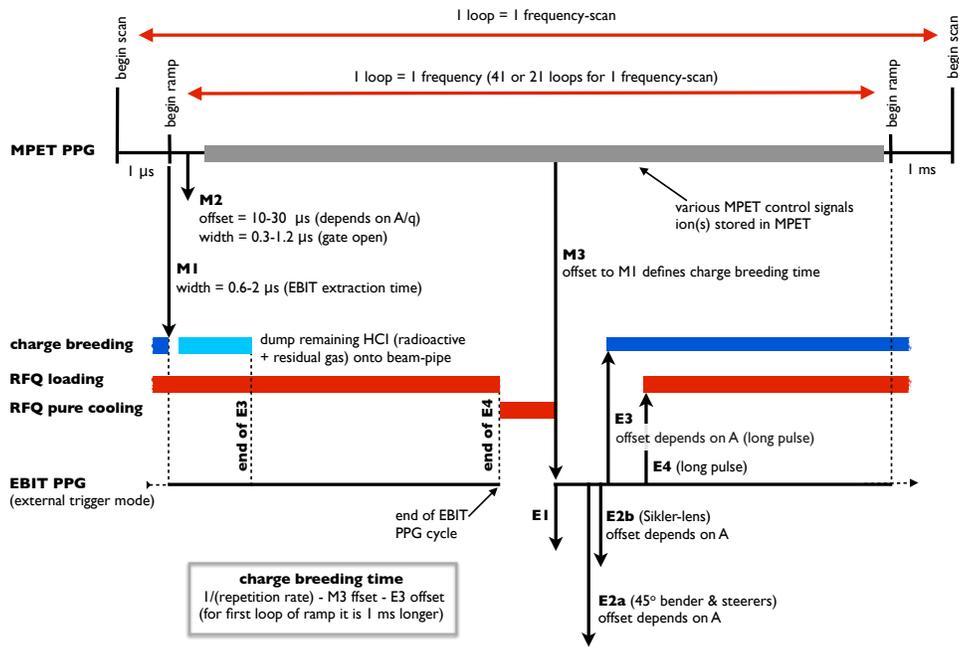
Figure A.7: Schematic of timings of MPET and EBIT PPG for beam transport and charge breeding. The signal names (e.g. M2) refer to the names given in Figure A.6. Timings on the x-axis are not to scale.

steps each of which requires one ion bunch. A measurement run consists of multiple frequency scans. The MPET PPG loops through a whole measurement run (see also Figure A.7). For each ion shot the EBIT and RFQ PPG are triggered one time each. RFQ ion accumulation, charge breeding in EBIT, and the measurement in the MPET are done in parallel. When the measurement at MPET of one ion bunch is completed at the MPET, the MPET PPG requests a new ion shot from the EBIT. Then, the EBIT PPG on its turn transfers the next ion bunch from the RFQ into the EBIT. This consecutive order means that for the first ion bunch of a measurement run no ions are stored in the MPET. If the beam gate in front of the RFQ is used, the second shot into the MPET is without ions of interest, as well. Figure A.7 gives deeper insight into the time intercorrelation of the individual pulses between different PPG as well as the timings of measurement control signals. Both EBIT and MPET PPG receive their time standard from a 100 MHz clock which is itself synchronized by a Rubidium frequency standard (Figure A.6). The RFQ PPG is inside a Faraday cage which hosts all electronics of the RFQ and is hence floated to the

RFQ bias. For simplicity, the RFQ PPG runs on its own 25 MHz clock which is currently not synchronized to the 100 MHz master clock. This results in a jitter between RFQ and EBIT PPG signals. It was measured to be approximately 60 ns, which is acceptable. Other communications from and to the inside of the Faraday cage such as the external PPG trigger are done via fibre signals.

A.5 The MPET vacuum

This section describes the work on the MPET vacuum system to improve the quality of the vacuum to minimize charge exchange of HCI with residual gas in the MPET. The pressure in the MPET section before working with charge bred ions (prior to summer 2009) was $\sim 2 \cdot 10^{-9}$ mbar.[2] A first improvement of the vacuum could be achieved by baking an ion pump at $\approx 200^o$ C while it was connected to the rest of the setup. The ion pump itself was not operating at this time, but its large surface area added significantly to the outgassing rate. The pressure after the bake-out of the ion pump was $\sim 8 \cdot 10^{-10}$ mbar.

As discussed in Section 3.7.8, charge exchange remained a significant challenge at this pressure. The quality of the vacuum was improved along several lines. A first attempt to moderately raise the temperature of the MPET vacuum tube in the bore of the superconducting magnet itself failed. Keeping tube and ion pump initially at 40°C for several days and later at 60 ^{o}C for a full week to increase the outgassing rate did not have any effect on the pressure when cooling down to room temperature again. In a next step, the titanium tube housing the MPET setup (see top of Figure 3.32) was retracted from the magnet bore and installed at a dedicated baking setup shown in Figure 3.36. The MCP detector was removed during the baking. The initial pressure before raising the temperature was $\approx 8 \cdot 10^{-9}$ mbar. The development of the pressure during and after the baking is documented at the bottom of Figure 3.36. The centre of the tube was brought to temperatures of up to $\approx 230^o$ C. The final pressure in the baking setup recorded about 3 weeks after the end of the baking was $\approx 5 \cdot 10^{-11}$ mbar- an improvement by more than 2 orders of magnitude. Ion gauges on both sides of the tube (see Figure 3.36) measured about the same pressure indicating that the pressure in the trap itself could be characterized by a similar value. Opposed to the success of an improved vacuum, the expansion and contraction of wires inside the tube during the baking led to a few shorted electrical circuits and a loss of an electrical connection to one electrode. All modifications to the wiring system which had to be carried out are

---

[2]Please note that this is not necessarily the pressure in the trap itself. The pressure was measured with an ion gauge which is in the same cross as a turbo molecular pump. All pressures in the MPET vacuum section were, if not otherwise stated, measured at the same position and are at least a sign of relative improvements.
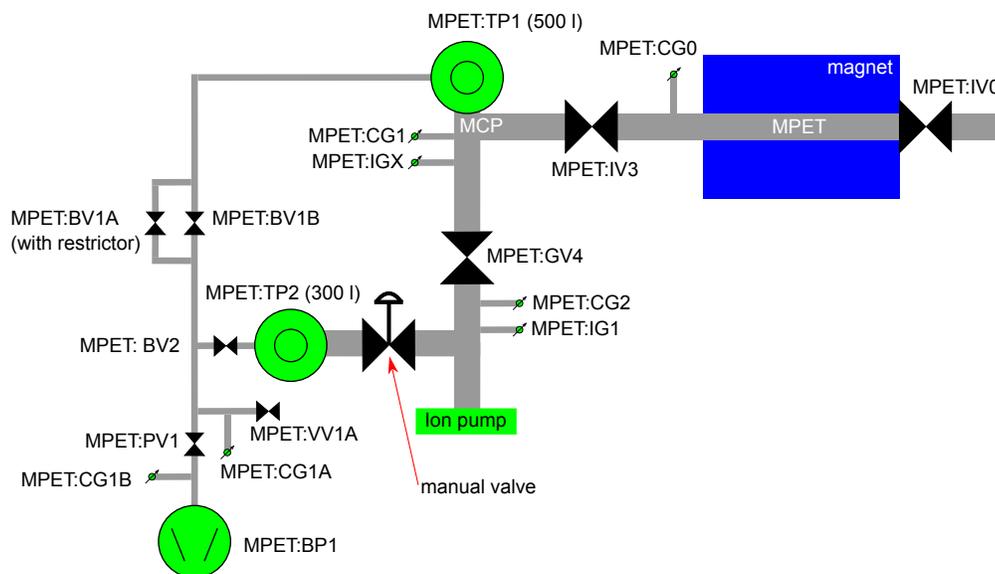
Figure A.8: Diagram of the vacuum system for the MPET. MPET, the detector for TOF, and the ion pump can be separated by valves. The abbreviations stand for ion valve (IV), gate valve (GV), backing valve (BV), venting valve (VV), ion gague (IG), convectron gauge (CG), turbo pump (TP), and backing pump (BP). To maintain the UHV in the MPET itself the valves MPET:IV3 and also MPET:GV4 are usually open. When MPET:IV3 has to be closed, the MPET section is pumped from the other side when MPET:IV0 is open.

documented in [211].

A.5.1   Hardware upgrade for MPET vacuum

The initial vacuum system around MPET consisted of one large volume containing the MPET structure, the MCP detector, and the ion pump. The main drawbacks of this setup were twofold. First, any need for repair on the MCP detector would require venting the full section. Considering that the MPET, the PLT, etc. are essentially pumping restrictions it takes a few weeks before pumping of the MPET section reaches its base pressure again. In this configuration, any detector failure could have led to the cancellation of an online experiment as a quick repair is not feasible. Furthermore, by venting the system, the large surface area of the ion pump could be saturated again, requiring another bake-out of the ion pump. As
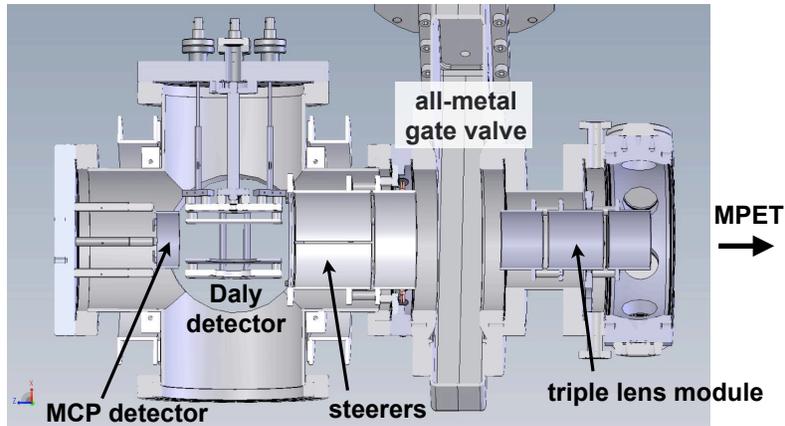
Figure A.9: Rendered technical drawing of the new optic elements on the extraction path to guide the ions to the new position of the MCP. A Daly detector is shown which has also been installed in the same 8" 6-way cross.

a second drawback, a separate baking of the ion pump was not possible because the ion pump could not be enclosed by a valve in a separate vacuum chamber for baking.

A new vacuum system as outlined in Figure A.8 was designed as a remedy to these shortcomings. The MCP detector which used to be installed at the end of the magnet bore (compare with Figure 3.32) is moved back into what is now called the detector cross. By closing the valves MPET:IV3 and MPET:GV4 it can be separated from the trap vacuum and from the ion pump. Hence, detector repairs can be done without venting the other vacuum sections. The vacuum chamber of the detector cross is small and after venting a reasonable pressure ($\sim 10^{-9}$ mbar) can be reached by pumping overnight. The 500 l/s turbo molecular pump (MPET:TP1) has previously not been part of the MPET vacuum setup.

The new position of the MCP detector required additional beam optics elements of which a model is shown in Figure A.9.[3] This setup also includes an MCP-based Daly detector [209, 210]. A detector in addition to the primary MCP detector provides an immediate alternative detection system for the TOF measurement in case of a detector failure. A Daly detector further has the advantage of increased detection efficiency and reduced damage due to radiation and heavy ion impact.

All new parts were cleaned and assembled following strict UHV procedures de-

---

[3]The majority of the new beamline optics has been designed previous to this work.
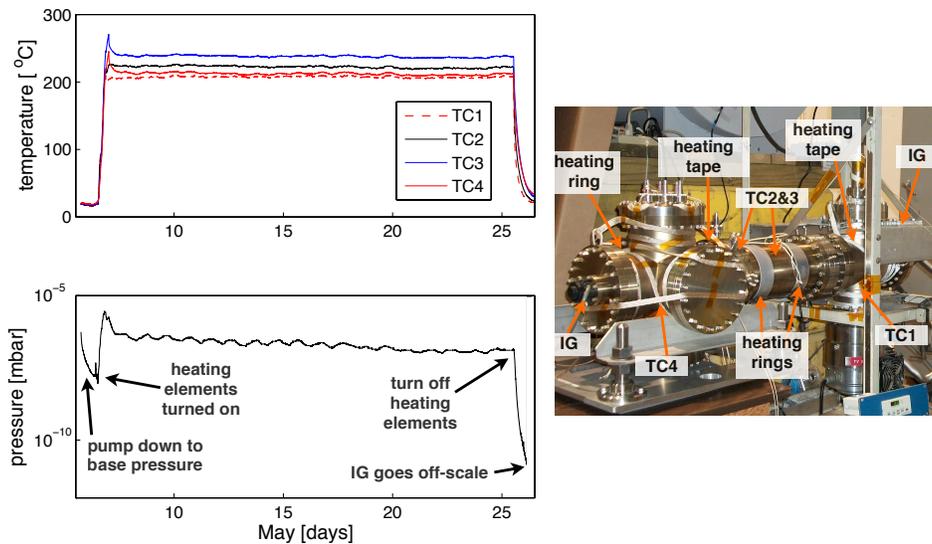
Figure A.10: Baking of the detector cross and the new beam optics elements along the extended extraction path. The picture on the right shows all heating and diagnostics devices before being wrapped in Al-foil and insulating material. The graphs on the left display temperatures and pressure during the baking.

veloped within the TITAN group [237]. Before their final installation, the detector cross including the detector setups (but without the MCPs) as well as the new optic elements were baked at temperatures above 200° C (see Figure A.10). After reducing the temperature to room-temperature, the pressure fell quickly below the detection limit of the ion gauge ($\approx 2 \cdot 10^{-11}$ mbar).[4]

Finally, the section housing the ion pump was baked in two steps. First, sealed by a blind CF flange instead of the valve MPET:GV4 it was heated to temperatures above 200° C at which it stayed for about a week. After the baking, the pressure quickly went below the detection limit of the ion gauge. After venting with N_2 and connecting the section to the valve MPET:GV4, it was baked a second time but at lower temperature ($< 200^o$ C) as recommended by the manufacturer of the gate valve. The valve was closed during the baking. The aim of this two-step process was to remove any oil molecules in the ion pump section during the high temperature baking. Any water entering the section after the venting and installation to the

---

[4]The reliability of an ion gauge at these low pressures in the $\sim 10^{-11}$ mbar range is, however, debatable.

rest of the MPET vacuum setup would be pumped out during the second bake-out at lower temperature.

In the final setup, i.e. with all valves open but with the ion pump turned off, the pressure during the mass measurement of the neutron deficient Rb was $\approx 6 \cdot 10^{-11}$ mbar measured at the ion gauge MPET:IG1. Later, when the ion pump was first tested, the pressure came down further and eventually went off-scale at the ion gauge. Hence, all these combined efforts improved the vacuum by 2 orders of magnitude in comparison to summer 2009 (when the pressure was measured on the same position). When MPET:IGX in the detector cross was briefly turned on, its pressure reading indicated $\approx 5 \cdot 10^{-11}$ mbar.

The current vacuum system has nevertheless a few shortcomings which need to be addressed in the future. Neither the MPET vacuum chamber nor the detector cross house their own ion gauges. These would be critical for proper interlocks regarding the separating vacuum valves and the power supplies for biasing detectors, trap, and beamline optics. In principle an ion gauge is part of the detector cross (see MPET:IGX in Figure A.8). However, it was found to interfere with the MCP detector. When the ion gauge was turned on, an overwhelming background rate of ≈ 15 kHz was registered at the MCP detector. Even moving the ion gauge out of direct sight of the MCP and the installation of a electrostatic barrier [238] for positively and negatively charged particles did not fully solve the problem.

Appendix B

Derivation of the Covariance Matrix due to Shared Reference Measurements

In the evaluation of individual frequency ratios R between the cyclotron frequency of the ion of interest and the reference ions (Equation 3.49), correlations between pairs of R are introduced due to shared references (compare Section 4.2.2). As shown in Figure B.1 there are two scenarios in which two measurements of the ion-of-interest share either one (Figure B.1a) or two (b) reference measurements. In the latter case, two or more measurement runs of the ion-of-interest are recorded between the same reference measurements.

Following the notation in Figure B.1a, the time periods between a measurement of the ion of interest and its neighbouring reference are
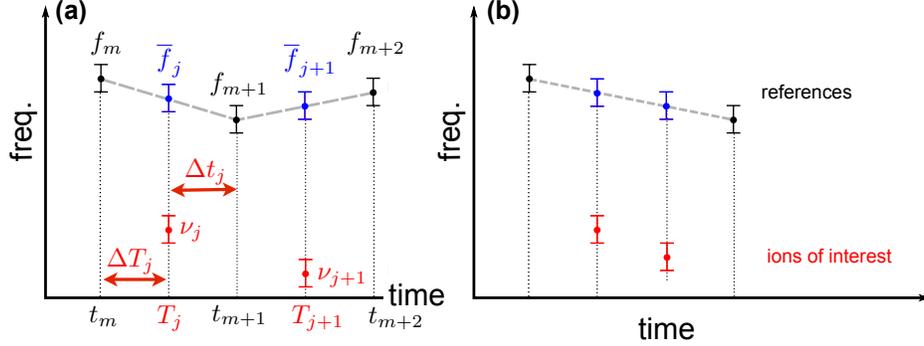
$$
\begin{aligned}
\Delta T_j &= T_j - t_m \\
\Delta t_j &= t_{m+1} - T_j.
\end{aligned}
\tag{B.1}
$$

Then, the interpolated cyclotron frequency of the reference at the time of the measurement run of the ion of interest is

$$
\overline{f}_j = \frac{1}{\Delta t_j + \Delta T_j} \left(f_{m+1} \cdot \Delta T_j + f_m \cdot \Delta t_j \right),
\tag{B.2}
$$

from which a frequency ratio

$$
R_j = \frac{\overline{f}_j}{\nu_j}
\tag{B.3}
$$

Figure B.1: Correlations in frequency ratios due to shared references. Two frequency ratios R_j and R_{j+1} correlated either by one (a) or two (b) common reference measurements.

is obtained. Since in Figure B.1a both R_j and R_{j+1} are according to Equation B.2 dependent on the measured cyclotron frequency f_m, R_j and R_{j+1} are statistically correlated. Assuming Gaussian uncertainties, the required error propagation for the weighted average of R relies on the covariance matrix

$$V_{ij} = cov(R_i, R_j) = \sum_{k,l} \frac{\partial R_i}{\partial f_l} \frac{\partial R_j}{\partial f_k} \cdot cov(f_l, f_k) + \left(\frac{\partial R_i}{\partial \nu_i}\right)^2 \sigma_{\nu_i}^2 \cdot \delta_{ij}, \quad \text{(B.4)}$$

where σ_{ν_i} is the measurement uncertainty on ν_i. Since all reference measurements themselves are statistically independent from each other, the covariance matrix between f_l and f_k is diagonal and equal to $cov(f_l, f_k) = \delta_{lk} \cdot \sigma_{f_k}^2$. Inserting Equation B.3 and Equation B.2 into the last equation yields the covariance matrix for the frequency ratios.
For the diagonal elements, one obtains

$$V_{(j)(j)} = \frac{1}{\nu_j^2(\Delta T_j + \Delta t_j)^2}\left(\sigma_{f_{m+1}}^2 \cdot \Delta T_j^2 + \sigma_{f_m}^2 \cdot \Delta t_j^2\right) + \left(\frac{R_j}{\nu_j}\right)^2 \sigma_{\nu_j}^2 \quad \text{(B.5)}$$

while the correlation between frequency ratios according to Figure B.1a is

$$V_{(j)(j+1)} = \frac{1}{\nu_j\nu_{j+1}(\Delta T_j + \Delta t_j)(\Delta T_{j+1} + \Delta t_{j+1})}\Delta T_j \cdot \Delta t_{j+1}.\sigma_{f_{m+1}}^2. \quad \text{(B.6)}$$

Finally for two frequency ratios which are based on the same two reference measurements such as in Figure B.1b, the correlation is

$$V_{ij} = \frac{1}{\nu_i \nu_j (\Delta T_i + \Delta t_i)^2} \left(\Delta T_i \cdot \Delta T_j . \sigma_{f_{m+1}}^2 + \Delta t_i \cdot \Delta t_j . \sigma_{f_m}^2 \right) \qquad \text{(B.7)}$$

From there, the weighted average over all individual frequency ratios is calculated to

$$\overline{R} = \frac{\sum_{i,j} (V^{-1})_{ij} R_j}{\sum_{i,j} (V^{-1})_{ij}} \qquad \text{(B.8)}$$

with an uncertainty of

$$\sigma_{\overline{R}} = \sqrt{\frac{1}{\sum_{i,j} (V^{-1})_{ij}}}. \qquad \text{(B.9)}$$